THEORETICAL AND EXPERIMENTAL INVESTIGATIONS ON RADIAL ELECTROMAGNETIC FORCES IN RELATION TO VIBRATION PROBLEMS OF INDUCTION MACHINES

A Thesis Submitted to the College of

Graduate Studies and Research

in Partial Fulfillment of the Requirements

for the Degree of Doctor of Philosophy

in the Department of Electrical Engineering

University of Saskatchewan

Saskatoon

By

Anil Balan

Saskatoon, Saskatchewan

June, 1997

University of Saskatchewan
College of Graduate Studies and Research

SUMMARY OF DISSERTATION

Submitted in Partial Fulfillment of the Requirements for the

DEGREE OF DOCTOR OF PHILOSOPHY

by

ANIL BALAN
Department of Electrical Engineering
University of Saskatchewan
1997

Examining Committee :

Dr. M.M. Gupta	Dean / Associate Dean, Dean's Designate, Chair College of Graduate Studies and Research
Dr. T.S. Sidhu	Advisory Committee Chairman, Department of Electrical Engineering
Dr. S.P. Verma	Supervisor, Department of Electrical Engineering
Dr. A. Hirose	Advisory Member, Department of Physics and Engineering Physics
Dr. A.M. El-Serafi	Advisory Member, Department of Electrical Engineering
Dr. H.C. Wood	Advisory Member, Department of Electrical Engineering

External Examiner :

Dr.-Ing. K. Reichert
Professor & Director,
Institut für Elektrische Maschinen,
ETH - Zentrum,
CH-8092,
Zurich, Switzerland.

Theoretical and Experimental Investigations on Radial Electromagnetic Forces in Relation to Vibration Problems of Induction Machines

Accurate assessment of the electromagnetic excitation forces and the vibration behaviour of stators is essential to arrive at a suitable design for quiet operation of an electrical machine. These electromagnetic forces are produced on the surfaces of the stator and rotor along the air-gap periphery. The physical mechanisms underlying the production of the electromagnetic forces, and the characteristics of the ensuing vibrations are described in this thesis.

In this thesis, comprehensive analytical methods are developed for the determination of the radial electromagnetic forces in squirrel-cage and wound-rotor induction machines. Various magnetic fields are generated due to the distribution of the windings in slots, slotting of the stator and rotor surfaces, and magnetic saturation of the iron. The air-gap fields are determined using the permeance method by expressing the MMF and the air-gap permeance as waves. In the analyses, the mutual interactions between the stator and rotor are incorporated. Their effects on the electromagnetic forces are discussed from the perspective of the production of vibrations.

Extensive investigations were conducted on a 7.5 kW squirrel-cage induction motor and a 70 kW wound-rotor induction motor to verify the validity of the analyses. The comparisons made between the experimental and the analytical results prove the general validity of the analytical methods. Conclusions are drawn with a view to determine the actual role played by the harmonic air-gap fields on the production of the electromagnetic forces and the ensuing vibrations. In the course of these investigations, an experimental set-up which is particularly suited for the measurement of magnetic fields, forces, resonances, vibrations and noise was developed.

A fundamental study on the vibration behaviour of electrical machine stators using an experimental modal-analysis is presented in the thesis. Modal-analysis is a process of forcing a structure to vibrate predominantly at a selected resonance. To achieve this distributed electromagnetic forces are used. Detailed investigations were conducted on the stator models of a 120 hp induction motor to study their vibration behaviour, and to critically examine the damping present in them. The interpretations of the results given in the thesis would help in acquiring a better understanding of the vibration behaviour of stators in relation to the problem of electromagnetic acoustic noise in electrical machines.

To my Mummy & Pappaji

and

Rukmini

PERMISSION TO USE

In presenting this thesis in partial fulfilment of the requirements for a Postgraduate degree from the University of Saskatchewan, I agree that the Libraries of this University may make it freely available for inspection. I further agree that permission for copying of this thesis in any manner, in whole or in part, for scholarly purposes may be granted by the professor or professors who supervised my thesis work or, in their absence, by the Head of the Department or the Dean of the College in which my thesis work was done. It is understood that any copying or publication or use of this thesis or parts thereof for financial gain shall not be allowed without my written permission. It is also understood that due recognition shall be given to me and to the University of Saskatchewan in any scholarly use which may be made of any material in my thesis.

Requests for permission to copy or to make other use of material in this thesis in whole or part should be addressed to:

Head,
Department of Electrical Engineering
University of Saskatchewan
Saskatoon, Saskatchewan S7N 5A9
Canada

ABSTRACT

Accurate assessment of the electromagnetic excitation forces and the vibration behaviour of stators is essential to arrive at a suitable design for quiet operation of an electrical machine. These electromagnetic forces are produced on the surfaces of the stator and rotor along the air-gap periphery. The physical mechanisms underlying the production of the electromagnetic forces, and the characteristics of the ensuing vibrations are described in this thesis.

In this thesis, comprehensive analytical methods are developed for the determination of the radial electromagnetic forces in squirrel-cage and wound-rotor induction machines. Various magnetic fields are generated due to the distribution of the windings in slots, the slotting of the stator and rotor surfaces, and the magnetic saturation of the iron. The air-gap fields are determined using the permeance method by expressing the MMF and the air-gap permeance as waves. In the analyses, the mutual interactions between the stator and rotor are incorporated. As the load increases, these interactions become prominent and influence significantly the nature of the air-gap field. Their effects on the electromagnetic forces are discussed from the perspective of the production of vibrations.

Extensive investigations were conducted on a 7.5 kW squirrel-cage induction motor and a 70 kW wound-rotor induction motor to verify the validity of the analyses. The comparisons made between the experimental and the analytical results prove the general validity of the analytical methods. Conclusions are drawn with a view to determine the actual role played by the harmonic air-gap fields on the production of the electromagnetic forces and the ensuing vibrations. In the course of these investigations, an experimental set-up which is particularly suited for the measurement of magnetic fields, magnetic forces, resonant frequencies, vibrations and noise was developed.

A fundamental study on the vibration behaviour of electrical machine stators using an experimental modal-analysis is presented in the thesis. Modal-analysis is a process of forcing a structure to vibrate predominantly at a selected resonance. In order to achieve this, distributed electromagnetic forces are used. Detailed investigations were conducted on the stator models of a 120 hp induction motor to study their vibration behaviour, and to critically examine the damping present in them. The physical interpretations of the results given in the thesis would help in acquiring a better understanding of the vibration behaviour of stators in relation to the problem of electromagnetic acoustic noise in electrical machines.

This work was supported by the National Sciences and Engineering Research Council of Canada through grant no. OGP0004324.

ACKNOWLEDGEMENTS

It is with deep appreciation and gratitude that the author expresses his thanks to Dr. S.P. Verma for his valuable guidance, encouragement and understanding throughout the duration of this research project. His provocative discussions, invaluable assistance and many hours of patience in the preparation of this thesis are especially acknowledged.

Also, the author wishes to extend his thanks to the members of the advisory committee for their valuable time and interest shown in the project, and to the staff members of the Department of Electrical Engineering who directly or indirectly extended their help in the course of the investigations.

Many thanks are due to Mr. Wayne McMillan and Mr. Henry Berg of the Central Workshop, College of Engineering, for their help in fabrication of the experimental models, and to Mr. Wen Yang and Mr. Chitra Khadka for their help in preparation and set-up of the experimental arrangements. The author would like to thank Mr. Rick White of Westinghouse Canada Inc., Saskatoon, for his advice on the installation of windings.

The financial assistance for this work provided by the National Sciences and Engineering Research Council of Canada through Grant No. OGP0004324 is thankfully acknowledged. The author would like to thank the Department of Electrical Engineering for providing the facilities, and also to Prof. H.C. Wood for the financial assistance provided for the fabrication of the models.

TABLE OF CONTENTS

LIST OF TABLES

LIST OF FIGURES

LIST OF PRINCIPAL SYMBOLS

$B(\theta,t)$	Air-gap flux-density distribution, T
E	Induced voltage, V
$F(\theta,t)$	Force-wave, N/m^2
I	Current, A
K_{vw1}	Stator winding factor for the ν^{th} order harmonic
K_{vw2}	Rotor winding factor for the ν^{th} order harmonic
L	Self-inductance, H
$M(\theta,t)$	MMF-wave
$M_{1,2}$ & $M_{2,1}$	Mutual inductances, H
N	Effective turns per coil in a stator or rotor phase-belt
R	Resistance, Ω
S	Number of stator slots
V	Voltage, V
Z	Number of rotor slots
[C]	Damping matrix
[F]	Force matrix
[I]	Identity matrix
[K]	Stiffness matrix
[M]	Mass matrix
f	Supply frequency, Hz
l_e	Effective length of stator-core
m	Longitudinal mode-shape
m_1 & m_2	Number of stator and rotor phases
n	Circumferential mode-shape
p	Number of pole-pairs of the fundamental field
q	Number of slots per pole per phase
r	Radius of the stator-bore, m
s	Slip
s_ν & s_{g_2}	Harmonic slip
t	Time, s
x	Displacement
y	Coil-pitch

α_S & α_R	Slot-angle of stator and rotor, mechanical radians
δ'	Corrected air-gap length, m
ζ	Damping-ratio
θ	Angular co-ordinate, mechanical radians
λ	Permeance, Wb/A
μ_0	Permeability of free space, H/m
ν, μ, ε	Harmonic orders
τ	Pole-pitch, m
ψ	Phase-angle, electrical radians
ω	Angular frequency, rad/s
$[\phi]$	Mode-shape matrix

—

subscripts

1	refers to stator
2	refers to rotor
k	k^{th} stator phase
n	n^{th} rotor mesh
b,z	z^{th} rotor bar
d	d^{th} rotor phase
S1,S2	slot-leakage
N1,N2	end-leakage

g_1, g_2, g_3, ρ, γ, η and σ are indices

1. INTRODUCTION

The ever increasing applications of electrical machines have resulted in a growing concern about the problems of noise produced by them. Modern electrical machine design trends are towards the use of higher currents and flux-densities, which often result in noisy electrical machines. The lowest cost per unit output is chosen as the principal design criterion and little or no attention is devoted to the noise and vibration problems. Further, in order to keep the machine size to a minimum and maximize efficiency, high speed motors are used wherever possible. Indiscrete reduction of the machine size can result in substantial decrease of vital vibration-damping present in the machine structure. This leads to an increase in the ensuing mechanical response of the machine stator. Such electrical machines are inevitably a source of considerable magnetic, windage and mechanical noise [1].

Polyphase induction machines are the most widely used drive motors in the industry. As well known, the two kinds of induction machines are the squirrel-cage type and the wound-rotor type. The squirrel-cage induction machines are known for their low cost, simplicity and robustness. Consequently, the majority of the polyphase induction motors manufactured, and in service, are squirrel-cage induction motors. From the consideration of the temperature rise of the rotor windings, the wound-rotor type polyphase induction motor is preferred when a large size motor is required. The design, construction and operation of these machines have improved considerably over the years. With respect to vibration and noise problems, however, much more understanding and the necessary improvements are still required.

The investigations reported in this thesis mainly concern the vibration and noise aspects of polyphase induction motors. Although the investigations are focused on induction machines, the fundamental results presented in this thesis will be applicable to other types of rotating electrical machines. It is of advantage at this stage to provide some information about the common applications of induction machines.

Polyphase induction motors span over a range of ratings from 1/2 hp to as large as 45000 hp, depending on the capability of the local electrical power system. Most motors convert at least 80% of their electrical input energy into useful mechanical output. For large machines, the efficiencies are often higher than 90%. The U.S. government owns four induction motors, each with a power rating of 45000 hp, and a synchronous speed of 720 rpm. These are perhaps the largest induction motors built until 1986 [2]. Table 1.1 shows the population of induction motors according to the power rating. Almost 70% of the electricity generated in Europe is used to drive motors. It has been estimated that if all of Europe's motors were as efficient as today's best designed induction motors, Europe's electricity demand can be reduced by about 3000 MW, and the carbon dioxide emissions reduced by about 13.4 million tonnes. If variable-speed drives were used on all pump and fan drives, these figures could be tripled. The biggest potential for raising efficiency is in small motors driving loads such as pumps, fans and compressors. They represent 60% of the total motor load [3]. However, the practical realization of variable-speed drives are often plagued with problems of increased vibration and noise levels, and other secondary drawbacks such as additional heating, torque-ripples etc.

1.1 The Noise Problem

Table 1.2 shows the classification of the electrical machine noise according to its origin, and it helps in explaining the nature and production of each of them. Mechanical noise is mainly associated with imbalances in the rotor assembly, and they usually

Table 1.1 : Estimated population of polyphase induction motors in the United States [2].

Horsepower Rating	Population
5 - 20	10,000,000
21 - 50	3,300,000
51 - 125	1,700,000
126 and larger	400,000

Table 1.2 : Sources of Acoustic Noise [4].

Electrical Machine Noise					
Category:	Ventilation			Electro-magnetic	Mechanical
	Broadband	Siren	Howling		
How the noise arises:	Rotation of structural parts in air Eddies, non-periodic fluctuation of air pressure	Relative movement between rotating and stationary parts Periodic fluctuation of air pressure	Excitation of resonance in cavities Periodic fluctuation of air pressure	Magnetic flux pulsations through the iron	Unbalanced rotor, bearing noise
Nature of noise:	Random Noise	Pure tones	Pure tones	Pure tones	Pure tones
Frequency:		Speed dependent	Speed independent	No. of slots, supply frequency & speed	Speed dependent

manifest as a source of concern in small size electrical machines. Magnetic noise and windage-noise predominate in medium and large size electrical machines [4]. The noise induced by the flow of air is called windage-noise, and it is associated with the ventilation system. The increased specific outputs of electrical machines, which have been realised by manufacturers in recent years, frequently dictate the need for increased ventilation of machines. Generally, windage-noise has a uniform distribution of intensity across the audio spectrum and is mainly associated with air turbulence. Occasionally, however, the pulsing of the air through a cavity or air duct can produce pure tone components at the resonances of the air cavity [1,5]. Magnetic noise is a basic source of noise and it is produced by the magnetic fields in a machine. Since the magnetic field is the medium through which the power is transferred between the stator and the

rotor, magnetic noise is unavoidable. The radial-forces, known as Maxwell's forces, that act on the stator and rotor are associated with the magnetic fluxes entering or leaving the iron surfaces. The harmonic content of the magnetic fields accentuates the problem of magnetic noise and they are also responsible for other undesirable effects such as parasitic torques and stray losses.

The effects on human-hearing from exposure to high levels of noise depend on the duration of the exposure. The damages resulting from exposure to different noise intensities and durations are well established. The associated hearing loss may be temporary or permanent. Apart from the employer/employee concerns with the inherent hazards of noise, added attention has been brought to focus through regulatory requirements. Under the Occupational Safety and Health Act, every employer is legally responsible for providing a workplace free of health hazards, such as excessive noise [6,7]. According to the Saskatchewan and Canadian legislation, the maximum allowable exposure is 85 dB(A) based on the time-weighted averages over an eight-hour day.

The maximum allowable noise levels associated with the operation of electrical machines of different sizes and speeds are stipulated in the various standards [8]. Although these noise levels represent the upper limit, they do not necessarily reflect upon the achievable levels with the present state of art in the design of electrical machines. Considering the physiological characteristics of the human ear, magnetic noise of electrical machines is particularly troublesome since it is characterised by many pure tones. In this connection, the British Standard for noise levels permitted in mixed residential and industrial areas - BS4142 requires the reduction of the broadband noise by 5 dB in the presence of pure tone components [9]. In practice, reducing the broadband noise by 5 dB is much more expensive and difficult than eliminating the pure tones. Even if the noise level is reduced, the pure tone components will be distinguishable and they continue to be a source of annoyance. It is, therefore, essential to eliminate or at least reduce the loudness of the pure tones in the electromagnetic noise produced by electrical machines.

Excessive amplitudes of vibrations can cause failures of components by metal fatigue, and cause radiation of noise and hence customer discomfort. To reduce the

noise generated by an electrical machine, it is more practical and economical to reduce the vibrations produced within the machine itself by adopting an appropriate design rather than to suppress the noise and vibrations through external means. As reported in several references [9-13], quiet operation of electrical machines is achieved through detailed engineering analysis of the total design and not by applying external remedies. It is of paramount importance to reduce the mechanical response of both the stator and the rotor to the electromagnetic forces. In view of the above, the determination of the exciting radial-forces and the vibration response of the machine structures are very important from the perspective of designing quieter electrical machines.

1.2 Review of the Published Literature

The noise producing Maxwell's forces are produced due to the pulsations of the magnetic fluxes through the iron members of an electrical machine. Determination of Maxwell's forces, therefore, requires accurate determination of the magnetic fields. The harmonics in the magnetic fields are produced due to the distribution of the current carrying conductors in slots around the periphery of the machine, slotting of the stator and rotor surfaces, magnetic saturation of the iron, eccentricity of the rotor and the harmonics in the power supply. The commonly used techniques for the determination of the magnetic fields are the permeance-wave method [1,14,15], the rotating field approach [16-18], the conformal transformation technique [19-21] and the finite element methods [22-25]. It is well known that the technique of conformal transformation is particularly suited to the slotting problems and it can account for sharp corners. In the conformal transformation technique, unfortunately, it is necessary to consider the iron boundaries to be highly permeable, which is not the case in practice. The effects of saturation cannot be easily incorporated in the conformal transformation techniques. The finite element and finite difference methods are well suited for the determination of flux distributions in a machine while treating the effects of iron saturation. The conformal, finite-element and finite-difference methods, however, require extensive computation and the results apply only to the assumed condition of loading. Therefore, although the finite element techniques are quite powerful and accurate, they may not be very effective and convenient for the determination of the magnetic forces. This is mainly due to the fact

that the vibration response of the electrical machine structure cannot be determined with the same level of accuracy as the magnetic forces. In addition, while determining the mechanical response of the electrical machine structure it is more important to know the frequency, circumferential and axial distributions of the magnetic forces accurately than the amplitudes alone. This information can be easily, and accurately, determined with the use of the permeance-wave approach. Since at any instant of time the spatial distribution of the air-gap flux is not uniform along the circumference, the air-gap field can be analyzed and represented as a series of rotating field-harmonics. The use of permeance-waves reveals all the field-harmonics with proper orders, and provides comprehensive information about the radial-forces. The permeance-wave approach has been commonly used by many investigators because of its ease and the physical perspective that it provides. Further, with the use of permeance-wave approach it is possible to study the effects of saturation [26-28], eccentricity [15] and time-harmonics in the power supply [29-32] easily. Oberettl [16,17] presents an interesting technique which provides information about the air-gap fields assuming that both the stator and rotor surfaces are smooth. In this technique the mutual interactions between the stator and rotor MMFs are considered. In reference [33], an analysis is developed for the determination of the air-gap fields of squirrel-cage induction motors by combining the permeance-wave approach and Oberettl's techniques to account for the mutual interactions between the stator and rotor windings. This analysis is simple and efficient, and it provides acceptable results for various components of the magnetic field and Maxwell's forces at desired load levels between no-load and full-load.

In order to reduce the radiated electromagnetic acoustic noise from electrical machines, it is important to understand the vibrational behaviour of stators. Vibrations, and therefore the radiated acoustic noise, can be reduced to a large extent if coincidences between the exciting force-frequencies and the resonant frequencies of the stator of an electrical machine are avoided. Often it is impossible to avoid such coincidences at all operating conditions, such as under variable frequency operation of electrical motors. Through the use of an analytical vibration model, a designer can predetermine the resulting vibrations and thereby optimize the motor design from the perspective of noise and vibrations. An accurate determination of the vibration characteristics and the

resonant frequencies of electrical machine stators is therefore of paramount importance in the design of quiet electrical machines.

Several analyses have been developed for the determination of the resonant frequencies of stators of electrical machines. Most researchers [1,34] confined their attention to the lowest resonant frequency associated with a particular mode of vibration. It was assumed that this frequency was the only significant resonant frequency of a stator when considering vibrational problems in electrical machines. Although this can be true for small size machines, it is certainly not the case in large machines where several resonant frequencies for each mode of vibration may lie within the critical frequency range of audible noise production [35,36]. Some of the early work in this area treated the stator as a simple ring or a thin cylindrical-shell model [34]. In these techniques, the teeth and the windings were either treated as additional mass or as cantilever beams [37]. A comprehensive analysis incorporating the effects of the teeth, windings and the frame was developed and reported in reference [9]. This analysis is based on the three dimensional theory of elasticity and it uses the energy method incorporating the Rayleigh-Ritz principles. The experimental validity of the analysis with respect to short, medium and long length stators is reported in references [38,39].

If the frequency of the exciting force coincides with a resonant frequency of the machine structure, the amplitude of vibrations will increase until the energy dissipated is equal to the energy supplied by the exciting forces. Damping, which is a measure of the energy dissipation in a vibrating system, is very beneficial in reducing the response of a system at resonance. In the analytical determination of the resonant frequencies and the associated mode-shapes satisfactory results can be achieved by neglecting the effects of damping. It is important, however, to know the amount and nature of damping present in the vibrating structure while determining its forced response. An accurate mathematical formulation of the damping is very complex in a practical structure. Nevertheless, it is possible to get good estimates of the damping forces and their nature using the experimental methods [40,41]. With regard to the actual contributions of the laminations and windings to the damping present in electrical machine stators, the required information is not available in the published literature to the knowledge of the author.

1.3 Objectives of the Thesis

As explained earlier, the various electromagnetic forces acting on the stator and rotor of an electrical machine may produce excessive vibrations and noise, especially when the frequencies of the exciting forces are equal to, or near, resonant frequencies of the machine structure. The vibrations, and subsequently the radiated noise level, produced by an electrical machine can be reduced to a large extent by designing the machine in such a manner that the mechanical response of the vibrating structure to the excitation forces is minimal.

Although extensive information on the determination of magnetic fields and the resonant frequencies is available in the literature, the information on the spectral distribution and magnitudes of the exciting radial-forces is extremely limited. A better understanding of the noise producing radial-forces will definitely help in achieving a good sonic design. Accordingly, a simple and comprehensive analysis needs to be developed for the calculation of the various field-harmonics and radial-forces in squirrel-cage and wound-rotor induction motors.

Most of the theoretical methods for the determination of the magnetic forces yield a multitude of force components having different circumferential distributions at various frequencies. To keep the analysis effective and manageable, it is often required to obtain a short list of dominant components. The identification of the significant components involves the consideration of the forces associated with fewer number of force-poles. In references [31,42], the authors have neglected the force components that have more than 4 pairs of force-poles. This condition is based on the assumption that the vibration amplitudes of the electrical machine structure diminish with increasing number of pairs of force-poles. This is valid for stators of small and medium size electrical machines. In the case of stators of large machines, many resonances with higher modes occur in the significant portion of the audible frequency range [35]. It is important to closely examine the amplitudes, frequencies and circumferential distributions of the radial-forces.

The basic rule of avoiding excitation of resonances for a machine operating from a sinusoidal source of supply at a constant frequency can be satisfied with some efforts. Such a stringent requirement can not be always met under all operating conditions, such as variable frequency operation of induction motors. At certain frequencies, the radial-

forces will excite some of the resonances of the machine structure. It is, therefore, necessary to investigate the vibration response of the machine structure to the various electromagnetic radial-forces at its resonances. Further, it would be necessary to examine the correlation between the circumferential mode of vibration associated with a resonance, and the circumferential distribution of the exciting electromagnetic radial-forces.

The conventional methods of experimental determination of the vibration behaviour involve the use of impulse or hammer excitation, and electromagnetic shakers which can provide a point-excitation. Due to the use of a point-excitation-system, even the resonances at or near a harmonic of the fundamental excitation frequency could be excited. Also, it is difficult to avoid interferences from other near-by resonances in the measurement. This is particularly true for laminated structures, such as stators and rotors of electrical machines, where there could be many resonant frequencies occurring close to each other [9,39]. The measurement of the modal-parameters are consequently plagued with inaccuracies when they are determined using a point-excitation-system. In view of these observations, experimental investigations on the vibration behaviour of electrical machine stators using distributed excitation forces is highly desired.

Although a variety of instruments for the measurement of sound and vibrations are commercially available, there exists a need to develop an experimental set-up which is particularly suitable for the study of noise and vibration problems of electric machines. The conventional methods for the measurement of resonant frequencies, vibration and noise are very laborious and time consuming [43]. It is proposed to develop a suitable measurement system based on digital processing of signals for the experimental measurement of resonant frequencies, vibrations and noise.

1.4 A Brief Description of the Thesis Contents

This thesis presents theoretical and experimental studies of the electromagnetic radial-forces produced in induction motors. The investigations are conducted with a view to understand and predict the nature of the ensuing vibrations. The analytical techniques and experimental investigations are provided to explain the production of the radial-forces and the resulting vibrations from the perspective of noise problems.

In Chapter 2, an analysis of a general nature is developed for the determination of the electromagnetic fields and radial-forces of squirrel-cage and wound-rotor type of induction motors. The analysis is based on the permeance-wave method for the determination of the air-gap fields. The use of permeance-waves reveals all the field-harmonics with proper orders, and provides comprehensive information about the radial-forces. The MMF distribution of the stator and rotor windings and the permeance variation of the air-gap of the induction machine are analyzed and modelled in the form of appropriate waves. The mutual interactions between the stator and rotor are determined and they are incorporated in the formulation of the MMF-waves. The permeance variations of the air-gap produced due to the presence of slots on the stator and rotor are considered in the permeance-wave. Magnetic saturation is treated as an additional effect. The effect of saturation is modelled as a variation in the air-gap permeance. Its role in context with the overall production of the exciting-forces is secondary. The general nature of the analysis permits easy extensions to incorporate the effects of eccentricity of the rotor, different winding arrangements and the time-harmonics in the supply.

In Chapter 3, a 10 hp (7.5 kW) squirrel-cage induction motor and a 94 hp (70 kW) wound-rotor induction motor are analyzed. After discussing the calculated results of the test motors, the experimental set-up and the procedures adopted to conduct the experimentation are described. Also, the effects of loading on the radial-forces and the ensuing vibrations are closely examined. The theoretical and experimental results are presented with a view to determine the actual role played by the air-gap harmonic fields on the radial-forces.

In Chapters 4 and 5, the vibration behaviour of stators of electrical machines are studied using electromagnetic forces, which are distributed over the entire surface of the stator. The conventional methods of experimentally testing the vibration behaviour of stators involve the use of a point-excitation. Although the point-excitation system provides useful information on the vibration response of the electrical machine structure, it is necessary to examine the response of the electrical machine structure to the distributed surface excitation which represents the actual condition in an electrical machine. In Chapter 4, the experimental set-up which was designed and built to test the

stator models of a 120 hp induction motor using surface excitation is described. The vibration response of the stator models to different circumferential distributions of the electromagnetic forces are studied, and the results of the experimental investigations are reported in Chapter 5. The distributed electromagnetic forces are used to individually excite the resonances of the stator models, and thereby assess the nature and amount of vibration damping present in the stator models.

Chapter 6 describes the considerations involved in the sonic design of induction motors suitable for variable frequency operation. The requirement of a wide and continuous range of speeds is popularly achieved by operating the induction motor from a variable frequency power source. Such operating conditions make it impossible to avoid coincidence between the excitation force-frequencies and the resonant frequencies of the machine. The choice of design parameters, such as the number of stator and rotor slots, determines the nature and distribution of the radial-forces. Finally, using the information with regard to the mechanical response of the stator of an electrical machine to distributed forces, the best choice of the slot-combination is identified from the perspective of vibrations and noise.

The important conclusions are provided in Chapter 7.

Six appendices are given at the end of this thesis. In Appendix A, the effects of the triplen-harmonic fields that are produced due to multiple armature reactions are described. The computation procedure for the determination of the magnetic fields and the radial-forces is provided in Appendix B. The design details of the rotor windings used for the electromagnetic surface excitation system are given in Appendix C. The relationship between the force-distribution and the circumferential mode of vibration is described in Appendix D. The resonances of the rotor structure used in the electromagnetic surface excitation system were determined using a magnetic shaker. These investigations are reported in Appendix E. Finally, in Appendix F, the nature of the damping mechanisms present in vibrating structures is described.

2. THEORETICAL ANALYSIS FOR THE CALCULATIONS OF MAGNETIC FORCES

The radial electromagnetic forces in induction motors, as already explained, play very important role in the production of audible noise and vibrations. The magnetic flux pulsations at the iron surfaces produce these radial-forces, which induce vibrations in the stator and rotor structures. An analysis for the calculation of the various field-harmonics and radial-forces in squirrel-cage and wound-rotor induction motors is presented in this chapter.

2.1 Introduction

The presence of harmonic-fluxes in the air-gap of an induction machine produces a variety of undesirable phenomena such as parasitic torques, stray-losses and electromagnetic noise. The radial-forces, known as Maxwell's forces, that act on the stator and the rotor are associated with the magnetic fluxes entering or leaving the iron surfaces. Therefore, an analysis of the vibrations and hence the sound generated by an electrical machine, can reveal the exact nature of the air-gap field. The harmonics in the air-gap field are produced due to the distribution of the current carrying conductors in slots, slotting of the stator and rotor surfaces and magnetic saturation of the iron. Also, another inadvertent source of harmonic production is the eccentricity of the rotor.

In reference [21], the authors have examined the influence of slot-combinations on the flux and force pulsations by employing a conformal transformation technique. It is well known that the technique of conformal transformation is particularly suitable for the slotting problems since it can account for sharp corners. In the application of conformal transformation technique, unfortunately, it is necessary to consider the iron-boundaries to be highly permeable which is not the case in practice. Therefore, the effects of saturation cannot be easily incorporated in the conformal transformation

technique. The finite-element and finite-difference methods are well suited for the determination of flux distributions in a machine which allow for iron saturation. However, these methods require extensive computing and the results apply only to the given conditions of loading.

Although, these techniques are quite powerful and accurate the effort involved may not be of great benefit for the determination of the magnetic forces in relation to the noise and vibration problems of electrical machines. This is mainly due to the fact that the vibration response of the structures of electrical machine cannot be determined to the same level of accuracy as the magnetic forces. Secondly, while determining the mechanical response of the electrical machine structures it is more important to know the frequency, the circumferential distribution and the axial distribution of the magnetic forces. The accurate determination of the magnitudes of the radial-forces is desirable but is not absolutely necessary. The required information can be easily obtained with the help of the permeance-wave approach. Since at any instant of time the spatial distribution of the air-gap flux is not uniform along the circumference, the air-gap field can be analyzed and represented as a series of rotating field components. The rotating field approach has been commonly used by many investigators because of its ease and the physical perspective that it provides. Furthermore, with the use of permeance-wave approach it is possible to study the effects of saturation, eccentricity and time-harmonics if present in the power supply [1,31,33,44].

Oberretl [16,17] presents an interesting technique which provides information about the air-gap fields assuming that both the stator and rotor surfaces are smooth. This technique considers the mutual interaction between the stator and rotor MMF's. The authors of reference [31] have predicted the noise produced by an inverter-fed motor. They considered the effects of harmonics in the inverter supply but neglected the effects of slotting and saturation. However, in actual machines the distribution and magnitudes of all the harmonic-fields are significantly affected by the permeance variations due to the presence of slots on the stator and rotor surfaces.

The permeance-wave approach lends itself easily to incorporate the effects of saturation and eccentricity [14,15,27,28]. The use of permeance-waves essentially involves the consideration of only the radial field components in the air-gap. Despite

this underlying approximation, the use of this method is justifiable since most of the noise producing electromagnetic forces are radially directed in an electrical machine. Also, the use of permeance-waves reveals all the field-harmonics with proper orders, and provides comprehensive information about the radial-forces.

In this analysis, the permeance-wave approach is adopted to determine the air-gap fields. In addition, the effects of multiple armature reaction and saturation have been incorporated in order to investigate their effects on the radial-forces.

2.2 The Analytical Approach

The permeance method has its premises in the idea of treating the air-gap MMF, permeance and flux-density to have a circumferential distribution along the air-gap. They are, therefore, modelled and expressed as appropriate waves. The MMF-waves are determined as the cumulative effect of the stator and rotor MMF's, taking into account the mutual interactions between them. The permeance-waves are formulated by incorporating the effects of slotting, and if necessary magnetic saturation and eccentricity. The air-gap flux-density is then found by the multiplication of the MMF and the permeance-waves. The Maxwell's force per unit area that acts on the stator and rotor surfaces is proportional to the square of the flux-density. Thus, the forces acting on the stator and rotor can be easily obtained from the air-gap flux-density distribution.

For the sake of simplicity the machine is assumed to operate on a symmetrical m_1-phase supply system. In so far as the acoustic noise producing magnetic forces are concerned, the dominant force components are produced due to the stator and rotor MMF-harmonics, and the permeance variations due to the stator and rotor slots. The mutual interactions between the stator and rotor, which significantly affect the forces, are taken into account. The effects of magnetic saturation and eccentricity can be treated as additional effects, as their role in context with the overall production of the exciting-forces is secondary.

2.3 MMF-waves

The MMF-waves are determined by assuming that all the current carrying conductors are located on smooth stator and rotor surfaces. To account for the reduced

average air-gap permeance in the presence of slots, a corrected value for the air-gap length is used while calculating the air-gap harmonic fields produced by the stator and rotor MMF's. The air-gap length extension factor is determined by using Carter's coefficient for stator and rotor slotting [14,19]. At no-load, the rotor currents are negligible and hence only the stator MMF acts across the air-gap. The stepped distribution of the stator MMF produces space harmonic-fields in the air-gap of the machine. As the load on the machine increases, the rotor slows down producing large circulating currents in it's windings. Consequently, the ampere turns of the rotor tend to demagnetise the machine, with the result that the stator draws additional current to maintain the mutual air-gap flux. The stator produced air-gap harmonic fields induce currents in the rotor windings at different slip frequencies, and their magnitudes depend on the rotor winding arrangement. The non-sinusoidal current sheet of the rotor produces additional harmonics in the air-gap. Further, the air-gap harmonic fields generated by the rotor induce currents in the stator windings at frequencies related to the number of rotor-bars and the speed of the rotor. This process of mutual interaction is called multiple armature reaction, as illustrated in Fig. 2.1. Detailed description of this phenomenon is given in reference [44]. Considerations up to the tertiary or quaternary reactions are sufficient for most induction machines [16,17]. The stator and rotor MMF's are found from their respective current sheets, and the net air-gap MMF is determined as the cumulative effect of both.

From the discussion aforementioned, the air-gap of the induction machine is assumed to have a constant uniform permeance, based on the corrected value of the air-gap length, δ'. Further, it is assumed that the iron has infinite permeability which will produce a stepped air-gap field having the same form as that of the MMF-wave.

To make the analysis of general nature, let the stator have m_1-phase windings, and the voltage impressed across the k^{th} phase be given by:

$$V_{1,k} = V_1 \sqrt{2} \cos\left(\omega t - (k-1)\frac{2\pi}{m_1} + \psi \right). \tag{2.1}$$

Accordingly, the current drawn by the k^{th} phase from the supply can be written as:

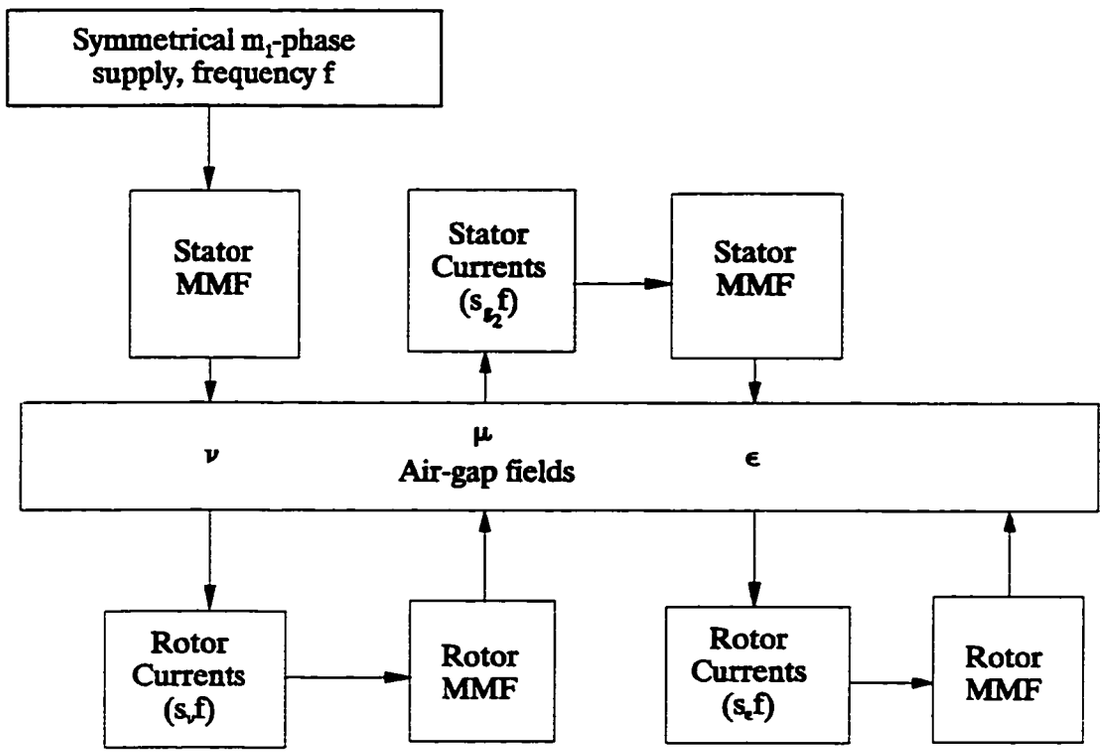

Figure 2.1 : Schematic diagram explaining multiple armature reaction.

$$I_{1,k} = \underset{(f)}{I_1}\ \sqrt{2}\ \cos\left(\omega t - (k-1)\frac{2\pi}{m_1}\right), \tag{2.2}$$

where $\underset{(f)}{I_1}$ represents the stator current of fundamental frequency, f and it lags the voltage by an angle ψ. The ν^{th} order harmonic air-gap field produced by an integral slot stator winding can be shown to be:

$$B_{1\nu}(\theta_1) = q_1 m_1 2p \frac{\mu_0 N_1}{\pi(\nu p)\delta'} K_{\nu w1} \underset{(f)}{I_1}\ \sqrt{2}\cos(\omega t - \nu p\theta_1), \tag{2.3}$$

where νp is the number of pole-pairs of the ν^{th} harmonic. Further,

ν = harmonic order, which is given by:

$$\nu = 2 m_1 g_1 + 1;\ g_1 = 0, \pm1, \pm2, \pm3, \ldots, \tag{2.4}$$

θ_1 = angular co-ordinate with respect to the stator,

q_1 = number of slots per pole per phase of the stator winding,

N_1 = effective number of turns per coil of the stator winding,

δ' = corrected air-gap length,

K_{vw1} = stator winding factor for the v^{th} harmonic,

$$K_{vw1} = \frac{\mathrm{Sin}\left(\frac{v\pi}{2m_1}\right)}{q_1 \sin\left(\frac{v\pi}{2m_1 q_1}\right)} \sin\left(v\frac{\pi}{2}\frac{y_1}{\tau_{p1}}\right), \tag{2.5}$$

$\frac{y_1}{\tau_{p1}}$ = coil-pitch referred to the pole-pitch.

2.3.1 Co-ordinate System

Since the rotor is revolving, it is necessary to establish a relationship between the stator and rotor co-ordinates. Referring to Fig. 2.2, the co-ordinate system for the stator and rotor can be easily obtained. Let the origin of the stator co-ordinate (θ_1), lie on the magnetic axis (AA_1) of the coil (CC_1). For squirrel-cage induction motors, the magnetic axis of a rotor mesh, formed by two bars and the end-rings, is chosen as the rotor reference axis. In Fig. 2.2, BB_1 represents the rotor reference axis, which is the magnetic axis of the mesh formed by the rotor bars z_1 and z_2. In the case of wound-rotor induction motors, the magnetic axis of a coil is chosen as the rotor reference axis. The circumferential location of any point in mechanical radians from the reference axis of the stator is denoted by θ_1, while its location in mechanical radians referred to the

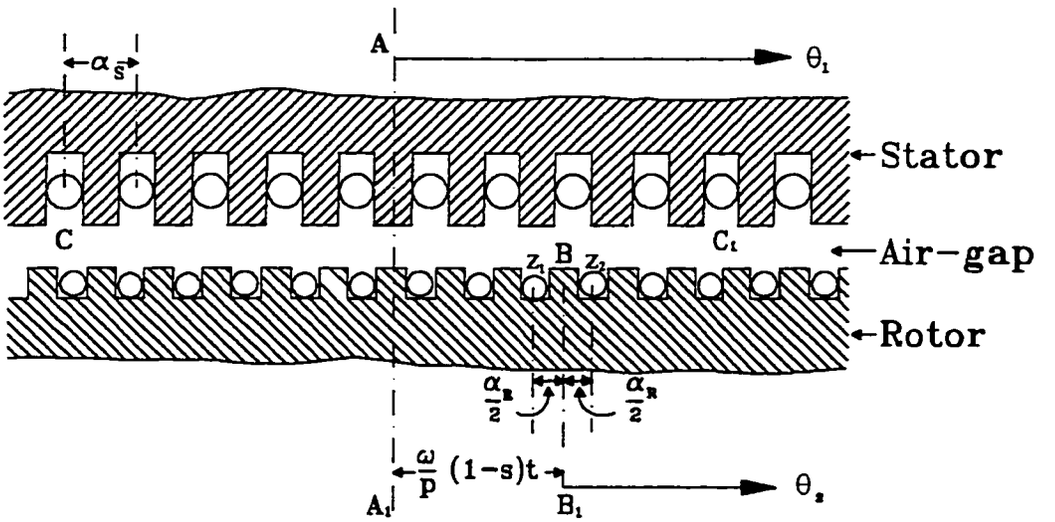

Figure 2.2 : Co-ordinate system for the stator and rotor.

rotor axis is denoted by θ_2. The symbols α_S and α_R are defined as:

$$\alpha_S = \frac{2\pi}{S} = \text{slot-angle of stator in mechanical radians, and} \tag{2.6}$$

$$\alpha_R = \frac{2\pi}{Z} = \text{slot-angle of rotor in mechanical radians.} \tag{2.7}$$

Since the rotor revolves with a speed of $\frac{\omega}{p}(1-s)$ radians per second, the relationship between θ_1 and θ_2 is given by:

$$\theta_1 = \theta_2 + \frac{\omega}{p}(1-s)t. \tag{2.8}$$

2.3.2 Flux-linkages of the Stator Produced Fields

The air-gap flux-density produced by the stator has various harmonics of order v. These air-gap fields link with the stator windings, and the rotor windings. The flux-linkages of these fields with the stator windings induce voltages in itself at the supply frequency. The flux-linkages of these fields with the rotor windings cause currents to flow in the rotor at frequencies dependent on its harmonic order v, and the speed of rotation of the rotor.

2.3.2.1 Stator Self-inductance

The voltage equation of the stator, considering primary armature reaction, includes all currents and voltages induced in the stator at the supply frequency. This equation can be constructed by equating the voltage applied to the stator winding and the various voltage drops in it. The voltage drops are chiefly due to the winding resistance and the induced voltages associated with its self and mutual flux-linkages.

In order to formulate the voltage equation for the stator, it would be necessary to know the self-inductance of the stator winding. The self-inductance of the stator winding with respect to the v^{th} order rotating air-gap field can be found by determining the total flux-linkages of this field with a particular phase per ampere current in that phase. The air-gap harmonic fluxes linking a coil in the k^{th} phase can be found by integrating the flux-density of the rotating air-gap field, given in Eqn. 2.3, over the span of the coil. The rate of change of this flux with time will give the induced voltage in

that coil. For an integral slot, symmetrical winding there are q_1 coils per phase-belt spread over a pole, and 2p phase-belts in a phase winding. Let 1,...,x,...,q_1 represent the coils in the phase-belt. The ν^{th} order harmonic flux linking one turn of the x^{th} coil in a phase-belt of the k^{th} phase is given by:

$$\phi_{x,k_\nu} = \int_{\theta_1 = (k-1)\frac{2\pi}{m_1 p} + (x-1)\alpha_s - \frac{\pi y_1}{2p\tau_{p1}}}^{\theta_1 = (k-1)\frac{2\pi}{m_1 p} + (x-1)\alpha_s + \frac{\pi y_1}{2p\tau_{p1}}} B_{1_\nu}(\theta_1)\, l_e\, r\, d\theta_1, \tag{2.9.a}$$

$$= l_e\, r\, q_1\, m_1\, 2p \frac{\mu_0 N_1}{\pi(\nu p)\delta'} K_{\nu w1} \left[\frac{2}{\nu p} \sin\left(\nu \frac{\pi}{2} \frac{y_1}{\tau_{p1}}\right)\right] \times I_{1(f)} \sqrt{2} \cos\left(\omega t - \nu p(k-1)\frac{2\pi}{m_1 p} - \nu p(x-1)\alpha_s\right), \tag{2.9.b}$$

where l_e is the effective length of the coil-sides and r is the radius of the stator-bore. The total flux of the ν^{th} order harmonic linking a phase-belt in the k^{th} phase is the phasor sum of all the fluxes linking the N_1 turns of the q_1 coils in that phase-belt, and it is given by:

$$\phi_{k_\nu} = N_1 \sum_{x=1}^{q_1} \phi_{x,k_\nu}, \tag{2.10.a}$$

$$= l_e\, r\, q_1^2\, m_1\, 4p \frac{\mu_o N_1^2}{\pi(\nu p)^2 \delta'} (K_{\nu w1})^2 I_{1(f)} \sqrt{2} \cos\left(\omega t - \nu p(k-1)\frac{2\pi}{m_1 p}\right). \tag{2.10.b}$$

From Eqn. 2.10.b, the self-inductance of a phase-belt in the k^{th} phase of the stator winding with respect to the ν^{th} order harmonic is given by:

$$L_{1,\nu} = l_e\, r\, q_1^2\, m_1\, 4p \frac{\mu_o N_1^2}{\pi(\nu p)^2 \delta'} (K_{\nu w1})^2. \tag{2.11}$$

The total voltage induced in a phase-belt of the k^{th} phase due to the ν^{th} order rotating air-gap field is the phasor sum of all the voltages induced in the q_1 coils of the phase-belt, and it is given by:

$$\underset{(f)}{\bar{E}_{k_\nu}} = -N_1 \frac{d}{dt} \sum_{x=1}^{q_1} \bar{\phi}_{x,k_\nu}, \tag{2.12.a}$$

$$= \omega l_e r q_1^2 m_1 4p \frac{\mu_0 N_1^2}{\pi (\nu p)^2 \delta'} (K_{\nu w1})^2 \underset{(f)}{I_1} \sqrt{2} \sin\left(\omega t - \nu p(k-1)\frac{2\pi}{m_1 p}\right). \tag{2.12.b}$$

The frequency of the self-induced voltage in the k^{th} phase due to the ν^{th} order rotating air-gap field is the same as the fundamental or the supply frequency. This is because, the ν^{th} order air-gap field has ν times the number of pole-pairs of the fundamental field, and it rotates with a circumferential velocity of $\frac{1}{\nu}$ times that of the fundamental. Hence all the fields of various harmonic orders ν, will induce voltages of frequency f. Accordingly, the total induced voltage in a phase-belt of the k^{th} phase due to the composite air-gap field is the phasor sum of the voltages induced by the various harmonic fields, and it is given by:

$$\underset{(f)}{\bar{E}_k} = \sum_{\nu=-\infty}^{\infty} \underset{(f)}{\bar{E}_{k_\nu}}. \tag{2.13}$$

Further, the total induced voltage in a phase-belt of the k^{th} phase can be expressed in terms of the self-inductance for the fundamental field and a coefficient to account for the harmonic fields. Therefore:

$$\underset{(f)}{\bar{E}_k} = \omega L_{1,p} \left[1 + \sigma_{d1,p}\right] \underset{(f)}{I_1} \sqrt{2} \sin\left(\omega t - (k-1)\frac{2\pi}{m_1}\right), \tag{2.14}$$

where $L_{1,p}$ is the self-inductance of a phase-belt in the k^{th} phase stator winding for the fundamental field and it can be obtained by substituting $\nu = 1$ in Eqn. 2.11, and $\sigma_{d1,p}$ is defined as the coefficient of harmonic-linkage. It is expressed as:

$$\sigma_{d1,p} = \left.\frac{\sum_{\nu=-\infty}^{\infty} L_{1,\nu}}{L_{1,p}}\right|_{\nu \neq 1} = \left.\sum_{\nu=-\infty}^{\infty} \left(\frac{K_{\nu w1}}{\nu p} \frac{p}{K_{w1}}\right)^2\right|_{\nu \neq 1}. \tag{2.15}$$

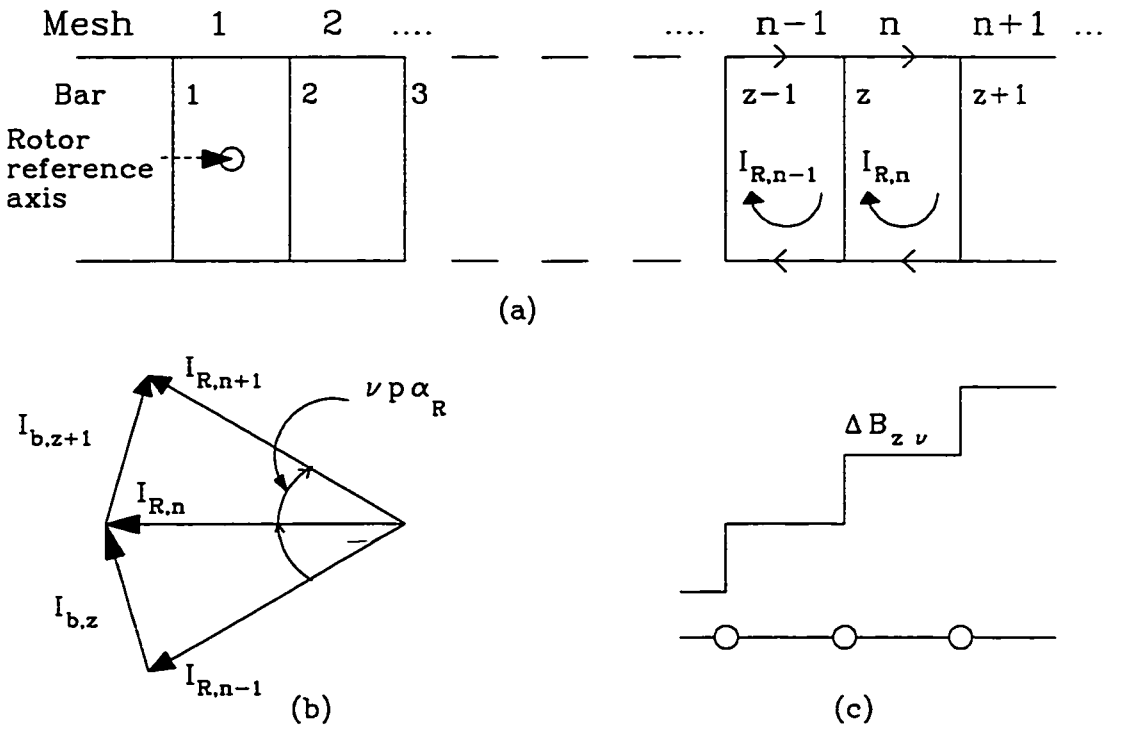

Figure 2.3 : Squirrel-cage rotor windings, rotor currents and phasor representation.

2.3.3 The Case of Squirrel-Cage Rotors

The squirrel-cage rotor windings consist of a series of rotor bar conductors, which are accommodated in the rotor slots. These bars are connected to a common conducting ring at each end. The bars carry equal currents, with mutual phase difference, induced by a particular field. The end-rings carry the summation of the adjacent bar currents. The currents through a rotor-mesh, which comprises of two adjacent rotor bars and the end-ring segments, Fig. 2.3, is used to construct the rotor voltage equations.

The mutual inductance of the stator to a rotor mesh is defined as the ratio of the total flux linked by the rotor mesh to the current in the stator windings. In reference [44], an expression was derived for the mutual inductance of the stator to a rotor mesh. The important equations are reproduced here for the sake of clarity.

2.3.3.1 Stator to Rotor Mutual Inductance

The flux-linkages of the stator fields with the rotor windings, produce currents in the rotor windings at the slip frequency. For a given speed of the rotor, the slip

depends on the order of the stator field. To determine the flux linking the rotor windings, it is convenient to refer the rotating air-gap flux-density, given in Eqn. 2.3, to the rotor co-ordinate θ_2. It is given by:

$$B_{1_\nu}(\theta_2) = q_1 m_1 2p \frac{\mu_0 N_1}{\pi(\nu p)\delta'} \underset{(f)}{I_1} \sqrt{2} \cos\left(\omega t - \nu p\theta_2 - \nu p \frac{\omega}{p}(1-s)t \right). \quad (2.16)$$

An examination of Eqn. 2.16 indicates that the ν^{th} order stator harmonic flux will induce a voltage in the rotor windings at a frequency given by:

$$s_\nu f = [1 - \nu(1-s)]f, \quad (2.17)$$

where s_ν is the slip associated with the ν^{th} order stator harmonic field.

The mutual inductance of the stator to the rotor mesh, with respect to the ν^{th} order harmonic field, is given by:

$$M_{1,2_\nu} = l_e r q_1 m_1 2p \frac{\mu_0 N_1}{\pi(\nu p)\delta'} K_{\nu w_1} \left[\frac{2}{\nu p} \sin\left(\nu p \frac{\alpha_R}{2} \right) \right]. \quad (2.18)$$

These mutual flux-linkages of the ν^{th} order stator harmonic fields with the n^{th} rotor mesh will induce a voltage in it, which is given by:

$$\underset{(s_\nu f)}{E_n} = -\frac{d}{dt}[\phi_{n_\nu}], \quad (2.19.a)$$

$$= s_\nu \omega M_{1,2_\nu} \underset{(f)}{I_1} \sqrt{2} \sin[s_\nu \omega t - (n-1)\nu p\alpha_R]. \quad (2.19.b)$$

Effects of Rotor-Skew

The expressions in Eqns. 2.18 and 2.19 represent the condition with no rotor-skew. Skewing of the rotor bars is commonly used to mitigate some of the MMF-harmonics produced by the squirrel-cage rotor. Theoretically, if the slots in the rotor core are skewed 2π electrical radians on the harmonic scale of a given slot harmonic produced by the stator windings, the voltage induced in the rotor bar for that harmonic along its length should cancel resulting in no net harmonic voltage. Since the

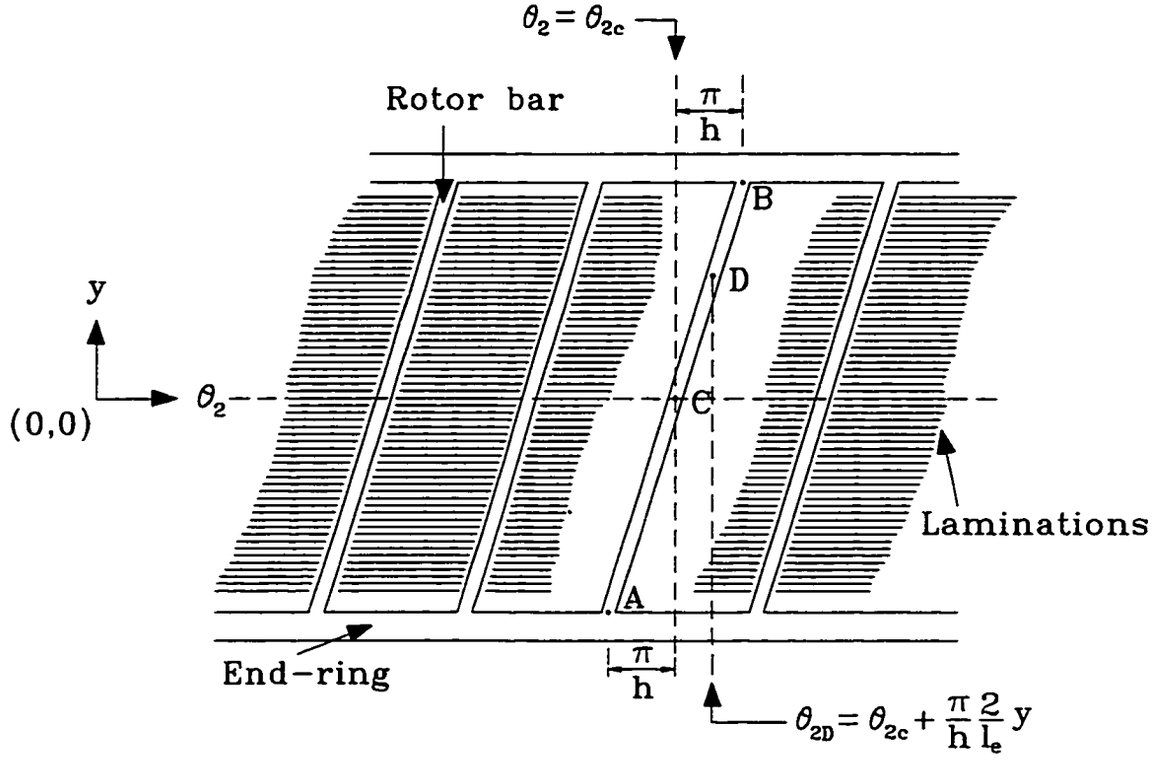

Figure 2.4 : Relationship used to derive the skew factor.

corresponding harmonic currents are absent in the rotor bars, some benefits are achieved in reduction of harmonic torques, additional losses and magnetic noise. In reality the rotor bars are short circuited by the steel rotor core randomly, and they are not fully predictable. This can provide a path for the currents to flow in the rotor core between points having a potential difference corresponding to harmonic voltages. Nevertheless, rotor-skewing is a useful and frequently used technique for small to medium-sized induction motors, and it is beneficial for many applications.

Fig. 2.4 shows a portion of the rotor surface with skewed rotor bars. The line AB represents the rotor bar under consideration. Point C on the rotor bar represents the axial centre of the bar. In practice, the amount of rotor-skew is often specified in stator or rotor slot-pitch. Further, it is usual to specify the advance in terms of the rotor slot-pitch.

The effects of the rotor-skew on the flux linkages of the rotor cage, and thereby the induced voltages, can be easily accounted for with the help of a skew-factor. The

skew-factor is used in the same manner as the winding factor for the stator or rotor windings. The skew-factor for the ν^{th} order harmonic is determined as follows. Let θ_{2C} be the angular location of point C in terms of the rotor co-ordinate system. Therefore, the angular location of any point D on the rotor bar is given by:

$$\theta_{2D} = \theta_{2C} + \frac{\pi}{h} \cdot \frac{2}{l_e} y. \tag{2.20}$$

Therefore the flux of the ν^{th} order stator produced harmonic field linking with the n^{th} rotor mesh can be obtained as:

$$\phi_{n_\nu} = \int_{y=-\frac{l_e}{2}}^{y=\frac{l_e}{2}} \int_{\theta_2=(n-1.5)\alpha_R+\frac{2\pi y}{hl_e}}^{\theta_2=(n-0.5)\alpha_R+\frac{2\pi y}{hl_e}} B_{1_\nu}(\theta_2)\, r\, d\theta_2\, dy, \tag{2.21.a}$$

$$= l_e\, r\, q_1\, m_1\, 2p \frac{\mu_0 N_1}{\pi(\nu p)\delta'} K_{\nu w1} \left[\frac{2}{\nu p} \sin\left(\nu p \frac{\alpha_R}{2}\right)\right] \left[\frac{\sin\left(\nu p \frac{\pi}{h}\right)}{\nu p \frac{\pi}{h}}\right] \tag{2.21.b}$$

$$\times \frac{I_1}{(s_\nu f)} \sqrt{2} \cos\left(s_\nu \omega t - \nu p(n-1)\alpha_R\right).$$

The revised value of the mutual inductance of the stator to the n^{th} rotor mesh, with respect to the ν^{th} order harmonic field and accounting for the rotor-skew is given by:

$$M_{1.2_\nu} = l_e\, r\, q_1\, m_1\, 2p \frac{\mu_0 N_1}{\pi(\nu p)\delta'} K_{\nu w_1} \left[\frac{2}{\nu p} \sin\left(\nu p \frac{\alpha_R}{2}\right)\right] \left[\frac{\sin\left(\nu p \frac{\pi}{h}\right)}{\nu p \frac{\pi}{h}}\right]. \tag{2.22}$$

2.3.3.2 Rotor Produced Harmonic Air-gap Fields

Under the action of the stator produced air-gap fields, currents are produced in the rotor windings in such a way that it opposes the flux-linkages causing the induced emf. The distribution of the rotor bars in slots around the periphery produces a non-sinusoidal current sheet on the rotor. The resulting air-gap fields produced by the rotor

will therefore be non-sinusoidal. As the air-gap permeance is uniform, the air-gap fields produced by the rotor will be of the same form as that of the rotor MMF. These fields are stepped in nature and they can be resolved into a Fourier-series consisting of various sinusoidal components of different orders. Thus, the rotor in addition to producing the harmonic fields of order ν, will also inject air-gap harmonic fields of different orders μ.

It was shown in reference [44] that the squirrel-cage rotor produces harmonic air-gap fields whose orders are given by:

$$\mu = \nu + g_2 \frac{Z}{p}; g_2 = 0, \mp 1, \mp 2, \mp 3, \ldots, \tag{2.23}$$

The various air-gap harmonic fields of order μ produced by the rotor due to the induced currents of frequency $s_\nu f$, are given by the expression:

$$B_{2_{\mu,\nu}}(\theta_2) = \frac{\mu_0 Z}{\pi(\mu p)\delta'} \sin\left(\mu p \frac{\alpha_R}{2}\right) \underset{(s_\nu f)}{I_R} \sqrt{2} \cos(s_\nu \omega t - \mu p \theta_2). \tag{2.24}$$

2.3.3.3 Flux-linkages of the Rotor Fields

The currents induced in the rotor windings can be split into separate components according to the frequency $s_\nu f$ at which they occur. The rotor fields produced by these currents establish flux-linkages with the rotor, and also with the stator windings. Since in the rotor windings there is no externally applied voltage, the sum of the induced voltages and the resistance drops will be zero. This condition is used to derive the rotor voltage equations.

2.3.3.4 Rotor Self-inductance

As discussed earlier, the voltage equations for the squirrel-cage rotor windings can be formulated in terms of the n^{th} rotor mesh. With respect to the μ^{th} order air-gap field produced by the rotor, the self-inductance of the n^{th} rotor mesh is defined as the ratio of the total flux linked with the rotor mesh to the current $\underset{(s_\nu f)}{I_R}$. The rate of change of this flux-linkage with time gives the voltage induced in the n^{th} rotor mesh.

The air-gap field produced by the rotor, and linking with the n^{th} rotor mesh is found by integrating the flux-density over the span of the n^{th} rotor mesh. It is given by:

$$\phi_{n_{\mu,v}} = \int_{\theta_2=(n-1.5)\alpha_R}^{\theta_2=(n-0.5)\alpha_R} B_{2_{\mu,v}}(\theta_2)\ l_e\, r\, d\theta_2, \tag{2.25.a}$$

$$= l_e r \frac{\mu_0 Z}{\pi(\mu p)^2 \delta'} 2\left[\sin\left(\mu p \frac{\alpha_R}{2}\right)\right]^2 \underset{(s_v f)}{I_R}\ \sqrt{2}\cos\left[s_v \omega t - (n-1)\mu p \alpha_R\right]. \tag{2.25.b}$$

Therefore, the self inductance of the n^{th} rotor mesh with respect to the μ^{th} order rotor air-gap field ($L_{2,\mu}$) is given by:

$$L_{2,\mu} = l_e r \frac{\mu_0 Z}{\pi(\mu p)^2 \delta'} 2\left[\sin\left(\mu p \frac{\alpha_R}{2}\right)\right]^2. \tag{2.26}$$

Hence, the voltage induced in the n^{th} rotor mesh due to the μ^{th} order air-gap field is given by:

$$E_{n_{\mu,v}} = -\frac{d}{dt}\left[\phi_{n_{\mu,v}}\right], \tag{2.27.a}$$

$$= s_v \omega L_{2,\mu} \underset{(s_v f)}{I_R}\ \sqrt{2}\sin\left(s_v \omega t - (n-1) v p \alpha_R\right). \tag{2.27.b}$$

An examination of Eqn. 2.27.b indicates that all the air-gap fields of order μ induce a voltage in the n^{th} rotor mesh at the same slip frequency, $s_v f$. Further, there is no phase-difference in the voltages induced by the various air-gap fields of order μ for different values of g_2, Eqn. 2.23. Therefore, the total voltage induced in the n^{th} rotor mesh, for all orders of μ, can be added up algebraically.

$$\underset{(s_v f)}{\bar{E}_n} = \sum_{\mu=-\infty}^{\infty} \underset{(s_v f)}{\bar{E}_{n_{\mu,v}}}, \tag{2.28.a}$$

$$= s_v \omega l_e r \frac{\mu_0 Z}{\pi \delta'} 2\left[\sin\left(v p \frac{\alpha_R}{2}\right)\right]^2 \underset{(s_v f)}{I_R} \sqrt{2} \sin\left[s_v \omega t - (n-1) v p \alpha_R\right] \times \sum_{\mu=-\infty}^{\infty} \frac{1}{(\mu p)^2}. \quad (2.28.b)$$

Eqn. 2.28.b is further simplified [44], and the total voltage of frequency $s_v f$ induced in the n^{th} rotor mesh is given by:

$$\underset{(s_v f)}{E_n} = s_v \omega l_e r \frac{\mu_0}{\delta'} \frac{2\pi}{Z} \underset{(s_v f)}{I_R} \sqrt{2} \sin\left[s_v \omega t - (n-1) v p \alpha_R\right]. \quad (2.29)$$

An examination of Eqn. 2.29 reveals that the self-inductance of any rotor mesh is:

$$L_{2,v} = l_e r \frac{\mu_0}{\delta'} \frac{2\pi}{Z}. \quad (2.30)$$

Also, $L_{2,v}$ can be defined as the self-inductance of the n^{th} rotor mesh, corresponding to all the flux-linkages produced by the rotor mesh currents of frequency $s_v f$. Also, this will represent the sum of all inductances ($L_{2,\mu}$), for various values of μ [44].

2.3.3.5 Rotor to Stator Mutual Inductance

The rotor produced air-gap fields that link the stator winding induce voltages and currents back in the stator windings at various harmonic frequencies. In the case of squirrel-cage induction motors, these harmonic frequencies are directly related to the number of rotor bars and the speed of rotation of the rotor. The mutual inductance of the k^{th} phase of the stator with respect to the μ^{th} order rotor air-gap field can be determined as the ratio of the total flux of the μ^{th} order field linking with the k^{th} phase to the current in the n^{th} mesh of the rotor.

In order to determine the flux-linkages of the rotor air-gap fields with the stator windings, it is convenient to refer the rotor air-gap flux-density to the stator co-ordinate θ_1. Rewriting Eqn. 2.24:

$$B_{2_{\mu,\nu}}(\theta_1) = \frac{\mu_0}{\delta'} \frac{Z}{2\pi(\mu p)} 2\sin\left(\mu p \frac{\alpha_R}{2}\right) \underset{(s_\nu f)}{I_R} \sqrt{2}\cos\left(s_{g_2}\omega t - \mu p \theta_1\right), \quad (2.31)$$

where s_{g_2} is the slip associated with the μ^{th} order air-gap field. It is given by:

$$\begin{aligned} s_{g_2} &= 1 + \mu - \nu\,(1 - s), \\ &= 1 + g_2 \frac{Z}{p}(1 - s). \end{aligned} \quad (2.32)$$

These flux linkages of the μ^{th} order field with the stator windings induce voltages and currents in the stator windings at the slip frequency $s_{g_2} f$. The integration of the air-gap flux-density of the μ^{th} order field over the span of the x^{th} coil in a phase-belt of the k^{th} phase will give the total flux linking with it. Thus:

$$\phi_{(x,k)_{\mu,\nu}} = \int_{\theta_1 = (k-1)\frac{2\pi}{m_1 p} + (x-1)\alpha_S - \frac{\pi y_1}{2p\tau_{p1}}}^{\theta_1 = (k-1)\frac{2\pi}{m_1 p} + (x-1)\alpha_S + \frac{\pi y_1}{2p\tau_{p1}}} B_{2_{\mu,\nu}}(\theta_1)\, l_e\, r\, d\theta_1, \quad (2.33.a)$$

$$\begin{aligned} &= l_e r \frac{\mu_0}{\delta'} \frac{Z}{2\pi(\mu p)} 2\sin\left(\mu p \frac{\alpha_R}{2}\right)\left[\frac{2}{\mu p}\sin\left(\mu \frac{\pi}{2}\frac{y_1}{\tau_{p1}}\right)\right] \\ &\times \underset{(s_\nu f)}{I_R} \sqrt{2}\cos\left(s_{g_2}\omega t - \mu p (k-1)\frac{2\pi}{m_1 p} - \mu p (x-1)\alpha_S\right). \end{aligned} \quad (2.33.b)$$

The total flux of the μ^{th} order rotor field, linking with a phase-belt in the k^{th} phase is obtained by the phasor sum of all the flux-linkages with the N_1 turns of the q_1 coils. Also since the rotor slots are skewed, the flux-linkages of Eqn. 2.33.b has to be multiplied by the skewing factor. It is therefore expressed mathematically as:

$$\phi_{k_{\mu,\nu}} = N_1 \frac{\sin\left(\mu p \frac{\pi}{h}\right)}{\mu p \frac{\pi}{h}} \sum_{x=1}^{q_1} \phi_{(x,k)_{\mu,\nu}}, \quad (2.34.a)$$

$$= l_e r \frac{\mu_0 Z N_1 q_1}{\pi (\mu p)^2 \delta'} \sin\left(\mu p \frac{\alpha_R}{2}\right) K_{\mu w1} \frac{\sin\left(\mu p \frac{\pi}{h}\right)}{\mu p \frac{\pi}{h}} \tag{2.34.b}$$

$$\times \underset{(s_v f)}{I_R} \sqrt{2} \cos\left(s_{g_2} \omega t - \mu p (k-1) \frac{2\pi}{m_1 p}\right).$$

From Eqns. 2.21 and 2.34 it follows that the skewing factor can be defined as:

$$K_{2S} = \left[\frac{\sin\left(\mu p \frac{\pi}{h}\right)}{\left(\mu p \frac{\pi}{h}\right)}\right], \tag{2.35}$$

for the μ^{th} order harmonic field. Therefore, the mutual inductance of the rotor to the stator $M_{2,1}$ with respect to the μ^{th} order rotor air-gap field is given by:

$$M_{2,1_\mu} = l_e r \frac{\mu_0 Z N_1 q_1}{\pi (\mu p)^2 \delta'} \sin\left(\mu p \frac{\alpha_R}{2}\right) K_{\mu w1} \frac{\sin\left(\mu p \frac{\pi}{h}\right)}{\mu p \frac{\pi}{h}}. \tag{2.36}$$

From Eqn. 2.34.b and Eqn. 2.36, the voltage induced in a phase-belt of the k^{th} stator phase due to the μ^{th} order rotor air-gap field is given by:

$$\underset{(s_{g_2} f)}{E_k} = s_{g_2} \omega M_{2,1_\mu} \underset{(s_v f)}{I_R} \sqrt{2} \sin\left[s_{g_2} \omega t - \left(1 + g_2 \frac{Z}{p}\right)(k-1) \frac{2\pi}{m_1}\right]. \tag{2.37}$$

It is seen from Eqn. 2.37, that all the rotor fields whose harmonic orders are such that:

$$\mu - \nu = g_2 \frac{Z}{p} \neq 0, \tag{2.38}$$

will induce a voltage in the stator winding at a frequency different from the supply frequency f. Further, the phase-shift of the induced voltages in the various phases due to different g_2 will be given by:

$$\gamma_{g_2} = \left(1 + g_2 \frac{Z}{p}\right)(k-1) \frac{2\pi}{m_1}. \tag{2.39}$$

2.3.3.6 Secondary Armature Reaction

The reaction of the stator to the rotor field harmonics is called secondary armature reaction. It should be emphasised that the voltages induced and the resulting currents in the stator windings due to the various harmonic rotor air-gap fields depend on the arrangement of the stator windings. In this analysis, it is assumed that the stator has a double-layer, integral-slot winding with all the phase-belts of a phase connected in series. The harmonic analysis of the stator MMF due to these induced voltages and currents will give the harmonic fields thus produced. The stator winding generates additional harmonic fields of order ε, and they are given by [44]:

$$\epsilon = 2\,m_1 g_3 + 1 + g_2\frac{Z}{p}; \qquad g_3 = 0, \mp 1, \mp 2, \mp 3, \ldots. \tag{2.40}$$

The air-gap flux-density of the stator harmonic fields of order ε is given by:

$$B_{1_\epsilon}(\theta_1) = q_1 m_1 2p \frac{\mu_0 N_1}{\pi(\epsilon p)\delta'} K_{\epsilon w1} \frac{I_1}{(s_{g_2} f)} \sqrt{2}\cos\left(s_{g_2}\omega t - \epsilon p\theta_1\right). \tag{2.41}$$

The resulting fields produced by these stator air-gap flux-densities of order ε establish flux-linkages with the stator and rotor windings. In the following sections, general expressions are derived for the self-inductance of the stator windings with respect to the ε^{th} order harmonic air-gap fields.

The total flux of the ε^{th} order harmonic field linking with the x^{th} coil in the k^{th} phase is given by:

$$\phi_{(x,k)_\epsilon} = \int_{\theta_1 = (1+g_2\frac{Z}{p})(k-1)\frac{2\pi}{m_1 p} + (x-1)\alpha_S - \frac{\pi y_1}{2p\tau_{p1}}}^{\theta_1 = (1+g_2\frac{Z}{p})(k-1)\frac{2\pi}{m_1 p} + (x-1)\alpha_S + \frac{\pi y_1}{2p\tau_{p1}}} B_{1_\epsilon}(\theta_1)\, l_e\, r\, d\theta_1, \tag{2.42.a}$$

$$= l_e r q_1 m_1 2p \frac{\mu_0 N_1}{\pi(\epsilon p)\delta'} K_{\epsilon w1}\left[\frac{2}{\epsilon p}\sin\left(\epsilon p\frac{\pi}{2}\frac{y_1}{\tau_{p1}}\right)\right] \tag{2.42.b}$$

$$\times \frac{I_1}{(s_{g_2} f)}\sqrt{2}\cos\left[s_{g_2}\omega t - \epsilon p(k-1)(1+g_2\frac{Z}{p})\frac{2\pi}{m_1 p} - \epsilon p(x-1)\alpha_S\right].$$

Therefore, the total flux of the ε^{th} order field linking with a phase-belt in the k^{th} phase can be found as:

$$\phi_{k_\epsilon} = N_1 \sum_{x=1}^{q_1} \phi_{(x,k)_\epsilon}, \tag{2.43.a}$$

$$\begin{aligned} &= l_e\, r\, q_1^2\, m_1\, 4p\, \frac{\mu_0 N_1^2}{\pi (\epsilon p)^2 \delta'} (K_{\epsilon w1})^2 \\ &\times \underset{(s_{g_2} f)}{I_1} \sqrt{2} \cos\left[s_{g_2} \omega t - \epsilon p (1 + g_2 \frac{Z}{p})(k-1) \frac{2\pi}{m_1 p} \right]. \end{aligned} \tag{2.43.b}$$

From Eqn. 2.43.b, the self-inductance of the k^{th} phase of the stator winding with respect to the ε^{th} order air-gap field harmonic is:

$$L_{1,\epsilon} = l_e\, r\, q_1^2\, m_1\, 4p\, \frac{\mu_0 N_1^2}{\pi (\epsilon p)^2 \delta'} (K_{\epsilon w1})^2. \tag{2.44}$$

All the voltages induced in the stator windings for various orders of ε, that are associated with the same g_2 in Eqn. 2.23, are of the same slip frequency $s_{g_2} f$. Hence, the voltage induced in a phase-belt of the k^{th} phase can be written as:

$$\begin{aligned} \underset{(s_{g_2} f)}{E_k} &= s_{g_2} \omega \left[\sum_{\epsilon=-\infty}^{\infty} L_{1,\epsilon} \right]_{g_2 = \text{constant}} \\ &\times \underset{(s_{g_2} f)}{I_1} \sqrt{2} \sin\left(s_{g_2} \omega t - (1 + g_2 \frac{Z}{p})(k-1) \frac{2\pi}{m_1} \right), \end{aligned} \tag{2.45.a}$$

$$\begin{aligned} &= s_{g_2} \omega \left\{ (L_{1,\epsilon})_{g_3 = 0} \left[1 + \sigma_{d1,g_2} \right] \right\}_{g_2 = \text{constant}} \\ &\times \underset{(s_{g_2} f)}{I_1} \sqrt{2} \sin\left[s_{g_2} \omega t - (1 + g_2 \frac{Z}{p})(k-1) \frac{2\pi}{m_1} \right], \end{aligned} \tag{2.45.b}$$

where σ_{d1,g_2} is defined as the coefficient of harmonic flux-linkage, and is expressed mathematically as:

$$\sigma_{d1,g_2} = \left. \frac{\left[\sum_{\epsilon=-\infty}^{\infty} L_{1,\epsilon} \right]_{g_3 \neq 0}}{\left[L_{1,\epsilon} \right]_{g_3=0}} \right|_{g_2 = \text{constant}} . \tag{2.46}$$

2.3.3.7 Tertiary Armature Reaction

The tertiary armature reaction involves the consideration of the effects of the stator harmonic fields of order ε on the rotor (Fig. 2.1). In order to determine the flux-linkages of the ε^{th} order stator air-gap field with the rotor, it is convenient to refer the ε^{th} order air-gap flux-density to the rotor co-ordinate θ_2. Rewriting Eqn. 2.41:

$$B_{1_\epsilon}(\theta_2) = q_1 m_1 2p \frac{\mu_0 N_1}{\pi(\epsilon p)\delta'} K_{\epsilon w1} \frac{I_1}{(s_{g_2} f)} \sqrt{2} \cos(s_{g_3} \omega t - \epsilon p \theta_2), \tag{2.47}$$

where s_{g_3} is the slip seen by the rotor to the ε^{th} order stator air-gap field. It is given by:

$$\begin{aligned} s_{g_3} &= [s_{g_2} - \epsilon(1-s)], \\ &= [1 - (2mg_3 + 1)(1-s)]. \end{aligned} \tag{2.48}$$

The stator air-gap harmonic fields of order ε, for constant values of g_3, will induce voltages in the rotor at the same slip frequency $s_{g_3} f$. Further for $g_3 = g_1$, the slip s_{g_3} is equal to s_v.

The total flux of the ε^{th} order harmonic field linking with the n^{th} rotor mesh is given by:

$$\phi_{n_\epsilon} = \int_{y=-\frac{l_e}{2}}^{y=\frac{l_e}{2}} \int_{\theta_2=(n-1.5)\alpha_R + \frac{2\pi y}{h l_e}}^{\theta_2=(n-0.5)\alpha_R + \frac{2\pi y}{h l_e}} B_{1_\epsilon}(\theta_2)\, r\, d\theta_2\, dy, \tag{2.49.a}$$

$$= l_e\, r\, q_1\, m_1\, 2p\, \frac{\mu_0 N_1}{\pi(\epsilon p)\delta'} K_{\epsilon w1} \left[\frac{2}{\epsilon p} \sin\left(\epsilon p \frac{\alpha_R}{2}\right)\right] \left[\frac{\sin\left(\epsilon p \frac{\pi}{h}\right)}{\epsilon p \frac{\pi}{h}}\right] \quad (2.49.b)$$

$$\times \underset{(s_{g_2} f)}{I_1} \sqrt{2} \cos\left(s_{g_2} \omega t - \epsilon p (n-1) \alpha_R\right).$$

Therefore, the voltage induced in the n^{th} rotor mesh due to the ε^{th} order stator air-gap field is:

$$\underset{(s_{g_3} f)}{E_n} = s_{g_3}\, \omega\, M_{1,2_\epsilon} \underset{(s_{g_2} f)}{I_1} \sqrt{2} \sin\left(s_{g_3} \omega t - \epsilon p (n-1) \alpha_R\right), \quad (2.50)$$

where $M_{1,2_\epsilon}$ is the mutual inductance of the stator to the rotor mesh with respect to the ε^{th} order harmonic air-gap field, and it is given by:

$$M_{1,2_\epsilon} = l_e\, r\, q_1\, m_1\, 2p\, \frac{\mu_0 N_1}{\pi(\epsilon p)\delta'} K_{\epsilon w1} \left[\frac{2}{\epsilon p} \sin\left(\epsilon p \frac{\alpha_R}{2}\right)\right] \left[\frac{\sin\left(\epsilon p \frac{\pi}{h}\right)}{\epsilon p \frac{\pi}{h}}\right]. \quad (2.51)$$

2.3.3.8 Voltage Equations

The voltage equations for the stator and the rotor considering primary, secondary and tertiary armature reactions are formulated and written in a matrix form. Since the stator has a double layer, integral slot winding, there are 2p phase-belts per phase. For a series connection, the total voltage induced in a stator phase winding will be 2p times the voltage induced in one phase-belt. With the help of Eqns. 2.1, 2.14, and 2.37, the voltage equation for the k^{th} phase winding at the supply frequency is obtained. The rotor fields of order $\mu = \nu$ induce voltages of supply frequency f, in the stator phase. These fields correspond to the condition $g_2 = 0$ in Eqn. 2.23. The required voltage equation for the supply frequency f is:

$$V_1\sqrt{2}\cos\left(\omega t-(k-1)\frac{2\pi}{m_1}\right)=\left\{R_{1,f}\underset{(f)}{I_1\sqrt{2}}+j\omega\left[2pL_{1,p}(1+\sigma_{d1,p})+L_{S1,p}+L_{N1,p}\right]\underset{(f)}{I_1\sqrt{2}}\right.$$
$$\left.+j\omega\sum_{\mu=-\infty}^{\infty}2pM_{2,1_\mu}\underset{(s_v f)}{I_R\sqrt{2}}\right\}_{g_2=0}\cos\left(\omega t-(k-1)\frac{2\pi}{m_1}\right). \tag{2.52}$$

In the above equation, $L_{S1,p}$ and $L_{N1,p}$ are the slot-leakage inductance and the end-connection leakage inductance of the stator, respectively.

Considering now Eqns. 2.37 and 2.45.b, the voltage equation for the k^{th} phase winding of stator at the harmonic slip frequency $s_{g_2}f$ is written as:

$$0=\left\{R_{1,s_{g_2}f}\underset{(s_{g_2}f)}{I_1\sqrt{2}}+js_{g_2}\omega\left[2p\left(L_{1,\epsilon}\right)_{g_3=0}(1+\sigma_{d1,g_2})+L_{S1,g_2}+L_{N1,g_2}\right]\underset{(s_{g_2}f)}{I_1\sqrt{2}}\right.$$
$$\left.+js_{g_2}\omega\sum_{\substack{\mu=-\infty\\ \mu\neq v}}^{\infty}2pM_{2,1_\mu}\underset{(s_v f)}{I_R\sqrt{2}}\right\}_{g_2=\text{constant}}\cos\left(s_{g_2}\omega t-(k-1)\frac{2\pi}{m_1}\right). \tag{2.53}$$

For the squirrel-cage rotor, the voltage equation is formulated in terms of the n^{th} rotor mesh. The voltage drops in the rotor mesh comprises of the drops caused by the resistances and the inductances of the circuit. Let ψ_n, be the total flux-linkages of the n^{th} rotor mesh, and E_n be the corresponding induced voltage. Therefore:

$$\sum\bar{I}_n R_n+\frac{d}{dt}\psi_n=\sum\bar{I}_n R_n-E_n=0 \tag{2.54}$$

The n^{th} rotor mesh, Fig. 2.3, consists of the bars z and z+1, and the end-ring segments on both sides of the bars, hence the resistive voltage can be formulated as:

$$\sum_{(s_v f)}\bar{I}_n R_{n,s_v f}=\underset{(s_v f)}{\bar{I}_{b,z}}R_b+2\bar{I}_{R,n}R_{R2}-\bar{I}_{b,z+1}R_b,$$
$$=\underset{(s_v f)}{I_R\sqrt{2}}\left[2R_{R2}+4R_b\sin^2\left(vp\frac{\alpha_R}{2}\right)\right]. \tag{2.55}$$

Similarly, the voltage drop in the n^{th} rotor mesh due to its leakage inductances can be

written as:

$$j s_v \omega \sum_{(s_v f)} \bar{I}_n L_n = j s_v \omega \sum_{(s_v f)} \bar{I}_R \left[L_{S2} + L_{R2} \right], \tag{2.56}$$

where L_{S2} and L_{R2} are the slot-leakage inductance and the end-ring leakage inductance of the rotor, respectively. Therefore, Eqn. 2.56 can be rewritten as:

$$= j s_v \omega \left[\underset{(s_v f)}{\bar{I}_{b,z}} L_{S2} - \underset{(s_v f)}{\bar{I}_{b,z+1}} L_{S2} + 2 \underset{(s_v f)}{\bar{I}_{R,n}} L_{R2} \right]. \tag{2.57}$$

Considering Eqns. 2.19.b, 2.22, 2.29 and Eqn. 2.50, the voltage equation for the squirrel-cage rotor mesh at frequency $s_v f$ is formulated as:

$$0 = \left\{ \left[2R_{R2} + 4R_b \sin^2\left(v p \frac{\alpha_R}{2} \right) + j s_v \omega \left(L_{2,v} + 2L_{R2} + 4L_{S2} \sin^2\left(v p \frac{\alpha_R}{2} \right) \right) \right. \right. \tag{2.58}$$

$$\left. \left. + j s_v \omega M_{1,2_v} \underset{(f)}{I_1 \sqrt{2}} \right\}_{g_3 = g_1 = \text{constant}} \cos\left(s_v \omega t - (n-1) v p \alpha_R \right).$$

It is convenient to represent this set of simultaneous equations, Eqns. 2.52, 2.53 and 2.58, in the form of a matrix which simplifies the determination of the solution. These equations can be written in the form of a matrix as:

$$\left[\frac{V}{\omega} \right] = \left[\frac{R}{\omega} \right] [I] + j [L][I], \tag{2.59}$$

where

$$[L] = \begin{bmatrix} L_{1,1} & M_{2,1} \\ M_{1,2} & L_{2,2} \end{bmatrix} \tag{2.60}$$

$$\left[\frac{V}{\omega}\right] = \begin{bmatrix} \frac{V_1\sqrt{2}}{\omega} \\ 0 \\ 0 \\ 0 \\ . \\ . \\ . \\ . \end{bmatrix} \qquad (2.61)$$

$$[I] = \begin{bmatrix} I_1\sqrt{2}\,(f)\big|_{g_2=0} \\ I_1\sqrt{2}\,(s_{g_2}f)\big|_{g_2=-1} \\ I_1\sqrt{2}\,(s_{g_2}f)\big|_{g_2=+1} \\ \vdots \\ I_R\sqrt{2}\,(s_\nu f)\big|_{g_1=0} \\ I_R\sqrt{2}\,(s_\nu f)\big|_{g_1=-1} \\ I_R\sqrt{2}\,(s_\nu f)\big|_{g_1=+1} \\ \vdots \end{bmatrix} \qquad (2.62)$$

$$\left[\frac{R}{\omega}\right] = \begin{bmatrix} \frac{R_{1,f}}{\omega}\Big|_{g_2=0} & 0 & 0 & 0 & . & . & . & . \\ 0 & \frac{R_{1,s_{g_2}f}}{s_{g_2}\omega}\Big|_{g_2=-1} & 0 & 0 & . & . & . & . \\ . & . & . & . & . & . & . & . \\ . & . & . & . & . & . & . & . \\ . & . & . & . & \frac{R_{n,sf}}{s\omega}\Big|_{g_1=0} & . & . & . \\ . & . & . & . & . & \frac{R_{n,s_\nu f}}{s_\nu\omega}\Big|_{g_1=-1} & . & . \\ . & . & . & . & . & . & . & . \\ . & . & . & . & . & . & . & . \end{bmatrix} \qquad (2.63)$$

The voltage equations are solved to obtain the various harmonic components of the currents in the stator and rotor windings. The term $\frac{\mu_0}{\delta'}$ in the expressions for the stator and rotor produced air-gap fields represents the permeance per unit area of the air-gap bounded by smooth stator and rotor surfaces. Thus, the net MMF acting across the air-gap is obtained by evaluating the expressions given in Eqns 2.3, 2.24 and 2.41 and omitting the term $\frac{\mu_0}{\delta'}$.

The MMF-waves thus determined assume the general form given by:

$$M(\theta,t) = \sum_{n=-\infty}^{\infty} M_n \cos\left(np\theta_1 - \omega_n t\right) . \tag{2.64}$$

2.4 Permeance-waves

The air-gap length of an induction machine is very small in comparison to the depth of the slots that are provided to accommodate the current carrying conductors. The presence of slots increases the air-gap reluctance by restricting the flux to a degree depending on the width of the slot-opening, and the length of the air-gap. The reduction in the flux due to this permeance variation is calculated from the physical features of the machine. The variation of the air-gap permeance is modelled in the form of appropriate permeance-waves [14]. The effects of magnetic saturation are ignored while calculating the permeance variation due to slotting. Saturation effects are incorporated later in the permeance-wave for a doubly slotted machine. The per-unit permeance for each member is calculated separately. It is assumed that one member is slotted while the other is smooth. The average permeance of the air-gap bounded by a smooth surface and a slotted surface is commonly found using Carter's coefficients [14,19], and it is taken as the base permeance in the calculation of the per-unit permeances. The two per-unit permeances are then multiplied, and the resulting product is further multiplied by the average value of the air-gap permeance to obtain the effective distribution of the air-gap permeance [44].

Generally, saturation causes further reduction in the flux in the middle region of the poles. The effects of saturation are modelled as a variation in the air-gap permeance having twice the pole-pairs of the fundamental field [26-28]. Hence, the resultant air-

gap permeance due to slotting and saturation is given in a general form as:

$$\lambda(\theta,t) = \lambda_0\left[1 + \sum_{\rho=1}^{\infty} \lambda_{S\rho}\cos(\rho S\theta)\right] \times \left[1 + \sum_{\gamma=1}^{\infty} \lambda_{R\gamma}\cos\left[\gamma Z\theta - \frac{\gamma Z}{p}(1-s)\omega t\right]\right] \times \left[\sum_{\eta=0}^{\infty} \lambda_{sa\eta}\cos\left[2\eta(p\theta - \omega t)\right]\right]. \quad (2.65)$$

2.5 Air-gap Flux-density Waves

The air-gap flux-density is obtained as the product of the MMF-waves and the permeance-waves. Since the stator and rotor windings are placed in the slots, some of the harmonics introduced by the MMF-wave will be indistinguishable from those caused by permeance variations due to slotting. Nevertheless, the harmonic composition of the air-gap flux-density can be calculated with reasonable accuracy, and the existence of various field components can be confirmed experimentally. The air-gap flux-density is expressed in a general form as:

$$B(\theta,t) = \sum_{\sigma=1}^{\infty} B_\sigma \cos(p_\sigma\theta - \omega_\sigma t + \theta_\sigma). \quad (2.66)$$

2.6 Radial-force Waves

The radial-force acting per unit area, on the stator and rotor surfaces is proportional to the square of the air-gap flux-density at a given location. This force can be found by squaring the expression in Eqn. 2.66, and then using the relationship :

$$F(\theta,t) = \frac{1}{2\mu_0} B^2(\theta,t). \quad (2.67)$$

The radial-forces acting on a stator or a rotor tooth will, therefore, be proportional to the square of the magnetic flux passing through it. Since the air-gap flux-density wave has components that rotate at different circumferential speeds in either direction, the force acting on a tooth will vary periodically. A force component of certain frequency of pulsation will produce sinusoidal deformations in the stator and rotor along the

circumference. It is appropriate and convenient to express these radial-forces as waves along the air-gap.

The expansion of Eqn. 2.67 will yield a variety of force-waves. The significance of a force-wave depends on its magnitude, frequency and the mode of excitation associated with it. In the event of the exciting force-frequency coinciding with a resonant frequency of the machine structure, even a small exciting force can give rise to appreciable vibrations. However, at conditions different from that at resonance, the amplitude of the forced vibrations will be determined by the magnitude of the exciting force-wave. Further, it should be emphasised that the flexural rigidity posed by the stator and rotor is much higher to the force-waves having large number of poles [1]. Consequently, in such a case the dynamic deflections produced will be quite small.

The force-waves that give rise to lower modes of vibration are more important with respect to the problem of noise and vibrations. The size of the machine is also an important factor in the consideration of the force-waves according to their number of poles. As the size of the machine increases, the mechanical response of its stator and rotor would increase to some of the force-waves that give rise to higher modes of vibration [35].

So far in this chapter, an analysis has been developed for determination of the noise producing radial-forces for squirrel-cage induction motors. In the following sections, a similar analysis is developed for wound-rotor induction machines. A wound-rotor induction machine is generally used when a large size machine is desired. While dealing with large size machines, the magnetic noise considerations become very important since the machine stator and rotor become more flexible and compliant to higher modes of vibrations.

2.7 Analysis for Wound-Rotor Machines

As in the case of squirrel-cage induction motors, the permeance-wave approach is used to determine the air-gap fields. Again, the MMF-waves are determined taking into account the multiple armature reaction effects. The stator of a wound-rotor induction machine has a configuration similar to that of squirrel-cage induction machine stators. Hence, the analysis for the stator produced magnetic fields of order ν is the

same as that developed in section 2.3.2.

The essential difference, in so far as this analysis is concerned, arises from the effects of the rotor windings. Since in practice it is not always possible to have an integer-slot polyphase winding in the rotor, the analysis has been extended to treat fractional-slot rotor windings. The rotor voltage equations are constructed in terms of the phase-currents at each of the slip-frequencies $s_\nu f$. In the following, general expressions are derived for the mutual inductances from the stator to the rotor and those relating to secondary and tertiary reaction effects.

2.7.1 Stator to Rotor Mutual Inductance

Let the rotor have 1, ..., d, ..., m_2 phase windings, with a rotor skewing of $\frac{2\pi}{h}$ mechanical radians. The flux linking with one coil in the d^{th} phase of the rotor windings is given by, Fig. 2.5:

$$\phi_{(x,d,\nu)} = \int_{y=-\frac{l_e}{2}}^{y=\frac{l_e}{2}} \int_{\theta_2=(d-1)\frac{2\pi}{m_2 p}+(x-1)\alpha_R-\frac{\pi y_2}{2p\tau_{p2}}}^{\theta_2=(d-1)\frac{2\pi}{m_2 p}+(x-1)\alpha_R+\frac{\pi y_2}{2p\tau_{p2}}} B_{1\nu}(\theta_2)\, r\, d\theta_2\, dy, \qquad (2.68.a)$$

$$= l_e\, r\, q_1\, m_1\, 2p \frac{\mu_0 N_1}{\pi(\nu p)\delta'} K_{\nu w1} \left[\frac{2}{\nu p}\sin\left(\nu p \frac{\pi}{2}\frac{y_2}{\tau_{p2}}\right)\right]\left[\frac{\sin\left(\nu p \frac{\pi}{h}\right)}{\nu p \frac{\pi}{h}}\right] \qquad (2.68.b)$$

$$\times \underset{(f)}{I_1}\sqrt{2}\cos\left[s_\nu \omega t - \nu p(d-1)\frac{2\pi}{m_2 p} - \nu p(x-1)\alpha_R\right].$$

Therefore, the total flux linking with the d^{th} phase of the rotor winding is given by:

$$\phi_{d,\nu} = 2p\left(\sum_{x=1}^{q_2} N_2 \cdot \phi_{x,d,\nu}\right), \qquad (2.69.a)$$

$$= M_{1,2,\nu}\underset{(f)}{I_1}\sqrt{2}\cos\left[(d-1)\frac{2\pi}{m_2}\nu - s_\nu \omega t\right], \qquad (2.69.b)$$

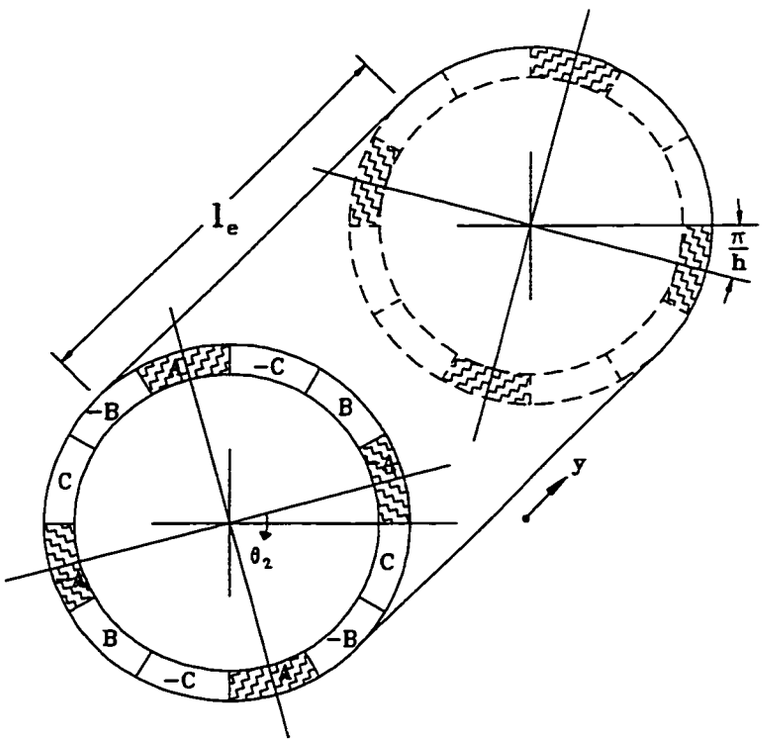

Figure 2.5 : Schematic diagram showing a typical wound-rotor winding arrangement with skew.

where;

$$M_{1,2_\nu} = l_e\, r\, q_1\, q_2\, m_1\, 4p^2\, \frac{\mu_0 N_1 N_2}{\pi (\nu p)^2 \delta'}\, K_{\nu w1}\, K_{\nu w2} \left[\frac{\sin\left(\nu p \frac{\pi}{h}\right)}{\nu p \frac{\pi}{h}} \right], \qquad (2.70)$$

is the mutual inductance of the stator windings to a rotor phase-winding, with respect to the ν^{th} order harmonic field.

2.7.2 Rotor Produced Harmonic Air-gap Fields

The wound-rotor differs from the squirrel-cage rotor in the sense that it limits voltages and currents induced in its windings under the action of the stator produced harmonic fields. This effect due to the polyphase windings on the rotor is beneficial in reducing the propagation of secondary effects associated with the harmonic air-gap fields. A generalised procedure is adopted in this analysis to also consider the effects

of having a fractional slot-winding.

Let n_2 be defined as a positive integer which represents the smallest denominator of the fraction $q_2 = \frac{Z}{2p\,m_2}$. As an example, if Z=28, p=2, m_2=3, then $q_2 = \frac{28}{12} = \frac{7}{3}$, and n_2=3. As a second example if Z=30, p=2, m_2=3, then n_2=2. Further, n_2=1 represents integer slot windings. Thus n_2 can assume odd or even integer values.

A voltage, and hence the corresponding current, will be induced in the rotor windings only when the stator produced harmonic fields of orders ν satisfy the following conditions:

For odd values of n_2 :

$$\nu n_2 = 2g' + 1;\ g' = 0, \pm1, \pm2, \pm3, \ldots \tag{2.71}$$

For even values of n_2 :

$$\nu n_2 = 2g';\ \ g' = 0, \pm1, \pm2, \pm3, \ldots \tag{2.72}$$

Eqn. 2.4 lists the various orders ν, of the harmonic fields produced by the stator windings. Only a few stator produced harmonic fields of order ν will satisfy the conditions given in Eqns. 2.71 and 2.72. Denoting these harmonic orders as ν_2, the voltage induced in the d^{th}-phase of the rotor windings is:

$$E_{1,2,d_{\nu 2}} = -\frac{d}{dt}\left[\phi_{d,\nu 2}\right], \tag{2.73.a}$$

$$= s_{\nu 2}\,\omega\, M_{1,2_{\nu 2}}\, I_{1\,(f)}\, \sqrt{2}\, \sin\left[s_{\nu 2}\,\omega\, t - (d-1)\frac{2\pi}{m_2}\frac{\nu_2}{r_2}\right], \tag{2.73.b}$$

where; for odd values of n_2 : $r_2 = 1 / n_2$, and for even values of n_2 : $r_2 = 2 / n_2$. These voltages produce currents in the rotor at slip-frequency ($s_{\nu 2}$f), and are given by:

$$I_{2,d\,(s_{\nu 2} f)}\ \sqrt{2} = I_{2\,(s_{\nu 2} f)}\ \sqrt{2}\, \cos\left[s_{\nu 2}\,\omega\, t - (d-1)\frac{2\pi}{m_2}\frac{\nu_2}{r_2}\right]. \tag{2.74}$$

It should be noted here that the phase-sequences of the voltages induced are the same for orders; ν_2 = 1, 7, 13, . . ., while it is negative for orders of ν_2 = 5, 11, . . .

These rotor currents produce harmonic air-gap fields of order μ, where;

$$\mu = \nu_2 + g_2\left(\frac{2m_2}{n_2}\right);\ g_2 = 0, \mp 1, \mp 2, \ldots \quad . \tag{2.75}$$

The various air-gap fields of order μ that are produced by the rotor due to the induced currents of frequency $s_{v2}f$ are given by :

$$B_{2_{\mu,v2}}(\theta_2) = m_2\, 2p\, q_2 \frac{\mu_0 N_2}{\pi(\mu p)\,\delta'} K_{w2,\mu} \frac{I_2}{(s_{v2})} \sqrt{2} \cos\left(s_{v2}\,\omega t - \mu p \theta_2\right). \tag{2.76}$$

2.7.3 Flux-linkages of the Rotor Fields

Similar to the case of squirrel-cage induction motors, the currents induced in the wound-rotor windings are split into separate components according to the frequency, $s_v f$, at which they occur. The rotor fields produced by these currents establish flux-linkages with the rotor and also the stator. Since in the rotor there is no externally applied voltage, the sum of the induced voltages will be equal to the voltage drops. This condition is used to construct the rotor voltage equation.

2.7.4 Rotor Self-inductance

The voltage equations for the wound-rotor are formulated in terms of the d^{th}-phase winding. With respect to the μ^{th} order air-gap field produced by the rotor, the self-inductance of the d^{th}-phase winding is defined as the ratio of the total flux linked with the d^{th}-phase winding to the rotor current I_2 at the slip-frequency $s_{v2}f$. The rate of change of this flux gives the voltage induced in the d^{th}-phase winding of the rotor. Therefore;

$$\phi_{(x,d,\mu)} = \int_{\theta_2 = (d-1)\frac{2\pi}{m_2 p} + (x-1)\alpha_R - \frac{\pi y_2}{2p\tau_{p2}}}^{\theta_2 = (d-1)\frac{2\pi}{m_2 p} + (x-1)\alpha_R + \frac{\pi y_2}{2p\tau_{p2}}} B_{2\mu}(\theta_2)\, l_e\, r\, d\theta_2, \tag{2.77.a}$$

$$= l_e\, r\, q_2\, m_2\, 2p\, \frac{\mu_0 N_2}{\pi(\mu p)\delta'} K_{\mu w2} \left[\frac{2}{\mu p} \sin\left(\mu \frac{\pi}{2} \frac{y_2}{\tau_{p2}} \right) \right] \tag{2.77.b}$$

$$\times \underset{(s_{v2} f)}{I_2} \sqrt{2} \cos\left[s_v \omega t - \mu p (d-1) \frac{2\pi}{m_2 p} - \mu p (x-1)\alpha_R \right].$$

Therefore, the total flux linked by the q_2 coils in the d^{th}-phase winding is:

$$\phi_{d,\mu} = 2p \left(\sum_{x=1}^{q_2} N_2 \cdot \phi_{x,d,\mu} \right) \tag{2.78.a}$$

$$= L_{2,\mu} \underset{(s_{v2} f)}{I_2 \sqrt{2}} \cos\left[(d-1) \frac{2\pi}{m_2} \mu p - s_{v2}\, \omega t \right] \tag{2.78.b}$$

where;

$$L_{2,\mu} = l_e\, r\, q_2^2\, m_2\, 4p^2 \frac{\mu_0 N_2^2}{\pi(\mu p)^2 \delta'} K_{vw2}^2. \tag{2.79}$$

is the self-inductance of the rotor windings with respect to the μ^{th} order harmonic field.

2.7.5 Rotor to Stator Mutual Inductance

Again, the rotor produced air-gap fields that link the stator winding induce voltages and currents back in the stator windings at various harmonic frequencies. In the case of wound-rotor induction motors, the harmonic frequencies at which the voltages are induced in the stator windings are related to the number of phases of the rotor windings, and the speed of the rotor. The mutual inductance of the k^{th}-phase of the stator with respect to the μ^{th} order rotor air-gap field can be determined as the ratio of the total flux of the μ^{th} order field linking with the k^{th}-phase to the current in the d^{th}-phase winding of the rotor.

Rewriting the air-gap flux-density produced by the rotor with reference to the stator co-ordinate θ_1;

$$B_{2_{\mu,v2}}(\theta_1) = 2p\,q_2\,m_2 \frac{\mu_0 N_2}{\pi(\mu p)\delta'} K_{w2,\mu} \frac{I_2}{(s_{v2} f)} \sqrt{2} \cos\left(s_{g_2}\omega t - \mu p \theta_1\right), \qquad (2.80)$$

where s_{g_2} is the slip associated with the μ^{th} order air-gap field, which is given by:

$$\begin{aligned} s_{g_2} &= 1 + \mu - v_2 (1 - s), \\ &= 1 + g_2 \frac{2m_2}{n_2} (1 - s). \end{aligned} \qquad (2.81)$$

These flux linkages of the μ^{th} order field with the stator windings induce voltages and currents in the stator windings at the slip frequency $s_{g_2} f$. The integration of the air-gap flux-density of the μ^{th} order over the span of the x^{th}-coil in a phase-belt of the k^{th}-phase will give the total flux linking with it. Thus:

$$\phi_{(x,k)_{\mu,v2}} = \int_{\theta_1 = (k-1)\frac{2\pi}{m_1 p} + (x-1)\alpha_S - \frac{\pi y_1}{2p\tau_{p1}}}^{\theta_1 = (k-1)\frac{2\pi}{m_1 p} + (x-1)\alpha_S + \frac{\pi y_1}{2p\tau_{p1}}} B_{2_{\mu,v2}}(\theta_1)\, l_e\, r\, d\theta_1, \qquad (2.82.a)$$

$$\begin{aligned} &= l_e\, r\, m_2\, q_2\, 2p \frac{\mu_0 N_2}{\pi(\mu p)\delta'} K_{w2,\mu} \left[\frac{2}{\mu p} \sin\left(\mu \frac{\pi}{2} \frac{y_1}{\tau_{p1}}\right)\right] \\ &\times \frac{I_2}{(s_{v2} f)} \sqrt{2} \cos\left(s_{g_2}\omega t - \mu p (k-1) \frac{2\pi}{m_1 p} - \mu p (x-1)\alpha_S\right) \end{aligned} \qquad (2.82.b)$$

The total flux of the μ^{th} order rotor field, linking with a phase-belt in the k^{th}-phase is obtained by the phasor sum of all the flux-linkages with the N_1 turns of the q_1 coils. Also, since the rotor slots are skewed, the flux-linkages of Eqn. 2.82.b has to be multiplied by the skewing-factor. It is, therefore, expressed as:

$$\phi_{k_{\mu,v2}} = N_1 \sum_{x=1}^{q_1} \phi_{(x,k)_{\mu,v2}} \frac{\sin\left(\mu p \frac{\pi}{h}\right)}{\mu p \frac{\pi}{h}}, \qquad (2.83.a)$$

$$= l_e r q_1 q_2 4p^2 m_1 m_2 \frac{\mu_0 N_1 N_2}{\pi (\mu p)^2 \delta'} K_{w1,\mu} K_{w2,\mu} \frac{\sin\left(\mu p \frac{\pi}{h}\right)}{\mu p \frac{\pi}{h}} \qquad (2.83.b)$$

$$\times \underset{(s_{v2} f)}{I_2} \sqrt{2} \cos\left(s_{g_2} \omega t - \mu p (k-1) \frac{2\pi}{m_1 p} \right).$$

Therefore, the mutual inductance of the rotor to the stator $M_{2,1}$ with respect to the μ^{th} order rotor air-gap field is given by:

$$M_{2,1_\mu} = l_e r q_1 q_2 4p^2 m_1 m_2 \frac{\mu_0 N_1 N_2}{\pi (\mu p)^2 \delta'} K_{w1,\mu} K_{w2,\mu} \frac{\sin\left(\mu p \frac{\pi}{h}\right)}{\mu p \frac{\pi}{h}}. \qquad (2.84)$$

From Eqn. 2.83.b and Eqn. 2.84, the voltage induced in a phase-belt of the k^{th}-stator phase due to the μ^{th} order rotor air-gap field is given by:

$$\underset{(s_{g_2} f)}{E_k} = s_{g_2} \omega M_{2,1_\mu} \underset{(s_{v2} f)}{I_2} \sqrt{2} \sin\left[s_{g_2} \omega t - \left(1 + g_2 \frac{2m_2}{n_2} \right) (k-1) \frac{2\pi}{m_1} \right]. \qquad (2.85)$$

It is seen from Eqn. 2.85, that all the rotor fields whose harmonic orders are such that:

$$\mu - \nu = g_2 \frac{2m_2}{n_2} \neq 0, \qquad (2.86)$$

will induce a voltage in the stator winding at a frequency different from the supply frequency f. Further, the phase-shift of the induced voltages in the various phases due to different g_2 will be given by:

$$\gamma_{g_2} = \left(1 + g_2 \frac{2m_2}{n_2} \right) (k-1) \frac{2\pi}{m_1}. \qquad (2.87)$$

2.7.6 Secondary Armature Reaction

As explained earlier, the stator will produce additional harmonic fields of order ε, where:

$$\epsilon = 2m_1 g_3 + 1 + g_2 \frac{2m_2}{n_2}; \qquad g_3 = 0, \mp 1, \mp 2, \mp 3, \ldots. \tag{2.88}$$

The air-gap flux-density of the stator harmonic fields of order ε is given by:

$$B_{1_\epsilon}(\theta_1) = q_1 m_1 2p \frac{\mu_0 N_1}{\pi(\epsilon p)\delta'} K_{\epsilon w1} \frac{I_1}{(s_{g_2} f)} \sqrt{2} \cos(s_{g_2} \omega t - \epsilon p \theta_1). \tag{2.89}$$

Continuing, the resulting fields produced by these stator air-gap flux-densities of order ε establish flux-linkages with the stator and rotor windings. In the following sections, general expressions are derived for the self-inductance of the stator windings with respect to the ε^{th} order harmonic air-gap fields.

The stator produced harmonic fields of the ε^{th} order are given in Eqn. 2.89. The total flux of the ε^{th} order linking with the x^{th}-coil in the k^{th}-phase stator winding is found as:

$$\phi_{(x,k)_\epsilon} = \int_{\theta_1 = (1+g_2\frac{2m_2}{n_2})(k-1)\frac{2\pi}{m_1 p} + (x-1)\alpha_s - \frac{\pi y_1}{2p\tau_{p1}}}^{\theta_1 = (1+g_2\frac{2m_2}{n_2})(k-1)\frac{2\pi}{m_1 p} + (x-1)\alpha_s + \frac{\pi y_1}{2p\tau_{p1}}} B_{1_\epsilon}(\theta_1)\, l_e\, r\, d\theta_1, \tag{2.90.a}$$

$$= l_e r q_1 m_1 2p \frac{\mu_0 N_1}{\pi(\epsilon p)\delta'} K_{\epsilon w1} \left[\frac{2}{\epsilon p} \sin\left(\epsilon p \frac{\pi}{2} \frac{y_1}{\tau_{p1}}\right)\right] \tag{2.90.b}$$

$$\times \frac{I_1}{(s_{g_2} f)} \sqrt{2} \cos\left[s_{g_2} \omega t - \epsilon p (k-1)(1+g_2\frac{2m_2}{n_2})\frac{2\pi}{m_1 p} - \epsilon p (x-1)\alpha_s\right].$$

Therefore, the total flux of the ε^{th} order field linking with a phase-belt in the k^{th}-phase can be found as:

$$\phi_{k_\epsilon} = N_1 \sum_{x=1}^{q_1} \phi_{(x,k)_\epsilon}, \tag{2.91.a}$$

$$= l_e r q_1^2 m_1 4p \frac{\mu_0 N_1^2}{\pi (\epsilon p)^2 \delta'} (K_{\epsilon w1})^2$$

$$\times \underset{(s_{g_2} f)}{I_1} \sqrt{2} \cos \left[s_{g_2} \omega t - \epsilon p (1 + g_2 \frac{2m_2}{n_2})(k-1) \frac{2\pi}{m_1 p} \right]. \quad (2.91.b)$$

From Eqn. 2.91.b, the self-inductance of the k[th]-phase of the stator winding with respect to the ε[th] order air-gap field harmonic is:

$$L_{1,\epsilon} = l_e r q_1^2 m_1 4p \frac{\mu_0 N_1^2}{\pi (\epsilon p)^2 \delta'} (K_{\epsilon w1})^2. \quad (2.92)$$

All the voltages induced in the stator windings for various orders of ε, that are associated with the same values of g_2 in Eqn. 2.75, are of the same slip frequency $s_{g_2} f$. Hence, the voltage induced in a phase-belt of the k[th]-phase can be written as:

$$\underset{(s_{g_2} f)}{E_k} = s_{g_2} \omega \left[\sum_{\epsilon = -\infty}^{\infty} L_{1,\epsilon} \right]_{g_2 = \text{constant}}$$

$$\times \underset{(s_{g_2} f)}{I_1} \sqrt{2} \sin \left(s_{g_2} \omega t - (1 + g_2 \frac{2m_2}{n_2})(k-1) \frac{2\pi}{m_1} \right), \quad (2.93.a)$$

$$= s_{g_2} \omega \left\{ (L_{1,\epsilon})_{g_3 = 0} \left[1 + \sigma_{d1,g_2} \right] \right\}_{g_2 = \text{constant}}$$

$$\times \underset{(s_{g_2} f)}{I_1} \sqrt{2} \sin \left[s_{g_2} \omega t - (1 + g_2 \frac{2m_2}{n_2})(k-1) \frac{2\pi}{m_1} \right], \quad (2.93.b)$$

where σ_{d1,g_2} is defined as the coefficient of harmonic flux-linkage, and is expressed mathematically as:

$$\sigma_{d1,g_2} = \left. \frac{\left[\sum_{\epsilon = -\infty}^{\infty} L_{1,\epsilon} \right]_{g_3 \neq 0}}{\left[L_{1,\epsilon} \right]_{g_3 = 0}} \right|_{g_2 = \text{constant}}. \quad (2.94)$$

2.7.7 Tertiary Armature Reaction

Considerations of the tertiary armature reaction involve determining the effects of the stator produced harmonic fields of order ε on the rotor. In the following, the mutual inductance of the stator to the rotor with respect to the ε^{th} order harmonic field is derived.

The total flux of the ε^{th} order linking with the x^{th}-coil of d^{th}-phase winding of the rotor is given by:

$$\phi_{(x,d,\epsilon)} = \int_{y=-\frac{l_e}{2}}^{y=\frac{l_e}{2}} \int_{\theta_2=(d-1)\frac{2\pi}{m_2 p}+(x-1)\alpha_R-\frac{\pi y_2}{2p\tau_{p2}}+\frac{2\pi y}{hl_e}}^{\theta_2=(d-1)\frac{2\pi}{m_2 p}+(x-1)\alpha_R+\frac{\pi y_2}{2p\tau_{p2}}+\frac{2\pi y}{hl_e}} B_{1_\epsilon}(\theta_2)\, r\, d\theta_2\, dy, \qquad (2.95)$$

Therefore, the total flux linking with the d^{th}-phase of the rotor windings is:

$$\phi_{d,\epsilon} = 2p\left(\sum_{x=1}^{q_2} N_2 \cdot \phi_{x,d,\epsilon}\right) \qquad (2.96.a)$$

$$= l_e\, r\, q_1\, q_2\, m_1\, 4p^2 \frac{\mu_0 N_1 N_2}{\pi(\epsilon p)^2 \delta'} K_{\epsilon w1} K_{\epsilon w2} \left[\frac{\sin\left(\epsilon p \frac{\pi}{h}\right)}{\epsilon p \frac{\pi}{h}}\right] \qquad (2.96.b)$$

$$\times \underset{(s_{g_2} f)}{I_1} \sqrt{2} \cos\left(s_{g_2}\omega t - \epsilon(d-1)\frac{2\pi}{m_2}\right).$$

Therefore, the voltage induced in the d^{th}-phase of the rotor windings due to the ε^{th} order stator air-gap field is:

$$\underset{(s_{g_3} f)}{E_d} = s_{g_3}\,\omega\, M_{1,2_\epsilon} \underset{(s_{g_2} f)}{I_1} \sqrt{2} \sin\left(s_{g_3}\omega t - \epsilon(d-1)\frac{2\pi}{m_2}\right), \qquad (2.97)$$

where $M_{1,2_\varepsilon}$ is the mutual inductance of the stator to the rotor with respect to the ε^{th} order harmonic air-gap field, and it is given by:

$$M_{1,2_\epsilon} = l_e\, r\, q_1\, q_2\, m_1\, 4p^2\, \frac{\mu_0 N_1 N_2}{\pi(\epsilon p)^2 \delta'}\, K_{\epsilon w1}\, K_{\epsilon w2} \left[\frac{\sin\left(\epsilon p \frac{\pi}{h}\right)}{\epsilon p \frac{\pi}{h}} \right]. \tag{2.98}$$

2.7.8 Voltage Equations

The voltage equations for the stator given in Eqns. 2.52 and 2.53 will hold good. For the wound-rotor, the voltage equations are formulated in terms of the d^{th}-phase rotor winding. The voltage drops in the rotor phase-winding comprises of the drops caused by the resistances and the inductances of the circuit. Therefore, considering Eqns. 2.73.b, 2.79, and 2.97, the voltage equation for the rotor at frequency $s_v f$ is formulated as:

$$\begin{aligned} 0 = \Bigg\{ & \left[R_{2,v} + j s_v \omega \left(L_{2,v} + L_{S2} + L_{N2} \right) \right] \underset{(s_v f)}{I_2 \sqrt{2}} \\ & + j s_v \omega M_{1,2_v} \underset{(f)}{I_1 \sqrt{2}} \Bigg\}_{g_3 = g_1 = \text{constant}} \cos\left(s_v \omega t - v(d-1)\frac{2\pi}{m_2} \right). \end{aligned} \tag{2.99}$$

As explained earlier for squirrel-cage induction motors, the voltage equations are organised in the form of matrices which aids in the determination of the solution. The calculated values of the currents are then substituted in the corresponding expressions to obtain the various harmonic field components. Adopting the procedure described in Section 2.3.3.8, the net MMF acting across the air-gap is obtained from the various harmonic field components. These are then appropriately modelled as MMF-waves for the wound-rotor induction motor.

2.7.9 Radial-force Waves

The permeance-waves are constructed for the wound-rotor induction motor in accordance with the description provided in Section 2.4. The air-gap flux-density waves are then obtained as the product of the MMF-waves and the permeance-waves. As described in Section 2.6, the radial-force waves are obtained by using the relationship

provided in Eqn. 2.67.

In the case of the squirrel-cage induction motor, the harmonic fields produced due to the rotor MMF-harmonics and the rotor permeance-harmonics are indistinguishable from each other. In contrast, in the case of wound-rotor induction motors these occur as distinct components. In wound-rotor induction machines, most of the radial-forces are produced at lower frequencies and they also have many more force components. They induce lower modes of vibrations.

2.8 Comments

In this chapter, an analysis of a general nature for the determination of the magnetic radial-forces in squirrel-cage and wound-rotor type induction motors has been presented. This method can be easily extended to incorporate the effects of different stator and rotor winding arrangements, while considering the mutual interactions between the stator and rotor MMF's. It also has the added advantage of using the permeance-wave method, and the analysis presents a convenient procedure for treating the effects of saturation.

In the next chapter, a squirrel-cage induction motor and a wound-rotor induction motor are analyzed to verify the validity of the analyses. Theoretical and experimental results are presented with a view to determine the actual role played by the air-gap harmonic fields on the radial-forces. Also, the effects of loading the motor on the radial-forces and the ensuing vibrations are critically examined in the following chapter.

3. CALCULATED RESULTS, EXPERIMENTAL PROCEDURES AND EXPERIMENTAL RESULTS

In the previous chapter, analyses for the calculation of the various field-harmonics and radial-forces in squirrel-cage and wound-rotor induction machines were developed. In this chapter, a 10 hp (7.5 kW) squirrel-cage induction motor and a 94 hp (70 kW) wound-rotor induction motor are analyzed to verify the validity of the analysis. After discussing the calculated results for the test motors, the experimental set-up and the procedures adopted to conduct the experimentation are described. The theoretical and experimental results are presented with a view to determine the actual role played by the air-gap harmonic fields on the radial-forces. Also, the effects of loading on the radial-forces and the ensuing vibrations are closely examined.

3.1 Calculated Results for the 10 hp Squirrel-Cage Induction Motor

In order to verify the validity of the analysis and to acquire a physical understanding of the nature of the radial-forces, extensive investigations were carried out on a 10 hp squirrel-cage induction motor. The salient design details of the test motor are provided in Table 3.1. Further details are available in reference [44].

The harmonic currents in the stator and rotor windings are determined using the theoretical analysis presented in Chapter 2. Some of the additional data required for the theoretical analysis is provided in Table 3.2. As discussed earlier, the harmonic air-gap fields produced by the stator and rotor MMF's are determined by assuming the stator and rotor surfaces to be smooth. A corrected value for the average air-gap length is used while determining the harmonic fields produced by the stator and rotor MMF's. The stator produced space-harmonic air-gap fields of order ν, have ν times the number of pole-pairs of the fundamental air-gap field. These air-gap fields rotate at $\frac{1}{\nu}$ times the synchronous speed. Further, the rotor produces harmonic fields of order μ. In accordance with Eqn. 2.23, the harmonic orders μ for the test machine are given by:

Table 3.1 : Relevant data for the 10 hp induction motor.

Output power	10 hp
Line voltage	460 V (Series Connection)
Rated speed	1740 rpm
Number of poles	4
Outside diameter of stator laminations	229 mm
Diameter of stator-bore	152.4 mm
Air-gap length	0.4 mm
Stator stack length	106 mm
Stator slot-opening	2.5 mm
Average stator tooth-width	6 mm
Stator slot-pitch	13.3 mm
Type of stator winding	Double layer lap
Number of stator slots	36
Coil-pitch	Slot 1 to 8
Number of rotor slots	43
Rotor slot-opening	1 mm
Rotor slot-pitch	11.14 mm
Rotor skew advance along the length of rotor, mech. rad.	$\frac{2\pi}{43}$

$$\mu = g_2 \frac{43}{2} + \nu ; \quad g_2 = 0, \mp 1, \mp 2, \mp 3, \ldots \tag{3.1}$$

As explained in Chapter 2, the secondary armature reaction of the stator to the rotor fields produces fields of order ε. The harmonic orders, ε, can be obtained from Eqn. 2.40, and for the test machine these are:

Table 3.2 : Additional parameters for the 10 hp squirrel-cage induction motor.

Carter's coefficient for stator slotting	1.145
Carter's coefficient for rotor slotting	1.127
Corrected value of the air-gap length, millimetre	0.512
Number of turns per coil in the stator winding	13
Number of slots per pole per phase of the stator winding	3
Resistance of the stator winding per phase, ohms	0.88
Stator slot-leakage inductance per phase, H	0.011
Stator end-winding leakage inductance, H	0.00465
Resistance of rotor bar, ohms	9.045×10^{-5}
Resistance of the end-ring segments between bars, Ω	2.234×10^{-6}
Rotor slot-leakage inductance, H	3.577×10^{-7}
Rotor end-ring segment leakage inductance, H	5.150×10^{-9}

$$\epsilon = 6g_3 + 1 + g_2 \frac{43}{2}; \quad g_3 = 0, \mp 1, \mp 2, \mp 3, \ldots \tag{3.2}$$

Table 3.3 lists the various air-gap field harmonics produced by orders ν, μ and ε in the test machine. In Table 3.3, the second column gives the pole-pairs associated with stator space-harmonic fields, i.e. (ν.p) pole-pairs for various values of g_1. The rotor produced harmonic air-gap fields with (μ.p) pole-pairs will be the same as the stator space-harmonic fields when $g_2 = 0$. For the various combinations of ν and g_2, the pole-pairs of the rotor produced fields (μ.p) is given in the cell which is common to the respective row and the column. It is noted that for the series connection of all the phase-belts in a phase winding, the harmonic orders ε of the fields produced due to secondary armature reaction will be the same as orders μ.

All the rotor produced fields listed in a particular column of Table 3.3 will induce currents in the stator windings at the same frequency. Similarly, all the stator produced fields listed on the same row will induce currents in the rotor cage winding at the same frequency. The rotor produced fields that correspond to $g_2 = +1$ and $g_2 = -2$,

Table 3.3 : Pole-pairs of the various air-gap harmonic fields produced in the test machine, for different values of g_1, g_2 and g_3.

g_1 \ g_2	*0*	*-1*	*+1* *	*-2* *	+2	*-3*	+3	g_3
0	2	-41	45	-84	88	-127	131	*0*
-1	-10	-53	33	-96	76	-139	119	*-1*
+1	14	-29	57	-72	100	-115	143	*+1*
-2	-22	-65	21	-108	64	-151	107	*-2*
+2	26	-17	69	-60	112	-103	155	*+2*
-3	-34	-77	9	-120	52	-163	95	*-3*
+3	38	-5	81	-48	124	-91	167	*+3*
-4	-46	-89	-3	-132	40	-175	83	*-4*
+4	50	7	93	-36	136	-79	179	*+4*

"Minus sign" denotes the fields which rotate in the direction opposite to that of the fundamental.
* Shaded area denotes fields that are of triplen orders.

are shown in the columns with darker back ground. These are triplen harmonic fields (i.e. the pairs of poles are a multiple of 3), and they induce zero-sequence voltages in the stator windings. Since the stator has a 3-phase winding connected in star, these rotor fields will be undamped, as evident from Appendix A.

The currents in a stator phase-winding and in a rotor mesh are calculated by solving the voltage Eqns. 2.52, 2.53 and 2.58. To have an appreciation of the magnitudes of the various currents in the stator winding, Table 3.4 provides the information at no-load and rated load conditions. The current components other than the fundamental at 60 Hz are produced by the harmonic rotor fields. It is recalled that the various rotor fields of order μ induce currents in the stator windings at different slip frequencies, which are given by:

$$s_{g_2} f = \left[g_2 \frac{Z}{p} (1 - s) + 1 \right] f . \tag{3.3}$$

As explained before, the triplen harmonic fields that correspond to $g_2 = +1$ and -2 induce zero-sequence voltages in the stator windings. Considering the test machine to be

operating at no-load (s = 0), these zero-sequence voltages will be induced at 1350 Hz and 2520 Hz. Since it is assumed that the star-point of the stator winding is not connected to the supply neutral, the zero-sequence currents cannot exist in the stator windings.

To have a better understanding of the magnitudes of the various currents in a rotor mesh, Table 3.5 provides information pertaining to the no-load and the rated load conditions. The component at the slip frequency (sf) is produced mainly by the fundamental air-gap field at the load condition. This current is quite small at no-load, but it increases as the rotor slows down with load. At the ideal no-load condition, i.e. slip = 0, the rotor revolves at the synchronous speed and hence there is no voltage induced in its squirrel-cage windings due to the stator fields produced by the fundamental current. As the machine is loaded, the rotor slows down and the currents in a rotor mesh increase with the load. The increase in the rotor current at the slip frequency (sf) would amplify all the rotor fields whose harmonic orders are listed in the first row of Table 3.3. The stator produced harmonic air-gap fields due to orders ν and ε, which are listed on the same row of Table 3.3, will induce currents in the rotor mesh at the same frequency. The frequencies of the induced currents that correspond to different harmonic orders, ν, are given by:

$$s_\nu f = [\,1 - \nu\,(1 - s)\,]f. \tag{3.4}$$

Again, the various MMF-harmonics produced by the harmonic currents were calculated both for the no-load and rated load conditions. The magnitudes of these MMF-harmonic components are listed in Table 3.6 and Table 3.7 for the no-load and rated load conditions, respectively

At no-load, the significant MMF-harmonic components are those due to the fundamental currents, ($g_1 = 0$, g_2=0), and the stator slot-MMF-harmonic components, ($g_1 = \pm 3$, $g_2 = 0$). Among the rotor produced MMF-harmonics those corresponding to the undamped field components shown in shaded columns of Table 3.6, are generally much higher than the other MMF-harmonic components. With load, most of the rotor produced MMF-harmonic components show an appreciable increase. Again for the case of the machine operating at load, the dominant MMF-harmonic components are those related to the stator slot-harmonics and the undamped fields.

Table 3.4 : Calculated values of the currents in a stator-phase winding at no-load and rated load conditions.

No-load, slip = 0		Rated load, slip = 0.033	
Freq., Hz	**Current, A**	**Freq., Hz**	**Current, A**
60	3.368970	60	10.998240
1230	0.023282	1187	0.099689
1350	0.000000	1307	0.000000
2520	0.000000	2435	0.000000
2640	0.000082	2555	0.002438
3810	0.000099	3682	0.001153
3930	0.000024	3802	0.000072
5100	0.000043	4930	0.000105
5220	0.000010	5050	0.000433

Table 3.5 : Calculated values of the currents in a rotor mesh at no-load and rated load conditions.

No-load, slip = 0		Rated load, slip =0.033	
Freq., Hz	**Rotor mesh current, A**	**Freq., Hz**	**Rotor mesh current, A**
0	0.220980	1.98	**695.840200**
360	1.320495	350.10	**4.311357**
	2.563116	346.14	**8.370069**
720	0.821297	698.22	**2.680831**
	0.101362	694.26	**0.303631**
1080	0.689019	1046.34	**2.249089**
	0.492671	1042.38	**1.920936**
1440	0.039188	1394.46	**0.128903**
	0.055921	1390.50	**0.262473**

Table 3.6 : Magnitudes of the various air-gap MMF-harmonics in Ampere-turns, produced in the test machine, for different values of g_1, g_2 and g_3 at no-load condition.

g_2 / g_1	*0*	*-1*	*+1* *	*-2* *	*+2*	*-3*	*+3*	g_3
0	319.86	0.0	0.2	0.0	0.0	0.0	0.0	*0*
-1	0.98	0.4	1.0	0.1	0.0	0.1	0.1	*-1*
+1	3.9	0.7	0.7	0.2	0.0	0.1	0.1	*+1*
-2	3.6	0.4	2.4	0.1	0.0	0.1	0.1	*-2*
+2	1.0	1.3	0.7	0.3	0.0	0.1	0.1	*+2*
-3	18.6	0.2	3.4	0.1	0.0	0.0	0.1	*-3*
+3	16.7	1.3	0.2	0.1	0.0	0.1	0.0	*+3*
-4	0.6	0.0	3.6	0.0	0.0	0.0	0.0	*-4*
+4	1.9	1.9	0.3	0.2	0.0	0.1	0.0	*+4*

* Shaded area denotes fields that are of triplen orders.

Table 3.7 : Magnitudes of the various air-gap MMF-harmonics in Ampere-turns, produced in the test machine, for different values of g_1, g_2 and g_3 at rated load condition.

g_2 / g_1	*0*	*-1*	*+1* *	*-2* *	*+2*	*-3*	*+3*	g_3
0	306.2	0.0	0.5	0.1	0.0	0.0	0.0	*0*
-1	3.2	1.2	3.3	0.4	0.0	0.2	0.2	*-1*
+1	12.7	2.3	2.4	0.6	0.1	0.3	0.2	*+1*
-2	11.9	1.3	7.7	0.5	0.1	0.3	0.3	*-2*
+2	3.1	4.3	2.2	0.8	0.1	0.4	0.2	*+2*
-3	60.7	0.8	11.0	0.3	0.1	0.2	0.2	*-3*
+3	54.5	3.9	0.7	0.4	0.0	0.2	0.1	*+3*
-4	1.9	0.1	11.7	0.1	0.0	0.1	0.1	*-4*
+4	6.3	6.4	0.9	0.7	0.0	0.3	0.1	*+4*

* Shaded area denotes fields that are of triplen orders.

Permeance-waves

As explained in chapter 2, the permeance-wave is constructed using the physical dimensions of the machine. The various coefficients and the average value of the air-gap permeance for the 10 hp squirrel-cage induction motor are provided in Table 3.8.

Flux-density waves

The air-gap flux-density is obtained as waves through the multiplication of the MMF and permeance-waves. From the perspective of noise and vibrations, it is important to know the flux pulsations through the teeth. Experimental information on the flux pulsations through a stator tooth is commonly obtained with use of search-coils. More description of the search-coils is provided later in this chapter in Section 3.3.3.2. Since the search-coil is a loop of copper conductor placed around a stator tooth at its tip, the voltage induced in the search-coil is proportional to the flux pulsations through the

Table 3.8 : Permeance-wave coefficients for 10 hp squirrel-cage induction motor.

Average value of the air-gap permeance per unit area, λ_0	2.45×10^{-3}, henrys/metre^2
Stator Permeance Coefficients	
Coefficient of order 1, λ_{S1}	0.207
Coefficient of order 2, λ_{S2}	0.173
Coefficient of order 3, λ_{S3}	0.127
Rotor permeance coefficients	
Coefficient of order 1, λ_{R1}	0.060
Coefficient of order 2, λ_{R2}	0.057
Coefficient of order 3, λ_{R3}	0.053
Saturation permeance coefficients	
Coefficient of order 0, $\lambda_{sa,0}$	1.000
Coefficient of order 1, $\lambda_{sa,1}$	0.250
Coefficient of order 2, $\lambda_{sa,2}$	0.088

tooth. In order to assess the accuracy of the air-gap field calculations, comparisons with the experimentally measured information are made. Hence, the calculation of the induced voltages in the tooth-width search-coil is required.

3.1.1 Voltage Induced in a Tooth-width Search-coil

The flux linking with the search-coil is obtained by integrating the air-gap flux density wave over the span of the search-coil. The rate of change of this flux will thus provide information on the voltages induced in the search-coil.

Figs. 3.1 and 3.2 show the spectra of the calculated values of the induced voltages in the stator search-coil at no-load and at the rated load, respectively. The amplitudes are shown on a log scale relative to the component at 60 Hz, so that even the smaller harmonic components can be displayed. The fundamental air-gap field, and all the stator space harmonic fields of order ν induce a voltage in the stator search-coil at the line-frequency, f. The components marked S1, S2 and S3 are produced either due to the harmonic rotor MMF's, and or the slotting effects. They occur at slip-dependent frequencies which are given by:

$$s_{g_2} f = \left[1 + g_2 \frac{Z}{p} (1 - s) \right] f . \tag{3.5}$$

Saturation harmonic fields induce voltages at 3f, 5f, 7f, ..., and the side-bands on either side of a slot-harmonic. These side-band components occur at frequencies of:

$$\left[(1 + 2\eta) + g_2 \frac{Z}{p} (1 - s) \right] f , \tag{3.6}$$

where $\eta = 0, \mp 1, \mp 2, \ldots$.

The magnitude of the fundamental air-gap field component at 60 Hz, and the saturation harmonic components at 180 Hz and 300 Hz remain relatively constant with the changes in load. All the slot-harmonics and their saturation side-band show an increasing trend with the increase in load. This increase is caused by the increase in the rotor MMF-harmonics with load. Also, some of the higher order effects of the rotor MMF become more pronounced with increase in the load.

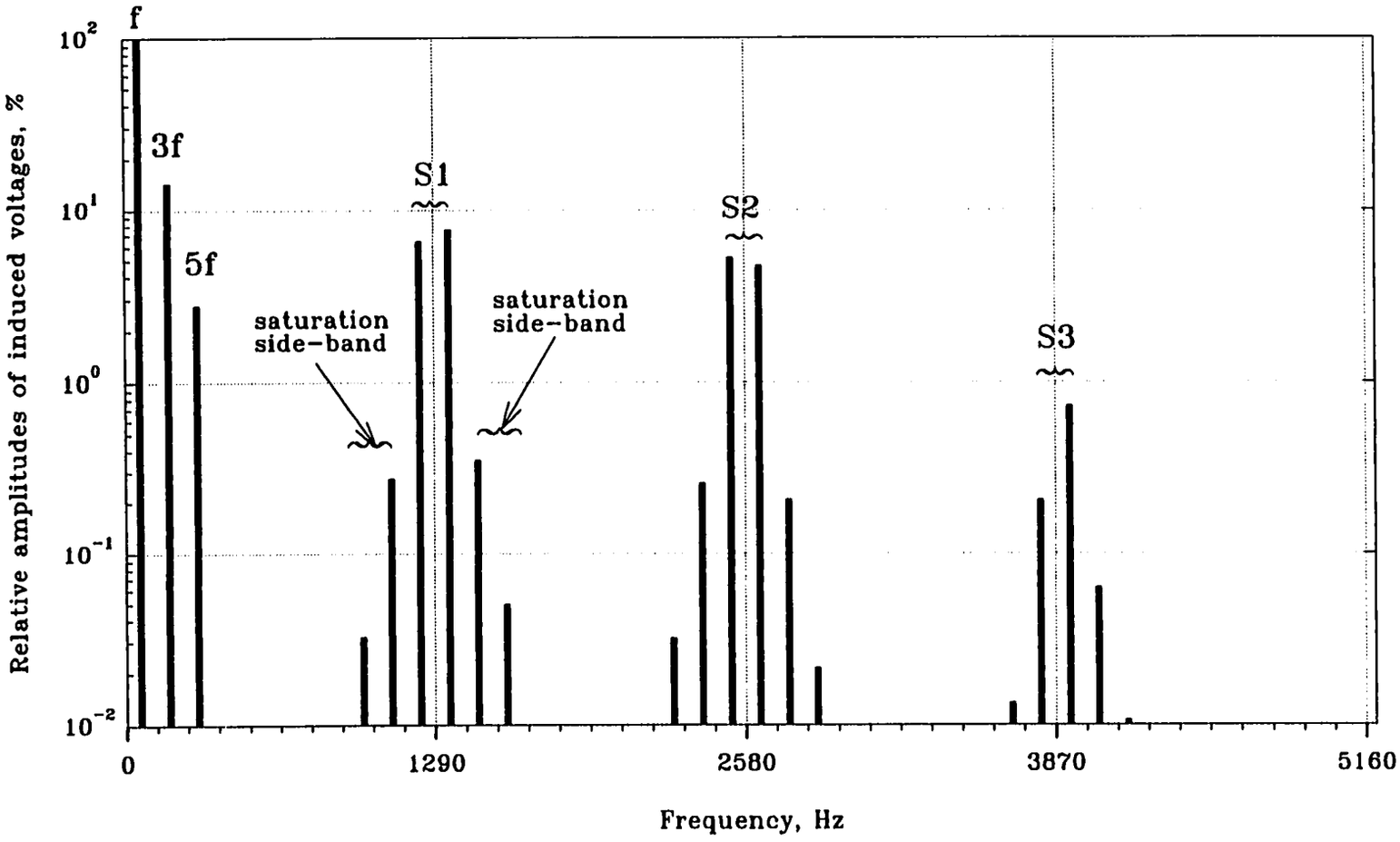

Figure 3.1 : Calculated spectral distribution of the voltages induced in a tooth-width search-coil for no-load, slip=0.

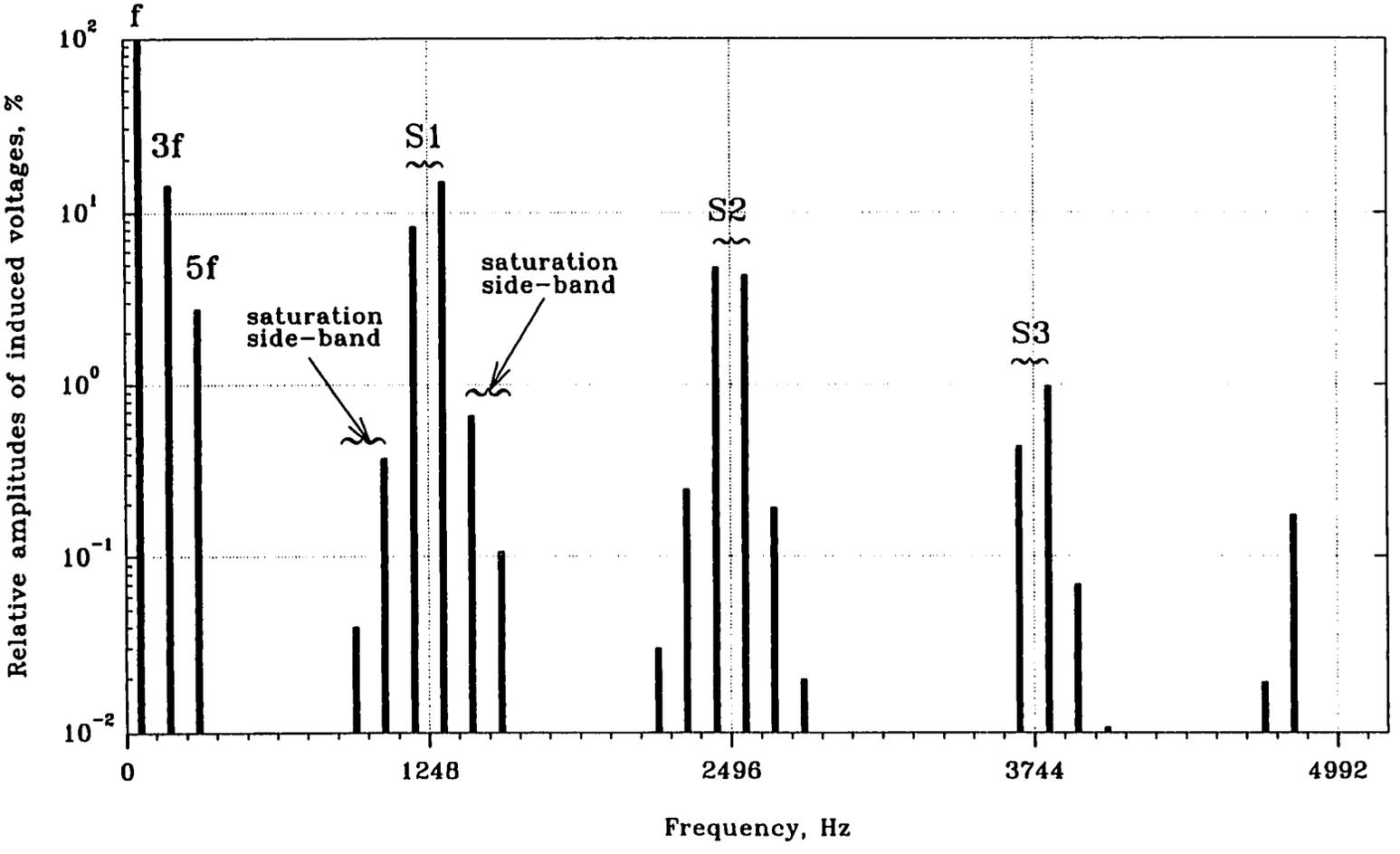

Figure 3.2 : Calculated spectral distribution of the voltages induced in a tooth-width search-coil for rated load, slip=0.033.

3.1.2 Radial-Forces

As explained in Section 2.6, the force-distribution is obtained as waves from the air-gap flux-density wave. The forces acting on a stator tooth is obtained by integrating the force-waves over the span of the stator tooth. The computation procedure for the determination of the radial-forces is provided in Appendix B.

Figs. 3.3 and 3.4 show the calculated spectra of the radial-forces that act on a stator tooth at no-load and at the rated load, respectively. The amplitudes of the various force components are shown in Newtons, and also as a percentage relative to the radial-force at twice the line frequency. This method of displaying the radial-forces has distinct advantage in identifying the various components, and also in tracing their origins. The significant force at twice the line frequency is predominantly produced by the fundamental air-gap field. The interaction between the slot-harmonic fields and the fundamental air-gap field produces forces at the slot-harmonic frequencies. Mathematical description of the production of the slot-harmonic forces has been given in reference [44], Appendix G. The slot-harmonic forces of orders 1 to 6 are identified in Figs. 3.3 and 3.4 as Fs1, ..., Fs6. The effects of saturation leads to the production of components at 4f, 6f, 8f, ..., and the side-bands on either side of each of the slot-harmonic forces.

It is observed that the loading of the induction motor results in an increase in the amplitudes of the slot-harmonic forces. Again, the increase in the rotor MMF-harmonics with load is the source for the increase in the amplitudes of the slot-harmonic forces. The increase in the MMF-harmonics also introduces higher saturation effects, which leads to the pronounced saturation side-band components in the force spectra at rated load conditions.

3.2 Calculated Results for the 70 kW Wound-Rotor Induction Motor

In order to acquire a physical understanding of the nature of the radial-forces in wound-rotor induction motors, a 70 kW induction motor is analyzed using the procedure detailed in the previous chapter. In reference [17], the author has reported the theoretical and experimental investigations on the harmonic currents induced in the stator and rotor windings of this 70 kW motor. As explained in Chapter 2, the author [17] has neglected

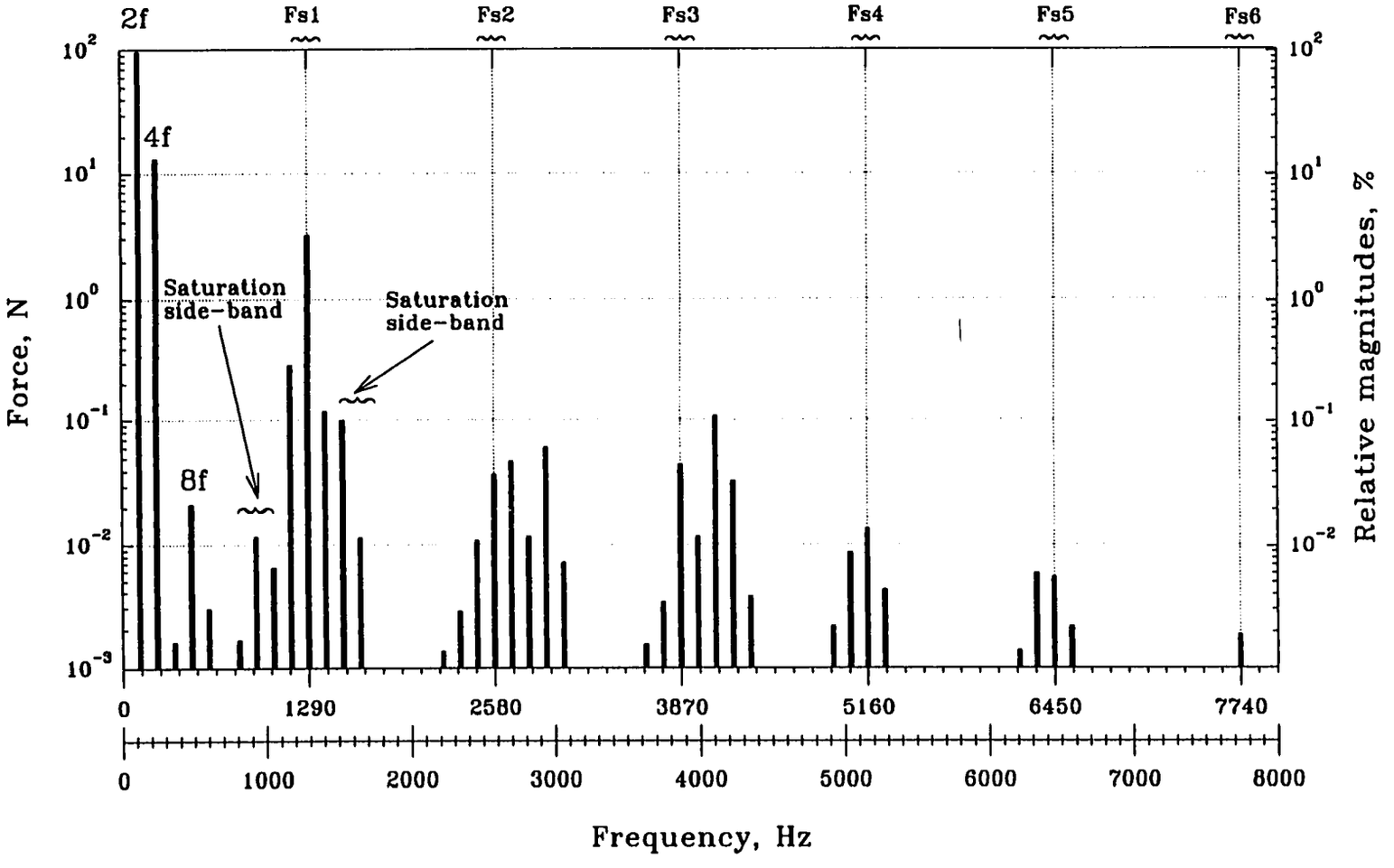

Figure 3.3 : Calculated spectral distribution of the forces acting on a stator tooth of the 10 hp squirrel-cage induction motor at no-load.

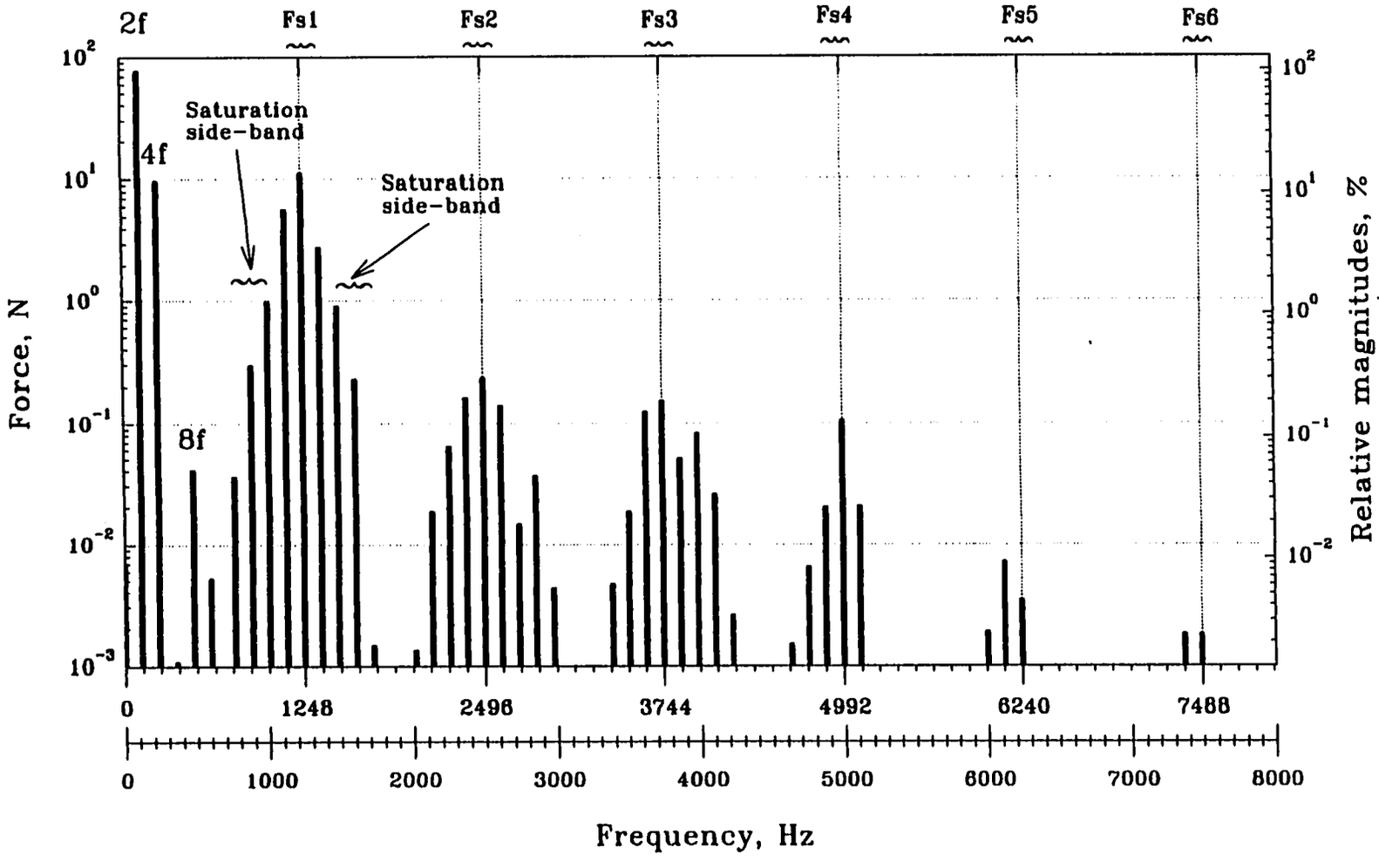

Figure 3.4 : Calculated spectral distribution of the forces acting on a stator tooth of the 10 hp squirrel-cage induction motor at rated load.

the effects of the permeance variations due to the slots and also neglected the effects of magnetic saturation. In the analysis presented herein, these effects are considered along with the multiple armature reaction effects.

In the following, the 70 kW motor is analyzed to obtain the noise producing radial-forces. The salient design details of the 70 kW wound-rotor induction motor are provided in Table 3.9. Fig. 3.5 shows the dimensions of the stator and rotor slots. Table 3.10 lists the pole-pairs of the various harmonic fields produced due to the multiple armature reaction. As in the case of squirrel-cage induction motors, the stator produces space-harmonic air-gap fields of orders ν, and they are listed in the first column of Table 3.10. In distinction to squirrel-cage motors, the rotor of a wound-rotor induction machine produces harmonic fields of order μ in accordance with the following relationship:

$$\mu = (6 g_2 + \nu) ; \quad g_2 = 0, \mp 1, \mp 2, \mp 3, \ldots . \tag{3.7}$$

Again, the secondary armature reaction of the stator to the rotor fields produces fields of order ϵ. The harmonic orders ϵ for the 70 kW wound-rotor induction machine are given by:

$$\epsilon = (6 g_3 + 1 + 6 g_2) ; \quad g_3 = 0, \mp 1, \mp 2, \mp 3, \ldots . \tag{3.8}$$

The rotor produced fields that induce voltages at the same frequency in the stator windings are listed on the same column. Similarly, all the fields listed on the same row of Table 3.10 will induce a voltage in the rotor windings at the same frequency.

The voltage equations, Eqns. 2.52, 2.53 and 2.99, are solved for the motor at no-load and rated load conditions. The cases of no-skewing, 1/48 skewing of the rotor slots and 5/6 chording of the stator windings are considered. The currents in the stator and rotor windings are provided in Tables 3.11, 3.12, 3.13 and 3.14. As expected, these currents agree quite well with those reported by the author in reference [17].

It is recalled from Chapter 2 that the various rotor produced harmonic fields of order μ induce voltages in the stator windings at frequencies given by:

$$s_{g_2} f = [g_2 \cdot 2 m_2 (1 - s) + 1] f . \tag{3.9}$$

It is observed from Table 3.11 and 3.12 that, in contrast to squirrel-cage induction motors, the current harmonics for wound-rotor induction motors occur at lower frequencies. For this machine, the current harmonics at 247 Hz and 347 Hz have

Table 3.9 : Salient data of the wound-rotor induction motor.

Output power	70 kW
Supply voltage, ∇ - Connection	430 V / Phase
Supply frequency	50 Hz
Number of poles	4
Air-gap length	0.9 mm
Number of stator slots	48
Stator bore diameter	261.8 mm
Stator length	298.4 mm
Stator slot-pitch	17.13 mm
Stator slot-opening	3 mm
Number of turns in series per phase of stator	64
Carters coefficient for stator slotting	1.091
Number of rotor slots	36
Rotor slot-pitch	22.69 mm
Rotor slot-opening	2 mm
Number of turns in series per phase of rotor	24
Carters coefficient for rotor slotting	1.031

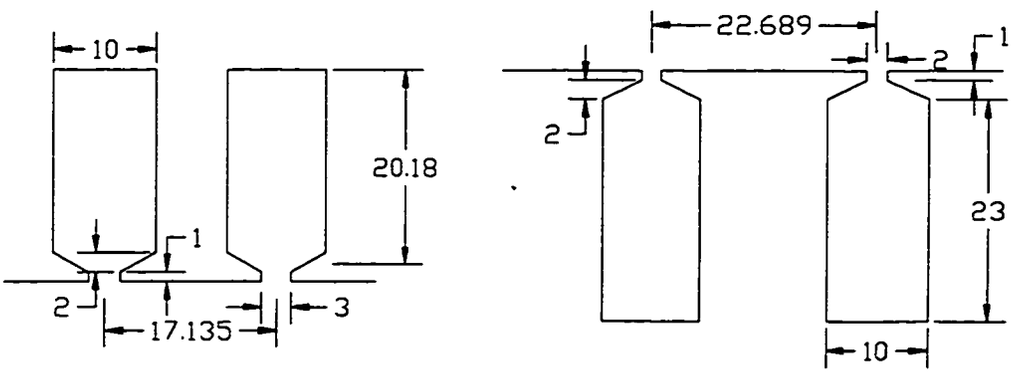

Figure 3.5 : Dimensions of the stator and rotor slots in mm.

Table 3.10 : Pole-pairs of the various air-gap harmonic fields produced in the 70 kW wound-rotor induction motor, for different values of g_1, g_2 and g_3.

g_1 \ g_2	0	-1	+1	-2	+2	-3	+3	-4	+4	g_3
0	2	-10	14	-22	26	-34	38	-46	50	0
-1	-10	-22	2	-34	14	-46	26	-58	38	-1
+1	14	2	26	-10	38	-22	50	-34	62	+1
-2	-22	-34	-10	-46	2	-58	14	-70	26	-2
+2	26	14	38	2	50	-10	62	-22	74	+2
-3	-34	-46	-22	-58	-10	-70	2	-82	14	-3
+3	38	26	50	14	62	2	74	-10	86	+3
-4	-46	-58	-34	-70	-22	-82	-10	-94	2	-4
+4	50	38	62	26	74	14	86	2	98	+4

"Minus sign" denotes the fields which rotate in the direction opposite to that of the fundamental.

substantial amplitudes and these range between 4 to 5 % of the fundamental. In the course of the investigations it is observed that the chording of the stator windings is more effective in reducing these current harmonics than the skewing.

To have a better understanding of the magnitudes of the various currents in a phase of the rotor windings, Tables 3.13 and 3.14 provide information pertaining to the no-load and rated load conditions, respectively. The increase in the fundamental rotor current at the slip-frequency (sf) with the load will amplify all the rotor fields whose pole-pairs are listed in the first row of Table 3.10. The stator produced harmonic fields of orders corresponding to ν and ε that are listed on the same row of Table 3.10 will induce currents in the rotor windings at frequencies given by:

$$s_\nu f = [\, 1 - \nu (1 - s) \,] f \,. \tag{3.10}$$

Again, as with the stator current harmonics, chording of the stator windings is more effective than the skewing of the rotor in reducing the harmonic components of the rotor currents.

After having calculated the various current harmonics, the MMF-harmonics produced due to the stator and rotor are then determined. The magnitudes of these

Table 3.11 : Calculated values of the currents in a stator phase-winding at no-load, f=50 Hz, 1499 rpm.

Freq., Hz *	Straight slots with no chording		1/48 rotor-skew and no chording		Straight slots and 5/6 stator-chording		1/48 rotor-skew and 5/6 stator-chording	
	Currents		Currents		Currents		Currents	
	A	%	A	%	A	%	A	%
50	**14.129**	**100.0**	**14.129**	**100.0**	**15.128**	**100.0**	**15.128**	**100.0**
-249.8	0.153	1.08	0.146	1.03	0.003	0.02	0.003	0.02
349.8	0.326	2.31	0.314	2.22	0.009	0.06	0.009	0.06
-549.6	0.035	0.25	0.031	0.22	0.035	0.23	0.030	0.20
649.6	0.048	0.34	0.042	0.30	0.038	0.25	0.035	0.23
-849.4	0.088	0.62	0.065	0.46	0.003	0.02	0.002	0.01
949.4	0.086	0.61	0.068	0.48	0.003	0.02	0.002	0.01
-1149.2	0.041	0.29	0.024	0.17	0.047	0.31	0.029	0.19
1249.2	0.062	0.44	0.040	0.28	0.068	0.45	0.045	0.30

* : Minus values for frequency indicates reversed phase-sequence.

Table 3.12 : Calculated values of the currents in a stator phase-winding at rated load, f=50 Hz, s=0.01, 1485 rpm.

Freq., Hz *	Straight slots with no chording		1/48 rotor-skew and no chording			Straight slots and 5/6 stator-chording		1/48 rotor-skew & 5/6 stator-chording		
	Calculated		Calculated		Measured[17]	Calculated		Calculated		Measured[17]
	A	%	A	%	%	A	%	A	%	%
50	**58.48**	**100**	**59.14**	**100**	**100**	**63.45**	**100**	**63.33**	**100**	**100**
-247	1.74	2.98	1.65	2.79	3.20	0.03	0.04	0.025	0.04	**0.84**
347	1.77	3.03	1.67	2.82	3.20	0.03	0.04	0.025	0.04	0.51
-544	0.30	0.51	0.27	0.46	0.40	0.27	0.42	0.241	0.38	0.48
644	0.30	0.52	0.27	0.46	0.52	0.27	0.42	0.241	0.38	0.47
-841	0.09	0.15	0.07	0.11		0.02	0.03	0.019	0.03	
941	0.09	0.15	0.07	0.11		0.02	0.03	0.019	0.03	
-1138	0.09	0.16	0.08	0.13		0.11	0.17	0.076	0.12	
1238	0.11	0.19	0.08	0.13		0.11	0.18	0.082	0.13	

* : Minus values for frequency indicates reversed phase-sequence.

Table 3.13 : Calculated values of the currents in a rotor phase-winding at no-load, f= 50 Hz, 1499 rpm.

Freq., Hz *	Straight slots and no chording		1/48 rotor-skew and no chording		Straight slots and 5/6 stator-chording		1/48 rotor-skew and 5/6 stator-chording	
	Currents		Currents		Currents		Currents	
	A	%	A	%	A	%	A	%
0.03	**10.47**	**100**	**10.46**	**100**	**10.83**	**100**	**10.82**	**100**
299.83	0.90	8.62	0.87	8.33	0.00	0.02	0.00	0.02
-299.77	0.41	3.91	0.39	3.74	0.01	0.06	0.01	0.06
599.63	0.13	1.24	0.12	1.12	0.10	0.93	0.09	0.84
-599.57	0.10	0.91	0.08	0.81	0.09	0.85	0.08	0.75
899.43	0.24	2.28	0.19	1.82	0.00	0.02	0.00	0.01
-899.37	0.24	2.32	0.18	1.74	0.00	0.02	0.00	0.02
1199.23	0.17	1.64	0.11	1.06	0.18	1.71	0.12	1.12
-1199.2	0.11	1.07	0.07	0.64	0.12	1.14	0.07	0.69

* : Minus values for frequency indicates reversed phase-sequence.

Table 3.14 : Calculated values of the currents in a rotor phase-winding at rated load, f=50 Hz, s=0.01, 1485 rpm.

Freq., Hz *	Straight slots and no chording		1/48 rotor-skew and no chording		Straight slots and 5/6 stator-chording		1/48 rotor-skew and 5/6 stator-chording	
	Currents		Currents		Currents		Currents	
	A	%	A	%	A	%	A	%
0.5	**146.52**	**100**	**147.39**	**100**	**152.83**	**100**	**152.43**	**100**
297.5	4.78	3.27	4.55	3.09	0.02	0.01	0.02	0.01
-296.5	4.50	3.07	4.29	2.91	0.09	0.06	0.08	0.06
594.5	0.82	0.56	0.72	0.49	0.69	0.45	0.62	0.40
-593.5	0.80	0.55	0.72	0.49	0.69	0.45	0.61	0.40
891.5	0.26	0.17	0.21	0.14	0.03	0.02	0.02	0.01
-890.5	0.27	0.18	0.18	0.12	0.03	0.02	0.02	0.01
1188.5	0.34	0.23	0.24	0.16	0.35	0.23	0.25	0.16
-1187.5	0.22	0.15	0.16	0.11	0.23	0.15	0.17	0.11

* : Minus values for frequency indicates reversed phase-sequence.

MMF-harmonics for the case of straight slots with no chording are provided in Tables 3.15 and 3.16 for the no-load and rated load conditions, respectively.

At no-load, the significant MMF-harmonic components are the fundamental (g_1=0, g_2=0), and the stator slot-MMF-harmonic components (g_1=±4, g_2=0). With the increase in load, most of the rotor produced MMF-components show an appreciable increase. The dominant components are those associated with the fundamental currents in the stator and rotor windings. These are the MMF-harmonic components listed in the first row and first column of Table 3.16.

The permeance-waves are constructed from the geometrical dimensions of the machine. For the saturated air-gap flux-density wave-shape, a form similar to that used for the 10 hp squirrel-cage induction motor is adopted for the 70 kW wound-rotor induction motor. Hence, the permeance coefficients for saturation have the same values as provided in Table 3.8. The air-gap flux densities and the force-waves are then calculated.

Having determined the force-waves, the forces acting on a stator tooth is calculated by integrating the force-waves over the surface of a stator tooth. The various significant components in the radial-force spectrum of the 70 kW wound-rotor induction motor are listed in Table 3.17. The important components in the force spectrum are the force at twice the line frequency and the components at the slot-harmonic frequencies. The slot-harmonic components are identified according to their orders as F_{S1} to F_{S4}. The n^{th} order slot-harmonic components occur at frequencies which are given by:

$$[2 - n \cdot 2m_2(1 - s)]f, \quad [n \cdot 2m_2(1 - s)]f, \quad [2 + n \cdot 2m_2(1 - s)]f.$$

Saturation effects produce the components at 4f, 6f, ... etc., and also the side-band components on either side of each of the slot-harmonic components. Table 3.17 also provides the amplitudes of the various force components at 1499 rpm and 1485 rpm, respectively.

Figs. 3.6 and 3.7 show the calculated spectra of the radial-forces acting on the stator teeth at no-load and the rated load, respectively. The force component at 100 Hz is mainly produced by the fundamental air-gap field, and also the various stator space-harmonic fields of order ν. The 100 Hz component exhibits a small decrease from 419 N to 366 N when the machine is loaded from no-load to its rated capacity. The

Table 3.15 : Magnitudes of the various air-gap MMF-harmonics, in Ampere-turns, at no-load condition.

g_1 \ g_2	0	-1	+1	-2	+2	-3	+3	-4	+4	g_3
0	395.70	5.09	2.94	1.93	2.00	6.77	6.06	1.13	0.86	0
-1	17.29	0.12	0.40	0.57	0.23	0.06	0.15	0.06	0.50	-1
+1	9.61	0.14	0.03	0.16	0.25	0.10	0.08	0.26	0.04	+1
-2	4.93	0.04	0.34	0.06	0.05	0.03	0.03	0.04	0.04	-2
+2	4.17	0.08	0.16	0.03	0.05	0.15	0.01	0.01	0.02	+2
-3	3.85	0.21	0.08	0.01	0.07	0.08	0.13	0.02	0.11	-3
+3	4.53	0.09	0.40	0.09	0.03	0.13	0.06	0.17	0.02	+3
-4	17.96	0.04	0.20	0.06	0.05	0.02	0.19	0.02	0.08	-4
+4	16.53	0.10	0.04	0.02	0.04	0.09	0.02	0.07	0.04	+4

(No chording of stator-coils and no skewing in rotor)

Table 3.16 : Magnitudes of the various MMF-harmonics, in Ampere-turns, at rated load condition.

g_1 \ g_2	0	-1	+1	-2	+2	-3	+3	-4	+4	g_3
0	377.58	70.90	41.36	26.97	28.01	94.79	84.81	15.77	12.02	0
-1	71.00	0.29	1.29	3.01	1.18	0.50	0.91	0.35	2.74	-1
+1	38.93	1.01	0.35	1.86	2.71	0.84	0.38	2.94	0.38	+1
-2	20.33	0.06	1.79	0.48	0.11	0.07	0.24	0.27	0.19	-2
+2	17.18	0.95	1.04	0.07	0.29	0.44	0.07	0.18	0.23	+2
-3	16.49	2.20	0.60	0.06	0.35	0.09	0.92	0.02	0.14	-3
+3	19.22	0.54	2.07	0.26	0.06	0.92	0.07	0.18	0.03	+3
-4	74.37	0.39	0.71	0.14	0.17	0.03	0.24	0.07	0.54	-4
+4	68.47	0.47	0.29	0.13	0.05	0.11	0.02	0.53	0.06	+4

(No chording of stator-coils and no skewing in rotor)

Table 3.17 : Important components in the force spectrum of the 70 kW wound-rotor induction motor at 1499 and 1485 rpm, f = 50 Hz.

Source	No-load, 1499 rpm			Rated load, 1485 rpm		
	Freq., Hz	Amplitude, Newtons	% relative to funda-mental	Freq., Hz	Amplitude, Newtons	% relative to funda-mental
Fundamental	**100.0**	**419.05**	**100**	**100.0**	**365.96**	**100**
Saturation	200.0	7.09	1.69	200.0	12.09	3.30
	300.0	25.54	6.09	300.0	20.31	5.55
	400.0	2.46	0.59	400.0	1.97	0.54
Saturation side-band	99.8	0.13	0.03	97.0	2.69	0.74
F_{S1} - 2f	199.8	5.38	1.28	197.0	67.86	18.54
F_{S1}	299.8	1.54	0.37	297.0	16.85	4.60
F_{S1} + 2f	399.8	1.76	0.42	397.0	26.34	7.20
Saturation side-band	499.8	0.06	0.01	497.0	11.75	3.21
Saturation side-band	399.6			394.0	1.28	0.35
F_{S2}-2f	499.6	0.31	0.07	494.0	7.70	2.10
F_{S2}	599.6	0.09	0.02	594.0	2.14	0.58
F_{S2} + 2f	699.6			694.0	7.32	2.00
Saturation side-band	799.6			794.0	1.48	0.40
Saturation side-band	699.4	0.27	0.06	691.0	4.21	1.15
F_{S3} - 2f	799.4	3.26	0.78	791.0	20.44	5.59
F_{S3}	899.4	0.53	0.13	891.0	4.34	1.19
F_{S3} + 2f	999.4	0.43	0.10	991.0	2.65	0.72
Saturation side-band	1099.4	0.13	0.03	1091.0	0.59	0.16
Saturation side-band	999.2			988.0	0.43	0.12
F_{S4} - 2f	1099.2			1088.0	4.56	1.25
F_{S4}	1199.2			1188.0	0.75	0.20
F_{S4} + 2f	1299.2			1288.0	0.62	0.17
Saturation side-band	1399.2			1388.0	0.13	0.04

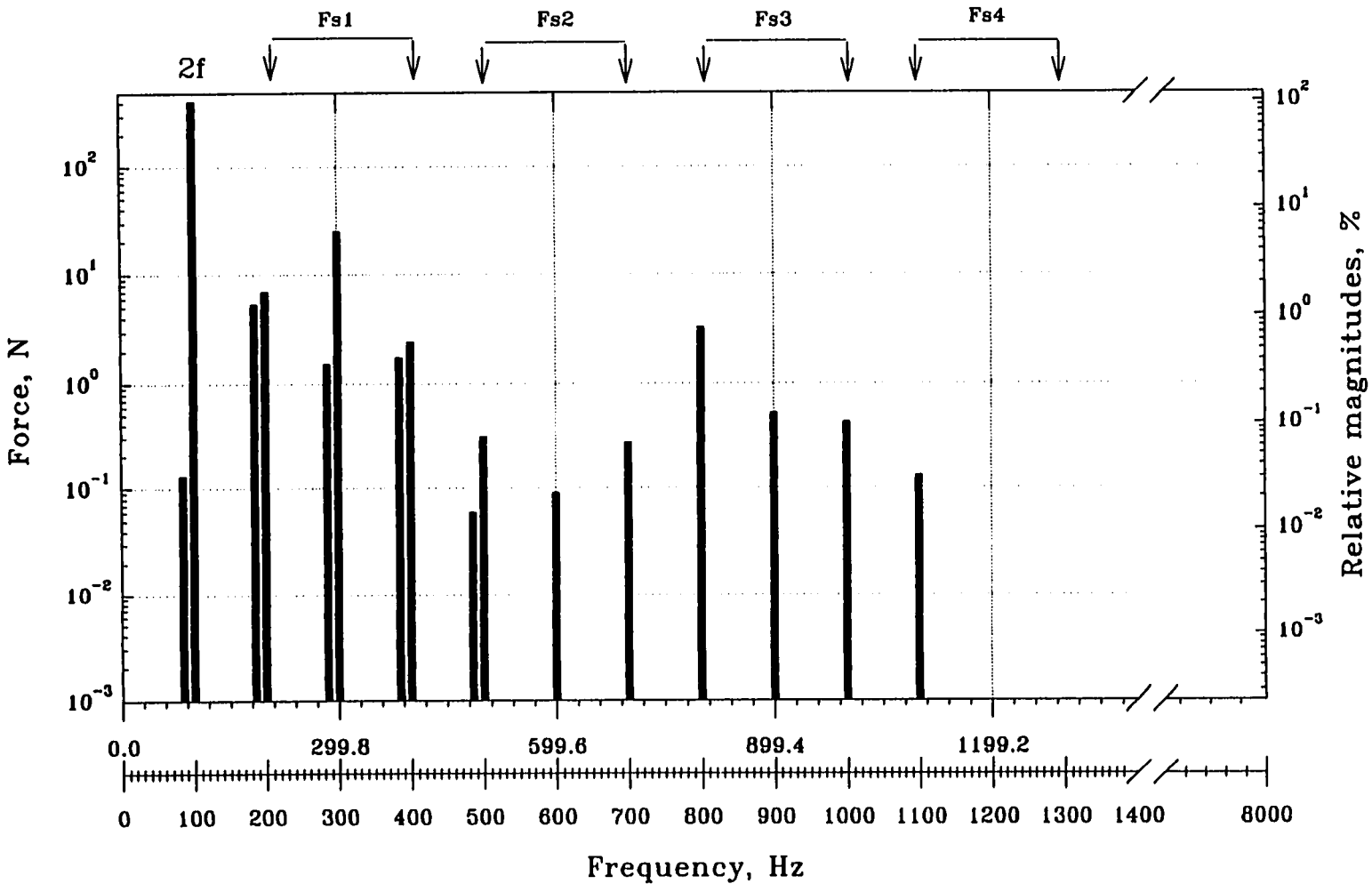

Figure 3.6 : Calculated spectral distribution of the forces acting on a stator tooth of the 70 kW wound-rotor induction motor at no-load, f=50 Hz, 1499 rpm.

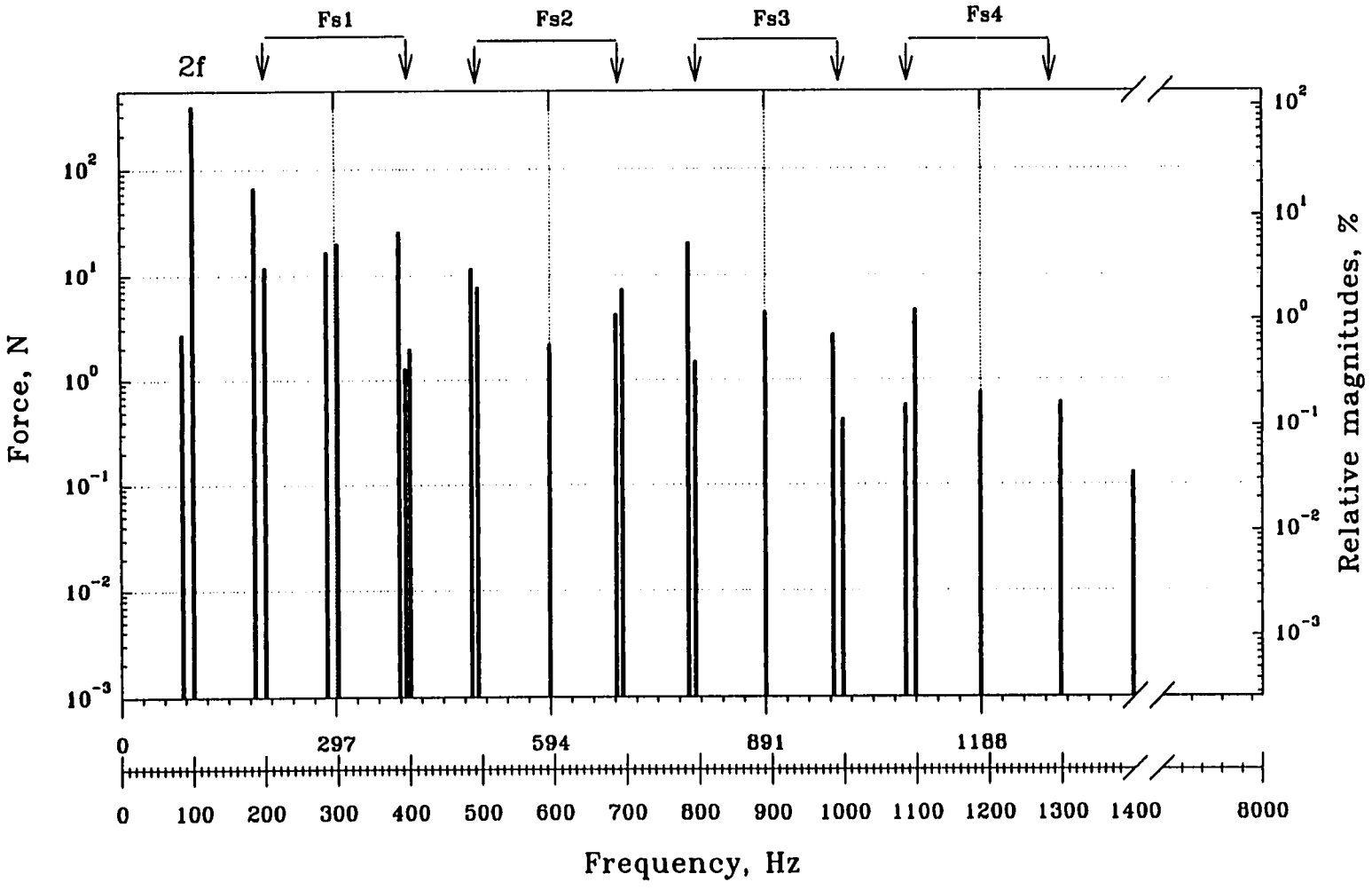

Fsn : n^{th} order slot-harmonic forces

Figure 3.7 : Calculated spectral distribution of the forces acting on a stator tooth of the 70 kW wound-rotor induction motor at rated load, f=50 Hz, 1485 rpm.

saturation components at 4f, 6f, and 8f decrease slightly with the increase in the load. The slot-harmonic components which were insignificant at no-load become very prominent with the load. At rated load, the dominant components in force spectrum are the slot-harmonic force components of orders 1 and 2.

The effects of using either a skewed-rotor, or 5/6 chording of the stator-coils, or both together on the slot-harmonic force components were closely examined. The amplitudes of the various slot-harmonic force components for each of these conditions were calculated neglecting the effects of saturation. Tables 3.18 and 3.19 provide the information for the cases of no-load and rated load conditions, respectively. These tables reveal that the chording of the stator-coils is more effective in reducing the amplitudes of the higher order slot-harmonic force components than the skewing of the rotor.

Comparing the spectra of the forces produced by the squirrel-cage and wound-rotor induction motors discussed in the foregoing, it is evident that the squirrel-cage induction motor is very rich in harmonics. In both the motors, the significant force components in these spectra are the slot-harmonic forces and their saturation side-bands. In the case of squirrel-cage induction motors, the slot-harmonic forces usually exist in distinct and separate frequency bands, and they are usually spread over a major portion of the audio-frequency range. In contrast, the force components for wound-rotor induction motors are confined to the lower portion of the audio-frequency range. The frequencies at which these slot-harmonic forces are produced depend on the number of phases on the rotor windings, and the speed of the machine. Since it is very common to use 3-phase windings on the stator and the rotor, the slot-harmonic forces do not occur separately as distinct bands in the force spectra of a wound-rotor induction motor. Further, it is often desired to have integral-slot windings due to the simplicity of its installation in the stator and rotor, which constrains the choice of the number of stator and rotor slots. The use of preferred number of slots, such as 36, 48, 72, 96, etc., lead to the various force components having a circumferential distribution with force-poles of 0, 4, and 8. In distinction, the squirrel-cage induction motors often have many more force components with force-poles less than 4. The force-distribution with fewer force-poles are more harmful from the perspective of noise and vibrations. The importance of the force-poles is discussed in the subsequent chapters.

Table 3.18 : Relative amplitudes of the slot-harmonic force components for the different arrangements at no-load, f=50 Hz, 1499 rpm.

Source	Freq., Hz	Straight slots and no chording	1/48 Rotor-Skew and no chording	Straight slots and 5/6 stator chording	1/48 Rotor-Skew and 5/6 stator chording
2f	**100.0**	**100.000%**	**100.000%**	**100.000%**	**100.000%**
F_{S1}	199.8	1.189%	1.189%	1.328%	1.327%
	299.8	2.050%	2.049%	2.122%	2.118%
	399.8	0.222%	0.217%	0.074%	0.071%
F_{S2}	499.6	0.059%	0.058%	0.019%	0.018%
	599.6	0.066%	0.063%	0.018%	0.018%
	699.6	0.011%	0.006%	0.020%	0.019%
F_{S3}	799.4	0.740%	0.726%	0.657%	0.653%
	899.4	0.698%	0.696%	0.977%	0.976%
	999.4	0.001%	0.001%	0.001%	0.001%
F_{S4}	1099.2	0.003%	0.003%	0.004%	0.004%
	1199.2	0.002%	0.002%	0.000%	0.000%
	1299.2	0.000%	0.000%	0.000%	0.000%

Table 3.19 : Relative amplitudes of the slot-harmonic force components for the different arrangements at rated load, f=50 Hz, 1485 rpm.

Source	Freq., Hz	Straight slots and no chording	1/48 Rotor-Skew and no chording	Straight slots and 5/6 stator chording	1/48 Rotor-Skew and 5/6 stator chording
2f	**100**	**100.000%**	**100.000%**	**100.000%**	**100.000%**
F_{S1}	197	18.587%	18.406%	20.155%	20.106%
	297	30.162%	29.812%	31.955%	31.825%
	397	3.421%	3.360%	1.529%	1.518%
F_{S2}	494	1.681%	1.666%	0.891%	0.879%
	594	3.985%	3.898%	1.010%	1.002%
	694	1.396%	1.379%	0.773%	0.767%
F_{S3}	791	3.689%	3.709%	2.121%	2.123%
	891	7.895%	7.796%	8.059%	8.018%
	991	0.194%	0.189%	0.154%	0.151%
F_{S4}	1088	1.001%	0.989%	0.940%	0.930%
	1188	0.240%	0.225%	0.046%	0.044%
	1288	0.057%	0.056%	0.051%	0.050%

In order to verify the validity of the theoretical calculations, and also to acquire a physical understanding of the nature of the radial-forces and the ensuing vibrations, extensive experimental investigations were conducted. In the following sections, the experimental set-up which has been developed along with the procedures that are adopted to measure the magnetic fields, magnetic forces, resonant frequencies, vibrations and the air-borne noise is described. Experimental results pertaining to the magnetic fields, forces and vibrations are then provided for the 10 hp squirrel-cage induction motor, and comparisons are made with the theoretical predictions.

3.3 Experimental Set-up and Procedures for Measurement of Resonances, Vibrations and Radiated Acoustic Noise

The conventional methods for the measurement of resonant frequencies, vibrations and noise are laborious and very time consuming. This section presents the laboratory-techniques which have been developed for the measurement of resonant frequencies, vibrations and noise based on digital processing of signals. The measurement set-up acquires and processes signals from several transducers with the help of a data-acquisition system and a personal-computer [43].

3.3.1 Introduction

The prediction of the vibration behaviour, and the sound radiated from electrical machines require accurate determination of the resonant frequencies and exciting radial-forces. Often experimental investigations are required to find the resonant frequencies, and also the forced vibration response. In addition, experimental information is needed to verify the validity of the theoretical predictions.

It is desired that the measurement set-up that has been developed be also capable of measuring and analyzing the radiated sound. To specify the noise produced by a machine, the testing has to be conducted in accordance to the test codes described in the various national and international standards [45,46]. The sound pressure level around an electric machine varies with distance from the machine, and also with angular location around it. The test codes stipulated in the various standards, therefore, require the calculation of the space averaged sound pressure level from the measurements taken

at a number of different points on an imaginary surface enclosing the machine. An array of fixed microphone positions is used for this purpose [45,46]. The measurements are commonly conducted by using a single microphone and moving it from one location to the next, or by having a number of fixed microphones and their outputs are sampled sequentially. The major limitation on the number of microphones is dictated by the number of signals that can be analyzed with the commercially available frequency analyzers. The cost of these frequency analyzers increases exponentially with the number of signals that it can process simultaneously, or sequentially, without human intervention. To obtain results with accuracy, the noise measurements are made in free-field conditions (anechoic chamber) and the measuring points are chosen to be as many as possible. Often for economical reasons, the number of measuring points is limited to 20 or less. The error introduced by having insufficient number of measuring points has been examined by the authors in reference [47].

Vibration measurements on electrical machines can be classified into two categories. The first category involves the determination of the resonances, and the vibration behaviour at resonance of the vibrating structure. The second category involves the vibration measurements made on the electrical machine structure during its operation. This, therefore, entails the determination of the forced response of the machine structure. The vibration measurements in general, irrespective of the objectives of the measurements, involve measurement of the vibration acceleration at various locations on the vibrating structure and ascertaining the relationship between the vibration signals. Since the conventional instruments usually limit the number of vibration signals that can be acquired and analyzed simultaneously, the measurements conducted using the conventional instruments are very time consuming and laborious.

The magnetic forces that induce vibrations, and thereby lead to acoustic noise being radiated by electrical machines, are generated due to the pulsations of the magnetic fluxes through the iron-members. The stresses known as Maxwell's stresses are generated at the surface of the iron members adjoining the small air-gap of an electrical machine. It is, generally, not possible to directly measure the Maxwell's stresses. However, there are two methods of indirectly obtaining information on the Maxwell's stresses. The first method involves the measurement of the flux-pulsations through the

iron surfaces with the help of search-coils, and then calculating the Maxwell's stresses from the flux-pulsations. The second method involves the measurement of the vibrations on the machine stator, and after knowing accurately the vibration behaviour of the stator the magnetic forces can be determined. In this second method, the vibration measurements can be made on the outside surface of the machine or at the surface of the stator-tooth. Although the vibration measurements made on a stator-tooth would have the least influence due to the mechanical response characteristics of the stator, it is plagued with many problems due to the harshness of the environment at the location of measurement. Also, the magnetic flux-densities in the air-gap are quite high and it is usually very difficult to avoid magnetic inference in the measuring arrangements. Most importantly, the physical space restrictions imposed by the length of the air-gap is a major limitation. The air-gap lengths vary from about a fraction of a millimetre for small machines to little over a millimetre for large machines. In view of the several difficulties mentioned above, information on the magnetic radial-forces is assessed from the search-coil signals and the vibration measurements made on the surface of the machine using piezoelectric vibration accelerometers. Although these are indirect means of measuring the magnetic radial-forces, both the methods provide very useful information.

3.3.2 Measurement Set-up

Although a variety of instruments for the measurement of sound and vibrations are commercially available, there exists a need to develop an experimental set-up that is particularly suitable for the study of noise and vibration problems of electric machines. The experimental set-up developed for such purposes is described in the following.

Fig. 3.8 shows the schematic block diagram of the measurement system. This system acquires signals from accelerometers, microphones and search-coils. Vibration measurements usually require a modal-analysis which involves the study of the vibration distribution along the machine or stator surface. To conduct a modal-analysis, it is therefore necessary to measure the vibration signals from different locations at the same instant of time. In order to achieve this requirement, a high speed data acquisition board with the capability of simultaneously acquiring data from the various channels is used.

In the case of microphones, the experimental arrangement multiplexes sequentially the microphone inputs and processes the information according to the test-code of a given standard.

The heart of the data acquisition and measurement system is a high speed data acquisition board. In the present system, the data acquisition board has the provision for 16 channels of single-ended analog inputs. Further, this board has the data acquisition speed of 250 kHz for A/D conversion with the resolution of 12 bits. For simultaneous acquisition, four sample-and-hold amplifiers are used to track and hold the various input channels while the A/D converter digitizes the amplifier outputs sequentially. Thus, a maximum sampling frequency of 50 kHz per channel is possible for simultaneous acquisition from the four channels.

Depending on the span of the search-coil used and the size of the machine, the voltage at the terminals of the coils may range from 0.2 V to tens of volts. Isolated wide-band signal conditioning modules, Analog Devices model 3B40/3B41, are used to condition these signals before they are fed to the A/D converter. These modules are designed to have a continuous differential input protection of upto 220 V at its input terminals. A transformer coupling is used in these signal conditioning modules for stable galvanic isolation between the input and the output. The magnetic coupling provides a reliable isolation upto 1500 V (peak) between the output and the input. The signal conditioning module has a plug-on ranging card which houses resistors that determines its gain.

Piezoelectric accelerometers are used to measure vibrations. The vibration signals are pre-conditioned using charge-amplifiers. The accelerometers are mounted on the machine surface using bee-wax. These accelerometers produce a signal proportional to the acceleration, and have a charge sensitivity of 3.2 pC/ms^2 and a voltage sensitivity of 2.71 mV/ms^2. For measurement of relative vibrations such as in a modal-analysis, the use of voltage-amplifiers provides satisfactory results. For an accurate measurement of the vibration levels, charge-amplifiers are preferred over the conventional voltage-amplifiers. The output voltage of the charge amplifier is proportional to the charge applied at the input. Thus, with a charge amplifier the transducer sensitivity is relatively independent of the cable length [48]. Brüel and Kjær Charge Amplifiers Type 2635 are

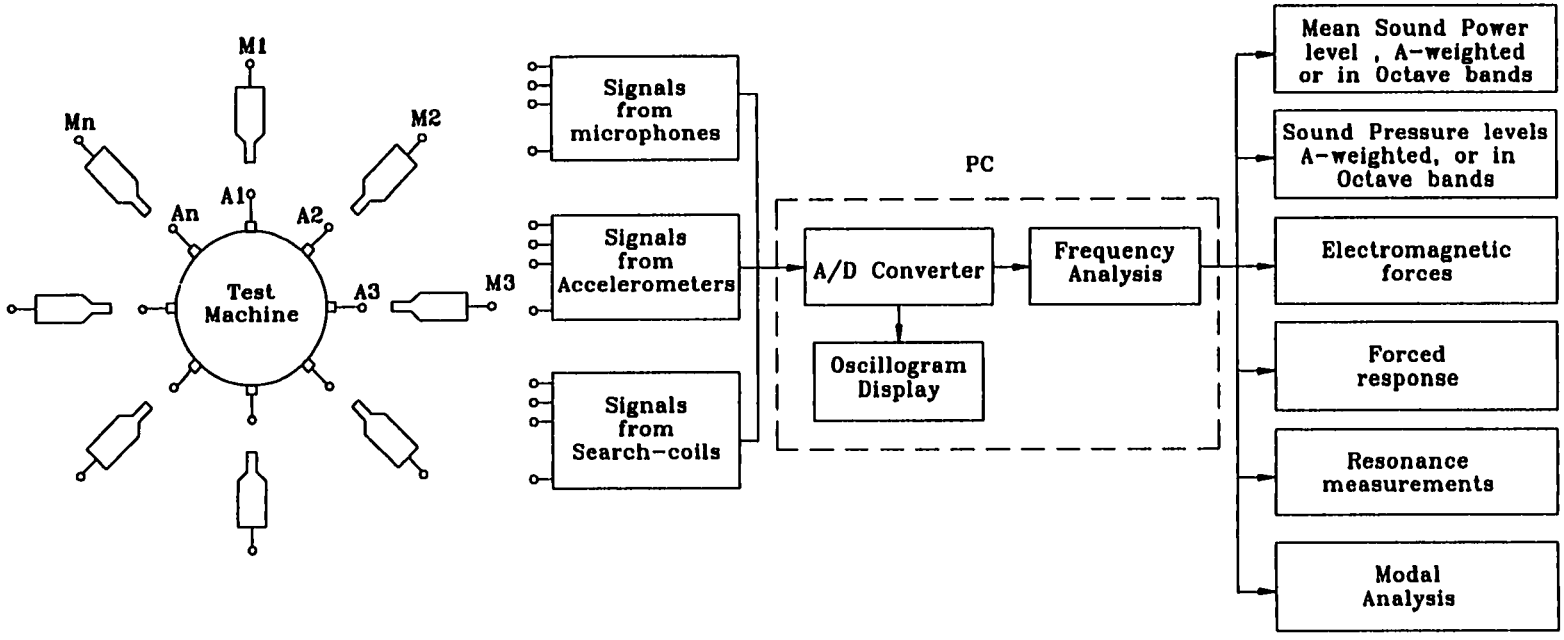

PC - Personal Computer
A1, A2, ..., An - Accelerometers
M1, M2, ..., Mn - Microphones

Figure 3.8 : Schematic diagram of the measurement set-up.

used in the experimental set-up. B&K 2635 is a four stage amplifier consisting of an input amplifier, low-pass filter amplifier, integrator amplifier and output amplifier. The overall gain of the B&K 2635 is adjusted in the input and integrator amplifiers in order to provide a rated output level switchable between 0.1 mV/unit to 1 V/unit in 10 dB steps. With these nine steps, the output signal level can be adjusted to best utilize the input requirement of ± 10 V for the A/D converter.

Condenser microphones are used in conjunction with microphone preamplifiers and they are interfaced to the data acquisition board. In addition, provisions are made to measure the voltage across the stator winding terminals and the currents through them using the wide-band amplifiers described above. The signals corresponding to the currents through the stator windings are obtained by sampling the voltage drop across a calibrated resistance which is connected in series with the stator circuit.

The final step in the measurement process involves the processing of the acquired signals and displaying the results. The data acquisition board has an on-board memory which allows storage of 2^{18} samples without the intervention of the PC's processor. A continuous data transfer mode is used that allows half of the on-board memory to be filled while the other half of the on-board data buffer is emptied into the PC-system memory. This permits the processing of the signals in almost real-time. The software developed for processing of the signals allows monitoring of the signals in the time-domain as an oscillogram with a continuous display of its peak and rms values. In addition, an FFT analysis is used to determine the frequency spectra of the vibration, sound and the force signals.

3.3.3 Procedures for the Measurements

In the following sections the methods adopted to acquire and process the various measurement are described. Also, the merits of automation in the measurement process are discussed.

3.3.3.1 Measurement of Resonant Frequencies

As mentioned earlier, a physical system exhibits two classes of vibrations, namely free and forced vibrations. Free vibrations take place when a system oscillates under the

action of the forces inherent in the system. A system, when given an initial disturbance, will vibrate at one or more of its natural frequencies. These frequencies exists as properties of the dynamical system and they are determined by its mass and stiffness distribution. Under free vibrations, the motion will continue ad infinitum in the absence of damping. Damping, therefore, indicates the nature of the dissipative sources within the vibrating structure.

Forced vibrations take place under the action of external forces. When the excitation force is oscillatory, the system is forced to vibrate at the excitation frequency. If the frequency of excitation coincides with one of the natural frequencies of the system, the amplitudes of the vibrations could build up to dangerously high levels. As very well known, this phenomenon is called resonance and the vibration amplitudes at resonance are limited only by the damping present in the system.

3.3.3.1.1 Magnetic Shaker Excitation

The test model is excited using an electromagnetic shaker, which excites the model at various frequencies using a pin. The exciter has a linear response from 400 Hz to 10 kHz. A beat-frequency oscillator together with a power amplifier is used to energize the coil of the shaker. The frequency of the oscillator can be varied continuously by linking it to an external drive. To acquire vibration signals, several accelerometers were mounted at different locations on the surface of the model under test. The basic method of measurement is similar to that reported in reference [9].

In the previous investigations, the frequency spectrum of the accelerometer signal was plotted, and the resonant peaks were identified from the plot. In the previous method, due to the use of point-excitation-system a peak in the plot would be registered when a harmonic of the fundamental excitation frequency coincides with a resonant frequency. The various peaks were then individually checked for fundamental excitation by observing the Lissajous-patterns on an oscilloscope. This procedure was repeated for several measuring points on the test-model. Only those resonances which showed persistence over most of the measuring points were recorded as resonances for the test-model.

In the present technique, the oscillator signal is acquired along with the signals from the various accelerometers. The software determines the frequency of the excitation signal, and the accelerometer signals are then filtered with a constant narrow width band-pass filter centred at the excitation frequency. Thus, the frequency response recorded using this technique eliminates the harmonic-resonances of the fundamental excitation frequency. Further, in the case of laminated stator models localised parasitic resonances were registered in the resonance plots using the previous technique [39,43]. These parasitic peaks are avoided in the present measuring system by comparing the acceleration levels at the various measuring locations. A resonance peak is registered only when two or more accelerometers show an appreciable change in the acceleration level. The present method has also the advantage of continuously exciting the model at a desired frequency and to observe the filtered output of upto six accelerometers. This greatly facilitates the determination of the mode-shape of vibrations at the various resonant frequencies. To determine the mode-shapes, the model is excited at the resonant frequency under investigation, and the phase differences in the filtered outputs of various acceleration signals are then used to find the mode of vibration associated with that resonant frequency.

3.3.3.1.2 Impulse Response

In the second method for detecting the resonant frequencies, hammer excitation technique is used to obtain the impulse response. In the theoretical sense, an impulse is a function of infinite amplitude with virtually zero width. In practice, the model is struck sharply with a force small enough to elicit a vibration response. Although this excitation deviates from that of an ideal impulse, it does excite all the significant resonances of the model. This method provides a quick procedure for finding the significant resonant frequencies. Since the energy distribution of the forcing spectra is actually a function of the pulse duration, the resonance amplitudes diminish with increasing frequencies. The vibration signal is measured with the help of 4 to 6 accelerometers, and the analog signal from one of the accelerometers is used to trigger the acquisition of the data. The ensuing vibrations are recorded, and the Fourier-analysis will reveal the significant resonant peaks of the model being tested.

The magnetic shaker excitation method and the impulse response technique are used in the present investigations to determine the resonant frequencies and their associated mode-shapes of electrical machine stators. The results and the comparisons are provided later in Chapter 5.

3.3.3.2 Measurement of Magnetic Radial-forces

The forces acting on a stator tooth are determined from the information contained in the induced voltage of a search-coil wound around the tooth. The search-coil which is placed at the top of the stator tooth, Fig. 3.9, provides information on the magnetic fluxes entering or leaving the stator tooth. The voltage induced in the search-coil is proportional to the rate of change of magnetic flux linking with it. The forces acting on the tooth are proportional to the square of magnetic flux pulsating through the tooth. Fig. 3.9 shows a part of the cross-sectional view of the machine stator, and explains the arrangement of the search-coils. The search-coils used have various spans ranging from the smallest of one tooth-width to the largest of one pole-pitch. Expressed mathematically, the voltage induced in a tooth-width search-coil is given by:

$$e = \sum_{n=1}^{\infty} e_n \sin(\omega_n t + \psi_n) = -\frac{d}{dt}\left[\sum_{n=1}^{\infty} \phi_n \cos(\omega_n t + \psi_n)\right] \tag{3.12}$$

where, e_n is the n^{th} harmonic component in the induced voltage at the harmonic frequency ω_n radians/sec. The integration of e_n with respect to time will give the net flux pulsating though the span of the search-coil with a frequency ω_n radians/sec. Since the tooth-width search-coil is mounted just under the tooth-lips at the surface of a stator tooth, the signal would provide information on the flux-pulsations through the stator tooth.

The force acting on a stator tooth can be determined from the well-known relationship:

$$\begin{aligned} F_t &= \frac{B_t^2}{2\mu_0} A_t \,, \\ &= \frac{\phi_t^2}{2\mu_0 A_t} \,, \end{aligned} \tag{3.13}$$

where, B_t and ϕ_t are the flux-density and the flux pulsating through a stator tooth, A_t is

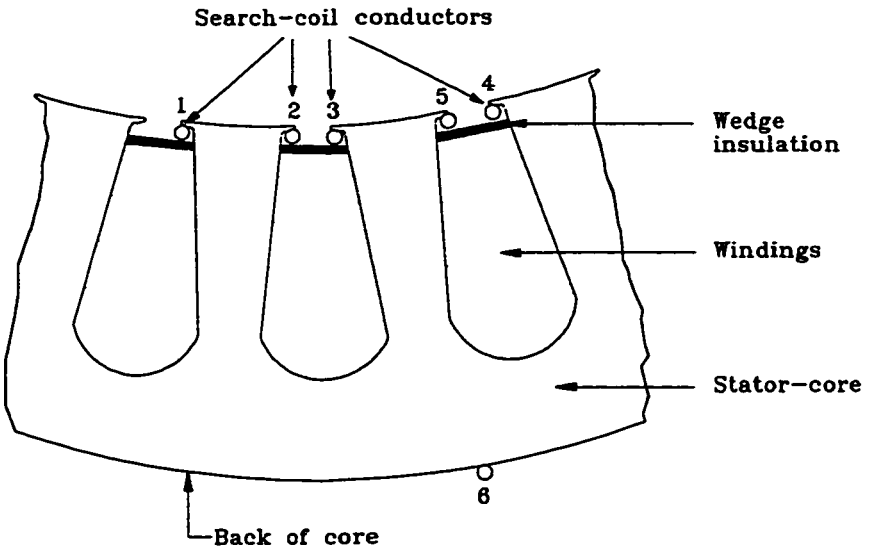

Figure 3.9 : Arrangement of the search-coils in the stator;
(1,2) : search-coil having a span of 1 tooth-width,
(3,4) : search-coil having a span of slot-pitch,
(5,6) : search-coil to sense the flux in the stator-core.

the area of the stator tooth-surface. Using Eqns. 3.12 and 3.13, the net force on the stator tooth is obtained as the sum of the various force components:

$$F_t = \frac{\left[\int e \cdot dt\right]^2}{2\mu_0 A_t}, \qquad F_t = \frac{\left[\sum_{n=1}^{\infty} \int e_n \sin(\omega_n t - \varphi_n) \cdot dt\right]^2}{2\mu_0 A_t}. \tag{3.14}$$

In an electric machine, the magnetic radial-forces occur at twice the supply frequency and at higher frequencies depending on the number of rotor slots and the supply frequency. To obtain the information on the magnetic flux pulsations through a stator tooth, the integration of the search-coil signal would lead to a low-pass filter effect. It, therefore, becomes difficult to determine the forces at higher frequencies from the squared flux-signal. To circumvent this problem, the significant peaks in the spectrum of the induced voltages are first isolated. The integration process is then achieved in the frequency domain by dividing the spectral components by their corresponding angular frequencies. The flux-signal is then squared to acquire information on the forces acting on a stator tooth.

3.4 Experimental Results of a 10 hp Squirrel-Cage Induction Motor

In order to verify the validity of the theoretical calculations, and to acquire a physical understanding of the nature of the radial-forces, extensive experimental investigations were carried out on a 10 hp, 4-pole, 3-phase squirrel-cage induction motor, the data for which has been provided in Table 3.1. The machine has 36 stator slots which contain a double-layer winding connected in star. The rotor cage winding is placed in 43 semi-closed rotor slots. To investigate the nature of the flux pulsations through a stator tooth, search-coils having a span equal to the tooth-width were used. The stator-core is supported by the frame with 8 ribs that are distributed around the circumference. The motor was isolated from the foundation using rubber pads, and also a flexible coupling was used to isolate the shaft from the loading device. Further, the end-shields were removed and the rotor was supported using pedestals on either side of the stator. This ensured the elimination of any rotor effects which could creep into the vibration measurements made on the stator. The vibration measurements were made on the stator frame at locations above the ribs. The test motor and its mounting assembly is shown in Fig. 3.10.

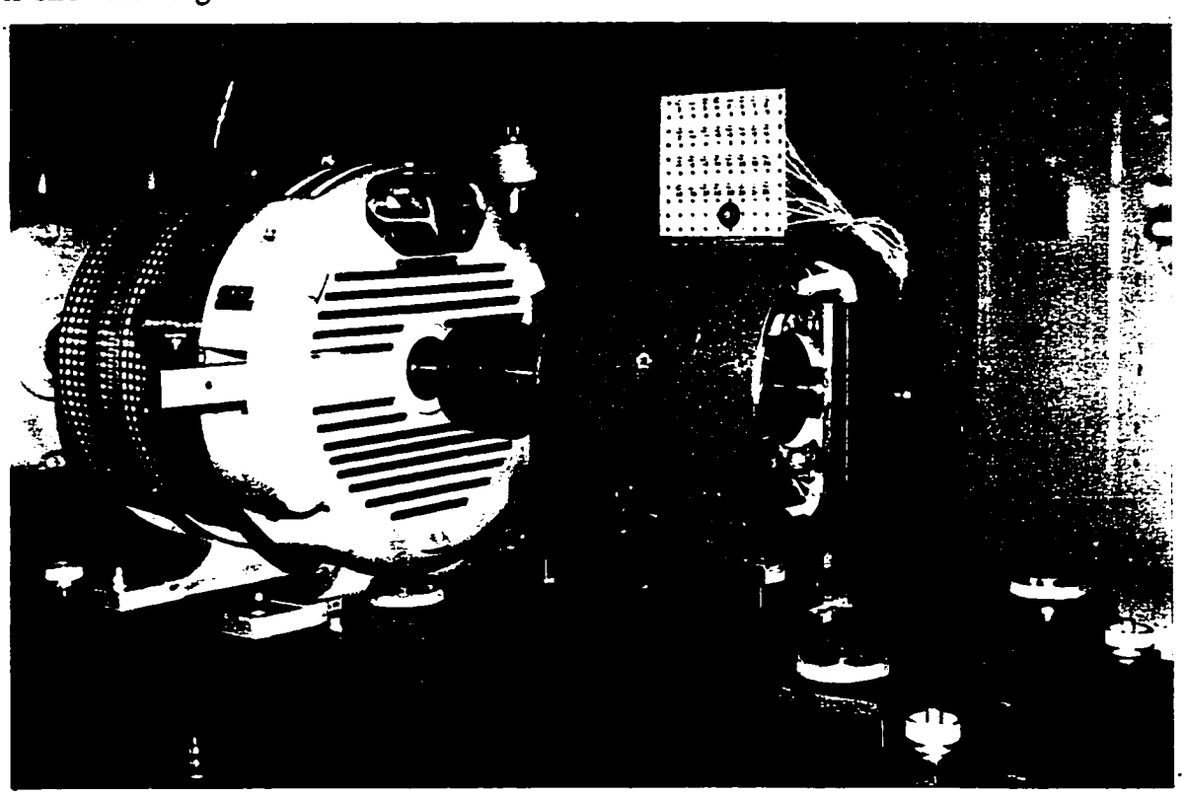

Figure 3.10 : Photograph of the test motor and mounting arrangements.

The oscillograms of the signals measured from a tooth-width search-coil at no-load and at rated load are shown in Fig. 3.11. The increase of the ripples in the oscillogram is indicative of the increase in the slot-harmonic components in the induced voltages with load. Figs. 3.12 and 3.13 show the experimentally measured spectra of the induced voltages at no-load and full rated load, respectively. An amplitude scale similar to that used in Figs. 3.1 and 3.2 has also been used here. The various components have been identified in these figures. A comparison of the spectra of the voltages induced in the tooth-width search-coil obtained through the theoretical calculations and the experimental measurements is made in the following:

i) All the components predicted by the analysis in the calculated results are distinctly present in the measured spectra of the induced voltages at no-load and rated load conditions, respectively. There are additional components which correspond to magnetic saturation effects in the measured spectra at 7f, 9f, 11f, and on either side of the slot-harmonic components. In the calculations, only two harmonic orders of the saturation permeance-wave were considered. The presence of additional components in the measured spectra reveals that further orders of magnetic saturation also need to be included.

ii) As explained earlier, the significant harmonic components in the spectra of the induced voltages are the slot-harmonic components at S1, S2, S3 and S4. Comparing the calculated and experimental values of the slot-harmonic components, it is observed that the correlation between the two is better for the full-load condition. In most cases, the difference between the predicted and measured amplitudes of the slot-harmonic components is within 5% of the amplitude of the fundamental component.

iii) Although the form chosen for the saturated wave-shape in the theoretical calculations is empirical, it does predict with reasonable accuracy the various components produced due to magnetic saturation effects. Further, since the terminal voltage is maintained constant at all the load levels the flux-densities and the level of magnetic saturation remain relatively constant in the theoretical calculations. This causes the amplitudes of the various saturation harmonic components in the calculated spectra to assume similar percentage values with

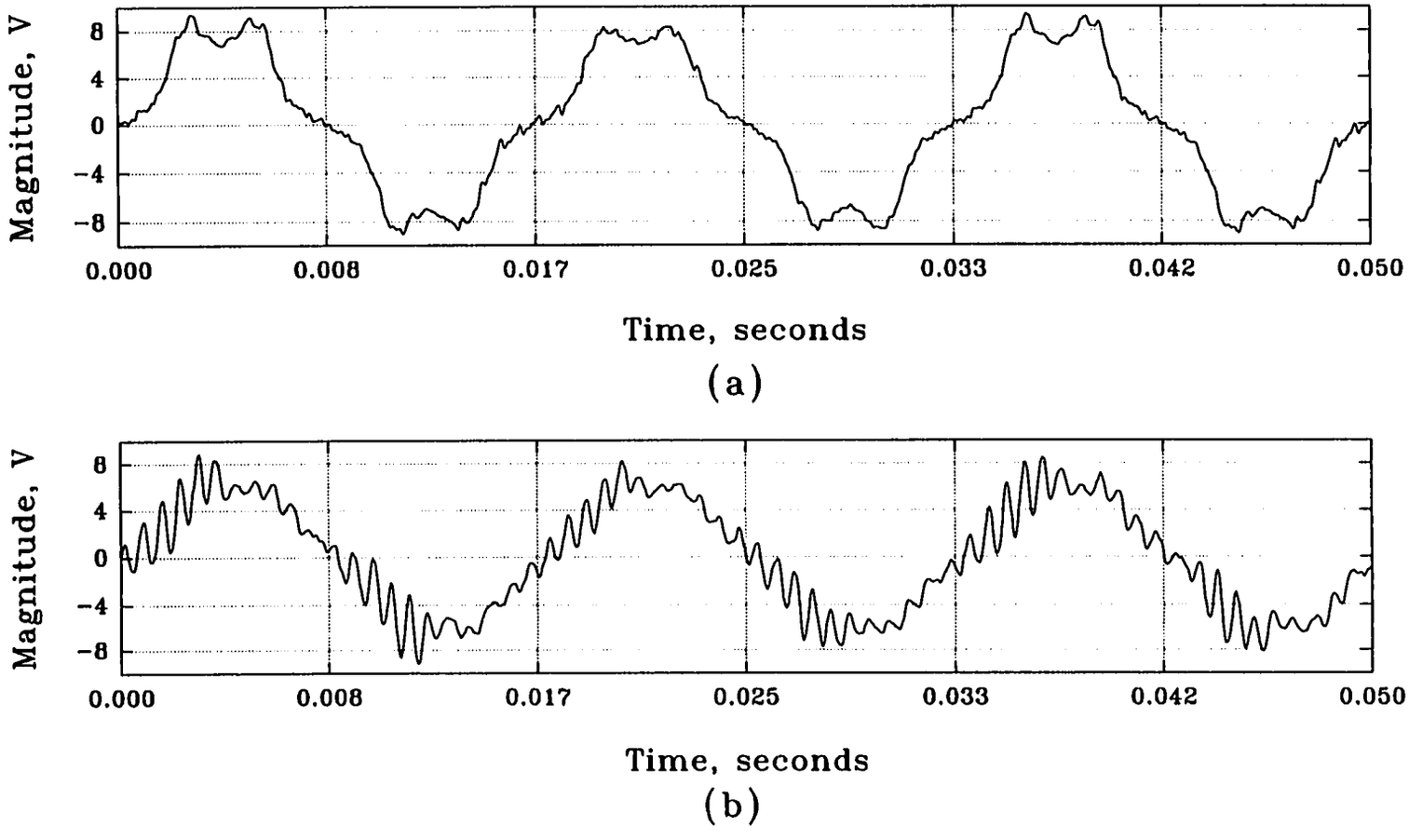

Figure 3.11 : Oscillogram of the signal measured from a tooth-width search-coil at no-load and full-rated load, respectively.
(a) No-load condition. (b) Full-load condition.

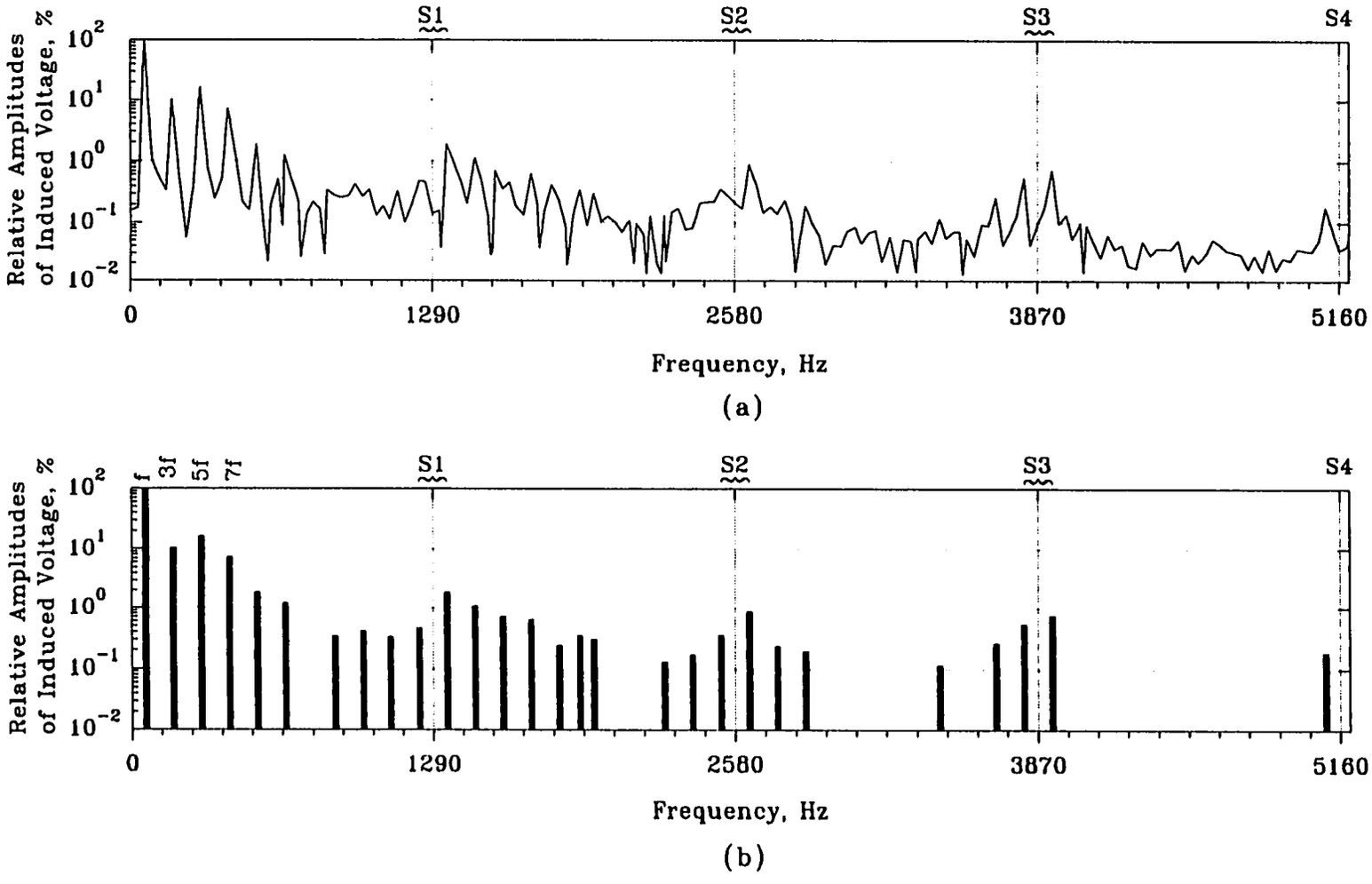

Figure 3.12 : Measured spectral distribution of the voltages induced in a tooth-width search-coil at no-load, slip = 0. (a) Frequency spectrum of the measured signal, (b) Display of the salient components.

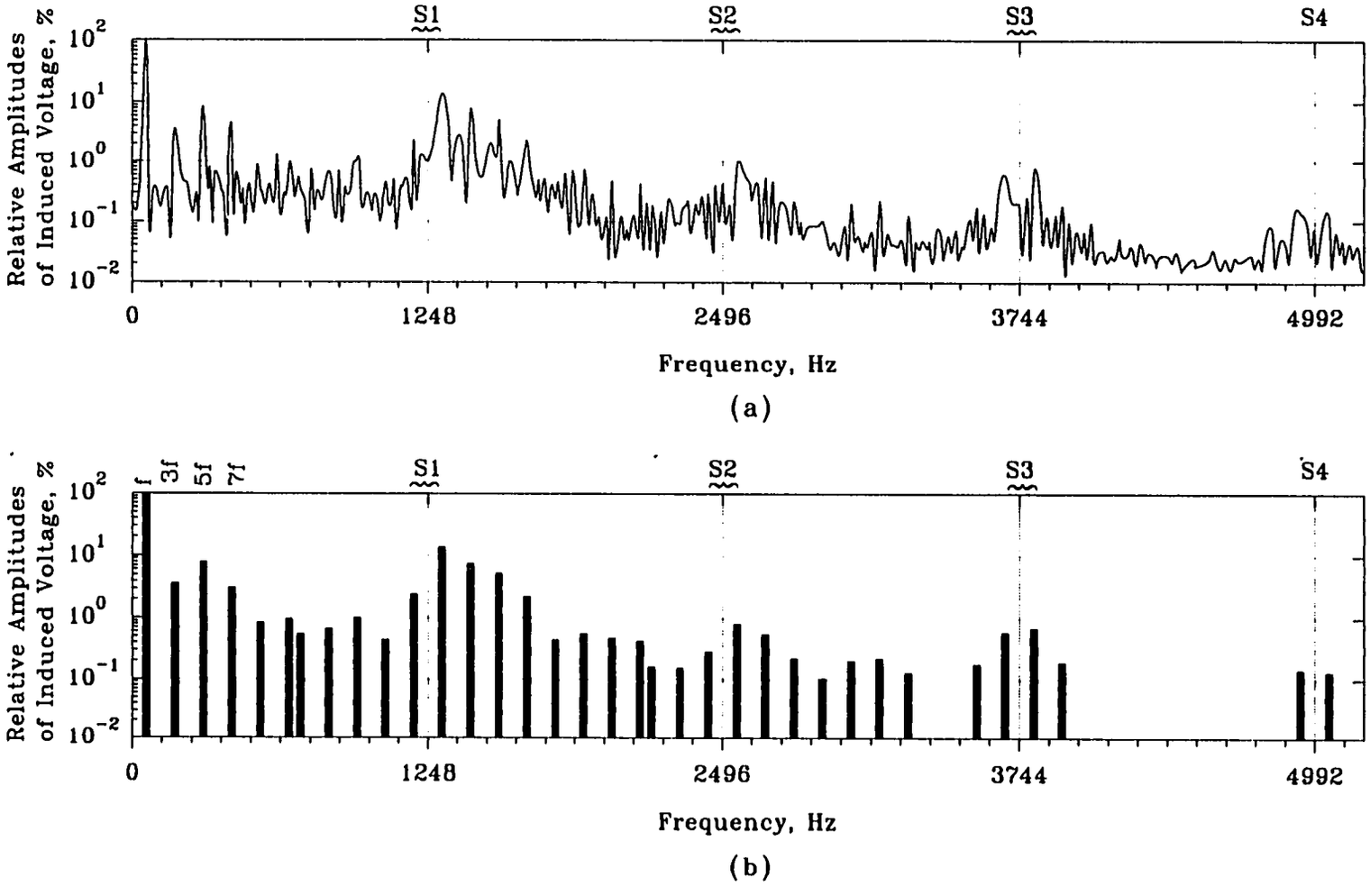

Figure 3.13 : Measured spectral distribution of the voltages induced in a tooth-width search-coil at rated load, slip = 0.033. (a) Frequency spectrum of the measured signal, (b) Display of the salient components.

respect to the fundamental component at the no-load and full load conditions. In contrast, in the measured spectra noticeable reductions are observed for the components at 3f, 5f, 7f and 9f from the no-load to the full load condition. Also, the saturation side-band components that are present on either side of each of the slot-harmonic components in the measured spectra have higher values than those predicted by the theoretical model. This suggests that the saturation of the teeth predominates over the saturation of other iron sections in the magnetic flux path. Consequently, saturation effects influence the slot-harmonic components significantly in comparison to the fundamental air-gap field. Hence, different values for the permeance-coefficients used to model saturation need to be incorporated in the calculations for the fundamental and slot-harmonic saturation field components.

The calculated values of the slot-harmonic components are, in general, slightly higher than those measured because of the insufficient treatment of the magnetic saturation effects. The experimental investigations suggest that the saturation effects may need to be revised in the theoretical procedures. As explained earlier in Chapter 2, the accuracy obtained here in the calculations of the air-gap field amplitudes is satisfactory from the perspective of noise and vibrations.

The vibration response was obtained by exciting the stator with an electromagnetic shaker. The stator has three major resonances at 730, 1942 and 2046 Hz. The resonant frequencies of the stator without windings was also measured [44]. The vibration spectra of the empty stator has a series of sharp peaks between 6 and 8 kHz. These peaks correspond to the lateral resonant frequencies of the stator teeth.

Figs. 3.14 and 3.15 show the spectra of the radial-forces acting on a stator tooth determined from the information provided by the voltage induced in a tooth-width search-coil when the machine was operating at no-load and rated load conditions, respectively. The important slot-harmonic components in the spectra of Figs. 3.14 and 3.15 are identified according to the frequencies at which they occur. In the following, comparisons are drawn between the calculated and measured spectra of the radial-forces acting on a stator tooth.

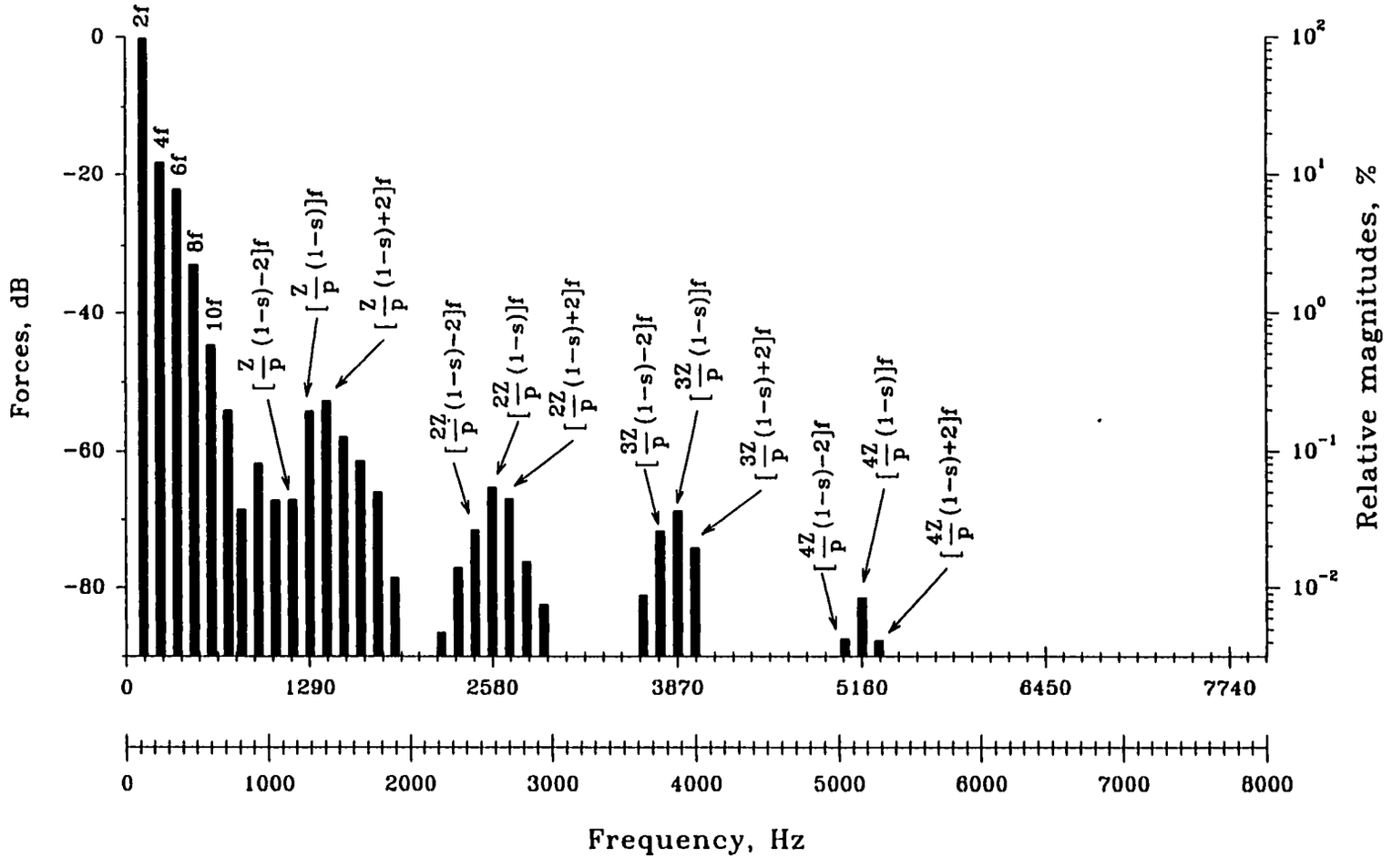

Figure 3.14 : Spectrum of the forces acting on a tooth of the 10 hp induction motor at no-load (slip = 0) determined from experimentally measured voltages of the search-coil.

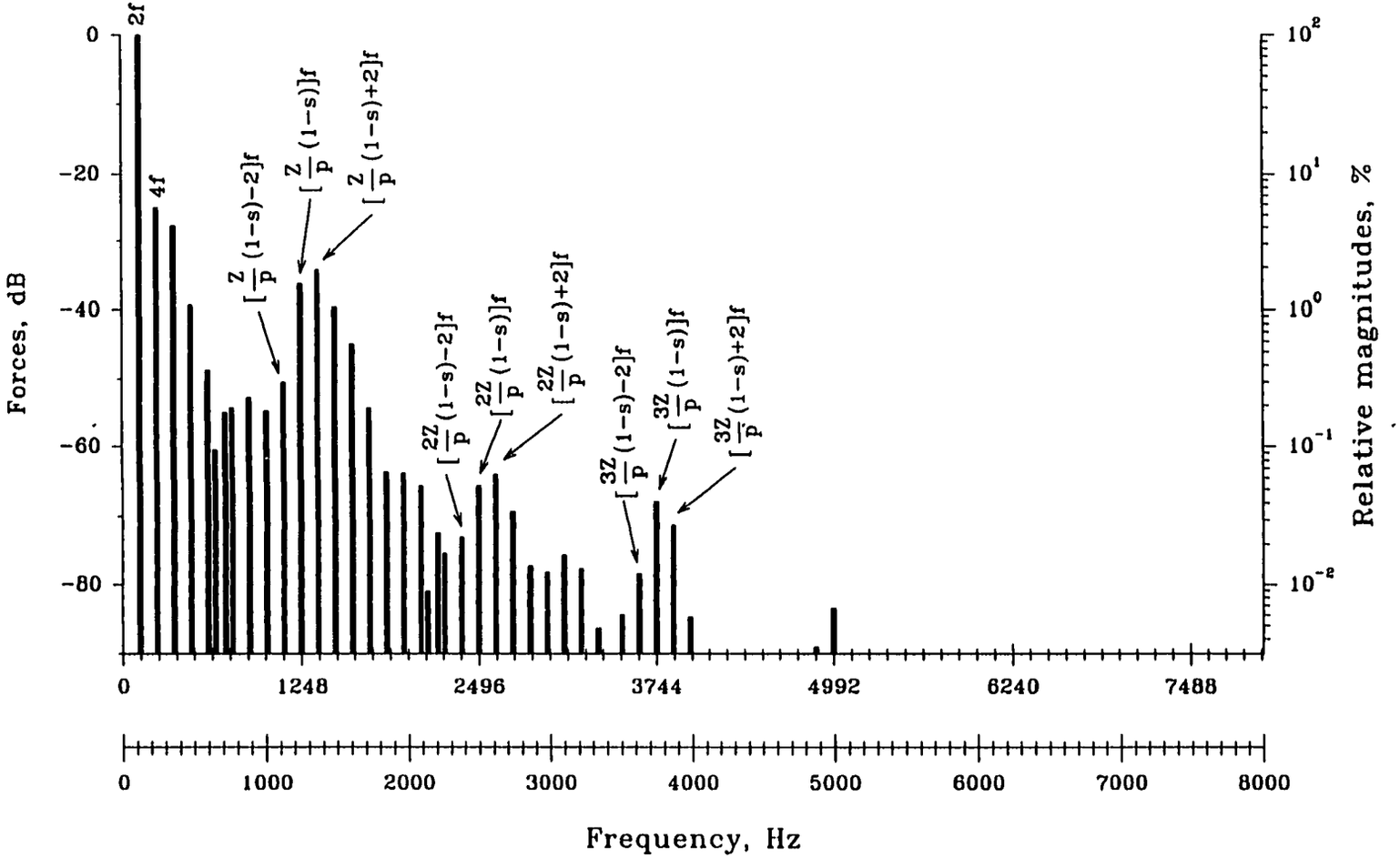

Figure 3.15 : Spectrum of the forces acting on a tooth of the 10 hp induction motor at rated load (slip = 0.033) determined from experimentally measured voltages of the search-coil.

i) Here again, all the components predicted by the theoretical calculations are present in the measured spectra of the forces. There are some additional components which correspond to magnetic saturation effects in the measured spectra at 8f, 10f, and those on either side of the slot-harmonic components.

ii) As explained earlier, the significant harmonic components in the spectra of the radial-forces are the slot-harmonic force components at F_{S1}, F_{S2}, F_{S3}, etc. Comparing the calculated and experimental values of the slot-harmonic force components, it is observed that the correlation between the two is better for the full-load condition as expected. In most cases, the difference between the predicted and measured amplitudes of the slot-harmonic force components is within 10% of the amplitude of the fundamental force component at 2f.

iii) The saturation force components at 4f, 6f, and the slot-harmonic side-band force components have higher values in the measured spectra than those predicted in the calculated spectra. In the theoretical calculations of the forces, the circumferential distributions of the forces were also considered. In view of the increasing flexural rigidity of electrical machine structures to higher modes of vibrations, only the force components with fewer than 8 pairs of force-poles were included in the calculation of the force spectra. The effects of saturation on the fundamental air-gap field produces the force components at 4f and 6f which are associated with 8 and 12 pairs of force-poles, respectively. Since the forces are determined through the measurement of flux and flux-pulsations, this may lead to some discrepancy between the calculated and measured values of the force components.

Although the measured values of the various force components are smaller than those calculated, nevertheless the measured spectra confirms the existence of all the predicted force components.

Figs. 3.16 and 3.17 show the measured spectra of the vibration signals when the machine was operating at no-load and rated load conditions, respectively. The various components in the spectra of Figs. 3.16 and 3.17 are identified according to the frequencies at which they occur. The components near important resonant frequencies are identified by ®. At no-load operation, only some of the 1^{st} and 6^{th} order slot-

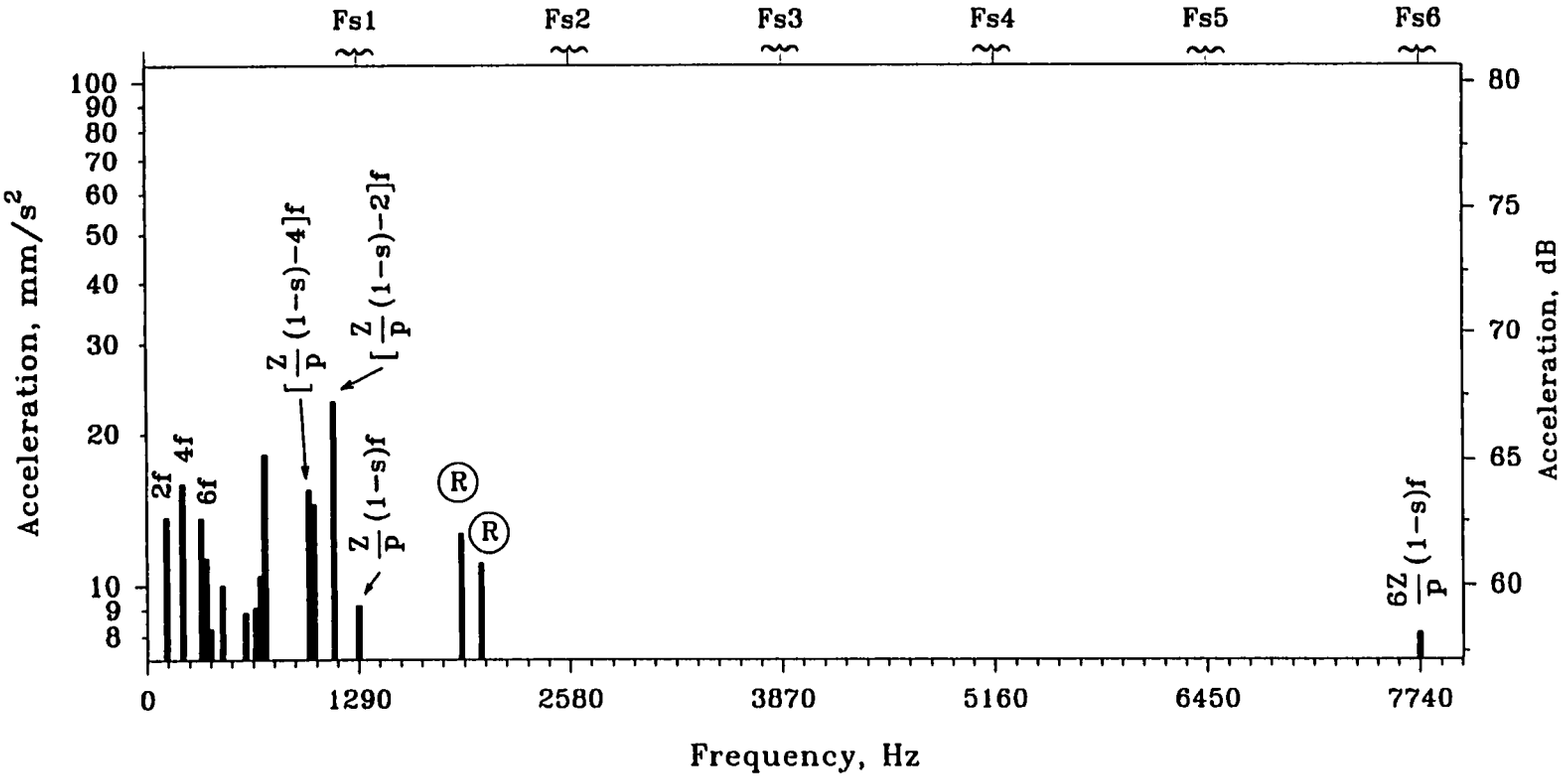

Figure 3.16 : Measured spectral distribution of the vibrations at no-load.

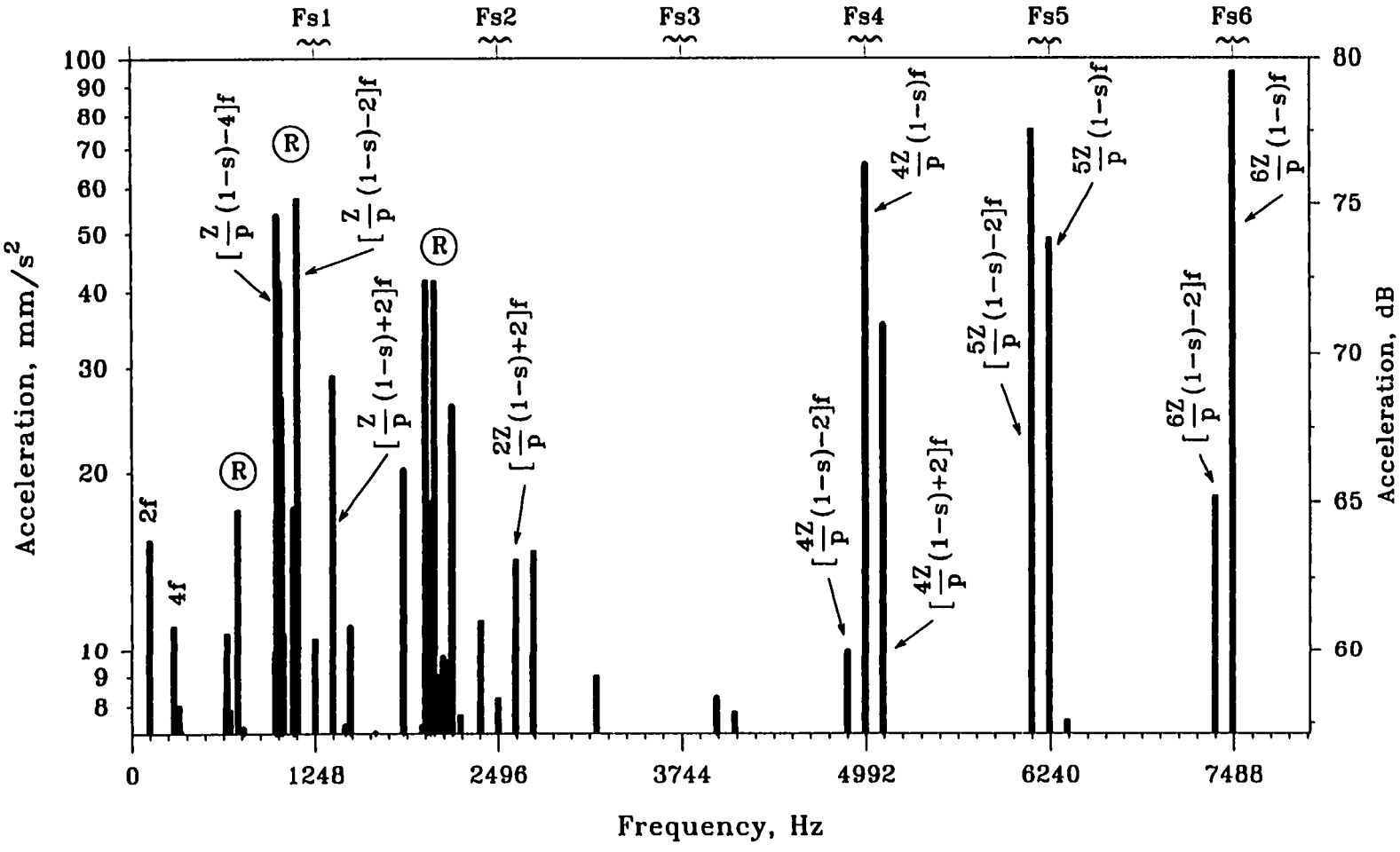

Figure 3.17 : Measured spectral distribution of the vibrations at full rated load.

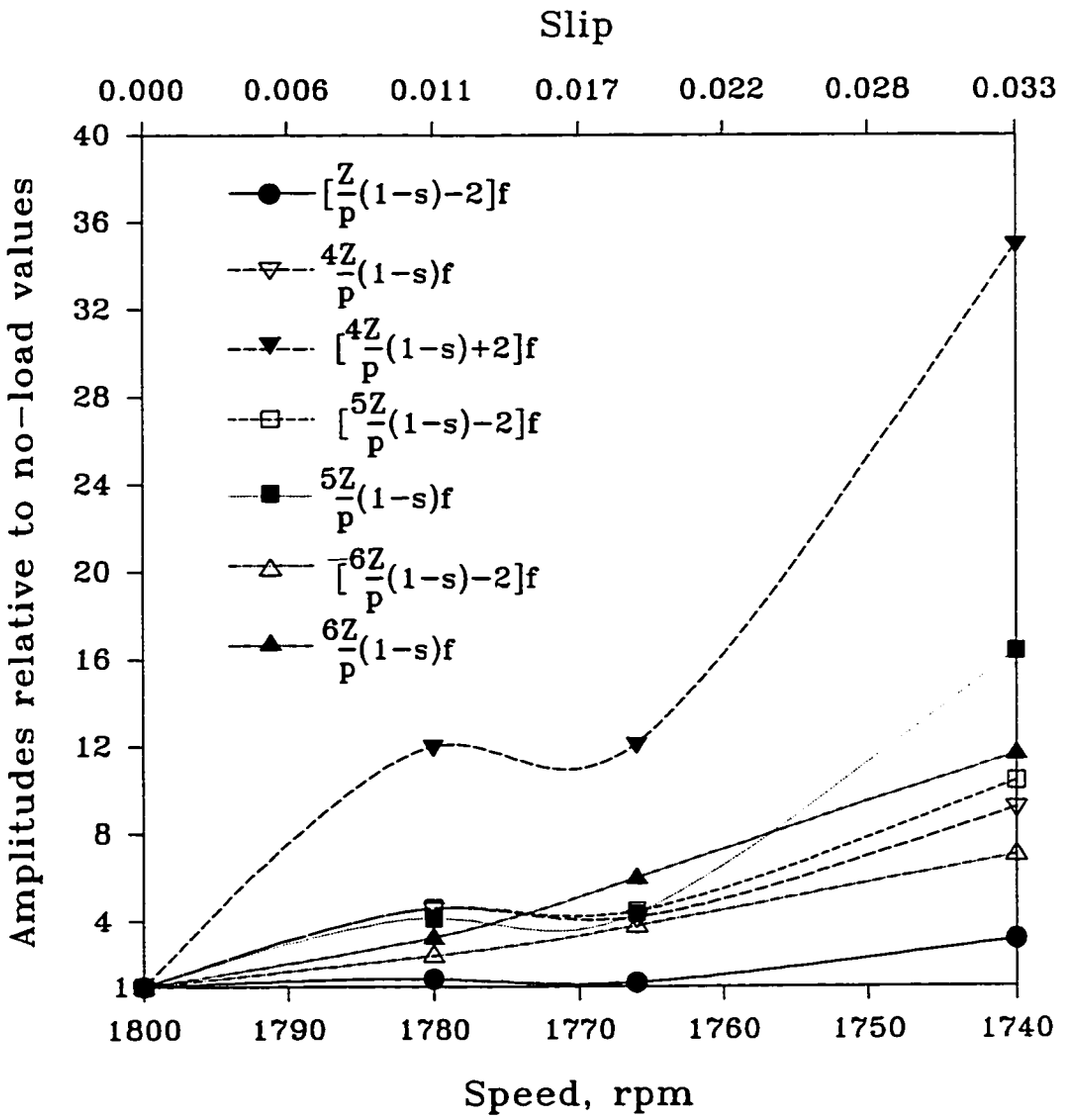

Figure 3.18 : Plot of the variation of the slot-harmonic vibration components with load, the amplitudes are shown relative to their magnitudes at no-load.

harmonic components are present in the vibration spectra. The calculated values of lower side-band of the 1st order slot-harmonic forces, produced due to saturation, have relatively small amplitudes. Due to their proximity to a resonant frequency at 1200 Hz, these components acquire large amplitudes in the measured vibration signals. It is interesting to note that the measured vibration spectra, when the machine was operating at rated load, indicates the presence of the 1st, 2nd, 4th, 5th and 6th order slot-harmonic components. The 1st order slot-harmonic forces, and its lower saturation side-band force

components, show an appreciable increase from their magnitudes at no-load. Also, the 2^{nd}, 4^{th}, 5^{th} and 6^{th} order slot-harmonic forces have substantially large amplitudes in comparison to their corresponding magnitudes at no-load. The stator exhibits a noticeable damping effect on the forced vibrations between 3 and 5 kHz.

The vibration measurements were made with varying load levels between no-load and full rated load conditions. Fig. 3.18 shows the variation of important slot-harmonic components in the measured vibration signal with load. The variations are plotted in terms of their amplitudes at no-load. Most of the slot-harmonic components increase to about 10 times their amplitudes at no-load. It is interesting to note that the 4^{th} order slot-harmonic component increases to about 35 times its no-load magnitude.

3.5 Comments

An analysis of a general nature for the determination of the radial-forces in induction motors was described in Chapter 2. In this chapter, the analysis is used to determine the stator and rotor currents, MMF's, air-gap fields and the radial-forces for a 10 hp squirrel-cage induction motor and a 70 kW wound-rotor induction motor. It is shown that the analysis can be easily extended to incorporate the effects of different stator winding arrangements, while considering the mutual interactions between the stator and rotor MMF's. Due to the suitability of the permeance-method, the effects of magnetic saturation on the air-gap fields and the radial-forces could be conveniently investigated.

Most of the noise producing electromagnetic forces are produced at the slot-harmonic frequencies and their saturation side-bands. Theoretical and experimental results presented in this chapter show that the magnitudes of the slot-harmonic forces and the ensuing vibrations increase significantly with load. The amplitudes of these forces are influenced by the stator and rotor winding arrangements. Further, the circumferential distribution of the noise producing radial-forces depend on the choice of the stator and rotor slots. Although, in this chapter, the amplitudes and frequencies of the various radial-forces have been studied to identify the various components in the vibration spectrum, there exists a need to investigate the vibration response of electrical machine structures to distributed electromagnetic forces. The first benefit of such a

study will aid in identifying the significant components from the vast majority of calculated force components. Secondly, since it may not always be feasible to apply the condition of isolating the force-frequencies from the resonant frequencies such as in variable frequency operation of electric motors, it is then essential to determine methods of rendering some of these force components ineffective in inducing high levels of vibrations even when it occurs close to resonances of the machine structure. In the following chapters, the experimental study of the vibration response of electrical machine stators to electromagnetic forces which are distributed over its entire surface is described.

4. ELECTROMAGNETIC SURFACE EXCITATION SYSTEM; THEORY, EXPERIMENTAL SET-UP, MODELS AND OPERATION

In this chapter, the electromagnetic excitation system for inducing vibrations in stators of electrical machines using distributed forces is described. After explaining the theory and the benefits of using distributed forces, the experimental set-up especially designed and built to achieve the distributed electromagnetic forces is described here. The chapter concludes with a summary of the capabilities of this electromagnetic excitation system.

4.1 Introduction

As explained earlier, forced vibrations in a system take place when the system oscillates under the action of external forces. When the excitation force is oscillatory, the system is forced to respond at the excitation frequency. If the frequency of excitation coincides with one of the natural frequencies, resonance is encountered. At the resonance, the distribution of the vibration displacements assumes well-defined sinusoidal patterns around the circumference and length of the model. These well-defined deformation patterns are commonly described as the circumferential and longitudinal modes of vibration. The circumferential mode of vibration, n, is defined as the number of cycles of deformation around the circumference of the model. The longitudinal mode of vibration, m, is defined as the number of half-cycles of deformations along the length of the model. The electromagnetic surface excitation system has been designed to prominently induce vibrations of a particular mode.

In an electrical machine, the electromagnetic forces that induce vibrations in the stator and rotor of a machine are distributed over the entire surface adjoining the air-gap. Further, depending on the number of poles of the magnetic fields these forces induce different modes of vibration. In the conventional methods for experimentally obtaining information on the resonances and their associated mode-shapes, a point-excitation

system is generally used. In the following, the merits and demerits of using a surface excitation system over a point-excitation system are discussed.

4.2 Theory Underlying the Electromagnetic Surface Excitation System

Practical structures such as stators of electrical machines are commonly analyzed using vibration system models having multiple degrees of freedom [41,49,50]. The properties of a continuous structure can be simulated to any desired accuracy by a system possessing a finite number of degrees of freedom. Each of these degrees of freedom corresponds to a natural frequency and its associated mode-shapes. Each natural frequency and the associated mode-shape can be examined individually. Considering a system with two degrees of freedom as shown in Fig. 4.1, the equations of motion of the system are:

$$\begin{aligned} m_1\ddot{x}_1 + (c_1+c_2)\dot{x}_1 - c_2\dot{x}_2 + (k_1+k_2)x_1 - k_2x_2 &= F_1, \\ m_2\ddot{x}_2 + (c_2+c_3)\dot{x}_2 - c_2\dot{x}_1 + (k_2+k_3)x_2 - k_2x_1 &= F_2, \end{aligned} \tag{4.1.a}$$

which can be written in a matrix form as:

$$\begin{bmatrix} m_1 & 0 \\ 0 & m_2 \end{bmatrix} \begin{Bmatrix} \ddot{x}_1 \\ \ddot{x}_2 \end{Bmatrix} + \begin{bmatrix} c_1+c_2 & -c_2 \\ -c_2 & c_2+c_3 \end{bmatrix} \begin{Bmatrix} \dot{x}_1 \\ \dot{x}_2 \end{Bmatrix} + \begin{bmatrix} k_1+k_2 & -k_2 \\ -k_2 & k_2+k_3 \end{bmatrix} \begin{Bmatrix} x_1 \\ x_2 \end{Bmatrix} = \begin{Bmatrix} F_1 \\ F_2 \end{Bmatrix}, \tag{4.1.b}$$

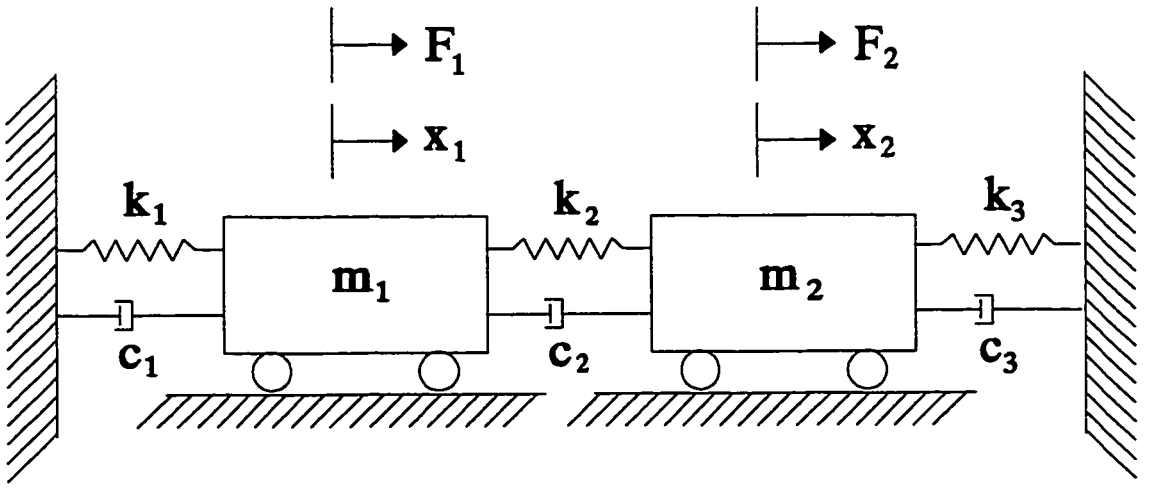

Figure 4.1 : A vibratory system with two degrees of freedom.

$$[m]\ddot{x}+[c]\dot{x}+[k]x = [F]. \tag{4.1.c}$$

Neglecting the effects of damping, the natural frequencies and the associated mode-shapes of the system can be easily determined. The effects of damping are discussed later in the next section. The equations of motion, therefore, reduce to:

$$[m]\ddot{x} + [k]x = 0. \tag{4.2.a}$$

Assuming a harmonic motion, i.e. $\ddot{x}_i = -\lambda_i x_i$, where $\lambda_i = \omega_i^2$, and ω_i is the angular frequency of oscillation. Eqn. 4.2.a can be rewritten as:

$$[-\lambda[m] + [k]]\ x = 0, \tag{4.2.b}$$

$$[[m]^{-1}[k] - \lambda[I]]x = 0, \tag{4.2.c}$$

where [I] is an identity matrix. For the set of equations in Eqn. 4.2.c, it is well known that a non-trivial solution exists if the determinant of the coefficients is zero. Thus:

$$|[m]^{-1}[k] - \lambda[I]| = 0. \tag{4.3}$$

Eqn. 4.3 is called the characteristic equation of the system. The roots of the characteristic equation are called eigen-values, and the undamped natural frequencies are determined from the relationship:

$$\lambda_i = \omega_i^2. \tag{4.4}$$

The eigen-vectors for the system in Eqn. 4.2.c, correspond to the deformation pattern of the structure for the corresponding natural frequencies [41,49]. A system with n degrees of freedom will have n eigen-values and n corresponding eigen-vectors. A particular eigen-value and the eigen-vector will satisfy Eqn. 4.2.c, giving:

$$[k]\{\phi_i\} = \lambda_i[m]\{\phi_i\}, \tag{4.5}$$

where $\{\phi_i\}$ is an eigen vector corresponding to λ_i. Premultiplying both sides with the transpose of another mode-shape vector $\{\phi_j\}$, we get:

$$\{\phi_j\}^T[k]\{\phi_i\} = \lambda_i\{\phi_j\}^T[m]\{\phi_i\}. \tag{4.6}$$

Similarly, the equation for the j^{th} mode can be premultiplied by the transpose of the i^{th} mode, and it is given as:

$$\{\phi_i\}^T [k] \{\phi_j\} = \lambda_j \{\phi_i\}^T [m] \{\phi_j\} . \tag{4.7}$$

As [m] and [k] are symmetric matrices,

$$\{\phi_j\}^T [k] \{\phi_i\} = \{\phi_i\}^T [k] \{\phi_j\} , \tag{4.8}$$

$$\{\phi_j\}^T [m] \{\phi_i\} = \{\phi_i\}^T [m] \{\phi_j\} . \tag{4.9}$$

Subtracting Eqn. 4.7 from Eqn. 4.6 yields:

$$0 = (\lambda_i - \lambda_j) \{\phi_i\}^T [m] \{\phi_j\} , \tag{4.10}$$

implying that when $\lambda_i \neq \lambda_j$ (i.e. considering two different natural frequencies),

$$\{\phi_i\}^T [m] \{\phi_j\} = 0 . \tag{4.11}$$

$$\text{Similarly,} \quad \{\phi_i\}^T [k] \{\phi_j\} = 0 . \tag{4.12}$$

Eqns. 4.11 and 4.12 define the orthogonal properties of the mode-shape vectors with respect to the system mass and stiffness matrices, respectively. In Eqn. 4.10, if i=j, then the two mode vectors are not necessarily orthogonal. Therefore Eqns. 4.11 and 4.12 are equal to some scalar constant other than zero. Therefore:

$$\{\phi_i\}^T [m] \{\phi_i\} = M_i , \tag{4.13}$$

$$\{\phi_i\}^T [k] \{\phi_i\} = K_i = \lambda_i M_i = \omega_i^2 M_i , \tag{4.14}$$

where M_i and K_i are called the generalized mass and stiffness, respectively.

4.2.1 Modal-analysis

The equations of forced motion neglecting the effects of damping are rewritten as:

$$[m] \{\ddot{x}\} + [k] \{x\} = \{F\} . \tag{4.15}$$

In solving the above equations for the response {x} for a particular set of exciting forces, the major obstacle encountered is the coupling between the equations. In Eqn. 4.15, it can be seen that while the stiffness matrix is symmetric it is not diagonal resulting in an elastic coupling.

If the system of equations can be uncoupled so that one can obtain diagonal mass and stiffness matrices, then each equation will be similar to that of a single degree of freedom system. These equations can be solved independently of each other. The process of deriving the system response by transforming the equations of motion into an independent set of equations is called modal-analysis [41].

The required co-ordinate transformation is one that decouples the system mass and stiffness, and therefore it yields diagonal mass and stiffness matrices. The orthogonal properties of the mode-shapes are used for this purpose. The $\{x\}$ co-ordinates are transformed to $\{\eta\}$ using the following relationship:

$$\{x\} = [\phi]\{\eta\}, \tag{4.16}$$

where $[\phi] = [\phi_1, \phi_2, ..., \phi_n]$ is referred to as the modal matrix and $\{\eta\}$ is called modal co-ordinates. Therefore, rewriting Eqn. 4.15 with respect to the new co-ordinates, we get:

$$[m]\{\ddot{x}\} + [k]\{x\} = \{F\}, \tag{4.17.a}$$

$$[m][\phi]\{\ddot{x}\} + [k][\phi]\{\eta\} = \{F\}. \tag{4.17.b}$$

Premultiplying both sides by the transpose of the modal matrix $[\phi]^T$, we obtain:

$$[\phi]^T[m][\phi]\{\ddot{x}\} + [\phi]^T[k][\phi]\{\eta\} = [\phi]^T\{F\}. \tag{4.18}$$

Eqn. 4.18 represents a set of equations of the form:

$$M_i\ddot{\eta}_i + K_i\eta_i = \{\phi_i\}^T\{F\} = F_i, \tag{4.19}$$

where each equation represents a single-degree of freedom system, M_i and K_i are the i^{th} modal mass (generalised mass) and i^{th} modal stiffness (generalised stiffness), respectively. Eqn. 4.19 forms the basis underlying the use of distributed force excitation of structures. Thus, if the excitation force is chosen such that it resembles a particular mode of vibration, the system response will be similar to that of a system with a single degree of freedom. This would permit each of the resonant frequencies to be individually examined.

The analysis presented in this section is summarised in the following:

(i) If the excitation force is oscillatory, the system is forced to respond at the excitation frequency. Resonance will occur when the frequency of excitation coincides with one of the natural frequencies of the vibrating structure.

(ii) The deformation patterns at resonance are called the mode-shapes of vibration. The orthogonal properties of the mode-shape vectors are used to diagonalise the mass and stiffness matrices.

(iii) Eqn. 4.19 forms the basis underlying the use of distributed force excitation of structures. When the distribution of the excitation forces is chosen such that it resembles a particular mode of vibration, the system response will be similar to that of a system with a single degree of freedom. This process of isolating the resonances would permit each of the resonances to be individually examined.

4.2.2 Vibration Damping Effects

The assumption, heretofore, that the vibrating system has no internal damping is only hypothetical. There are several types of damping that are present in the real systems, and they are commonly classified as viscous, hysteresis, frictional, aerodynamic, etc. Although it is very difficult to ascertain the nature of damping present in a system, certain simplifying assumptions can be made to account for them. First, it is assumed that the distribution of the damping is proportional. By proportional damping it is implied that the damping matrix [c] is proportional to the stiffness matrix [k] or the mass matrix [m], or to some linear combination of the two. Therefore,

$$[c] = \alpha[m] + \beta[k], \tag{4.20}$$

where α and β are some constants. Due to the assumption of proportional damping, the co-ordinate transformation that diagonalises the mass and stiffness matrices will also diagonalise the damping matrix. Thus the coupled equations of motion for a proportionally damped system can be uncoupled to many single-degree of freedom systems as:

$$M_i\ddot{\eta}_i + C_i\dot{\eta}_i + K_i\eta = \{\phi_i\}^T\{F\} = F_i. \tag{4.21}$$

When the damping matrix is not proportional to the mass or the stiffness matrix, it cannot be diagonalised using the modal matrix. Hence, the equations of motion for a non-proportionally damped system cannot be uncoupled. Damped vibration modes do exist for non-proportionally damped systems [41]. For non-proportionally damped systems, the vibration modes in the presence of damping are different from the

undamped vibration modes. This difference is manifested by the fact that for undamped natural modes, all points on the structure pass through their equilibrium positions simultaneously, which is not the case for the complex modes associated with non-proportionally damped systems.

For the undamped modes, various parts of the structure move either in phase or 180° out of phase with respect to each other. In the case of non-proportionally damped structures, there are other phase differences between the various parts of the structure, which result in complex mode-shapes. This difference in the vibration response at a resonance is manifested by the fact that for undamped modes all points on the structure pass through their equilibrium positions simultaneously, which is not the case for the complex modes. Thus, the undamped modes have well-defined nodal points and appear as a "standing wave", while for complex modes the nodal points are not stationary [41].

The vibration response of a continuous structure, i.e. a multiple degree of freedom system, to any force can be represented by the superposition of the responses in its individual modes, considering each mode to respond as a single degree of freedom system. The forced vibration response of a continuous structure can therefore be obtained in terms of its modal parameters provided the mass, damping and stiffness of the structure are accurately known. It is sufficient to know the mass and the stiffness of the structure to satisfactorily determine the natural frequencies of the structure. For the determination of the forced response, it is additionally required to know the damping present in the structure. In general it is very difficult to determine the type of damping present in a structure, however it can be deduced with reasonable accuracy from the experimental data. The previous studies of machine stators, references [9,43,51], indicate the presence of well-defined mode-shapes at the various resonant frequencies, thereby indicating the presence of proportional damping.

4.2.3 Benefits of a Surface Excitation System

A vibration response test involves the quantitative measurement of the effect of a vibratory force on a structure. If the structure is linear and elastic, and excited by a sinusoidal force, then the resulting vibratory motion will be directly proportional to the exciting force and at the same excitation frequency. Measurement of the exciting force

and the resulting motion at a number of points over a range of frequencies would be sufficient to describe the vibratory behaviour of the structure.

The first part of information that can be extracted from the vibration response is the natural frequencies of the structure. It can be shown theoretically [40,49] that the peaks in the vibration response will be displaced slightly from the undamped natural frequencies due to the effect of damping. The second part of information is the amount of damping at a particular mode. This is usually determined by the sharpness of the resonant peaks, and it is measured in terms of the loss-factor. The loss-factor is defined as the ratio of the -3 dB (half power level) bandwidth to the centre frequency. Generally, the use of point-excitation may be sufficient to draw these inferences from the vibration response of a lightly damped structure, whose natural frequencies are widely spaced. However, such a test is not very suitable for actual stator models as they possess significant amount of damping and may also have resonant frequencies very close to each other [9,51,52].

To mitigate some of these difficulties, a distributed force excitation is preferred over the single point-excitation. By using a distributed excitation force, a larger amount of energy can be fed more uniformly into the structure. This is especially true for laminated stators where the vibration energy is quickly dissipated within the structure producing widely different vibration amplitudes at various locations. Further, a particular mode of vibration at a resonant frequency can be isolated with the use of a distributed force. The distributed force is chosen such that only the mode of interest is dominantly excited in that frequency range. The structure would then respond only in that principal mode as a single degree of freedom system, and the modal parameters can be easily determined.

4.3 Stator Models

The electromagnetic surface excitation system is used to test the vibration behaviour of two stator models. Model I is a smooth thick cylindrical shell made of mild steel. The model is shown in Fig. 4.2, and its dimensions are also given in Table 4.1. The dimensions of this model are exactly the same as the stator of an actual 4-pole, 550 V, 120 hp induction motor. The Model II is made from about 1090 stator

laminations, which were punched for the 120 hp induction motor mentioned above. The details of the laminations used in Model II are shown in Fig 4.3, and its dimensions are provided in Table 4.1. The laminations are held together with the help of eight bolts placed equidistantly along the circumference, and two end pressure-plates. These end pressure-plates are slotted to form teeth which match with that of the stator laminations. Photographs of Model I and Model II are given in Figs. 4.4 and 4.5. 14 gauge copper wires are installed in the slots of Model II so that they resemble the actual windings installed in an electrical machine stator. In order to avoid any possible asymmetries, the overhang sections of the windings have been trimmed off in Model II.

4.4 Electromagnetic Surface Excitation Set-up

A rotor was designed and built, having special constructional features, to house the windings required to excite the stator models using distributed electromagnetic forces. The physical details of the rotor structure are also provided in Table 4.1. The windings that are installed on the rotor are designed to induce the circumferential modes n = 0, 1, 2, 3 and 4 of vibrations. For this purpose, two separate windings, one with 2 magnetic poles and the other with 4 magnetic poles, are installed on the rotor. The windings are so designed that there is virtually no mutual inductive coupling between these two windings. This allows simultaneous operation of both the windings.

4.4.1 Design of the Rotor Structure

The constructional features of the rotor structure are shown in Figs. 4.6 and 4.7. The rotor body is formed by stacking the laminations of the 120 hp induction motor rotor on the shaft. The laminations are compressed using two non-magnetic steel end-pressure plates. Grinding on the body of the rotor was done to obtain the required outside-diameter. In order to meet the stringent power requirement of windings, the air-gap length between the stator and rotor is kept small. To overcome the difficulty of assembling the set-up, an elaborate mounting arrangement, which includes rails and pedestals, was designed and built. The stator and rotor structures are seated on rubber pads to avoid any vibration transmission through the supporting structure.

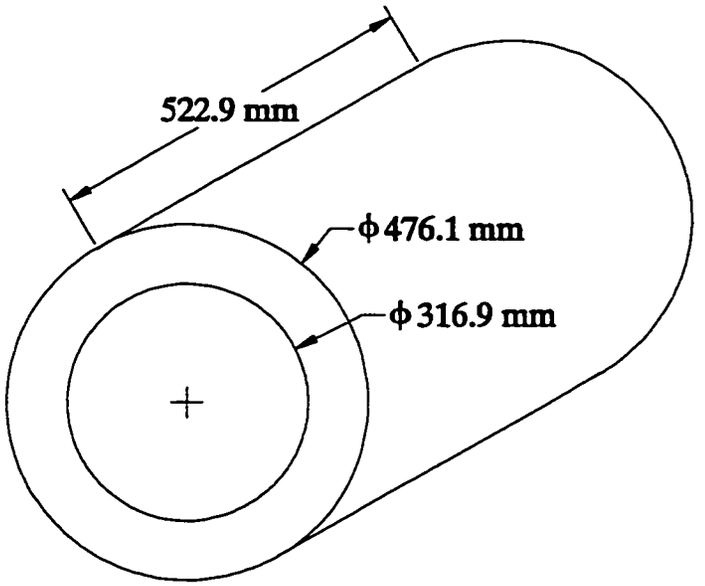

Figure 4.2 : Dimensions of the 120 hp stator-shell, Model I.

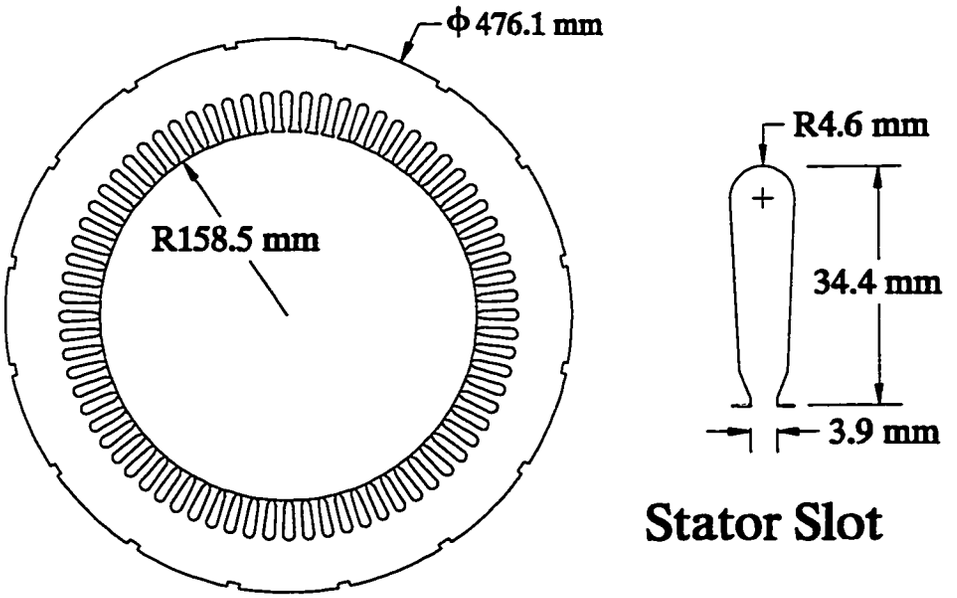

Figure 4.3 : Details of the 120 hp induction motor stator laminations used in Model II.

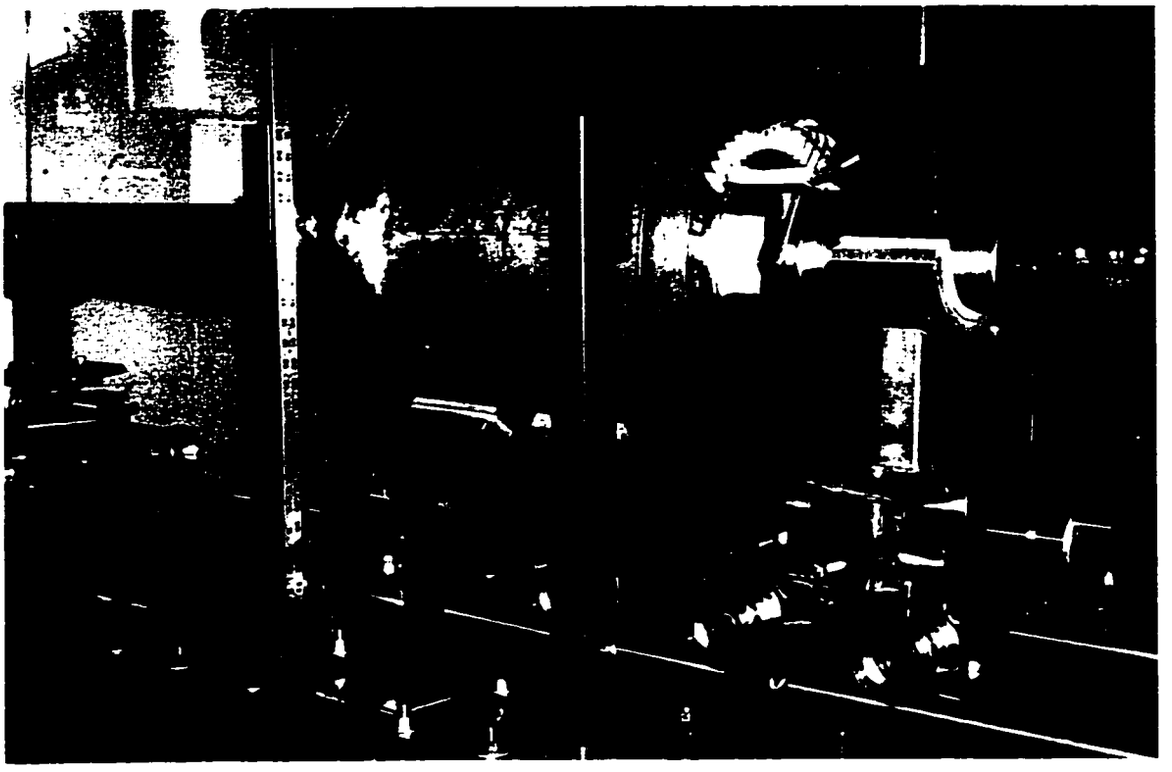

Figure 4.4 : Photograph of Model I.

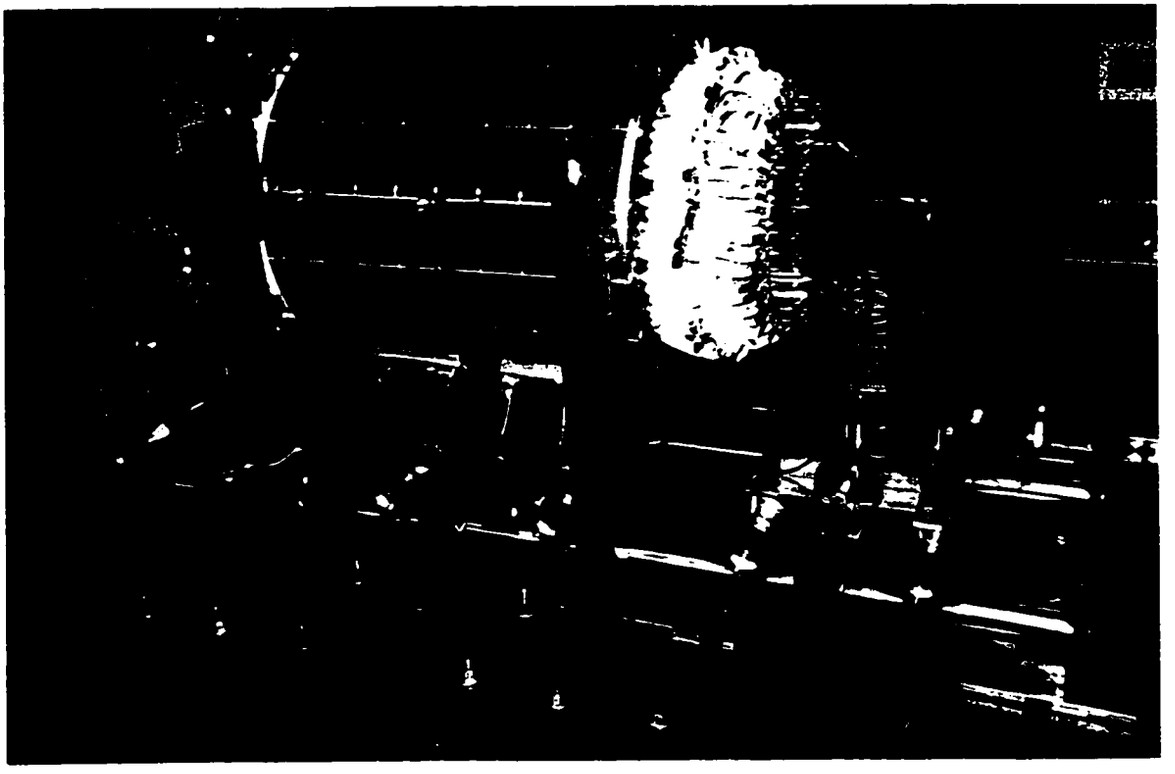

Figure 4.5 : Photograph of Model II.

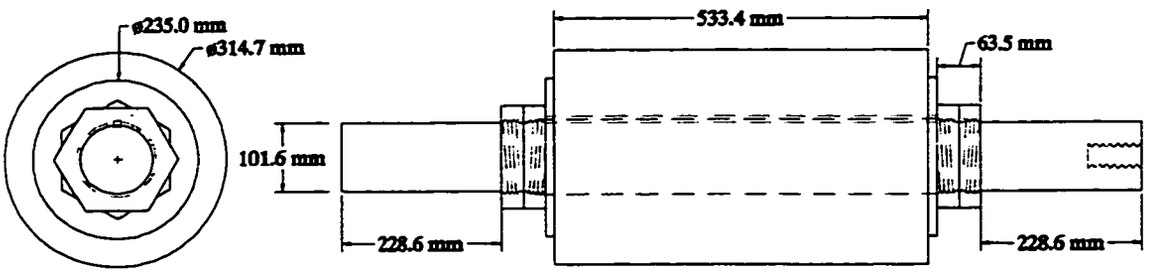

Figure 4.6 : Front and side-views of the rotor.

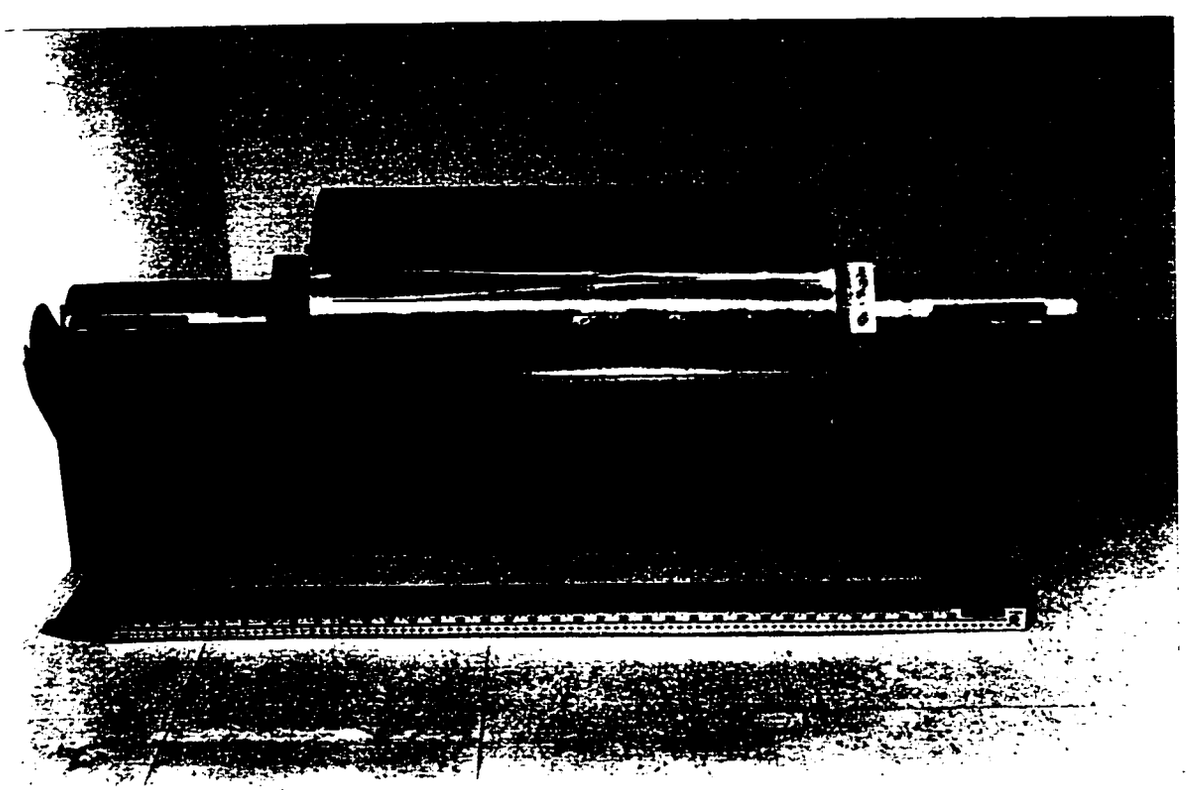

Figure 4.7 : Photograph of the rotor.

Table 4.1 : Salient dimensions of the Stator models and the rotor.

Outside Diameter of Stator Shell-model, mm	476.1
Outside Diameter of Stator, mm	476.1
Length of Stator Shell-model, mm	522.9
Length of Stator, mm	522.9
Stator-shell bore diameter, mm	316.9
Stator bore diameter, mm	316.9
Outside diameter of rotor, mm	314.706
Air-gap length, mm	1.097
Length of rotor, mm	533.4
Weight of rotor structure, kgs	327.27
Weight of Stator Shell-model, kgs	404.40
Outside diameter of Shaft, mm	111.125
Length of Shaft, mm	1143
Number of Slots on Stator	72
Number of Slots on Rotor	56

4.4.2 Details of Rotor Windings

As mentioned earlier, the windings are installed in the rotor to produce distributed electromagnetic forces which induce n = 0, 1, 2, 3 and 4 modes of vibration. The two windings produce pulsating magnetic fields having 2 and 4 poles, respectively.

Let the 2-pole winding produce a magnetic field in the air-gap having a maximum flux-density of $\hat{B}_{2p}$. Thus, the air-gap flux-density distribution due to 2-pole winding is given by:

$$B(\theta,t) = \hat{B}_{2p}\cos(\theta)\cos(\omega_{2p}t), \tag{4.22}$$

where B(θ,t) is the net air-gap flux-density distribution due to the 2-pole winding.

Similarly, let the 4-pole winding produce a magnetic field in the air-gap having a maximum flux-density of $\hat{B}_{4p}$. Thus, the air-gap flux-density distribution due to the 4-pole winding is given by:

$$B(\theta,t) = \hat{B}_{4p}\cos(2\theta)\cos(\omega_{4p}t), \tag{4.23}$$

where B(θ,t) is the net air-gap flux-density distribution due to the 4-pole winding.

These windings can be excited separately, or can be excited simultaneously. For the case, when both the windings are excited together, the net air-gap flux-density is given by:

$$B(\theta,t) = \hat{B}_{2p}\cos(\theta)\cos(\omega_{2p}t) + \hat{B}_{4p}\cos(2\theta)\cos(\omega_{4p}t). \tag{4.24}$$

The forces acting on the stator surface due to the presence of the magnetic field are given as:

$$F(\theta,t) = \frac{[B(\theta,t)]^2}{2\mu_0}. \tag{4.25}$$

Substituting Eqn. 4.24 in Eqn. 4.25, the net force-distribution acting on the stator surface is given by:

$$\begin{aligned} F(\theta,t) = {} & \frac{\hat{B}_{2p}^2}{8\mu_0}\left[1 + \cos(2\theta) + \cos(2\omega_{2p}t) + \cos(2\theta)\cos(2\omega_{2p}t)\right] \\ & + \frac{\hat{B}_{4p}^2}{8\mu_0}\left[1 + \cos(4\theta) + \cos(2\omega_{4p}t) + \cos(4\theta)\cos(2\omega_{4p}t)\right] \\ & + \frac{\hat{B}_{2p}\hat{B}_{4p}}{4\mu_0}\left[\cos(\theta)\cos\left[(\omega_{2p}+\omega_{4p})t\right] + \cos(\theta)\cos\left[(\omega_{2p}-\omega_{4p})t\right]\right] \\ & + \frac{\hat{B}_{2p}\hat{B}_{4p}}{4\mu_0}\left[\cos(3\theta)\cos\left[(\omega_{2p}+\omega_{4p})t\right] + \cos(3\theta)\cos\left[(\omega_{2p}-\omega_{4p})t\right]\right]. \end{aligned} \tag{4.26}$$

The various terms in Eqn. 4.26 are rearranged according to the mode of vibration they will induce, and they are listed in Table 4.2. It can be seen from Table 4.2 that for each mode there exists two force components. For modes n = 0, 2 and 4, only one winding needs to be used. To induce vibrations of modes n=1 and n=3, both the windings are excited using the same frequency. This would produce the desired force components at

Table 4.2 : List of force components due to the presence of a 2-pole and 4-pole magnetic field distribution in the air-gap.

Mode, n	Frequency, Hz	Magnitude, N	Source
0	$2f_{2p}$	$(\hat{B}_{2p})^2 / (8\mu_0)$	2-pole winding
0	$2f_{4p}$	$(\hat{B}_{4p})^2 / (8\mu_0)$	4-pole winding
1	$f_{2p} + f_{4p}$	$\hat{B}_{2p}\hat{B}_{4p} / (4\mu_0)$	2- & 4-pole windings
1	$f_{2p} - f_{4p}$	$\hat{B}_{2p}\hat{B}_{4p} / (4\mu_0)$	2- & 4-pole windings
2	$2f_{2p}$	$(\hat{B}_{2p})^2 / (8\mu_0)$	2-pole winding
3	$f_{2p} + f_{4p}$	$\hat{B}_{2p}\hat{B}_{4p} / (4\mu_0)$	2- & 4-pole windings
3	$f_{2p} - f_{4p}$	$\hat{B}_{2p}\hat{B}_{4p} / (4\mu_0)$	2- & 4-pole windings
4	$2f_{4p}$	$(\hat{B}_{4p})^2 / (8\mu_0)$	4-pole winding

twice the excitation frequency. The other force components which are also produced corresponding to the difference terms in Eqn. 4.26, result in a non-pulsating or time independent steady force.

The amplitudes of the air-gap flux-densities, $\hat{B}_{2p}$ and $\hat{B}_{4p}$, are chosen such that they would be sufficient to induce an appreciable level of vibrations in the stator models. It is desirable to keep the air-gap length as small as possible to alleviate the load on the power supply. In view of the physical constraints imposed by the stator models and the rotor with respect to their size and weight, the air-gap length was set to be 1 millimetre. After careful considerations with respect to the high frequency limit imposed by the power supply, it was chosen to have a nominal value for the maximum amplitude of air-gap flux-density at 0.05 Tesla. It was, therefore, possible to excite the stator models with a sinusoidally distributed force having a maximum amplitude of about 15 Newtons. At lower frequencies, it is possible to circulate higher currents through the windings and thereby achieve higher values of the air-gap flux-densities, and hence the forces acting

on the stator-models.

As mentioned earlier, two separate windings having 2 and 4 magnetic poles are installed on the rotor. These windings are energised using a single-phase variable-frequency power supply to produce the required pulsating force-distributions. Further, provisions are also made to connect the coils of the windings in a 3-phase configuration. The 3-phase windings are energised from a 3-phase variable-frequency power supply to produce rotating force-distributions capable of inducing vibrations of modes n=2 and n=4. The design details of the coil-arrangements and their connections are provided in **Appendix C.**

4.5 Analysis of the Distributed Forces

In this section, the winding arrangements used for inducing vibration modes of n=0 to n=4 are analyzed. The force-distributions, thus produced, are calculated and analyzed to determine its suitability for the electromagnetic surface excitation system. In addition, the rotating force-distributions obtained by using the 3-phase connections of the 2-pole winding are also analyzed.

4.5.1 Pulsating Forces for Mode n=2 Vibrations

The pulsating force-distribution needed for inducing the n=2 circumferential mode of vibration is obtained by energising the 2-pole winding from a single-phase supply. The force-distribution produced with this configuration is stationary, and the forces thus produced pulsate at twice the frequency of the power supplied to the 2-pole winding. The various coil-groups shown in Fig. C1 are connected in series, and a current of constant value of 2.5 Amperes is maintained through the 2-pole windings while the supply frequency is varied from 200 Hz to 5 kHz. This frequency range of the power supply corresponds to a frequency range of 400 Hz to 10 kHz for the forces.

The important information for the operation of the 2-pole winding in this configuration is provided in Table 4.3. The air-gap MMF, the resulting flux-density and the associated force-distribution were calculated, and they are shown in Fig. 4.8. The x-axis in Fig. 4.8 represents the circumferential location and it is denoted in terms of the rotor slot-numbers from 1 to 56. The vibration measurements are made on 16

Table 4.3 : Salient calculated information for the 2-pole winding.

Salient Details of 2-Pole Winding	
Number of turns per coil	2
Number of coils connected in parallel per slot	24
Maximum value of the air-gap flux-density produced, Tesla	0.088
Total current drawn from the power supply, Amperes	2.5
Net terminal inductance of winding, mH	26.2
Maximum value of the force acting on the rotor tooth, Newtons	57.24
Force acting on the rotor teeth under a pole, Newtons	535.61
Total force acting on the Stator model, Newtons	1071.23

equidistant points along the outside circumference of the stator models, and their locations are identified in Fig. 4.8. Since the forces are produced on the rotor teeth, the force-distribution is shown in terms of rotor tooth numbers in Fig. 4.8.c.

Since the magnetic flux produced under the north-pole is same as that under the south-pole, the important orders of the space-harmonics in the flux-density distribution will be of odd orders. They are of orders 3, 5, 7, etc. The 3^{rd} order space-harmonic will have three times the pairs of poles as that of the fundamental field, thereby it produces a force component that will induce n=6 mode of vibration. Similarly, the 5^{th} and 7^{th} order space-harmonic components will induce circumferential modes of n=10 and n=14, respectively. The deflections produced on the stator are inversely proportional to the 4^{th} power of the mode of vibration [13]. The magnitudes of the 3^{rd}, 5^{th}, and 7^{th} order space-harmonics are much smaller than the fundamental component. Therefore the effects of the space-harmonics in the force-distribution will be minimal, and they can be neglected.

The force acting on a rotor tooth is proportional to the square of the flux-density at the location of the tooth. Since the air-gap flux-density distribution consists of the fundamental and the various space harmonics, the force-distribution will have additional

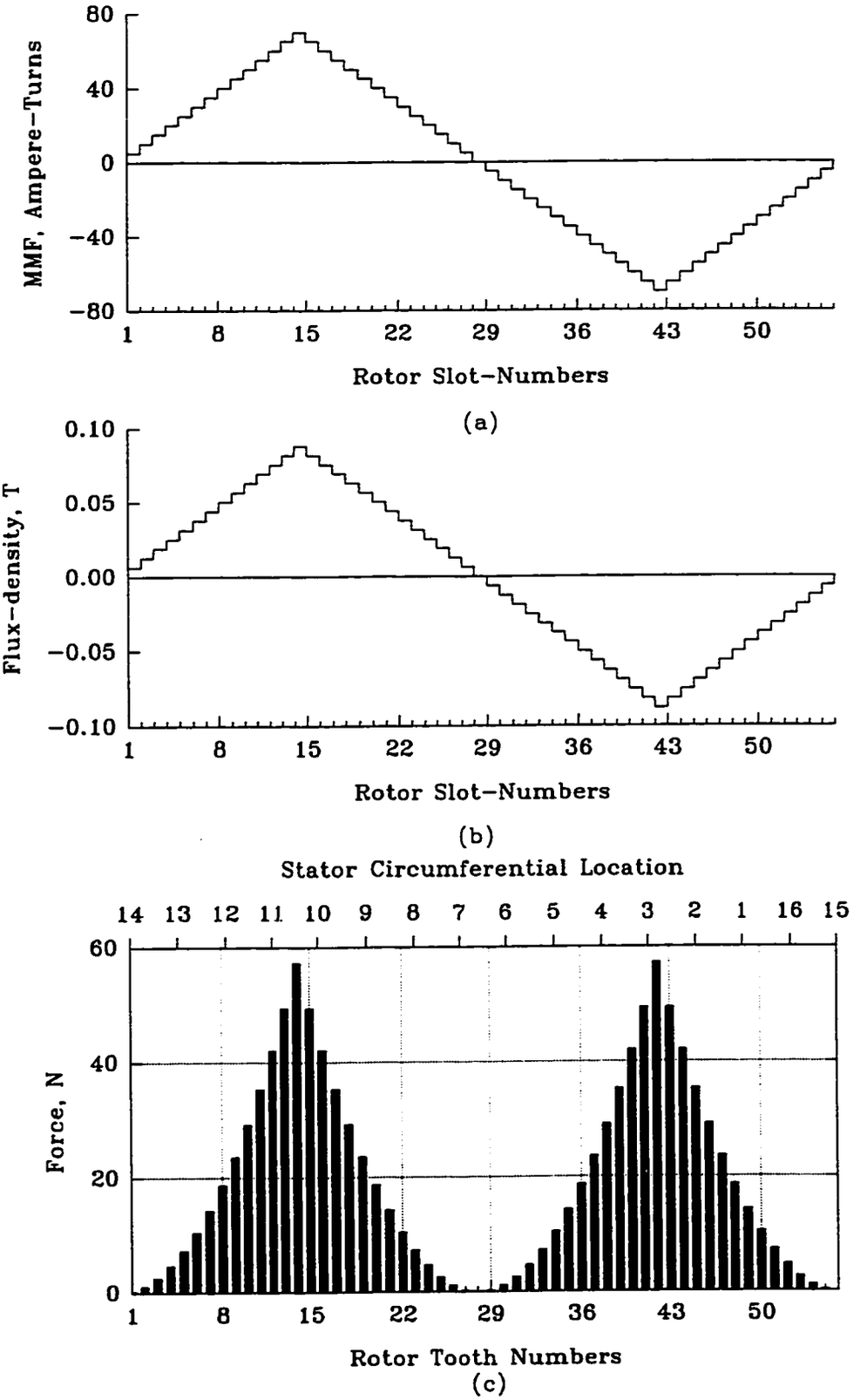

Figure 4.8 : Air-gap MMF, flux-density and radial force-distributions produced by the 2-pole winding.

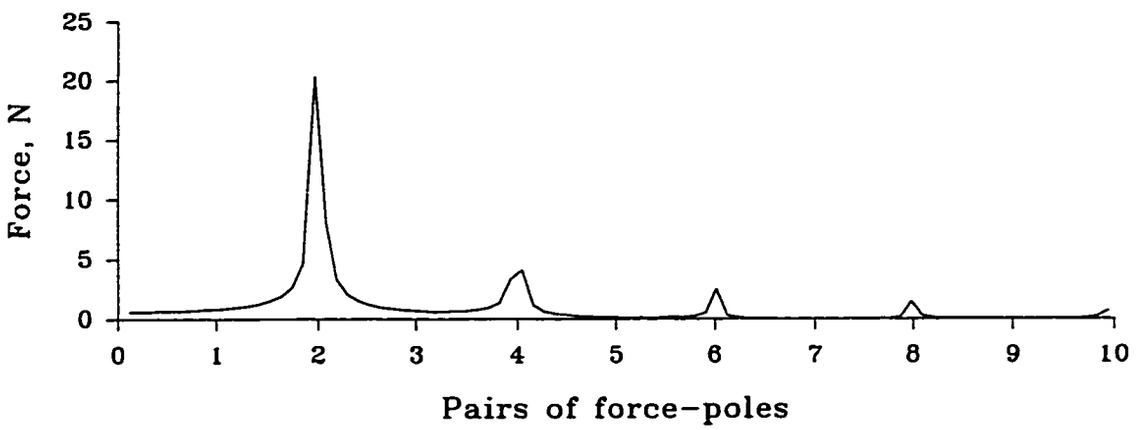

Figure 4.9 : Fourier components in the circumferential distribution of the pulsating forces produced by the 2-pole winding.

components corresponding to the interaction terms in the expansion of square function of the flux-density. The interaction between the fundamental and the space-harmonic flux-density components will produce force components with 4, 8, 10, etc., pairs of force-poles. Fig. 4.9 shows the Fourier components in the circumferential distribution of the forces. Further as explained in Appendix D, the pairs of force-poles correspond to the associated mode of operation.

4.5.2 Pulsating Forces for Mode n=4 Vibrations

The pulsating force-distribution required to induce the n=4 circumferential mode of vibration is obtained by energising the 4-pole winding from the single-phase supply. The force-distribution produced with this configuration is stationary, and forces that are produced pulsate at twice the frequency of the power supply. The various coil-groups of Fig. C2 are connected in series, and a current of 5 Amperes is maintained constant through the 4-pole winding while varying the frequency from 200 Hz to 5 kHz. This frequency range of the power supply provides a frequency range of 400 Hz to 10 kHz for the forces.

The important information for the operation of the 4-pole winding in this configuration is provided in Table 4.4. The air-gap MMF, flux-density and the

Table 4.4 : Salient calculated information for the 4-pole winding.

Salient Details of 4-Pole Winding	
Number of turns per coil	2
Number of coils connected in parallel per slot	24
Maximum value of the air-gap flux-density produced, Tesla	0.088
Total current drawn from the power supply, Amperes	5.0
Net terminal inductance of winding, mH	15.1
Maximum value of the force acting on the rotor tooth, Newtons	57.24
Force acting on the rotor teeth under a pole, Newtons	269.85
Total force acting on the Stator model, Newtons	1079.41

associated force-distribution were calculated and these are shown in Fig. 4.10. The circumferential distribution of the forces is also shown in polar co-ordinates in Fig. 4.10.d.

The Fourier components in the circumferential distribution of the forces produced by the 4-pole winding is shown in Fig. 4.11. It should be observed that the total force exerted on the stator in both the cases of modes n=2 and n=4 is kept approximately same. This ensures that the amount of total vibrational energy fed to the stator is virtually kept at the same level.

4.5.3 Pulsating Forces for Modes n=1 and n=3 Vibrations

Due to the constraints of space in the rotor slots, no separate winding arrangements were installed for producing a force-distribution with 1- or 3- force-poles. However as explained in Section 4.4.2, a combined excitation of existing 2-pole and 4-pole windings can be used to obtain the force-distribution necessary to induce n=1 and n=3 circumferential modes of vibrations. The coil-groups in the individual windings were connected in series. A current of 1.25 Amperes was maintained through the 2-pole winding, while the current through the 4-pole winding was maintained constant at

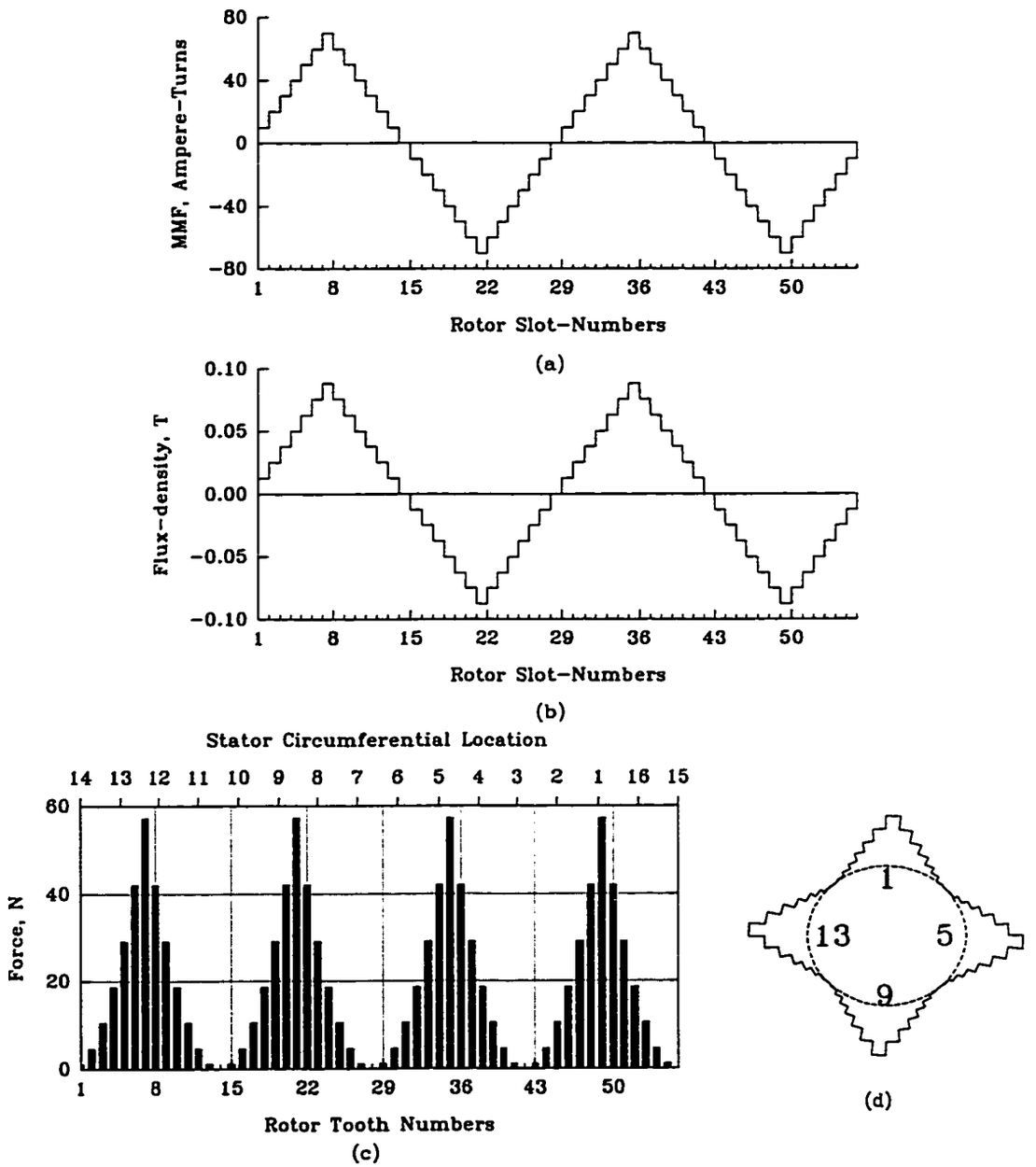

Figure 4.10 : Air-gap MMF, flux-density and radial force-distributions produced by the 4-pole winding.

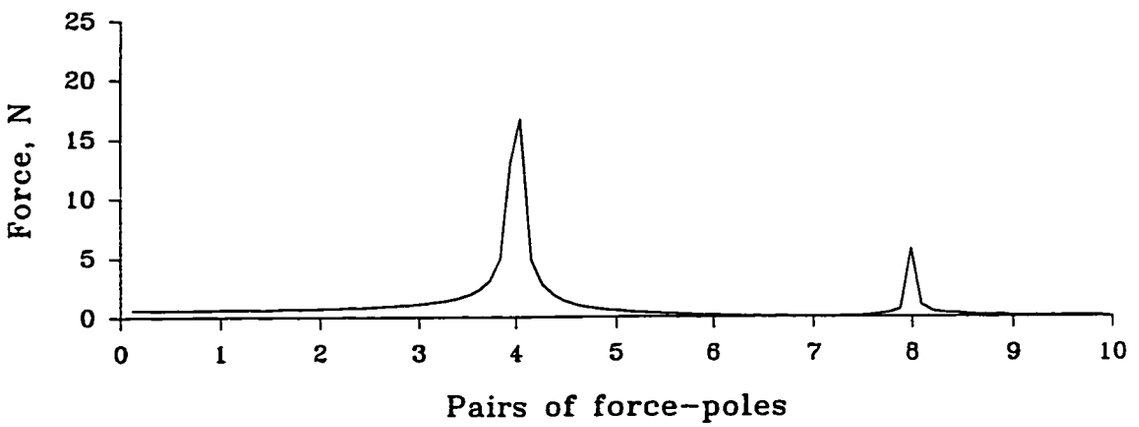

Figure 4.11 : Fourier components in the circumferential distribution of the pulsating forces produced by the 4-pole winding.

2.5 Amperes throughout the frequency range of 200 Hz to 5 kHz. The air-gap MMF, flux-density and force-distribution produced by the combined excitation of the 2-pole and 4-pole windings were calculated and these are shown in Fig. 4.12. Fig. 4.12.d shows the circumferential distribution of the forces in polar co-ordinates. Fig. 4.13 shows the Fourier components in the circumferential distribution of the forces. This arrangement produces force-distributions giving rise to mode n=1 and mode n=3 vibrations, having amplitudes of about 8 and 7 Newtons, respectively.

4.5.4 Rotating Forces for Mode n=2 Vibrations

The coils of the 2-pole winding were connected in a 3-phase configuration in order to produce a rotating force-distribution with 2 pairs of force-poles. The coils of the 2-pole winding is connected in accordance to the winding diagram provided in Appendix C, Fig. C4. The three phases are connected in star, and a current of 4.71 Amperes was maintained through each of the phases when the frequency of the supply is varied from 200 Hz to 5 kHz. The air-gap MMF, flux-density and the associated force-distribution were calculated and they are shown in Fig. 4.14. Again, the circumferential distribution of the forces is shown in polar co-ordinates in Fig. 4.14.d. The Fourier components in the circumferential distribution of the forces

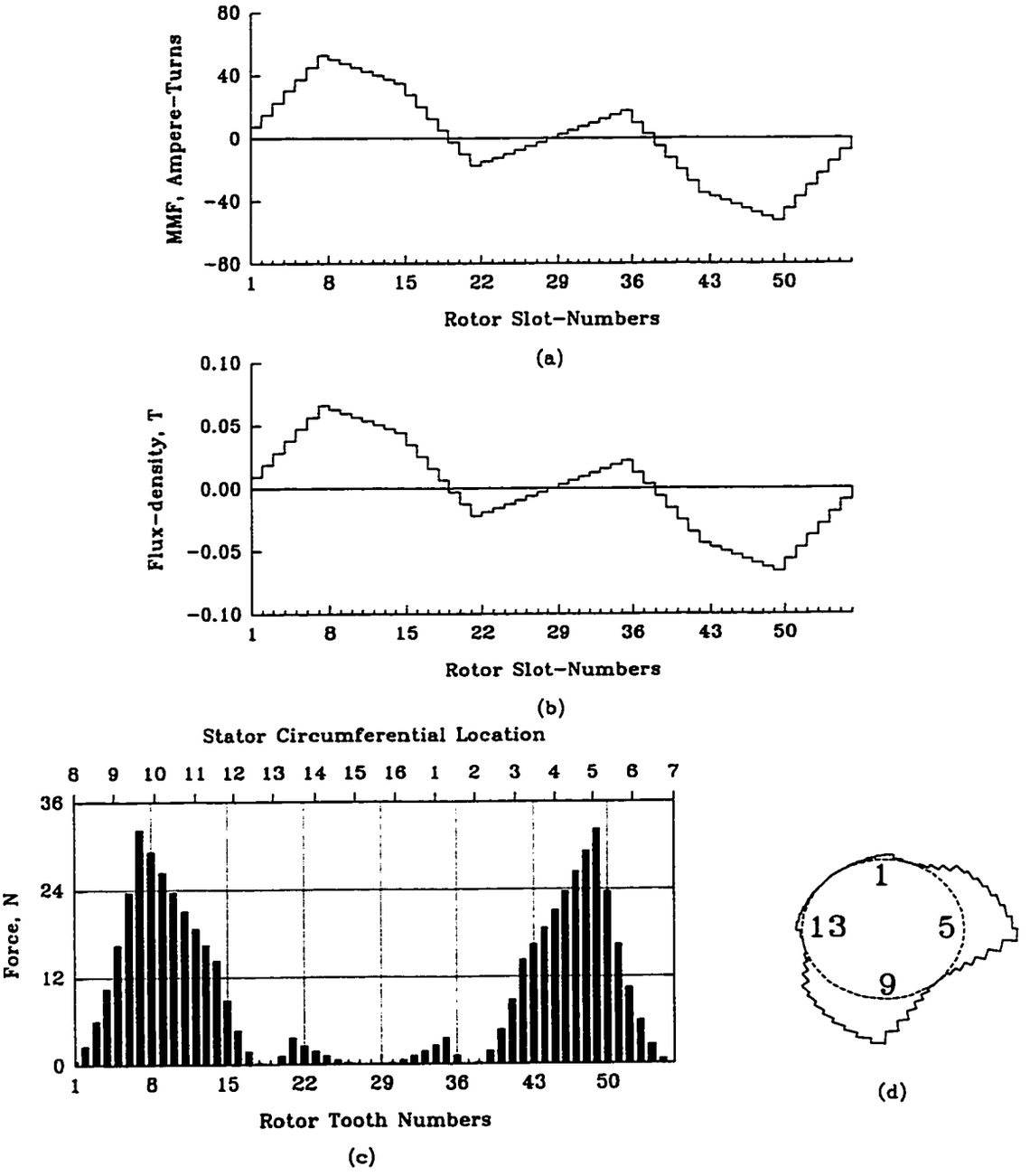

Figure 4.12 : Air-gap MMF, flux-density and radial force-distributions produced by the combined excitation of the 2-pole and 4-pole windings.

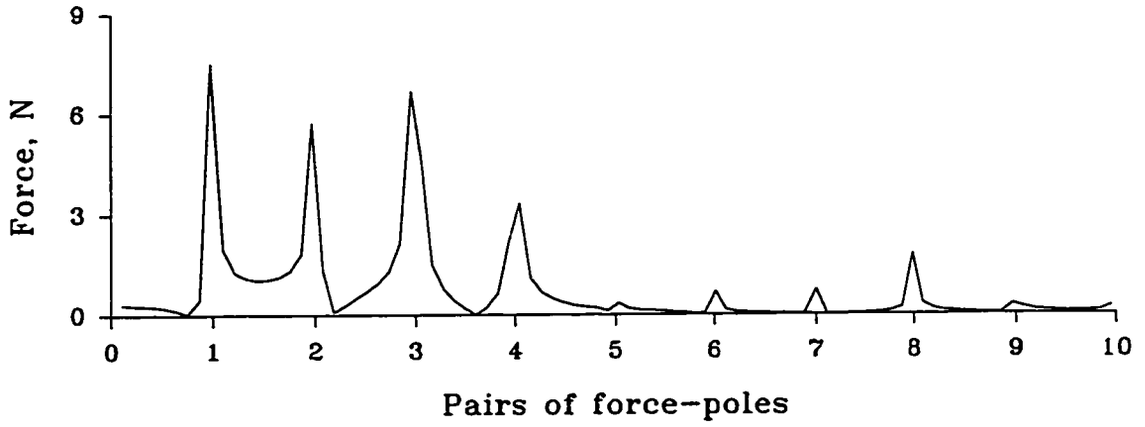

Figure 4.13 : Fourier components in the circumferential distribution of the pulsating forces produced by the combined excitation of the 2-pole and 4-pole windings.

produced by the 3-phase connections of the 2-pole winding are shown in Fig. 4.15. This arrangement produces a rotating force-distribution with 2 pairs of force-poles having an amplitude of 30 Newtons.

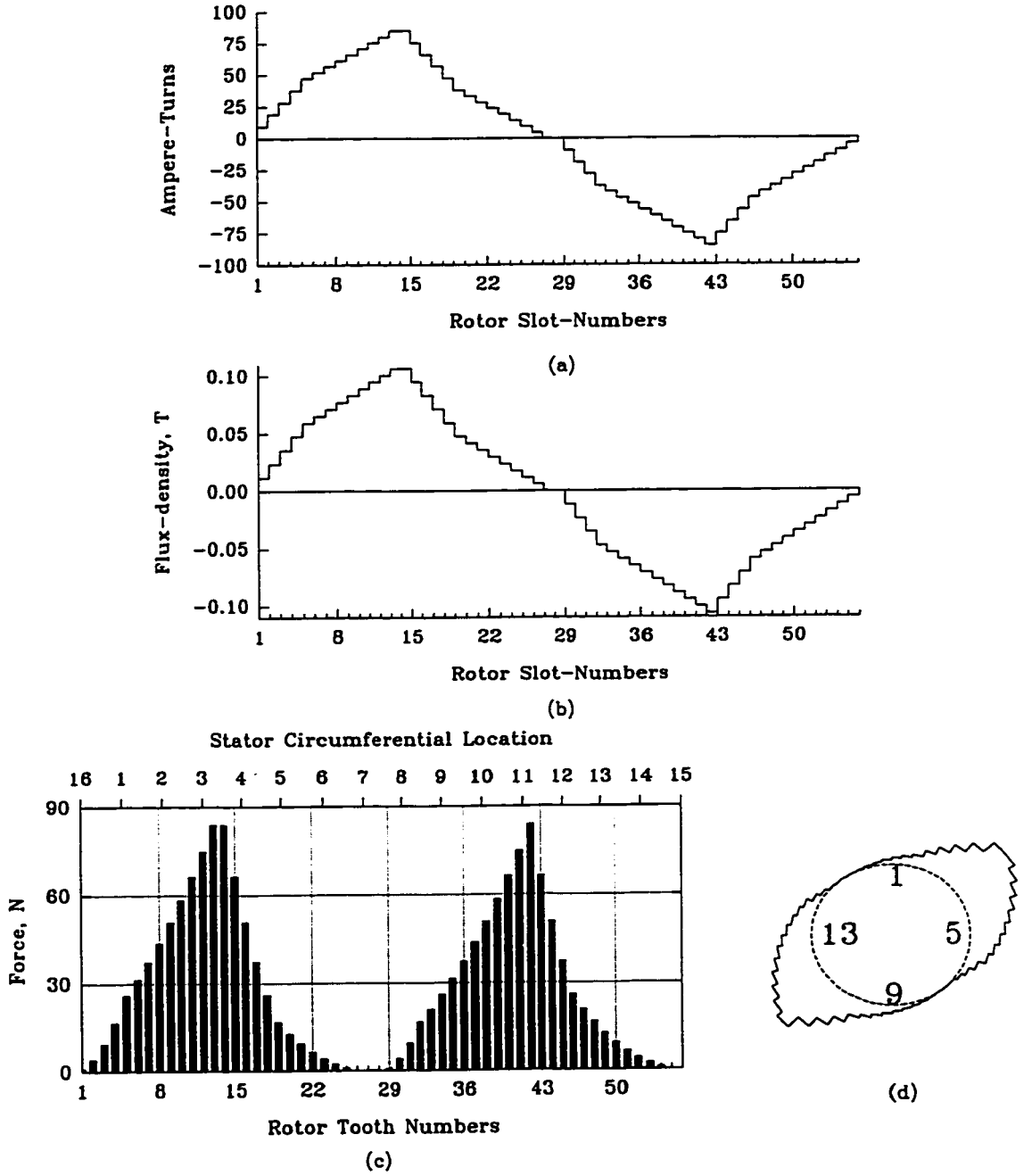

Figure 4.14 : Air-gap MMF, flux-density and radial force-distribution produced by the 2-pole winding when connected in a 3-phase configuration.

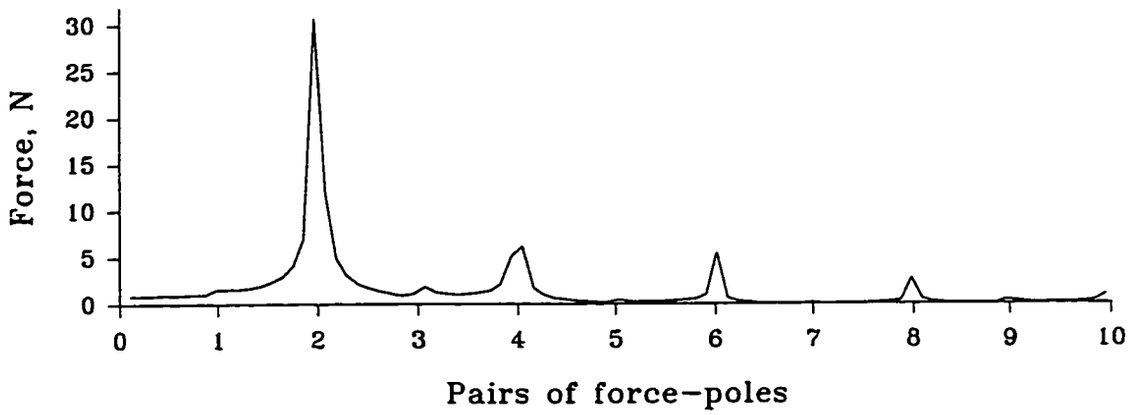

Figure 4.15 : Fourier components in the circumferential distribution of the rotating forces produced by the 2-pole winding.

4.6 Summary

In this chapter, the basis underlying the modal-analysis is described. To conduct a modal-analysis on the stator models of a 120 hp induction motor, force-distributions over the entire surface of the stator model are used. The desired force-distributions are achieved by electromagnetic excitation of specially designed windings. The experimental arrangements involve the design and construction of a rotor which houses a 2-pole and a 4-pole winding. The electromagnetic forces produced have distributions which help in selectively exciting resonances of the stator models. Using the experimental set-up described in this chapter it is possible to induce vibrations of modes n=0, 1, 2, 3, and 4 in the stator models. In the next chapter, the results of the experimental investigations on the vibration behaviour of the two stator models using the distributed electromagnetic forces are described.

5. EXPERIMENTAL INVESTIGATIONS ON THE VIBRATION BEHAVIOUR OF THE INDUCTION MOTOR STATOR MODELS

The experimental results of the investigations conducted on the 120 hp induction motor stator models using impulse and distributed electromagnetic forces are presented in this chapter. Additionally, the resonances of the rotor structure were determined using a magnetic shaker, and these investigations are reported in detail in Appendix E. In Chapters 2 and 3, the spectra of force-components for squirrel-cage and wound-rotor induction motors were presented. It was observed that a multitude of force-components were present at the various frequencies. To keep the analysis simple and manageable, it is often necessary to identify the significant force-components with respect to their ability in inducing vibrations in the stator of an electrical machine. The important attributes of the various force-components are their amplitudes, circumferential distribution and the frequencies at which they occur. The importance of these aspects are closely examined in this chapter.

As explained earlier, it is not possible to avoid excitation of all the resonances of the machine structure under certain operating conditions, in particular the variable frequency operation. In general, it is only when resonances are excited which produce high levels of vibrations creating the vibration and noise problems. One of the objectives of these investigations is to find the importance of the force-distribution on the vibration behaviour at a resonance. It, therefore, involves an examination of the correlation between the circumferential distribution of the forces and the circumferential mode of vibration associated with the resonance.

In the modelling of vibration systems, it is essential to know the damping present in the system under investigation. It is often difficult to theoretically model the amount and type of damping present in practical structures. Hence, one has to frequently resort to the experimental information. For the accurate experimental determination of damping, ideally it is required to excite the vibrating structure at each of its resonances

individually. Since each resonance of a practical structure is associated with different circumferential and longitudinal modes of vibration, the selective excitation is of benefit and it is possible with the use of the distributed electromagnetic forces described in the previous chapter.

5.1 Vibration Response of the Stator-Shell Model

The first model tested under the various force-distributions is the smooth stator-shell model, which has been described in the previous chapter. From the perspective of vibration analysis, the stator-shell is a simple model which permits the desired experimentation with considerable ease. Since the stator-shell model is a solid steel structure, the damping present in this structure would be small. The resonance peaks in the vibration response are expected to be distinct and the amount of force required to dominantly excite the structure at the resonances would be small.

5.1.1 Impulse Response

The impulse response of the stator-shell model was measured by striking the model lightly at a location on the centre-plane. The ensuing vibrations were also measured on the centre-plane. All the resonances with anti-symmetric longitudinal modes of vibrations, i.e. m=1,3,5, . . ., will have a node of vibration on the centre-plane of the model, while the resonances with axi-symmetric longitudinal modes will have an anti-node on the centre-plane of the stator-shell. Further, the circumferential location of the excitation and also the measurement location are so chosen that they would be near an anti-node of vibration for all the axi-symmetric resonances. Using a Fourier-analysis of the measured signal, the spectral composition of the vibration acceleration is determined. The impulse response of the stator-shell model when it was excited and measured on the centre-plane is shown in Fig. 5.1. The amplitudes of acceleration levels are plotted on a logarithmic scale versus frequency. The acceleration amplitudes are shown in mm/sec^2, and also in dB relative to 10^{-2} mm/sec^2.

The resonances of the stator-shell model were investigated in detail and the experimental results were obtained using the point-excitation technique by the authors in references [51,53]. The impulse response technique is an elegant and fast procedure,

and it provides good results for lightly damped structures [43]. The response of any vibration system to an impulse excitation will be to excite all its significant resonances. The various peaks in the impulse response, therefore, correspond to the resonances of the stator-shell model. These peaks correspond very well to the resonances reported by the authors in references [51,53]. Table 5.1 lists the resonances of the stator-shell model investigated in this study. These resonances are selected such that they represent resonances of circumferential modes n=0 to 5. Further, for each of the circumferential modes of vibration an axi-symmetric and an anti-symmetric resonances are chosen. The various peaks of interest in the impulse response are identified according to the item serial numbers given in Table 5.1. As expected, it is evident from the impulse response shown in Fig. 5.1 that the axi-symmetric resonances of the stator-shell model are quite pronounced, i.e. resonances corresponding to items # 1, 4, 6, 7, 9 and 11.

Table 5.1 : Selected resonances and associated modes of the stator-shell model.

S.No.	Frequency, Hz	Circumferential mode, n	Longitudinal mode, m	Type
1	1242	2	0	Axi-symmetric
2	1432	2	1	Anti-symmetric
3	3032	1	1	Anti-symmetric
4	3197	3	0	Axi-symmetric
5	3432	3	1	Anti-symmetric
6	3456	1	2	Axi-symmetric
7	3942	0	0	Axi-symmetric
8	4154	0	1	Anti-symmetric
9	5513	4	0	Axi-symmetric
10	5729	4	1	Anti-symmetric
11	8012	5	0	Axi-symmetric
12	8193	5	1	Anti-symmetric

Fig. 5.2 shows the impulse response of the stator-shell model when it was excited on an off-centre plane. In this case, the vibration measurements are made away from the centre-plane of the shell. Here, resonances with both axi-symmetric and anti-symmetric longitudinal modes are excited well. The resonant peaks of interest are again identified according to Table 5.1.

5.1.2 Response to 2 Pairs of Force-Poles Pulsating Force Excitation

The stator-shell model was excited using the force-distribution produced by the 2-pole winding when it was energised from a variable-frequency single-phase supply. The vibration measurements were made on the centre-plane and also on an off-centre plane. The corresponding spectra of the measured vibration acceleration signals are shown in Figs. 5.3 and 5.4, respectively. The spectra are plotted in similar manner as that of the impulse response. The various resonant peaks are again identified according to Table 5.1. The amount of vibrational energy injected into the stator-shell with the distributed electromagnetic forces is much higher than that injected with the impulse excitation. Consequently, the vibration accelerations measured are about 20 dB or ten times greater than those measured using the impulse excitation.

One of the benefits of inducing higher levels of vibrations in the stator model is that the resonance peaks are very well defined and their peak amplitudes are much greater than the ambient noise present in the acceleration signal. Further, as expected the peaks corresponding to the anti-symmetric resonances # 2,3,5,8,10 and 12 have very small amplitudes when the measurements are made on the centre-plane. These anti-symmetric resonances have significantly higher amplitudes when measured on the off-centre plane, except for anti-symmetric resonance #12 which had a node of vibration close to the measurement location. In general, it is observed from the spectra of Figs. 5.3 and 5.4 that in this excitation configuration the resonances associated with circumferential modes of 0, 2, and 4 are excited well. The resonance peaks corresponding to modes n=1, 3 and 5 have relatively smaller amplitudes. More detailed comparisons of the various spectra are provided later in this chapter.

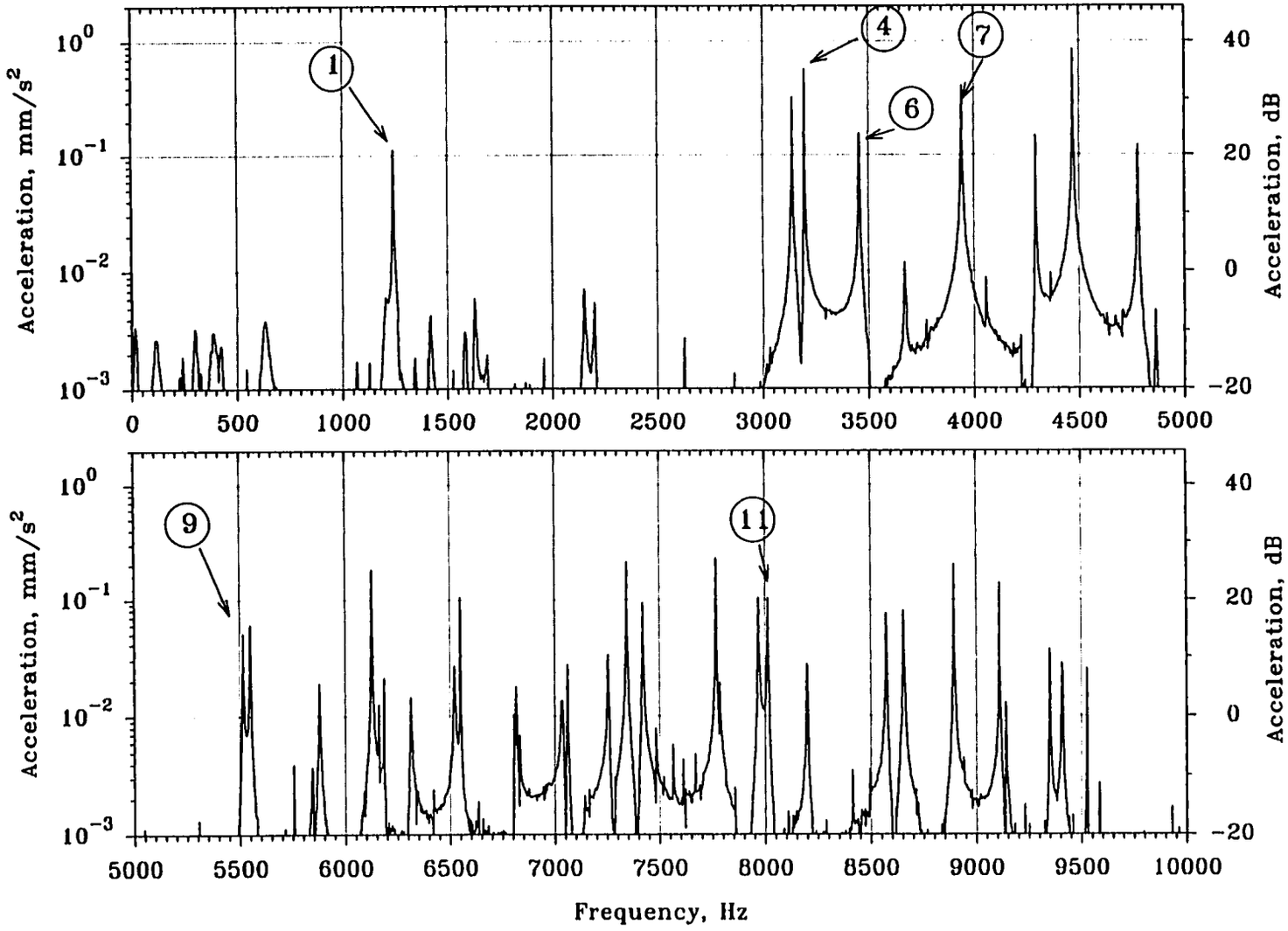

Figure 5.1 : Impulse response of the stator-shell model measured on a centre-plane.

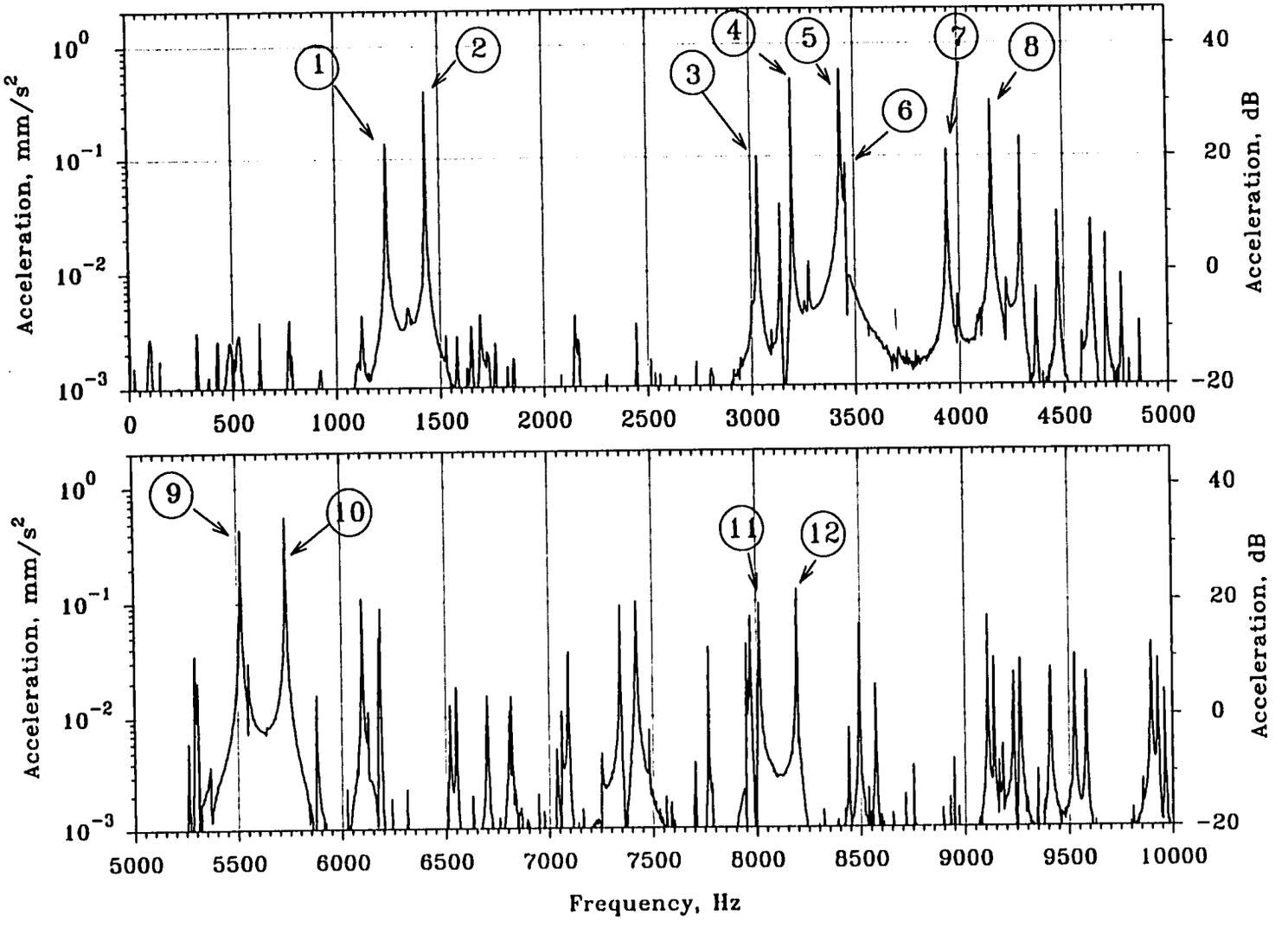

Figure 5.2 : Impulse response of the stator-shell model measured on the off-centre plane.

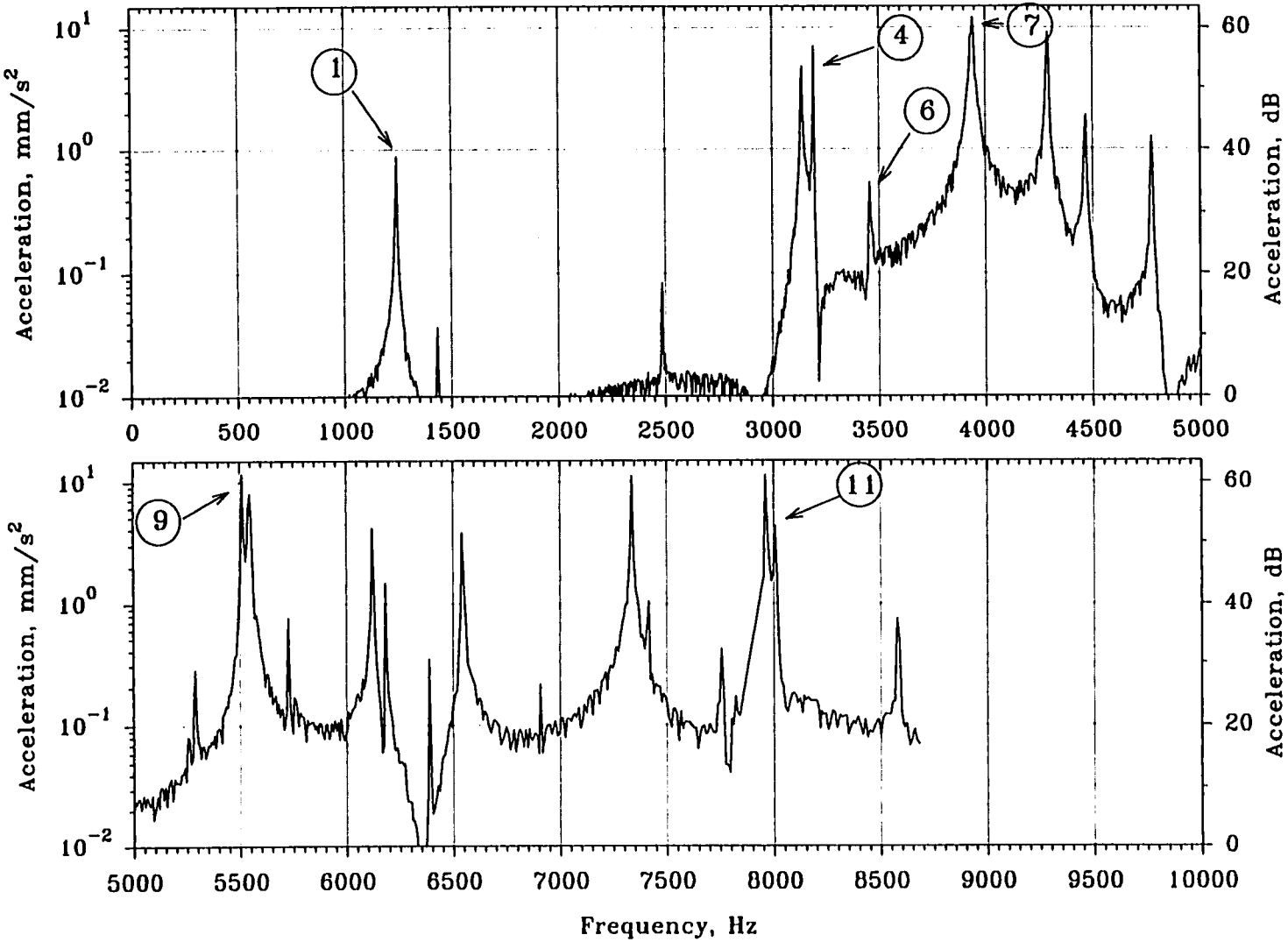

Figure 5.3 : Vibration response of the stator-shell model to a 2 pairs of force-poles pulsating force measured on a centre-plane.

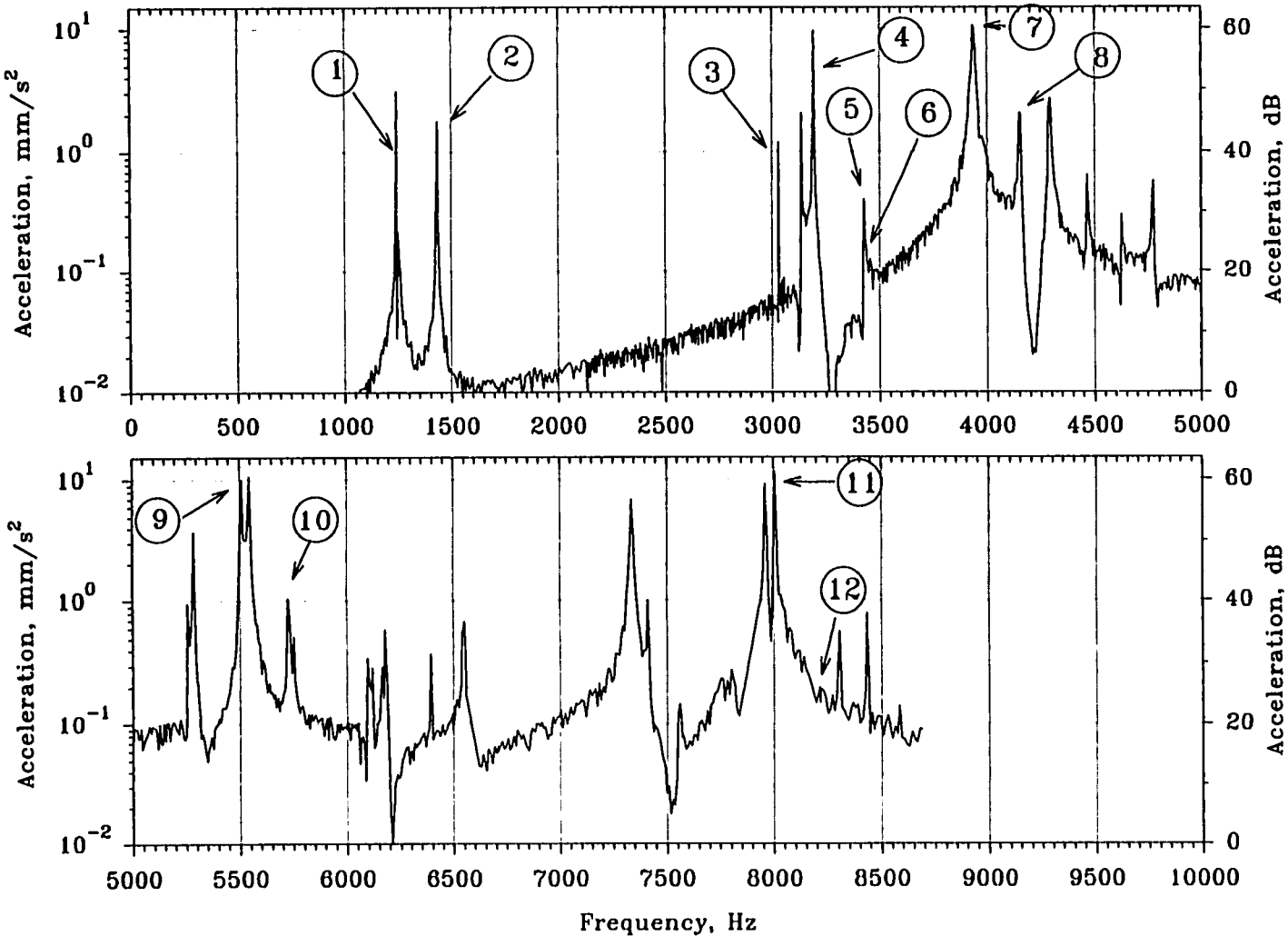

Figure 5.4 : Vibration response of the stator-shell model to a 2 pairs of force-poles pulsating force measured on the off-centre plane.

5.1.3 Response to 4 Pairs of Force-Poles Pulsating Force Excitation

Vibration measurements were made on the stator-shell model when it was excited using the 4 pairs of force-poles pulsating force-distribution, which was produced by energising the 4-pole winding from a single-phase variable-frequency supply. Again, the vibration measurements were made on the centre-plane and also on an off-centre plane. The corresponding spectra of the measured vibration acceleration signals are shown in Figs. 5.5 and 5.6, respectively. These spectra are plotted similar to the earlier plots, and the various peaks have been identified.

Comparing the spectra of the induced vibrations in Figs. 5.5 and 5.6 with those measured using the 2-pole winding, i.e. Figs. 5.3 and 5.4, the following observations are made:

(i) It is observed that the ambient level of vibrations at frequencies away from the resonance peaks has increased. For the frequency range of 1500 Hz to 3000 Hz, the vibration levels measured using the 4-pole winding are about 20 dB higher.

(ii) As expected, the vibration levels at the resonance peaks corresponding to circumferential modes n=0 and 4 are prominent. It is interesting to note that in this excitation configuration, the resonances corresponding to n=3 and n=5 circumferential modes of vibration are excited better than with the 2-pole winding. In comparison to the previous case, some of the peaks in these two spectra are flattened.

5.1.4 Response to 1 and 3 Pairs of Force-Poles Pulsating Force Excitation

Vibration measurements were also made on the stator-shell model when it was excited using the 1 and 3 pairs of force-poles pulsating force-distributions which were produced by energising the 2-pole and 4-pole windings simultaneously from a single-phase variable-frequency supply. Here again, the vibration measurements were made on the centre-plane and also on an off-centre plane. The corresponding spectra of the measured vibration acceleration signals are shown in Figs. 5.7 and 5.8, respectively. These spectra are plotted in the same manner as the earlier plots, and the various peaks have been identified.

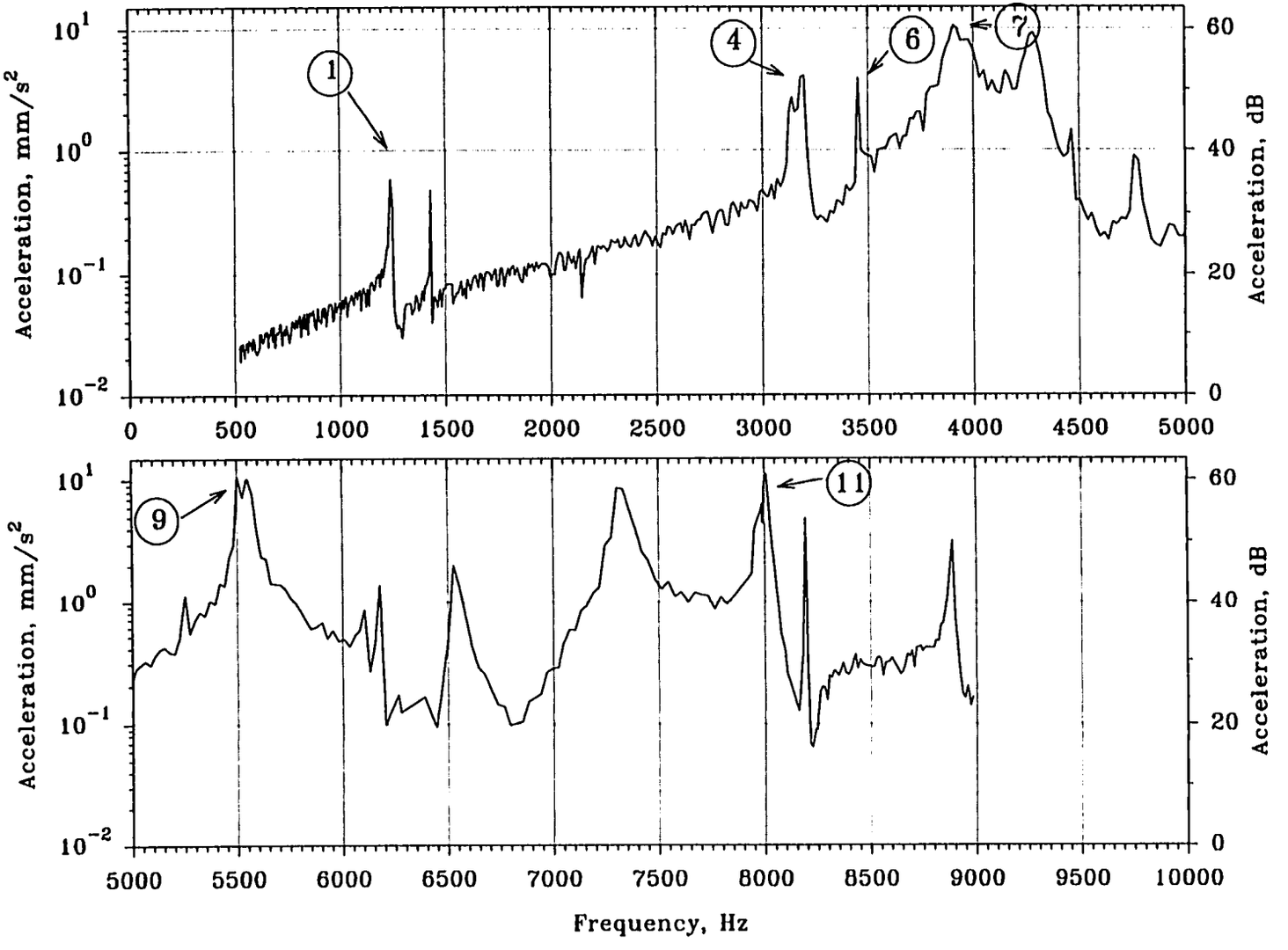

Figure 5.5 : Vibration response of the stator-shell model to a 4 pairs of force-poles pulsating force measured on a centre-plane.

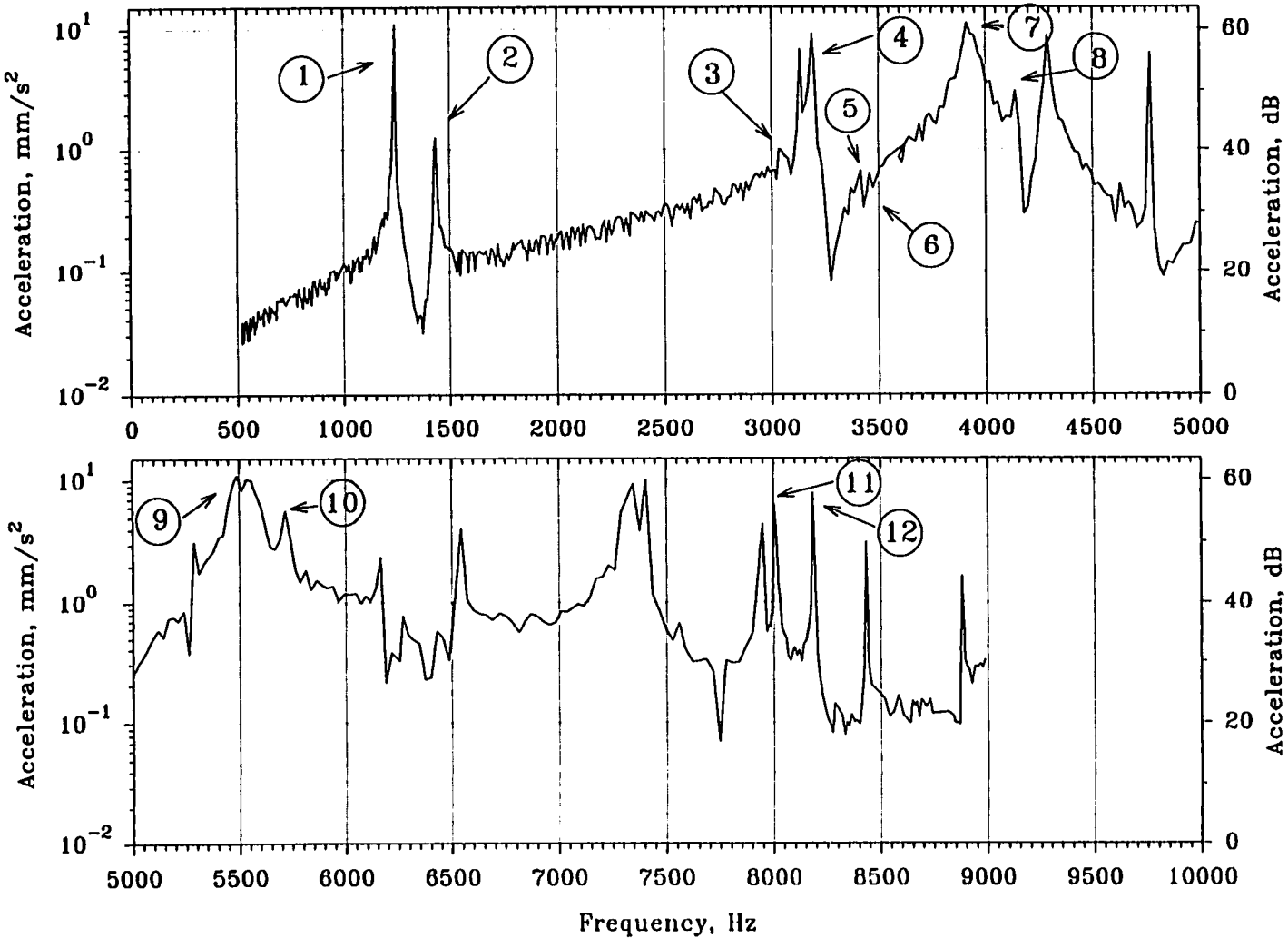

Figure 5.6 : Vibration response of the stator-shell model to a 4 pairs of force-poles pulsating force measured on the off-centre plane.

Comparing the spectra of the induced vibrations shown in Figs. 5.7 and 5.8 with those measured using the 2-pole and 4-pole windings, i.e. Figs. 5.3, 5.4, 5.5 and 5.6, the following observations are made:

(i) It is observed that the ambient level of vibration at frequencies away from the resonance peaks are similar to those measured with the 2-pole winding arrangement.

(ii) As expected, the resonances corresponding to circumferential modes n=0, 1 and 3 are prominently excited. In this excitation configuration, the resonances corresponding to mode of n=5 vibrations are also very well excited. However, since the force-distribution produced by using this arrangement has Fourier-components corresponding to 2 and 4 pairs of force-poles, the resonances with n=2 and n=4 modes of vibration are also excited.

5.1.5 Response to 2 Pairs of Force-Poles Rotating Force Excitation

In order to examine the effect of rotation of the force-distributions on the vibration response of the stator-shell model, the shell model was excited using the 2-pole winding when it was connected in a 3-phase configuration. The predominant force component produced using this arrangement has 2 pairs of force-poles and it rotates in the air-gap at the synchronous speed corresponding to the frequency of the 3-phase supply. Since the frequency of the 3-phase oscillator in the power supply had to be manually changed, these tests were conducted only in the frequency range of the selected resonances. These plots are shown later in the chapter while discussing the damping present at each of the selected resonances.

5.1.6 Comparison of Vibration Amplitudes at the Resonances

In all the spectra shown earlier, the accelerometer was placed at a fixed location while varying the excitation signal through the frequency range of interest. A judicious choice was made to keep the accelerometer away from a node of vibration. In order to measure the maximum values of vibration amplitudes at the resonances, the accelerometer was moved around the periphery of the stator-shell model to measure the vibration acceleration levels at an anti-node of the vibration. The acceleration levels

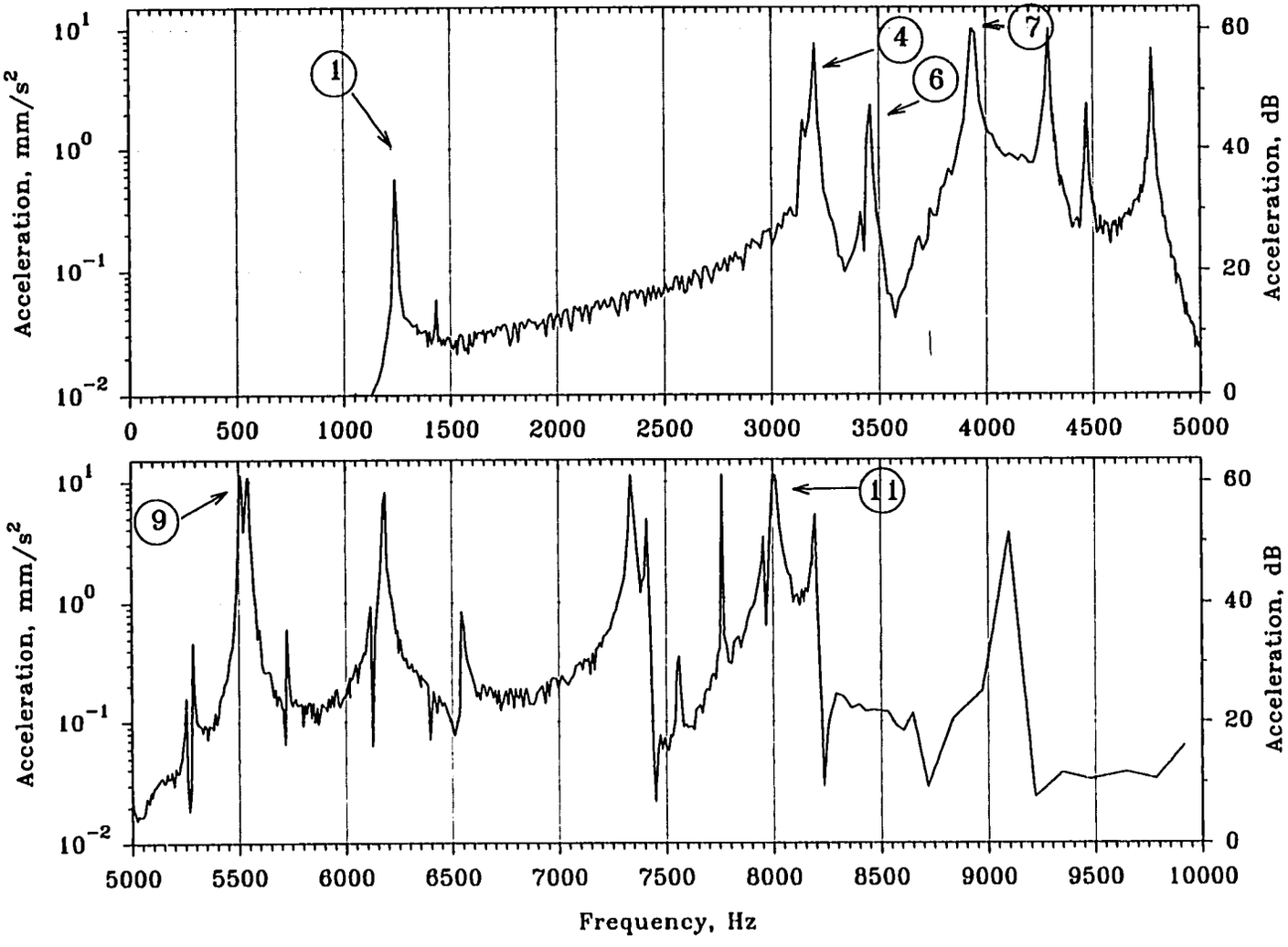

Figure 5.7 : Vibration response of the stator-shell model to a combined 1 and 3 pairs of force-poles pulsating force measured on a centre-plane.

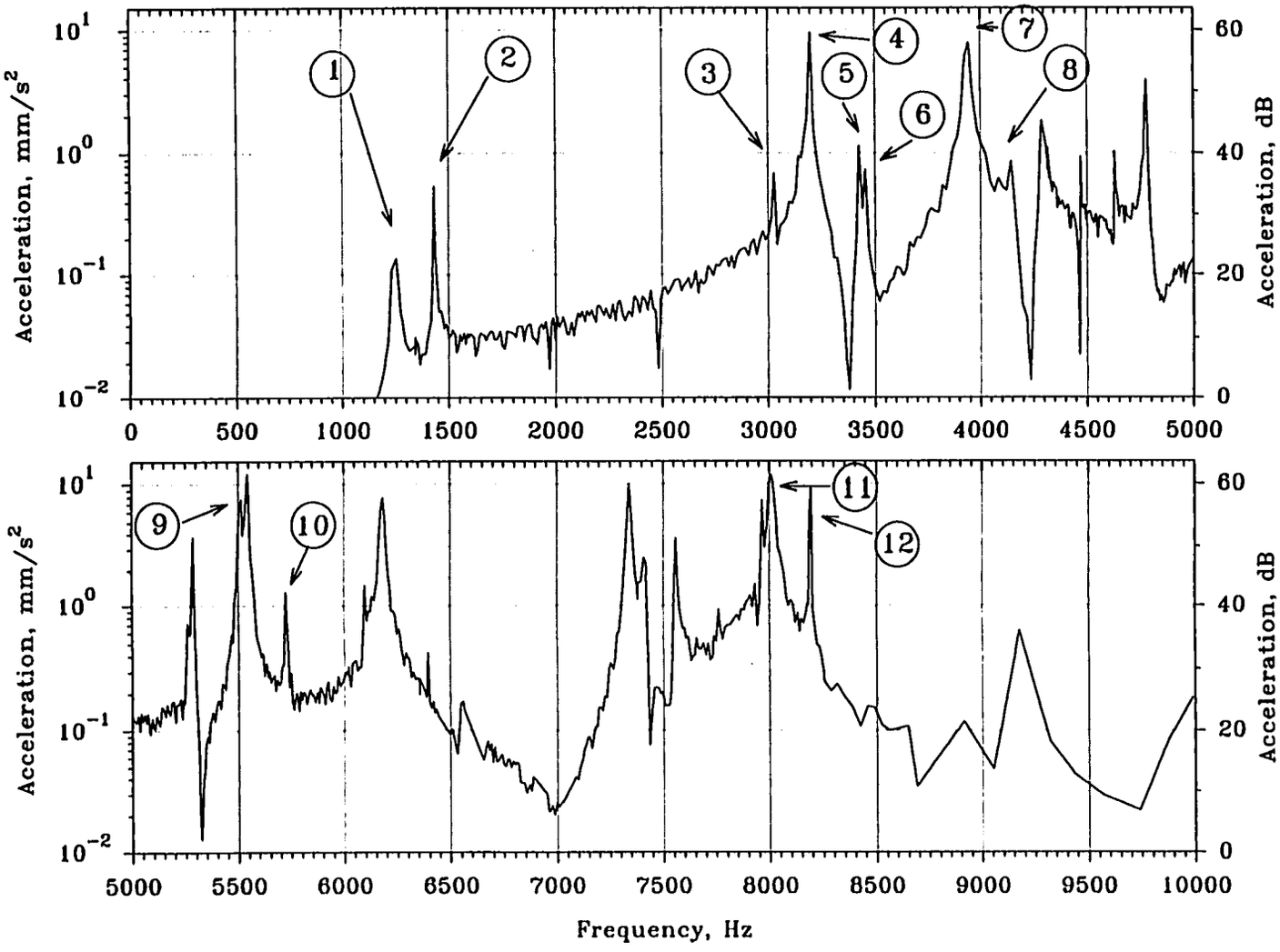

Figure 5.8 : Vibration response of the stator-shell model to a combined 1 and 3 pairs of force-poles pulsating force measured on the off-centre plane.

measured are provided in Table 5.2 in dB relative to 0.01 mm/sec^2. Using the analysis provided in Chapter 4, the calculated values of the total, maximum and average forces that act on the stator-shell model are also provided in Table 5.2. The vibrational force acting on the stator-shell model for the pulsating force-distributions with 2 and 4 pairs of force-poles are similar. However, it should be noted that they are different for the combined excitation of the windings and 3-phase operation of the 2-pole winding.

Although the amplitudes of pulsating force-distributions with 2 and 4 pairs of force-poles are almost identical, it is observed that the maximum acceleration levels measured with the 4 pairs of force-poles are higher in most cases by about 10 to 15 dB.

Table 5.2 : Maximum values of acceleration measured in dB relative to 0.01 mm/sec^2 at selected resonances of the stator-shell model using different electromagnetic force-distributions.

Freq., Hz	**n**	**m**	**2 pairs of force-poles**	**4 pairs of force-poles**	**1 & 3 pairs of force-poles**	**2 pairs of force-poles**
Force type			Pulsating	Pulsating	Pulsating	Rotating
Total force, N			1071.23	1079.41	537.66	1600.00
Maximum force, N			57.24	57.24	32.20	83.97
Average force, N			19.13	19.28	9.60	28.57
3942	0	0	57.1 dB	73.4 dB	60.6 dB	56.0 dB
4154	0	1	30.0	42.2	36.3	34.0
3456	1	2	24.4	37.9	44.5	33.8
3032	1	1	21.6	27.9	29.9	15.9
1242	2	0	27.4	31.1	27.9	43.6
1432	2	1	25.4	35.3	23.4	36.3
3197	3	0	28.2	56.1	61.3	50.0
3432	3	1	15.9	15.4	36.6	31.0
5513	4	0	38.4	65.3	53.9	67.6
5729	4	1	28.6	41.4	32.5	47.0
8012	5	0	47.3	62.3	63.0	43.9
8193	5	1	*	*	*	29.2

* : could not be measured, (n = circumferential mode, m = longitudinal mode).

The difference is almost twice for the mode n=4 resonance at 5513 Hz. Interestingly, the maximum values of the accelerations measured at the mode n=2 resonances of 1242 Hz and 1432 Hz were higher with the pulsating force-distribution of 4 pairs of force-poles. The other resonance which was significantly excited by the force-distribution with 4 pairs of force-poles is the mode n=3 resonance at 3197 Hz.

The total force associated with the combined excitation of the 2-pole and 4-pole windings is roughly one-half, in comparison, that acts on the stator-shell model. As explained in Chapter 4, the force-distribution produced in this case has Fourier-components with 1, 2, 3, and 4 pairs of force-poles. Therefore, it is expected that most of the resonances of the stator-shell will be well excited. With this arrangement, pronounced increases in the acceleration levels were observed at the mode n=1 resonances of 3456 Hz and 3032 Hz, and also at the mode n=3 resonances of 3197 Hz and 3432 Hz. The maximum vibration accelerations at modes n=1 and n=3 resonances are at least 6 dB or twice the values obtained with other force-distributions.

The 3-phase operation of the 2-pole winding produces a much higher total force in the stator-shell model. The prominent Fourier-components associated with this force-distribution have 2, 4, and 6 pairs of force-poles. As shown in Chapter 4, the fundamental component with 2 pairs of force-poles is the dominant one. At the mode n=2 resonances of 1242 Hz and 1432 Hz, this force-distribution induced high levels of vibrations. Surprisingly, this force-distribution was equally effective in inducing the mode n=4 vibrations at 5513 Hz and 5729 Hz. Also, this force-distribution was able to induce the n=1 and n=3 modes of vibrations.

At the mode n=0 resonances of 3942 Hz and 4154 Hz, as expected, all the force-distributions gave rise to significantly high levels of vibrations. For the circumferential mode n=5, the resonance at 8012 Hz was excited well by the combined 2-pole and 4-pole winding arrangement, and also the pulsating force-distribution with 4 pairs of force-poles.

In general, all the force-distributions were able to excite the resonances of the stator-shell model irrespective of the type of the associated circumferential mode. The measured values of the maximum acceleration levels were significantly higher for force-distributions with pairs of force-poles that matched the circumferential mode of

vibrations. It was observed that there is significant coupling between the force-distributions with 4 pairs of force-poles and the mode n=2 vibrations, and vice-versa.

5.1.7 Damping-Ratios at the Various Resonances

All mechanical structures, including electrical machine stators and rotors, have many built-in mechanisms for dissipating the vibrational energy. Often damping prevents extraneously excited vibrations from being noticed, and the importance and need for damping is frequently not recognised. As advances are made towards building efficient light-weight structures, some of the damping normally present in the structure is inadvertently eliminated. Hence the damping mechanisms need to be studied and efforts be made to incorporate more damping in these re-designed structures in a more reliable and cost-effective way [54].

Damping in mechanical structures appear in many forms such as viscous, hysteresis, frictional, Coulomb's, etc. The properties of the damping mechanisms differ from each other, and not all of them are equally suitable to mathematical formulation. Fortunately, small amount of damping has very little influence on the resonant frequencies, which are normally calculated by neglecting the effects of damping. However, in calculating the response under forced-vibration it is necessary to include the damping effects. Often one has to resort to experimental information to determine the damping present in practical structures.

The present experimental set-up and the measurement techniques permit the calculation of the damping-ratio associated with each mode of vibration with more accuracy and simplicity. The amount of damping present at a particular mode is derived from the amplitude response curve at the resonance. Damping is determined from the sharpness of the peak, and it is normally measured in terms of the Loss-Factor given by the ratio:

$$\zeta = \frac{\omega_2 - \omega_1}{2\,\omega_0}, \tag{5.1}$$

where ω_0 is the natural frequency, and ω_1 and ω_2 are frequencies on either side of the natural frequency where the peak amplitude is reduced by 3 dB, and ζ is called the damping-ratio. To eliminate any interference from other near-by resonances, a "least-

error square curve-fit" is used through the experimental data points to obtain the damping-ratio. The damping model, which is general enough to cover the viscous, hysteresis and frictional damping, is used for the curve fitting procedure [55].

Theoretically, the damping-ratio ζ is defined as the ratio of the damping present in the vibrating structure at a resonance to the critical damping associated with that resonance [49]. It is mathematically expressed as:

$$\zeta = \frac{c}{c_c} = \frac{c}{2\sqrt{km}} = \frac{c}{2m\omega_0}, \tag{5.2}$$

$$\therefore c = \zeta \cdot (2m\omega_0),$$

where c_c is the critical damping, m is the mass of the vibrating structure and ω_0 is the undamped natural frequency of vibration. The equations of motion provided in Eqn. 4.1, Chapter 4, are written in terms of the damping-coefficient c. Using Eqn. 5.2, the damping-coefficients associated with the various resonances can be determined from the measured damping-ratios.

The amplitude response at the selected resonances of the stator-shell are shown in Figs. 5.9 to 5.13. The damping-ratio is estimated using the vibration response of the stator-shell to different excitation force-distributions. The damping-ratios corresponding to the various resonances of the stator-shell model are listed in Table 5.3. It is seen from Table 5.3 that the damping-ratios measured using electromagnetic forces are much greater than that obtained using impulse (hammer) excitation. It is well-known that when a cyclic magnetic field is applied to a ferromagnetic material, some of the energy supplied is transformed into heat through the phenomenon of eddy-current losses, magnetic hysteresis losses and losses through mechanical deformations. Mechanical stress and magnetic fields have a similar effect on the movement of the magnetic-domains through the property of magnetostriction such that the cycles of stress result in magneto-mechanical hysteresis. Adams [54] has shown that the magneto-mechanical energy dissipation per cycle varies as σ^n, where σ is the cyclic stress and n is a constant ranging from 3.27 to 8.78 for commonly used steels. The magneto-mechanical hysteresis effect is responsible for the significant difference in the damping-ratios between those measured using impulse excitation and using electromagnetic forces.

Since the stator shell is a homogenous steel structure, the damping present in it is very small. Although measurement of damping in such lightly damped structures is often associated with experimental difficulties, considerable effort was made to keep the measurement errors as small as possible. Due care was taken to obtain sufficient number of data points to construct the vibration response curves. In the case of impulse response, the sampling frequency and the number of data samples measured were chosen such that the vibration levels are obtained at intervals of 2 Hz. For the single-phase pulsating force-distributions, a beat-frequency oscillator was used. As explained in Chapter 3, the oscillator is linked mechanically to an external drive in order to vary its frequency. Further since the frequency of the oscillator varies on a logarithmic scale, even with very low drive-speeds, the frequency of the oscillator varied in fairly big steps. This resulted in limiting the data points required for the construction of the response curves at different frequencies. In the case of the rotating force arrangement, the frequency of the 3-phase oscillator had to be varied manually due to inherent difficulties of the oscillator-circuits.

In Figs. 5.9 to 5.13, it is seen that the resonant frequency drifts by a few Hertz, which indicates the presence of damping other than hysteresis damping. The drift of resonant frequency could also be due to the differential influence of the neighbouring resonances. Another factor which contributes to the variation of the damping-ratio is the temperature-rise of the stator-shell. During the tests conducted using the distributed electromagnetic forces, it was not possible to prevent the stator-shell from getting warm. Although the stator-shell was cooled using a forced draft from a fan, the model got much warmer when excited using 4 pairs of force-poles pulsating force and the 2 pairs of force-pole rotating force-distributions as compared to the other electromagnetic force-distributions. In general, raising the temperature causes a reduction in the damping [54].

Fig. 5.9 shows the measured vibration response to the various excitation arrangements at 3942 Hz. Since this resonance is associated with n=0 and m=0 modes of vibrations, all the excitation arrangements excite this resonance effectively. The damping-ratios determined using the various excitation systems are provided in Table 5.3. Fig. 5.10 shows the measured vibration response to the various excitation

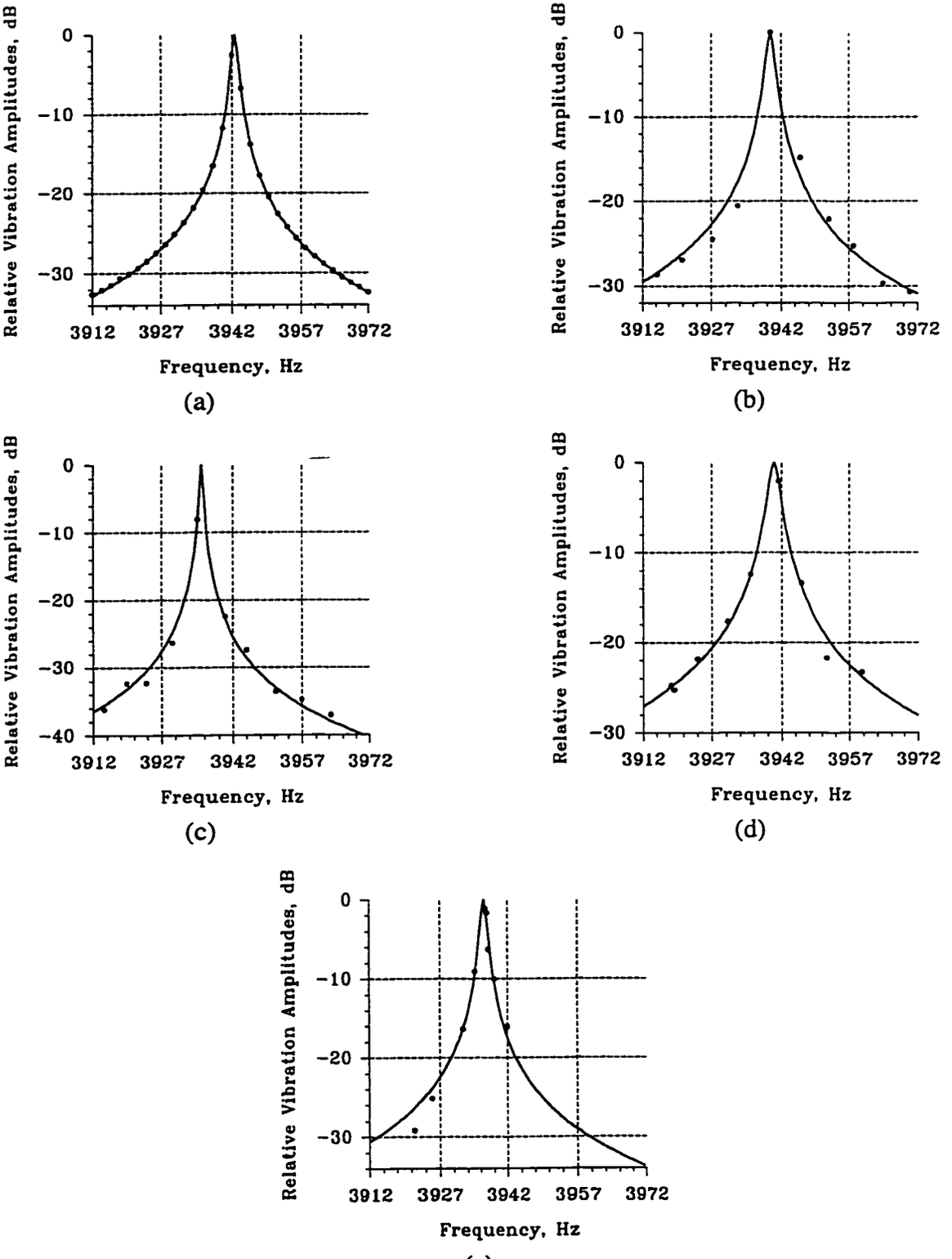

Figure 5.9 : Measured vibration response at the resonance of 3942 Hz, n=0, m=0 using;
(a) Impulse excitation, (b) 2 pairs of force-poles pulsating force,
(c) 4 pairs of force-poles pulsating force, (d) 1&3 pairs of force-poles pulsating force,
(e) 2 pairs of force-poles rotating force.

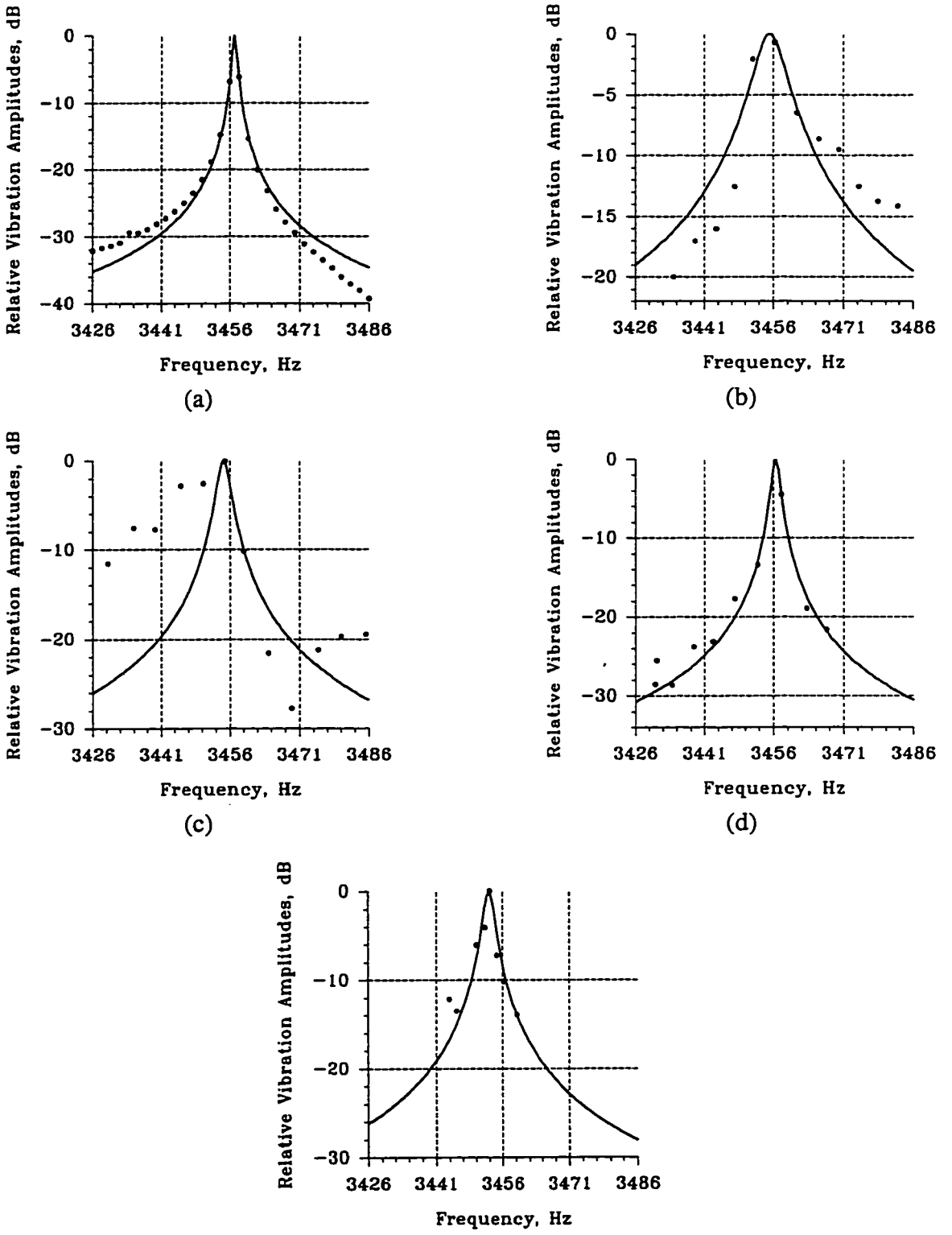

Figure 5.10 : Measured vibration response at the resonance of 3456 Hz, n=1, m=2 using
(a) Impulse excitation, (b) 2 pairs of force-poles pulsating force,
(c) 4 pairs of force-poles pulsating force, (d) 1&3 pairs of force-poles pulsating force,
(e) 2 pairs of force-poles rotating force.

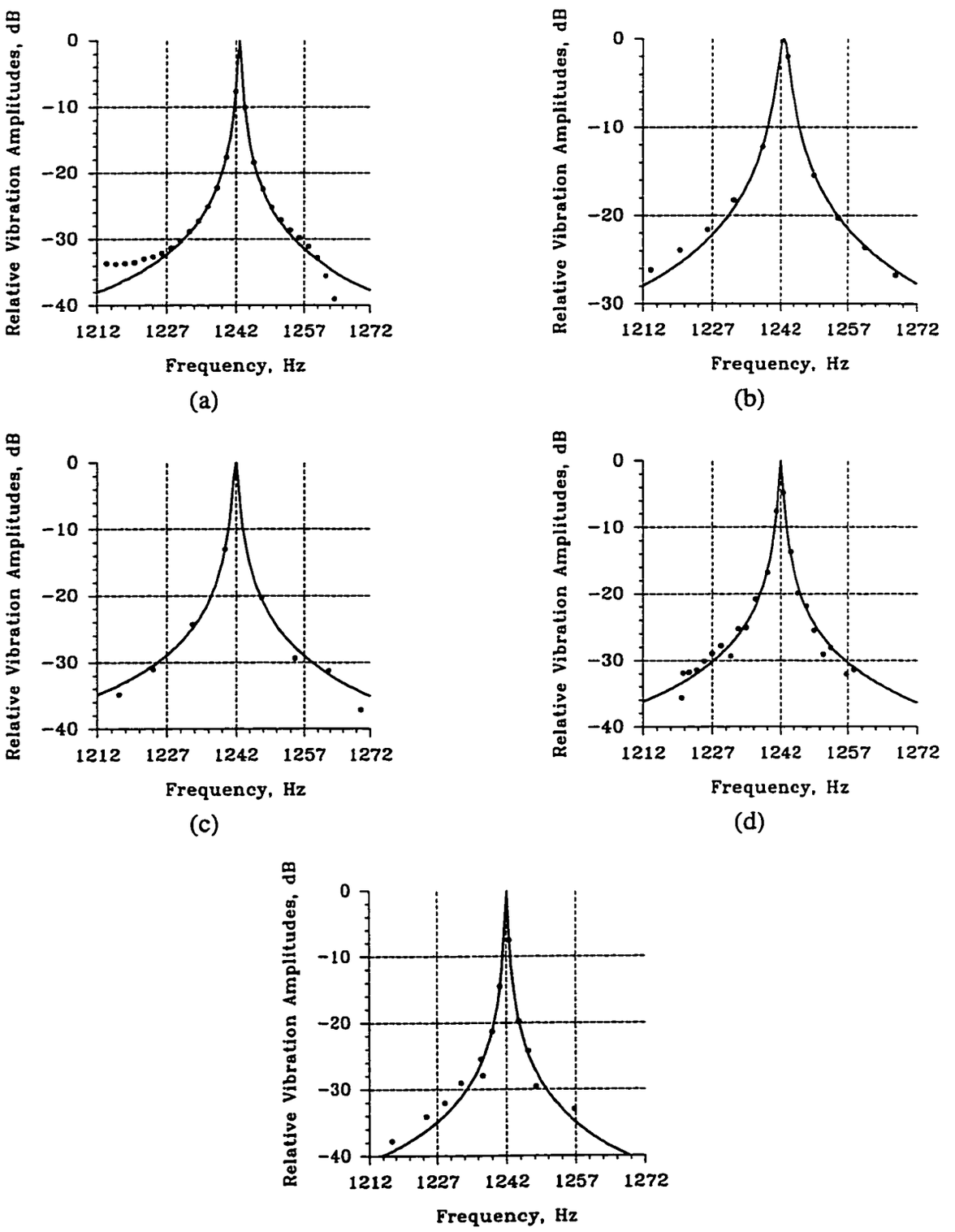

Figure 5.11 : Measured vibration response at the resonance of 1242 Hz, n=2, m=0 using
(a) Impulse excitation, (b) 2 pairs of force-poles pulsating force,
(c) 4 pairs of force-poles pulsating force, (d) 1&3 pairs of force-poles pulsating force,
(e) 2 pairs of force-poles rotating force.

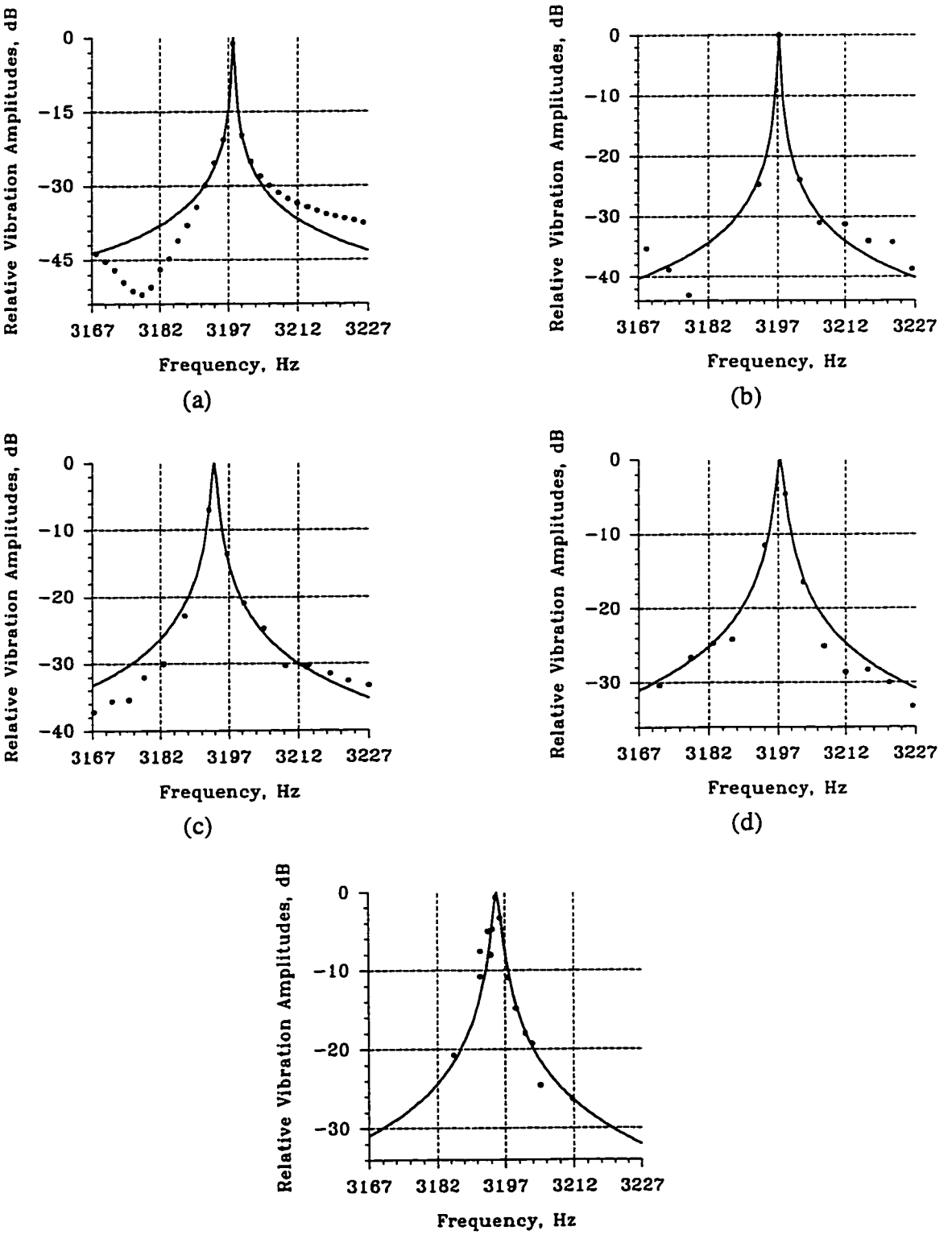

Figure 5.12 : Measured vibration response at the resonance of 3197 Hz, n=3, m=0 using
(a) Impulse excitation, (b) 2 pairs of force-poles pulsating force,
(c) 4 pairs of force-poles pulsating force, (d) 1&3 pairs of force-poles pulsating force,
(e) 2 pairs of force-poles rotating force.

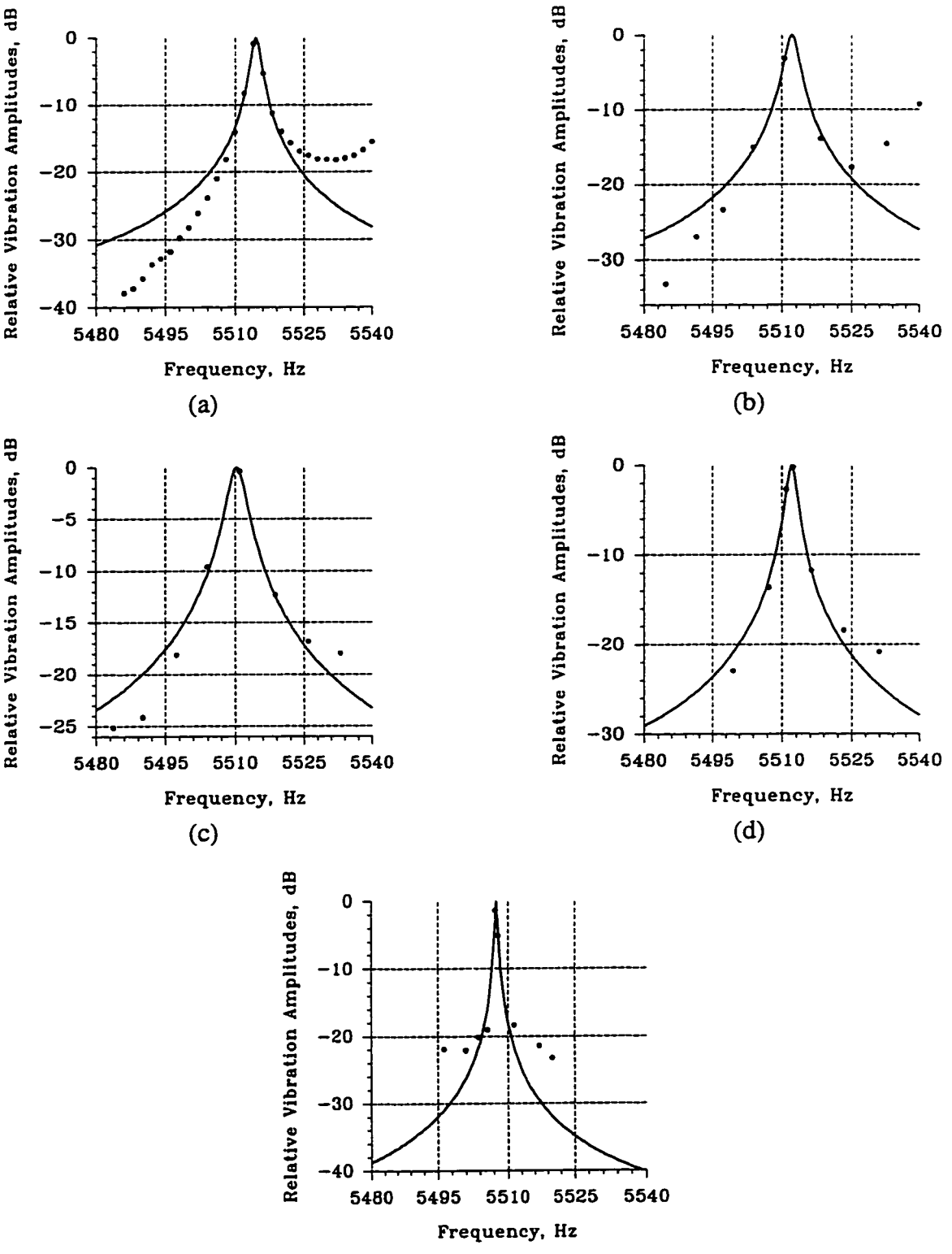

Figure 5.13 : Measured vibration response at the resonance of 5513 Hz, n=4, m=0 using
(a) Impulse excitation, (b) 2 pairs of force-poles pulsating force,
(c) 4 pairs of force-poles pulsating force, (d) 1&3 pairs of force-poles pulsating force,
(e) 2 pairs of force-poles rotating force.

Table 5.3 : Damping-ratios for resonances of the stator-shell model with different excitation force-distributions.

S.No	Freq	n	m	Impulse excitation	Pulsating 2 pairs of force-poles excitation	Pulsating 4 pairs of force-poles excitation	Pulsating 1&3-pairs of force-poles excitation	Rotating 2 pairs of force-poles excitation
1	1242	2	0	0.00061	0.00195	0.00086	0.00074	0.00043
2	1432	2	1	0.00046	0.00072	0.00053	0.00064	0.00060
3	3032	1	1	0.00065	0.00108	*	0.00024	0.00238
4	3197	3	0	0.00012	0.00037	0.00036	0.00053	0.00050
5	3432	3	1	0.00019	0.00233	*	0.00091	0.00055
6	3456	1	2	0.00031	0.00189	0.00082	0.00058	0.00076
7	3942	0	0	0.00035	0.00047	0.00017	0.00063	0.00036
8	4154	0	1	0.00031	0.00037	0.01089	0.00026	0.00021
9	5513	4	0	0.00036	0.00050	0.00074	0.00040	0.00011
10	5729	4	1	0.00008	0.00098	*	0.00045	0.00047
11	8012	5	0	0.00019	0.00091	0.00056	0.00038	0.00017
12	8193	5	1	0.00014	0.00261	0.00028	0.00065	*

* : Could not be measured, (n = circ. mode, m = long. mode).

arrangements at 3456 Hz. This resonance is associated with n=1 and m=2 modes of vibration. There is another resonance at 3432 Hz, which is associated with n=3 and m=1 modes of vibrations. Since the resonance at 3456 Hz is an axi-symmetric resonance, the vibration measurements were made on the centre-plane to avoid interference from the resonance at 3432 Hz. It is observed that the interference from the neighbouring resonance at 3432 Hz is negligible, except for Fig. 5.10(c). Further, better vibration responses are obtained with the impulse excitation and the combined 1 and 3 pairs of force-poles excitation. Fig. 5.11 shows the measured vibration responses to the various excitation arrangements at 1242 Hz. This resonance is associated with n=2 and m=0 modes of vibrations. Although all excitation systems give a similar form to vibration response curve, it is surprising that the pulsating force with 2 pairs of force-poles gives the highest value for the damping-ratio. Fig. 5.12 shows the measured vibration

response to the various excitation arrangements at 3197 Hz. This resonance is associated with n=3 and m=0 modes of vibrations, and it is best excited using the force-distribution with 1 and 3 pairs of force-poles. Also, there is an interfering resonance at 3139 Hz (n=2, m=2). Since both the resonances are axi-symmetric resonances, the measurements were made closer to the antinode for the resonance at 3197 Hz. Surprisingly, here again, a higher value for the damping-ratio was obtained with the force-distribution that best excites this resonance, Fig. 5.12(d). In Fig. 5.13, the measured vibration responses to the various excitation arrangements at 5513 Hz are shown. This resonance is associated with n=4 and m=0 modes of vibrations, and it is best excited using the force-distribution with 4 pairs of force-poles. The closest neighbouring resonance is at 5548 Hz (n=0 and m=0). Again, a higher value for the damping-ratio was obtained with the force-distribution having 4 pairs of force-poles, Fig. 5.13(c). As expected, for all the resonances the vibration response measured with the pulsating and rotating 2 pairs of force-poles excitations were similar.

The damping ratios obtained with the various excitation arrangements for the resonances investigated herein are listed in Table 5.3. The values for the damping-ratios measured using impulse excitation varied from a high of 0.00061 at 1242 Hz to a low of 0.0008 at 5729 Hz. Damping-ratios measured using the electromagnetic forces are higher than those determined using the impulse excitation. Further with the electromagnetic force-distributions, the damping-ratio determined was slightly higher for the force-distribution that best excites the resonance. This suggests that elevated levels of vibrations may be expected over a slightly wider range of frequencies for force-distributions whose force-pole-pairs match the circumferential mode of vibrations.

5.1.8 Mode-Shapes Measured at the Various Resonances

The distribution of the vibration amplitudes along the surface of the vibrating structure is referred to as its mode-shape. It was interesting to observe that a standing-wave type deformation pattern was measured for all resonances irrespective of the type of the excitation force used. Even in the case of rotating force-distribution, distinct and stationary nodes were observed on the stator-shell model. The circumferential modes of vibrations were well defined patterns of deformation for all the exciting force-

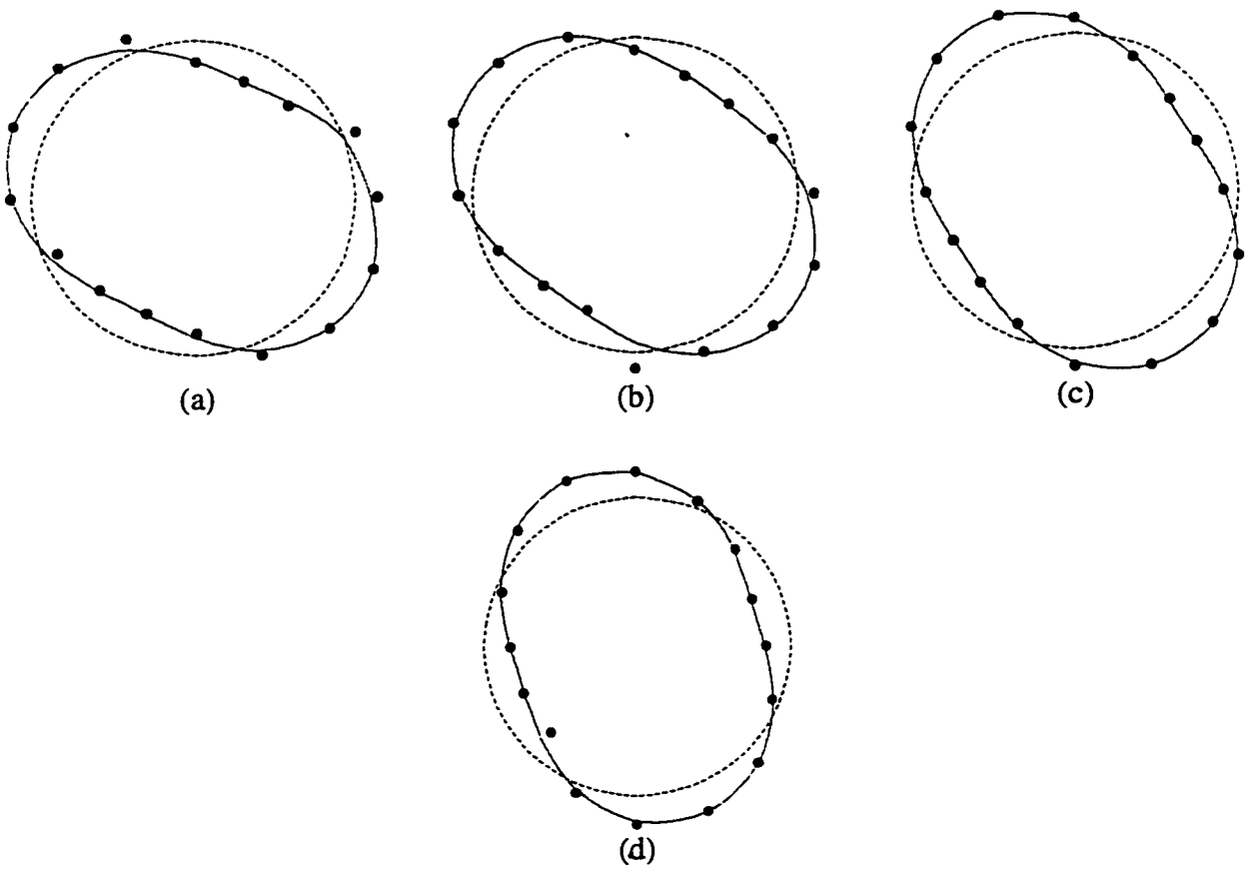

Figure 5.14 : Circumferential mode-shapes measured at 1242 Hz using;
(a) 2 pairs of force-poles pulsating excitation,
(b) 4 pairs of force-poles pulsating excitation,
(c) 1 & 3 pairs of force-poles pulsating excitation,
(d) 2 pairs of force-poles rotating excitation.

distributions. Figs. 5.14 and 5.15 shows the n=2 and n=3 circumferential modes of vibration measured at 1242 Hz and 3197 Hz, respectively.

5.2 Vibration Response of the Laminated Stator with Windings

The constructional features of the 120 hp induction motor stator are provided in Chapter 4. The results of the experimental investigations conducted on the 120 hp induction motor stator model using the different excitation systems are described in the following sections.

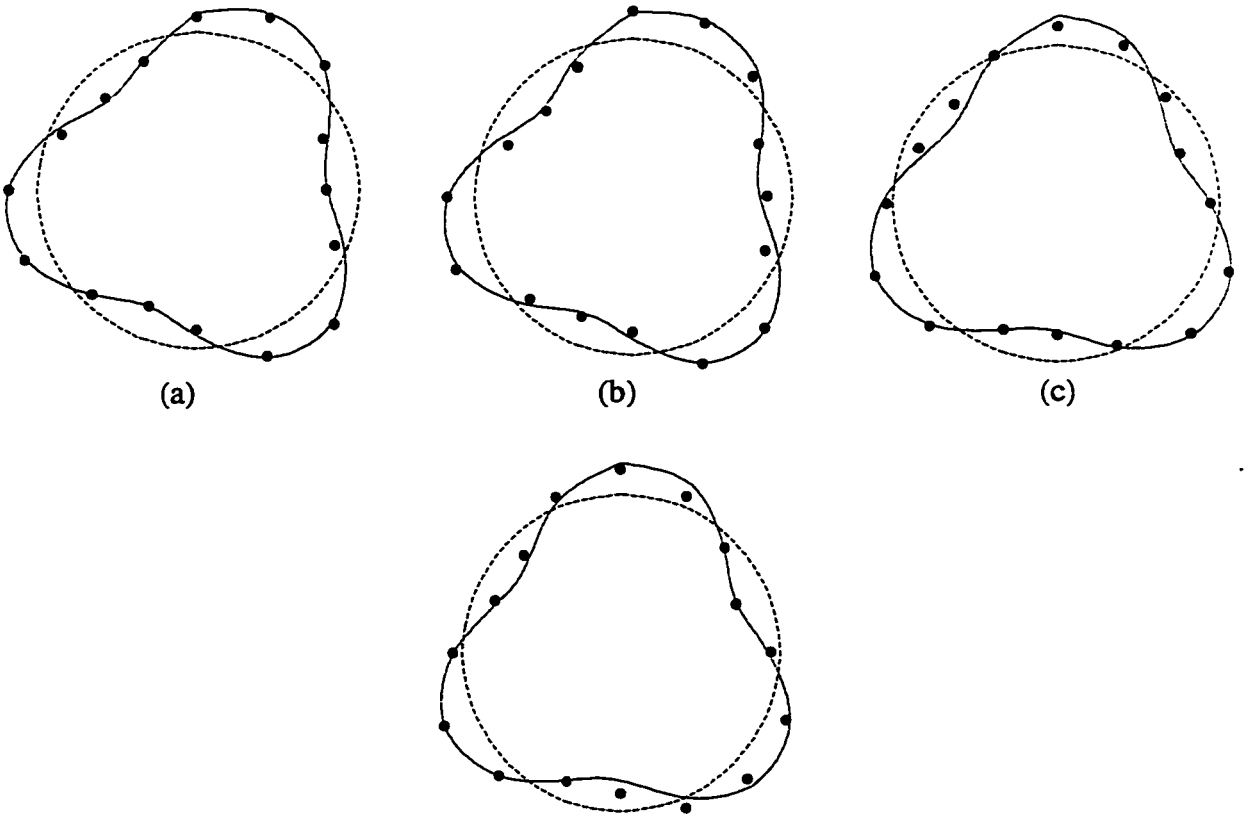

Figure 5.15 : Circumferential mode-shapes measured at 3197 Hz using;
(a) 2 pairs of force-poles pulsating excitation,
(b) 4 pairs of force-poles pulsating excitation,
(c) 1 & 3 pairs of force-poles pulsating excitation,
(d) 2 pairs of force-poles rotating excitation.

5.2.1 Impulse Response

The impulse response of the stator model was measured by striking the model at a location on the centre-plane, and the ensuing vibrations were also measured on the centre-plane. The impulse response of the stator model is shown in Fig. 5.16. The amplitudes of acceleration levels are plotted versus frequency on a logarithmic scale. The acceleration amplitudes are shown in mm/sec^2 and in dB relative to 10^{-2} mm/sec^2. In contrast to the vibration behaviour of the stator shell model, the laminated stator model did not show the presence of any anti-symmetric longitudinal resonances. This behaviour of the stator model was also observed by the authors in reference [39,51]. In the present stator model, the end-turns of the windings were trimmed in order to make the stator model physically symmetrical. The authors of reference [39,51] attributed the

Table 5.4 : Selected resonances and associated modes of the stator model.

S.No.	Frequency, Hz	Circumferential mode, n	Longitudinal mode, m
1	470	2	0
2	631	2	4
3	1801	3	2
4	1907	2	2
5	2055	3	4
6	2306	3	2
7	2491	4	0
8	3016	0	0
9	3339	0	0
10	3820	5	4
11	4325	1	6

absence of anti-symmetric longitudinal resonances in the stator model to the presence of asymmetries in the model. Although the stator model is symmetrical in the present investigation, the anti-symmetric longitudinal modes could not be observed. Table 5.4 lists the resonances of the stator model investigated in this study. Here again, these resonances are selected such that they represent resonances of circumferential modes n=0 to 5. The various peaks of interest in the impulse response are identified according to Table 5.4. The resonant frequencies measured here correlate well with those measured by the authors of references [39,51].

In addition to the fact that the impulse excitation technique is time and labour efficient, it has provided more detailed information in comparison to the magnetic-shaker technique [51]. It is also observed from Fig. 5.16 that the various resonant peaks are very much flattened indicating the presence of significantly higher damping.

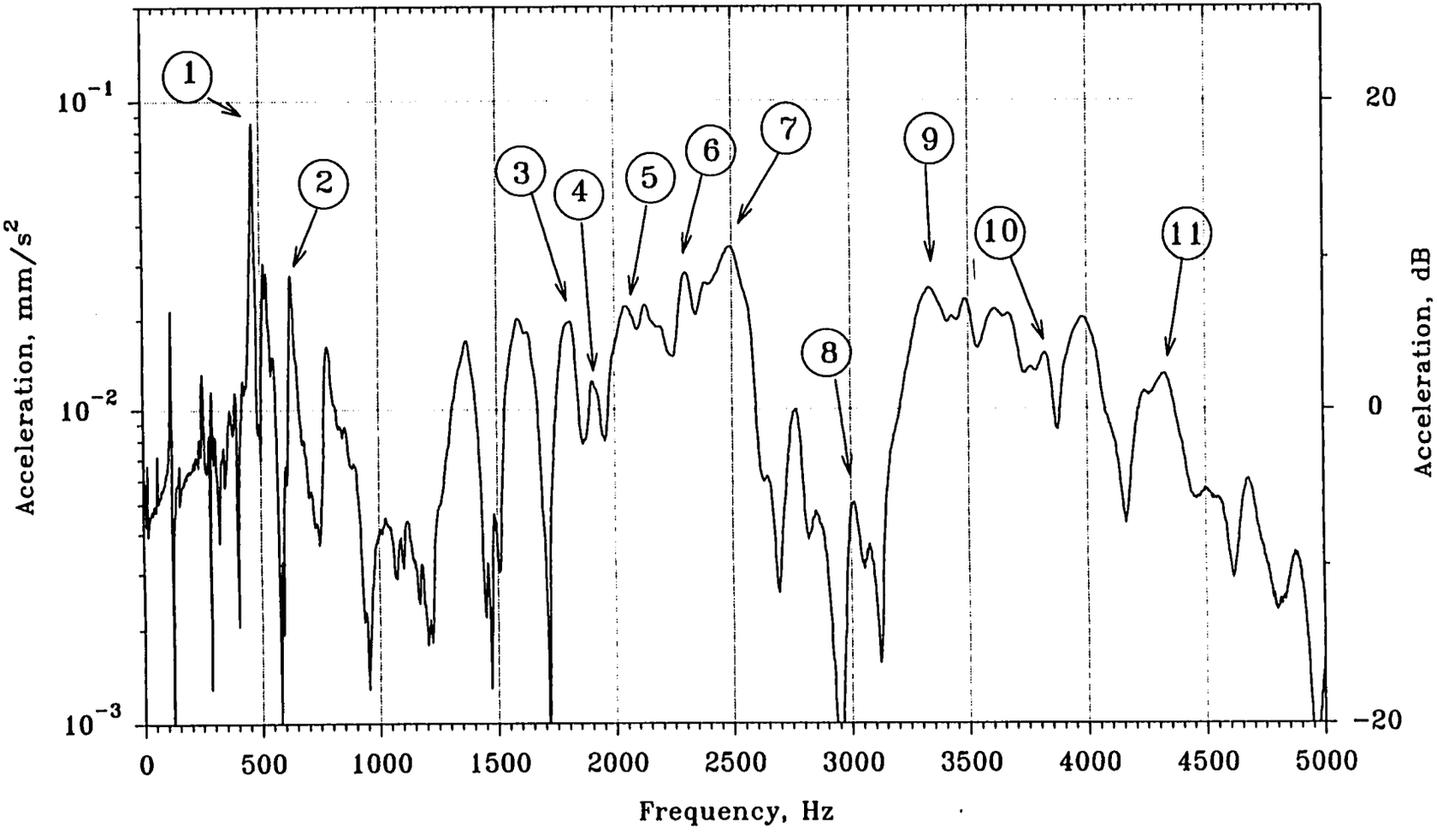

Figure 5.16 : Impulse response of the 120 hp stator, model II, measured on a centre-plane.

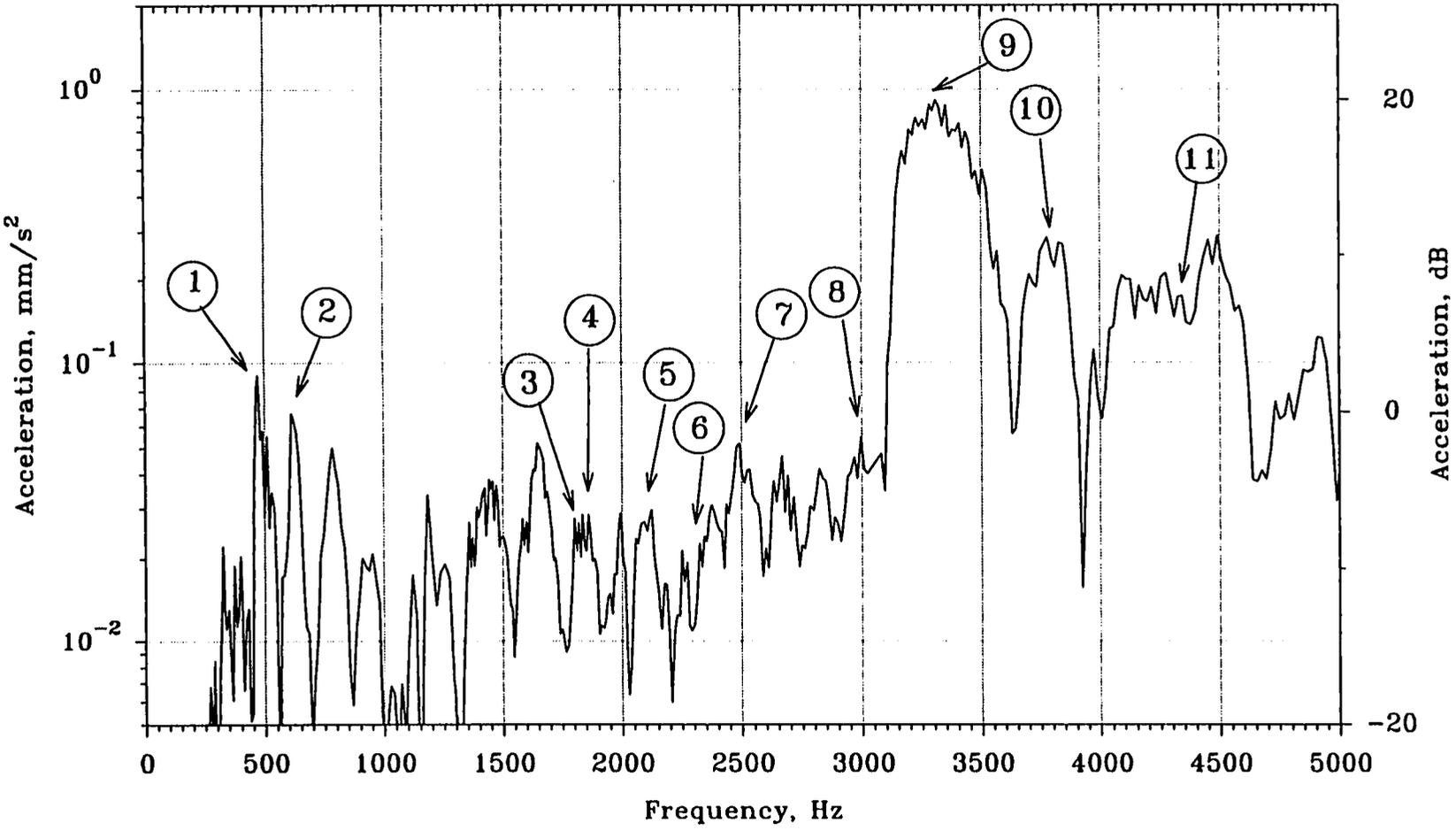

Figure 5.17 : Vibration response of the 120 hp stator, model II, to a 2 pairs of force-poles pulsating force measured on a centre-plane.

5.2.2 Response to 2 Pairs of Force-Poles Pulsating Force Excitation

The stator model was then excited using the force-distribution produced by the 2-pole winding when it was energised from a single-phase variable-frequency supply. The vibration measurement were made on the centre-plane, and the spectrum of the measured vibration accelerations is shown in Fig. 5.17. The spectrum is plotted similar to the impulse response plot, and the various resonance peaks are identified according to Table 5.4.

In contrast to the spectra obtained with impulse excitation, the vibration levels induced in the stator model with the 2-pairs of force-poles excitation is significantly higher. In the case of impulse excitation, since most of the vibration energy is confined to the lower-frequencies the vibration amplitudes decrease with increasing frequencies. As explained earlier, the magnitudes of the forces are kept at the same level over the entire frequency range of the measurement with the distributed electromagnetic force excitation. It is observed from the spectrum that the resonance peaks associated with mode n=2, i.e. resonances #1 and #2, and mode n=0, i.e. resonance #9, are prominently excited. In general, the stator exhibits significant amount of damping and most of the resonance peaks are flattened. Comparing the spectrum of Fig. 5.17 with that obtained for the stator shell-model, Fig. 5.3, it is observed that the average level of vibrations for the laminated stator is about 20 dB lower.

5.2.3 Response to 4 Pairs of Force-Poles Pulsating Force Excitation

Vibration measurements were made on the stator model when it was excited using the 4 pairs of force-poles pulsating force-distribution which was produced by energising the 4-pole winding from a single-phase variable-frequency supply. Again, the vibration measurements were made on the centre-plane, and the corresponding spectrum of the measured vibration acceleration signals are shown in Figs. 5.18. The spectrum is plotted similar to the earlier plots, and the various peaks have been identified.

It is observed from the spectrum of Fig. 5.18 that all the resonances under consideration are excited in the stator model. The resonance peaks corresponding to the mode n=0, i.e. resonance #8, #9, and mode n=2, i.e. resonances #1 and #2, are well excited. Due to the proximity of the measurement-location to a node for the n=4 resonance at 2491 Hz, the resonance peak #7 is not very well defined in this spectrum.

5.2.4 Response to 1 and 3 Pairs of Force-Poles Pulsating Force Excitation

Vibration measurements were also made on the stator model when it was excited using the 1 and 3 pairs of force-poles pulsating force-distribution which was produced by energising the 2-pole and 4-pole windings simultaneously from a single-phase variable-frequency supply. Here again, the vibration measurements were made on the centre-plane. The corresponding spectrum of the measured vibration acceleration signals is shown in Fig. 5.19. The spectrum is plotted similar to the earlier plots, and the various peaks have been identified.

It is observed from the spectrum of Fig. 5.19 that the resonances corresponding to modes n=1 and n=3, i.e. resonances #3, #5, #6, and #11, are well excited. Also the resonance at 3820 Hz which is associated with n=5 mode of vibration, appears as a distinct resonance peak.

5.2.5 Response to 2 Pairs of Force-poles Rotating Force Excitation

In order to examine the effect of rotation of the force-distributions on the vibration response of the stator model, the model was excited using the 2-pole winding when it was connected in the 3-phase configuration. The predominant force component produced using this arrangement has 2 pairs of force-poles and it rotates in the air-gap at the synchronous speed corresponding to the frequency of the 3-phase supply. As explained earlier, the frequency of the 3-phase oscillator in the power supply had to be manually changed. Hence, these tests were conducted only in the frequency range associated with the selected resonances. These plots are shown later in the chapter while discussing the damping present at each of these selected resonances.

5.2.6 Comparison of Vibration Amplitudes at Various Resonances

As explained earlier for the stator-shell model, in order to measure the maximum vibration amplitudes at a resonance, the accelerometer was moved around the periphery of the stator model and placed at an anti-node of vibrations. The acceleration levels measured are provided in Table 5.5 in dB relative to 0.01 mm/sec^2. Again, the total, maximum and average values of the force acting on the stator model for the various force-distributions are also provided in Table 5.5.

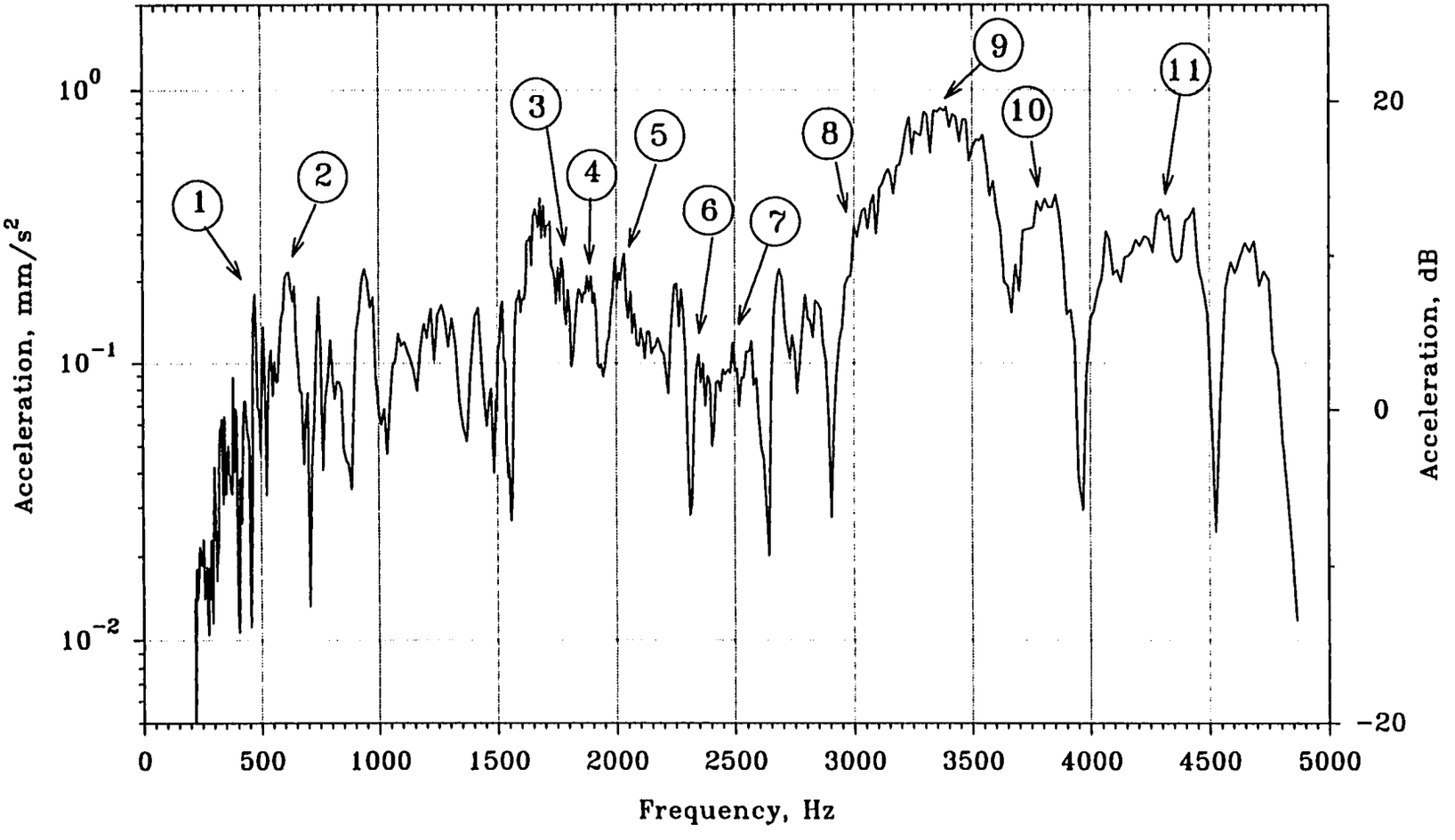

Figure 5.18 : Vibration response of the 120 hp stator, model II, to a 4 pairs of force-poles pulsating force measured on a centre-plane.

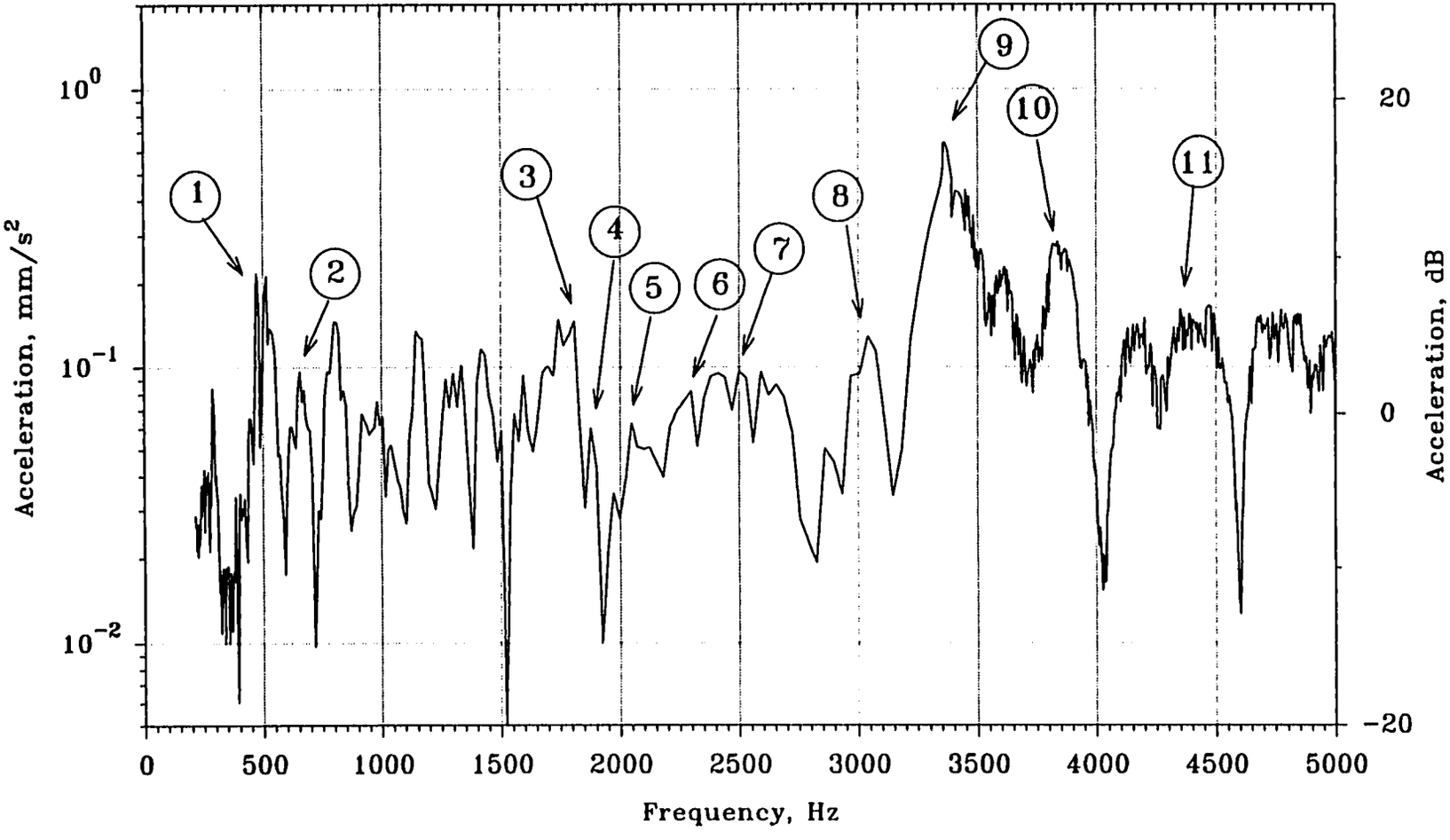

Figure 5.19 : Vibration response of the 120 hp stator, model II, to a combined 1 and 3 pairs of force-poles pulsating force measured on a centre-plane.

Table 5.5 : Maximum values of acceleration measured in dB relative to 0.01 mm/sec^2 at selected resonances of the laminated stator model using different electromagnetic force-distributions.

Freq., Hz	**n**	**m**	**2 pairs of force-poles**	**4 pairs of force-poles**	**1 & 3 pairs of force-poles**	**2 pairs of force-poles**
Force type			Pulsating	Pulsating	Pulsating	Rotating
Total force, N			1071.23	1079.41	537.66	1600.00
Maximum force, N			57.24	57.24	32.20	83.97
Average force, N			19.13	19.28	9.60	28.57
470	2	0	19.5 dB	25.1 dB	24.6 dB	30.5 dB
631	2	4	16.4	26.9	18.1	18.8
1801	3	2	13.6	19.6	16.4	*
1907	2	2	10.2	14.7	7.9	14.7
2055	3	4	*	13.2	16.1	*
2306	3	2	6.4	*	17.0	*
2491	4	0	18.3	20.8	16.7	*
3016	0	0	17.3	35.3	8.0	*
3339	0	0	25.2	38.6	36.1	34.1
3820	5	4	28.5	26.6	29.0	*
4325	1	6	9.5	30.4	22.7	19.8

* : could not be measured distinctly, (n = cir. mode, m = long. mode).

Although the amplitudes of the pulsating force-distributions with 2 and 4 pairs of force-poles are almost identical, it is observed that the maximum acceleration levels measured with the 4 pairs of force-poles are higher in most cases by about 6 to 12 dB. In comparison with the case of the stator-shell model, this difference is smaller, which can be attributed to the laminated structure of the model. In this case, significant difference in the vibration levels were observed for the mode n=0 resonances at 3016 Hz and 3339 Hz.

The force-distribution produced by the combined excitation of the 2-pole and 4-pole windings excites well most of the resonances of this stator model. With this arrangement, pronounced increase in the acceleration levels was observed at the mode

n=3 resonances of 2055 Hz and 2306 Hz, and also at the mode n=5 resonances of 3820 Hz.

It is interesting to note that the rotating force-distribution produced by the 3-phase operation of the 2-pole winding did not excite distinctly all the resonances of the stator model. It was quite effective in inducing the mode n=2 vibrations at 470 Hz, 631 Hz and 1907 Hz, and also mode n=0 vibration at the resonance of 3339 Hz.

In general, at the mode n=0 resonances of 3016 Hz and 3339 Hz all the force-distributions gave rise to significant levels of vibrations. For the circumferential mode n=5, the resonance at 3820 Hz was excited well by the combined 2-pole and 4-pole winding arrangement, and the pulsating force-distribution with 4 pairs of force-poles was also effective.

Since the damping present in the laminated stator model is much higher than that present in the stator-shell model, the vibration amplitudes measured here are obviously much smaller. In general, the measured values of the maximum acceleration levels were higher for force-distributions with pairs of force-poles that matched the circumferential mode of vibrations. Here again, it was observed that there is significant coupling between the force-distributions with 4 pairs of force-poles and the mode n=2 vibrations, and vice-versa.

5.2.7 Damping-Ratios at the Various Resonances

The amplitude response at the selected resonances of the laminated stator model are shown in Figs. 5.20 to 5.24. The damping-ratios are estimated using the vibration response of the model to different excitation force-distributions. Table 5.6 provides the damping-ratios corresponding to the various resonances of the stator model. It is observed from Table 5.6 that the damping-ratios measured using electromagnetic forces are, in most cases, greater than those obtained using impulse (hammer) excitation at lower frequencies. The damping present in the stator model is about 10 to 100 times greater than that present in the solid stator-shell model. The measured values of the damping-ratios varied between 0.015 and 0.056. Here again, the measured values of the damping-ratios depend on how well the resonance is excited using a particular force-distribution.

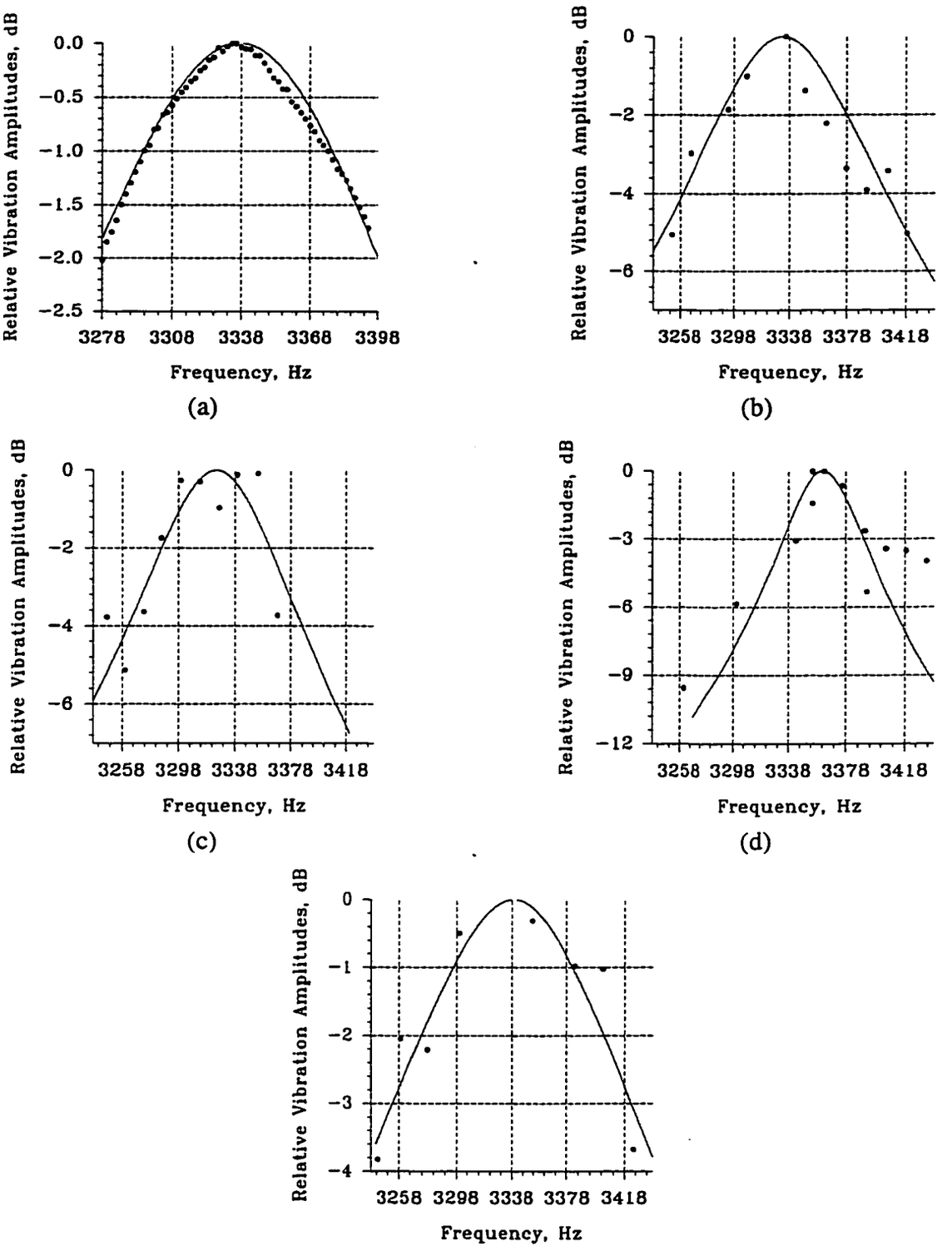

Figure 5.20 : Measured vibration response at the resonance of 3339 Hz, n=0, m=0 using
(a) Impulse excitation
(b) 2 pairs of force-poles pulsating force
(c) 4 pairs of force-poles pulsating force
(d) 1&3 pairs of force-poles pulsating force
(e) 2 pairs of force-poles rotating force

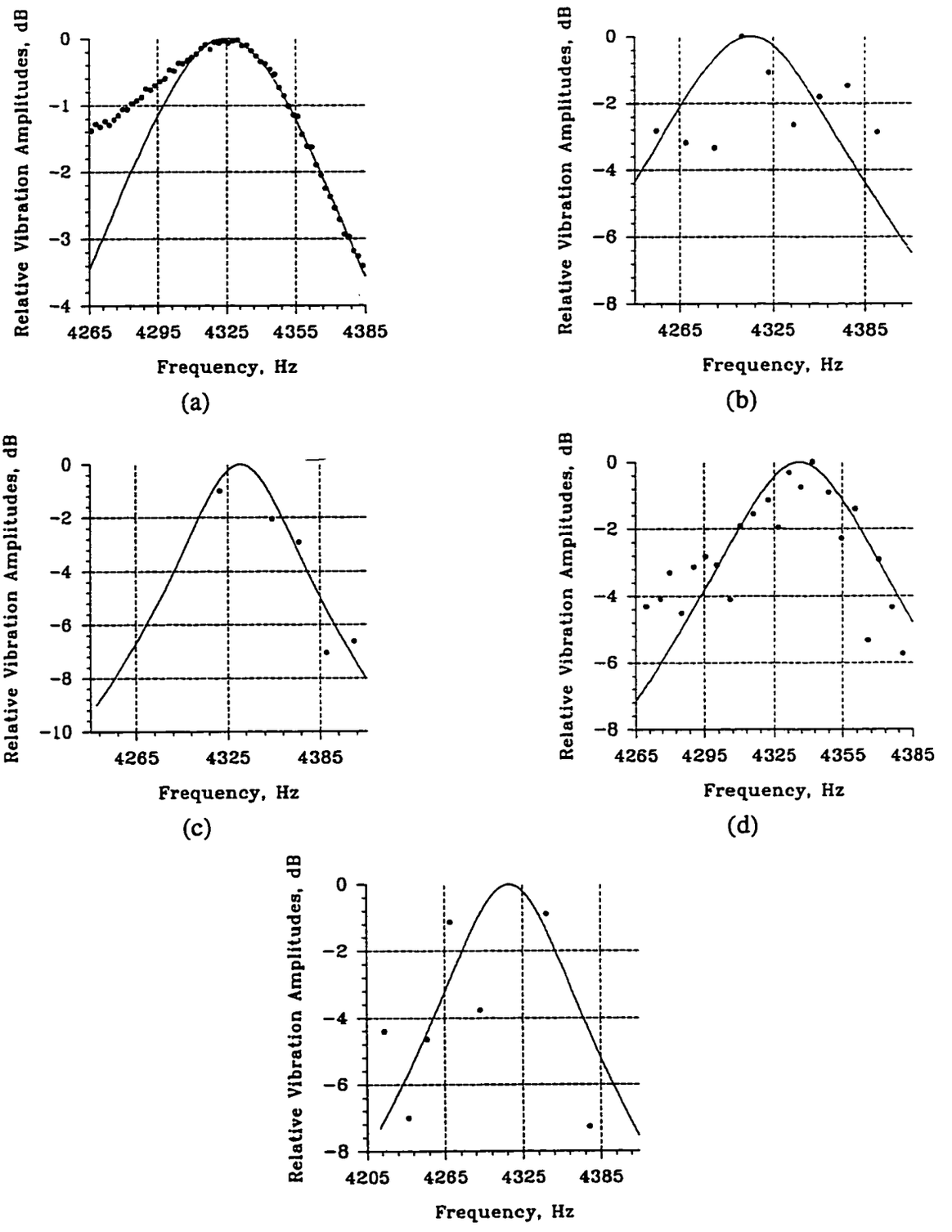

Figure 5.21 : Measured vibration response at the resonance of 4325 Hz, n=1, m=5 using
(a) Impulse excitation
(b) 2 pairs of force-poles pulsating force
(c) 4 pairs of force-poles pulsating force
(d) 1&3 pairs of force-poles pulsating force
(e) 2 pairs of force-poles rotating force

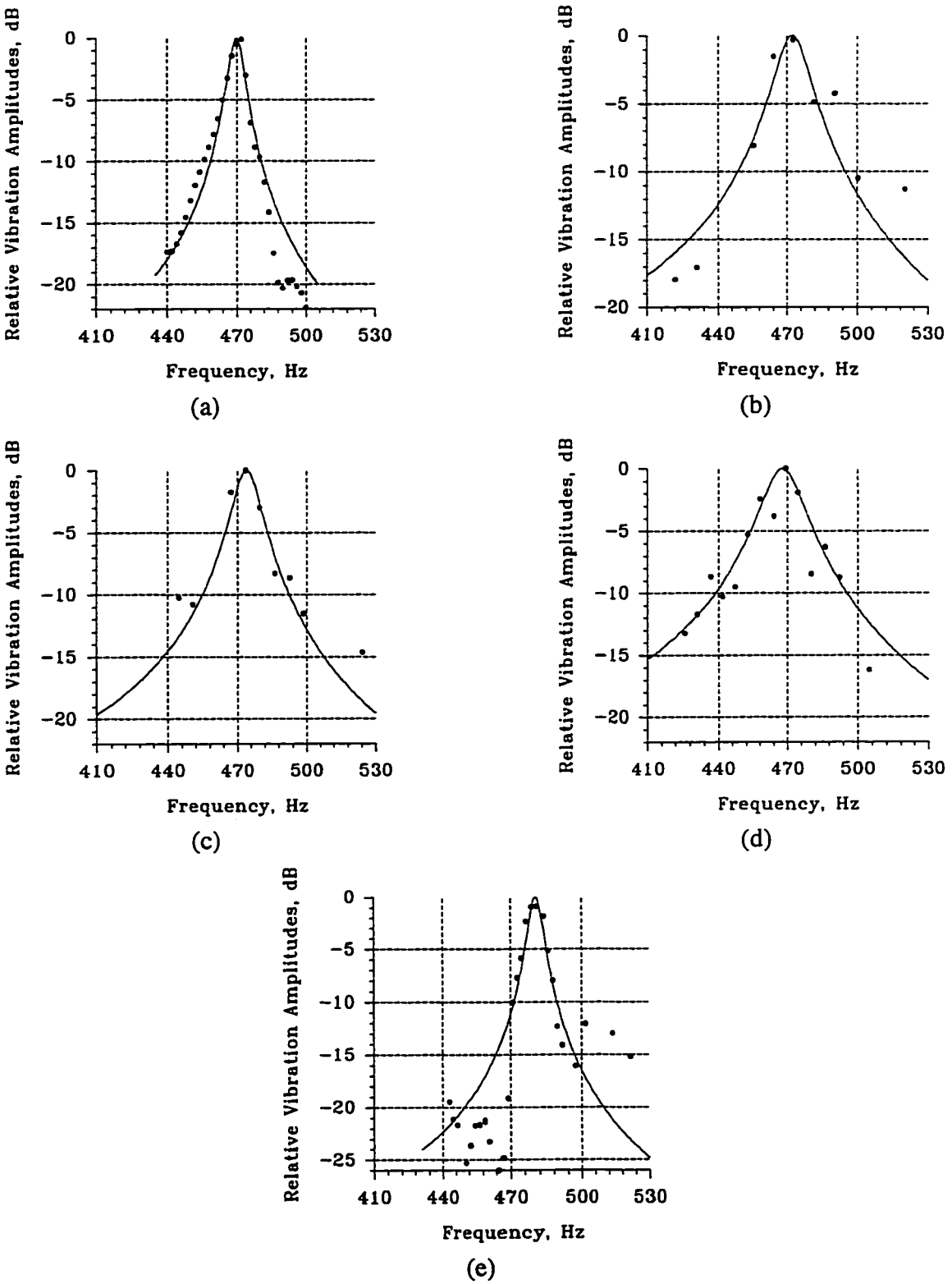

Figure 5.22 : Measured vibration response at the resonance of 470 Hz, n=2, m=0 using
(a) Impulse excitation
(b) 2 pairs of force-poles pulsating force
(c) 4 pairs of force-poles pulsating force
(d) 1&3 pairs of force-poles pulsating force
(e) 2 pairs of force-poles rotating force

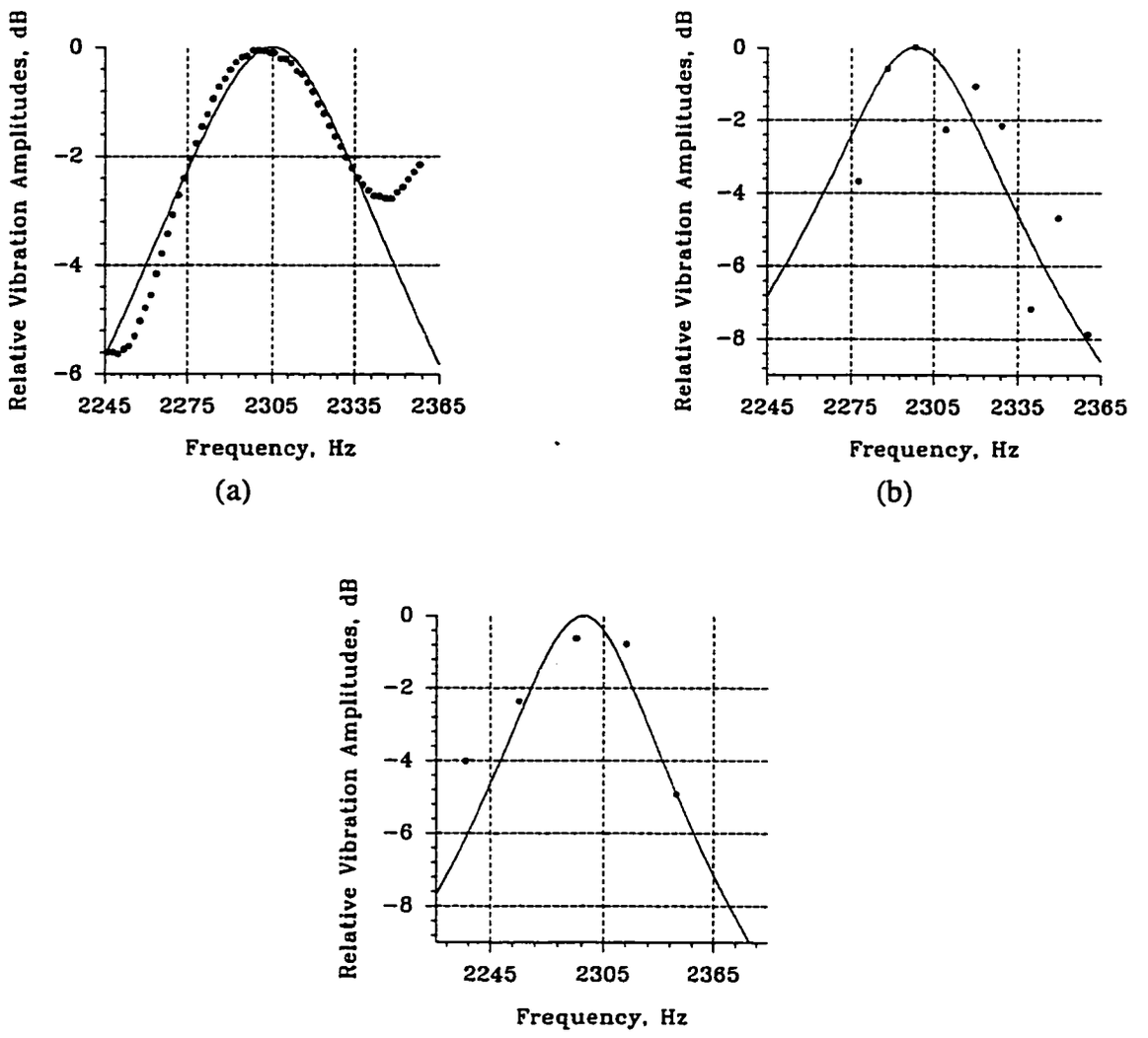

Figure 5.23 : Measured vibration response at the resonance of 2306 Hz, n=3, m=2 using (a) Impulse excitation (b) 2 pairs of force-poles pulsating force (c) 1 & 3 pairs of force-poles pulsating force.

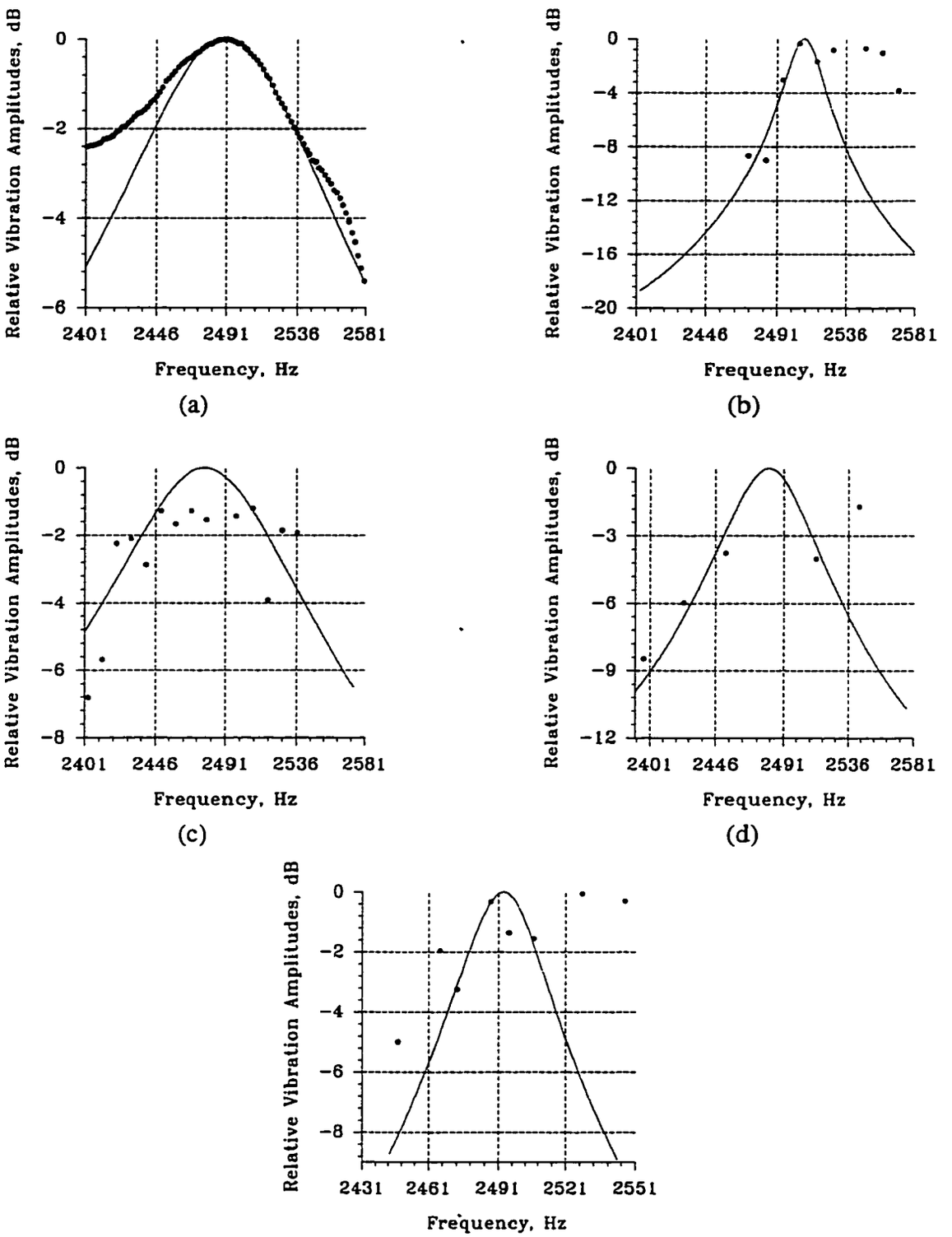

Figure 5.24 : Measured vibration response at the resonance of 2491 Hz, n=4, m=0 using
(a) Impulse excitation
(b) 2 pairs of force-poles pulsating force
(c) 4 pairs of force-poles pulsating force
(d) 1&3 pairs of force-poles pulsating force
(e) 2 pairs of force-poles rotating force

Table 5.6 : Damping-ratios at resonances of the laminated stator model with different excitation force-distributions.

S.No	Freq	n	m	Impulse excitation	Pulsating 2 pairs of force-poles excitation	Pulsating 4 pairs of force-poles excitation	Pulsating 1&3 pairs of force-poles excitation	Rotating 2 pairs of force-poles excitation
1	470	2	0	0.01567	0.03257	0.02640	0.04018	0.01241
2	631	2	4	0.01621	0.03781	0.07738	0.02702	0.01624
3	1801	3	2	0.03346	0.05151	0.01292	0.04384	*
4	1907	2	2	0.02346	0.02133	0.00993	0.02785	0.02032
5	2055	3	4	0.05632	*	0.04116	0.03558	*
6	2306	3	2	0.03135	0.02343	*	0.03066	*
7	2491	4	0	0.04690	0.00955	0.04232	0.02388	*
8	3016	0	0	0.01341	0.01397	0.05165	0.01859	*
9	3339	0	0	0.04844	0.03537	0.03021	0.01658	0.05078
10	3820	5	4	0.02029	0.01569	0.01414	0.01748	*
11	4325	1	6	0.02484	0.02642	0.01638	0.01589	0.02175

* : Could not be measured, (n = circumferential mode, m = longitudinal mode).

5.2.8 Mode-shapes measured at the various resonances

For the circumferential mode-shapes, a "standing-wave" type deformation pattern was observed for all resonances irrespective of the type of the excitation force used. Even in the case of rotating force-distribution, distinct and stationary nodes were observed on the laminated stator model. Fig. 5.25 and 5.26 show n=2 and n=3 circumferential and longitudinal modes of vibrations measured at 470 Hz and 1801 Hz, respectively. In contrast to the stator-shell model, the longitudinal mode shapes measured at the various resonances of the laminated stator model were not very regular. However, since the nodes of vibration along the length of the stator could be detected with certainty, the longitudinal modes associated with the various resonances could be determined. Fig. 5.27 shows the measured modes n=0 and n=1 at 3339 Hz and 4325 Hz, respectively.

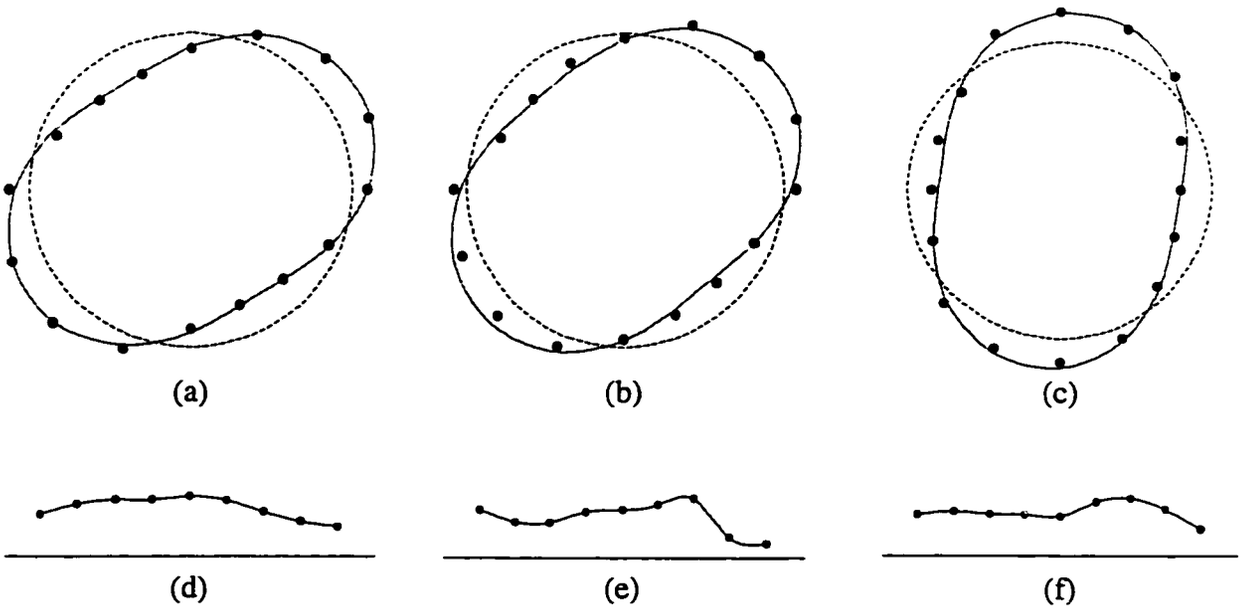

Figure 5.25 : Circumferential and longitudinal mode-shapes at 470 Hz measured using;
(a,d) 2 pairs of force-poles pulsating excitation,
(b,e) 4 pairs of force-poles pulsating excitation,
(c,f) 1 & 3 pairs of force-poles pulsating excitation.

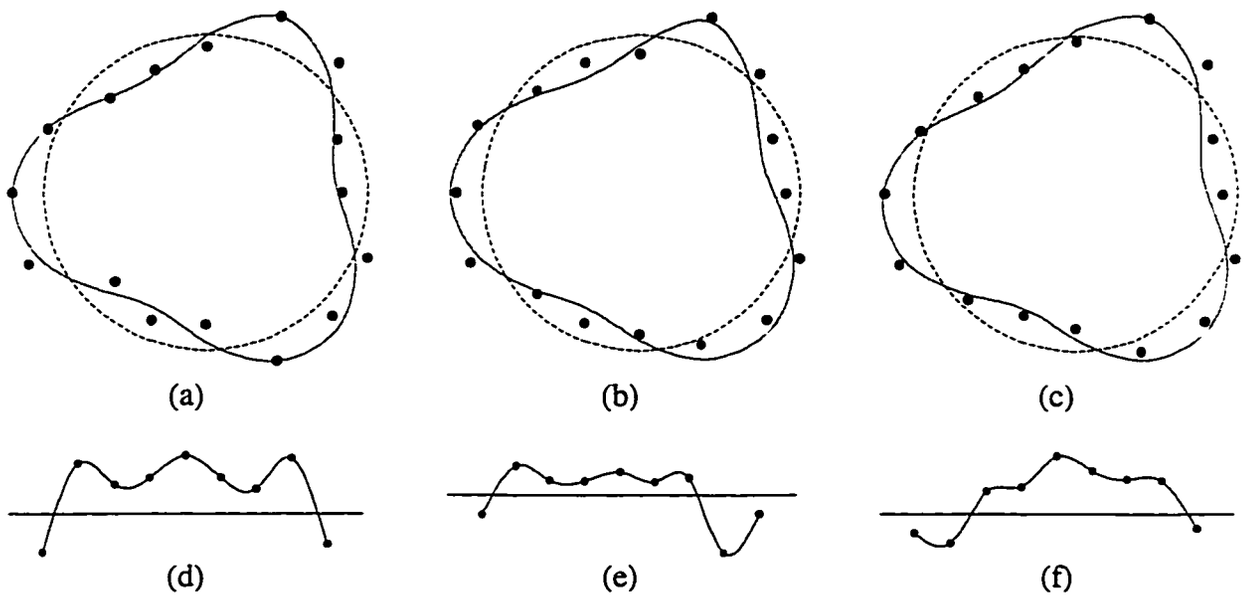

Figure 5.26 : Circumferential and longitudinal mode-shapes at 1801 Hz measured using;
(a,d) 2 pairs of force-poles pulsating excitation,
(b,e) 4 pairs of force-poles pulsating excitation,
(c,f) 1 & 3 pairs of force-poles pulsating excitation.

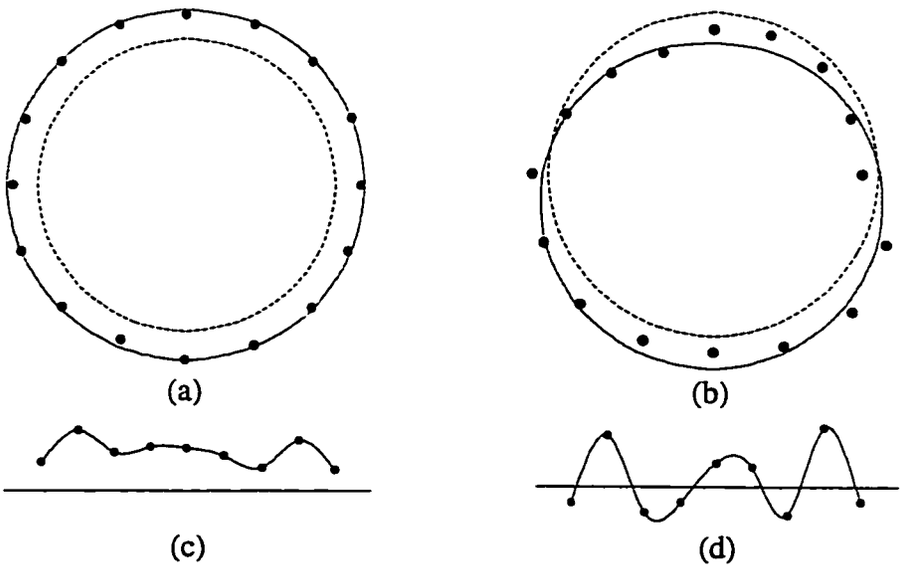

Figure 5.27 : Circumferential and longitudinal mode-shapes at;
(a,c) 3339 Hz measured using 4 pairs of force-poles pulsating excitation,
(b,d) 4325 Hz measured using 1 & 3-force-pole pulsating excitation.

5.3 Summarising Comments

The experimental investigations presented in this chapter are summarised in the following from the perspective of vibration testing and designing of quiet electrical machines.

(i) From the viewpoint of experimentally investigating the vibration behaviour of electrical machine stators, the main advantage of the distributed excitation forces is the ability to excite resonances selectively. It was observed that the best vibration response, at the various resonances of the stator models, was obtained with the force-distribution that had the same pairs of force-poles as the circumferential mode of vibration associated with the corresponding resonance. Further, the experimental results revealed that there is a significant amount of coupling between the mode n=2 resonances and the force-distribution with 4 pairs of force-poles, and vice versa.

(ii) The distributed electromagnetic forces facilitate the injection of substantially more vibrational energy, and uniformly, into the test models. This was especially important for the laminated stator model with windings.

(iii) The damping present in the stator-shell and laminated stator models were investigated in detail. It was sought experimentally to excite each of the resonances individually so that the damping-ratios could be obtained from the vibration response plots. The damping-ratios were obtained using the various force-distributions and an effort was made to minimise the influence from other near-by resonances in the measurements. The values of the damping-ratios from the well defined vibration-responses are selected, and they are summarised in Table 5.7.

Table 5.7 : Damping-ratios measured at the selected resonances of the stator-shell and the laminated stator models.

Stator-shell model				**Laminated stator with windings**			
Freq., Hz	**n**	**m**	ζ	**Freq., Hz**	**n**	**m**	ζ
1242	2	0	0.00043	470	2	0	0.01241
1432	2	1	0.00046	631	2	4	0.01621
3032	1	1	0.00024	1801	3	2	0.01292
3197	3	0	0.00012	1907	2	2	0.02032
3432	3	1	0.00019	2055	3	3	0.03558
3456	1	2	0.00031	2306	3	2	0.03066
3942	0	0	0.00017	2491	4	0	0.04232
4154	0	1	0.00021	3016	0	0	0.05165
5513	4	0	0.00011	3339	0	0	0.03021
5729	4	1	0.00008	3820	5	4	0.01748
8012	5	0	0.00017	4325	1	6	0.01638
8193	5	1	0.00014				

(iv) The damping-ratios obtained for the solid stator-shell model is within the range of values 1 x 10^{-4} to 6 x 10^{-4}, reported for steel [50]. In reference [51], although it was reported that the damping-ratios for the stator-shell model are not frequency dependent, the present experimental investigations prove the contrary. The results exhibit that there is considerable decrease in the damping-ratio with frequency. As explained in Appendix F, the decrease of the damping-ratios with frequency signifies the predominance of friction-damping.

(v) It is observed in the case of the laminated stator model with windings that the damping-ratios are not consistent with the resonant frequencies. This suggests the presence of non-linear damping effects which are normally present in structures which are built using many materials. This is indicative of the energy dissipation at the boundaries of the various structural elements. The values of the damping-ratios obtained for this model are approximately 10 to 100 times of that obtained for the solid stator-shell model. From Eqn. 5.2, it is evident that the actual damping present is proportional to the resonant frequency and the damping-ratio. It, therefore, follows that the actual damping present in the laminated stator model at higher frequencies will be much larger.

(vi) Another significant advantage of using the distributed electromagnetic forces is their ability to induce vibrations in the stator models uniformly. This results in well defined sinusoids in the measurement of the circumferential mode-shape patterns as predicted by the theory [9,51].

(vii) From the perspective of designing quieter machines and achieving lower levels of vibrations, it is critical that the force-frequency be away from the resonant frequency. It was observed in these experimental investigations that the resonances of the stators were excited by most of the distributed force arrangements. Further, at resonance, the amplitudes of the vibrations depend to a smaller extent on the type of force-distribution. In the course of the investigations, it was ascertained that the force-frequency overrides the importance of the force-distribution.

(viii) Significantly lower levels of vibrations can be achieved at the mode n=1 and n=3 resonances of the machine structure by ensuring that the force-distributions which match these mode-shapes either not exist or are made as small as possible. For the vibrations at modes n=2 and n=4 resonances, both the force-distributions with 2 and 4 pairs of force-poles are equally effective.

(ix) Contrary to the prevalent rationale in the literature [56], it was observed that stationary "standing-wave" deformation patterns of vibrations were produced at the resonances even with rotating force-distributions.

(x) Even when the machine structure was excited exactly at the resonant frequencies of the rotor, there was no measurable difference in the acceleration levels measured on the stator models. In most cases, the audible sound radiated did not show any perceivable change. It is to be noted that in the present experimental arrangements, there is no mechanical or physical connection between the rotor structure and the stator models.

It is seen from the results presented in this chapter, that lower levels of vibrations can be achieved even at resonance conditions by designing the electromagnetic forces to have circumferential distribution different from the circumferential mode associated with corresponding resonance. In the next chapter, the implications of induction motor design parameters such as the number of stator and rotor slots on the circumferential distribution of the electromagnetic forces are described and examined with reference to the variable frequency operation.

6. CONSIDERATIONS FOR THE REDUCTION OF VIBRATIONS AND NOISE IN THE DESIGN OF INDUCTION MOTORS FOR VARIABLE FREQUENCY OPERATION

In Chapters 2 and 3, the vibration behaviour of induction motors operating on a fixed frequency supply was analyzed. In this chapter, the implications of operating the induction motor on a variable-frequency supply are discussed. Design considerations are then explained with a view to reduce the vibrations and noise produced by the various magnetic forces. Experimental information on the variable-frequency operation of the 10 hp squirrel-cage induction motor, described in Chapter 2, is provided to verify the validity of some of the design considerations.

6.1 Introduction

The induction motor is essentially a constant speed motor when operated under normal conditions and supplied by a fixed frequency source. There are numerous applications where it is desirable, if not necessary, to have an adjustable-speed drive motor. The conventional variable-speed drive system consists of a dc drive motor, which requires considerably greater initial cost for a given size of the machine and also costly control equipment. In addition, the dc motors require more maintenance and also a dc power supply. The simplicity of the construction, ruggedness, ease of operation and recent advances in the development of solid-state power supply have made the squirrel-cage induction motor a very promising adjustable-speed ac drive motor. As the frequency conversion systems continue to be technically improved, the maximum kVA capability is constantly increasing, and the induction motors are being widely used by application engineers nowadays.

As explained earlier, under constant frequency and sinusoidal voltage operation a variety of radial magnetic force components are produced at different frequencies. At a fixed supply frequency operation, it is possible with some difficulty to avoid coincidences between the exciting forces and the resonances of the machine structure.

As the frequency of the supply is varied in order to increase or decrease the motor speed, these magnetic forces also drift with the supply frequency. Consequently, it is not possible to avoid excitation of resonances at all operating speeds. In addition, most frequency conversion equipment produce voltages that are rich in harmonics which further aggravate the problems. The net effect of impressing all these supply harmonics on the stator winding is to produce increased undesirable effects such as heating, parasitic torques, stray-losses, radiated noise and vibrations. Analytically, the effects of the power supply harmonics are treated individually and the net effect is determined by applying the principle of superposition. In the discussions presented in this chapter, it is assumed that the motor is operated from a variable-frequency power source having sinusoidal voltages.

6.2 Considerations for the Radial-Forces

The synchronous speed of an induction motor can be controlled by varying the supply frequency. In order to maintain approximately constant flux-density, the line voltage is also varied along with the frequency. In practice, the terminal voltage is controlled so that the ratio of phase-voltage to the frequency is kept constant. This type of speed control is commonly called the "constant volts per hertz" control. Since the air-gap flux-densities are maintained constant at the various frequencies, the torque produced by the motor and also the magnitudes of the magnetic radial-forces remain nearly the same. In Table 6.1, the frequencies at which the dominant radial-force components occur in the force spectra of squirrel-cage and wound-rotor induction motors are listed. It is evident from Table 6.1 that the frequencies at which the various radial-force components occur drift according to the supply frequency [33]. Consequently, it is impossible to avoid excitation of resonances of the stator-structure if a continuous range of operating speed is desired.

In the next section, the implications of the choice of number of stator and rotor slots on the circumferential distribution of the radial-forces are discussed. Also, some of the other commonly used techniques to mitigate the impairing effects of the radial-forces are described.

Table 6.1 : Frequencies of the important components in the force spectra of squirrel-cage and wound-rotor induction motors.

Source	Squirrel-cage induction motor	Wound-rotor induction motor
	Frequency	**Frequency**
Fundamental	2f	2f
Saturation	4f, 6f, 8f, ...	4f, 6f, 8f, ...
Saturation side-band	$\left[4 - n\frac{Z}{p}(1-s)\right]f$	$\left[4 - n \cdot 2m_2(1-s)\right]f$
(F_{Sn} - 2f)	$\left[2 - n\frac{Z}{p}(1-s)\right]f$	$\left[2 - n \cdot 2m_2(1-s)\right]f$
F_{Sn}	$\left[n\frac{Z}{p}(1-s)\right]f$	$\left[n \cdot 2m_2(1-s)\right]f$
(F_{Sn} + 2f)	$\left[2 + n\frac{Z}{p}(1-s)\right]f$	$\left[2 + n \cdot 2m_2(1-s)\right]f$
Saturation side-band	$\left[4 + n\frac{Z}{p}(1-s)\right]f$	$\left[4 + n \cdot 2m_2(1-s)\right]f$

6.2.1 Effects of stator and rotor slot-combinations

As generally known, the use of inappropriate combination of the number of stator and rotor slots is associated with undesirable effects such as cogging, crawling and increased magnetic noise. Some rules for slot-combinations that are commonly followed [57] are:

(a) [(S-Z) / 2p] is chosen to be an integer to avoid cogging torques.

(b) asynchronous harmonic torques are reduced if Z does not exceed [1.25 S].

(c) to limit synchronous harmonic torques, Z is not made equal to S or (S±2p).

The analytical techniques developed in this thesis, Chapters 2 and 3, are used to calculate the air-gap fields and the radial-forces with a view to identify the merits and

demerits of the choice of a particular combination of stator and rotor slots. In the following, the effects of using 42, 43 or 44 rotor bars in the 10 hp squirrel-cage induction machine described in Chapter 2 are analyzed.

In Table 6.2 are listed the pole-pairs of the various harmonic fields which will be generated in the test machine due to multiple armature reaction effects when the rotor has 42, 43 or 44 rotor bars using the procedure adopted for Table 3.3. The undamped triplen harmonic fields produced by the rotor are shown in columns with a shaded background. It is interesting to note that in the case of Z = 42, the triplen harmonic rotor fields are not produced. Consequently, all the rotor produced fields will be damped by the stator and the corresponding current components in the stator windings will be small. In general, no triplen harmonic fields are produced when the number of rotor bars Z is divisible by three.

The distribution of the radial-forces that acts on the stator and rotor surfaces was also calculated for Z = 42 and 44. Table 6.3 gives the force-pole-pairs of the important slot-harmonic forces for 42, 43 and 44 rotor bars. Comparing the spectra of the forces that act on a stator tooth for Z = 42, 43 and 44, it is observed that there is a decrease in the number of significant force components with the increase in the difference between the number of stator and rotor slots (Z - S). This is due to the fact that the number of force-poles increase with the increase in the difference (Z - S). Also, from the perspective of noise and vibrations the forces with higher number of poles are less important compared to the forces with fewer poles. The choice of using an odd number of rotor bars, such as Z = 43, would give rise to forces with odd number of force-pole-pairs. The choice of Z = 44 produces forces with either 0, 4 or 8 pairs of force-poles only. When the number of rotor bars is such that (Z - S) is an even multiple of p, the pole-pairs associated with the forces will also be an even multiple of p.

Although there is no significant difference in the amplitudes and frequency contents of the forces for Z = 42, 43, and 44, the choice of Z = 44 seems to be better from the consideration of the induced modes of vibrations associated with these forces. It is evident from Table 6.3 that the lower modes of vibrations, eg. n=1, 2, and 3 are not induced in the case of Z = 44, which is of significant importance from the perspective of vibrations and noise.

Table 6.2 : Pole-pairs of the various air-gap harmonic fields produced in the test machine due to multiple armature reaction effects for different values of rotor bars (Z = 42, 43 and 44).

	Z = 42					Z = 43					Z = 44					
g_1 \ g_2	0	-1	1	-2	2	0	-1	1	-2	2	0	-1	1	-2	2	g_3
2	2	-40	44	-82	86	2	-41	45	-84	88	2	-42	46	-86	90	0
-10	-10	-52	32	-94	74	-10	-53	33	-96	76	-10	-54	34	-98	78	-1
14	14	-28	56	-70	98	14	-29	57	-72	100	14	-30	58	-74	102	1
-22	-22	-64	20	-106	62	-22	-65	21	-108	64	-22	-66	22	-110	66	-2
26	26	-16	68	-58	110	26	-17	69	-60	112	26	-18	70	-62	114	2
-34	-34	-76	8	-118	50	-34	-77	9	-120	52	-34	-78	10	-122	54	-3
38	38	-4	80	-46	122	38	-5	81	-48	124	38	-6	82	-50	126	3
-46	-46	-88	-4	-130	38	-46	-89	-3	-132	40	-46	-90	-2	-134	42	-4
50	50	8	92	-34	134	50	7	93	-36	136	50	6	94	-38	138	4

Table 6.3 : Pole-pairs associated with the important forces for rotor bars; Z = 42, 43 & 44.

Source	Z = 42		Z = 43		Z = 44	
	Freq., Hz	Pairs of Force-poles	Freq., Hz	Pairs of Force-poles	Freq., Hz	Pairs of Force-poles
Fundamental	120	4	120	4	120	4
Saturation	240	8	240	8	240	8
	360	8	360	10	360	4
	480	8	480	8	480	8
	600	4	600	4	600	4
Saturation side-band	1020	6	1050	1	1080	4
1st order slot-harmonics (F_{S1})	1140	6 & -6	1170	3	1200	4
	1260	6	1290	7	1320	8
	1380	2	1410	1	1440	4
Saturation side-band	1500	6	1530	3	1560	4
Saturation side-band	2280	4	2340	6	2400	8
2nd order slot-harmonics (F_{S2})	2400	8	2460	2	2520	4
	2520	4	2580	2	2640	4
	2640	4	2700	6 & -6	2760	4
Saturation side-band	2760	8	2820	10	2880	8
Saturation side-band	3540	10	3630	1	3720	4
3rd order slot-harmonics (F_{S3})	3660	6 & -6	3750	3	3840	8
	3780	2	3870	3	3960	4
	3900	2	3990	1	4080	8
Saturation side-band	4020	10	4110	7	4200	4
Saturation side-band	4800	8	4920	8	5040	8
4th order slot-harmonics (F_{S4})	4920	4	5040	2 & -2	5160	8
	5040	8	5160	8	5280	4
	5160	8	5280	4	5400	4
Saturation side-band	5280	8	5400	10	5520	4
Saturation side-band	6060	2	6210	1	6360	4
5th order slot-harmonics (F_{S5})	6180	6	6330	5	6480	4
	6300	2	6450	1	6600	8
	6420	2	6570	3	6720	8
Saturation side-band	6540	6	6690	7	6840	8

6.2.2 Other Means of Mitigating the Undesirable Effects of the Radial-Forces

A straightforward, but uneconomical, method to decrease the magnetic noise is achieved by decreasing the air-gap flux-density. This method provides a noise power level reduction proportional to the 4^{th} power of the reduction in the flux-density [42]. Flux-density reduction is an expensive solution and it should be applied only after other possibilities of noise reduction have been explored.

The slots of low and medium-power induction machines are often skewed to achieve some relief from the magnetic noise. Generally, the most undesirable components of the magnetic forces are produced by the first order stator slot-harmonic air-gap fields. To be most effective, the skewing is usually chosen to be one stator slot-pitch. If the rotor slots are skewed and the rotor bars or coils are not properly insulated from the laminated rotor core, then equalising currents are produced between the various bars of the rotor. This often leads to localised overheating and adversely affects the torque characteristics. The provision of the insulation to reduce inter-bar currents frequently result in much higher manufacturing costs. In the case of medium and large size induction machines with long rotors, skewing of the rotor conductors can result in significant torsional vibrations and hence the noise radiated from these machines. In small and medium size machines of smaller lengths, the torsional natural frequencies of vibrations are above 10 kHz. For such motors proper skewing can be effective to control the vibrations and noise [2,13].

Eccentricity of the rotor results from the lack of strict control on the manufacturing and assembly processes for mass-produced machines. Eccentricity of the rotor is an inadvertent source of noise production, and the undesirable effects of eccentricity are best controlled using parallel paths with equalisers in the stator winding arrangements [15].

6.3. Considerations with Regard to Mechanical Response

It was seen in the previous chapters that lower levels of vibrations can be achieved even at resonance conditions by mismatching the number of pairs of force-poles of the radial-forces from the mode of vibration associated with the resonances. For stators of medium and small size electrical machines, the important modes of

vibrations at resonance are n=0, 1, 2, 3, and 4. For large size machines, the resonances associated with higher modes of vibration may also be significant [35]. It was observed from the experimental investigations conducted on the 120 hp induction motor stator models, that the mode n=0 vibration is excited equally well with most force-distributions at the resonant frequencies corresponding to n=0. The resonances associated with odd modes of vibrations, n=1 and n=3, do not respond very well to force-distributions having even number of pairs of force-poles. Consequently, the reduction in the vibration amplitudes thus obtained, and the sound radiated thereby, can be as much as 20 dB. As already discussed in Chapter 5, the force-distributions with 2 or 4 pairs of force-poles do excite well the resonances associated with both modes n=2 and n=4, their corresponding vibration amplitudes diminish rapidly as their excitation frequency is moved away from the resonance frequency.

The individual laminations are usually not segmented for small motors, but they are usually segmented in the case of larger machines. The stack of laminations is held in compression by various mechanical means such as axial keying. The stator stack is supported by the frame of the motor. The core is sufficiently stiff to be entirely functional mechanically. It was observed from the experimental investigations on the 120 hp induction motor stator that the windings and the laminations do contribute significantly to the damping present in the stator-structure. In references [36,38], the authors have demonstrated that the damping in the stator-structure reduces considerably when it is impregnated and varnished. Impregnating the stator provides increased insulation between the stator coils and the stator body, which can be achieved by using better insulation material in the slot.

6.4 Experimental Results Obtained by the Variable Frequency Operation of the 10 hp Squirrel-Cage Induction Motor

Experimental investigations were conducted on the 10 hp squirrel-cage induction motor whose design details are provided in Chapter 3. The motor was operated from a sinusoidal voltage source and the supply frequencies were varied from 24 Hz to 96 Hz. This frequency range translates to a speed range from 720 rpm to 2900 rpm. During

these tests, the supply voltage was varied along with the supply-frequency in order to keep the flux levels approximately same. The impulse response of the stator of the 10 hp induction motor was measured using the hammer excitation, and it is shown in Fig. 6.1. The vibration of the stator was also determined using the magnetic shaker procedure [33]. The resonance peaks were individually examined, and these resonances are provided in Table 6.4. Table 6.5 provides the frequencies at which the various slot-harmonic forces occur when the test motor is operated at different supply frequencies. The experimental investigations were conducted at no-load conditions. The operating speeds of the motor are also provided in Table 6.5. The associated slip at these speeds are provided in percentage values in Table 6.5.

Fig. 6.2(a) shows the magnitudes of twice the supply-frequency component in the vibration signals measured on the surface of the test motor, when the motor was operated at different supply frequencies. The supply-frequencies were so chosen such that some of the slot-harmonic forces would be close to few of the resonant frequencies of the stator. The measured vibration levels are shown on a logarithmic scale in mm/sec^2, and also in dB relative to 10^{-2} mm/sec^2. The frequencies at which these vibration components occur are shown on the scale at the top of the plot. It is observed from Fig. 6.2(a) that twice the supply-frequency component of the vibrations increases by about 20 dB over the frequency range from 24 Hz to 96 Hz. For the sake of explanation, a section of the response of the stator in the corresponding frequency range is shown in Fig. 6.2(b). It is observed from the impulse response that there are no resonances of the stator in this frequency range. It should be mentioned here that in the case of large machines, resonances of the stator may occur in this lower end of the audio frequency range [35].

Fig. 6.3 shows the measured magnitudes of vibration components corresponding to the 1^{st} order slot-harmonic forces. In addition, the impulse response of the stator in the corresponding frequency ranges is shown on the plots. It is observed that the 1^{st} order slot-harmonic component at $(F_{S1}-2f)$ is most effective in inducing vibrations of mode n=2 at resonances of 730 Hz and 970 Hz. The mode n=3 resonance at 1930 Hz is best excited by the 1^{st} order slot-harmonic component, $(F_{S1}+2f)$. It is recalled from Table 6.3 that the significant pairs of force-poles associated with the slot-harmonic force

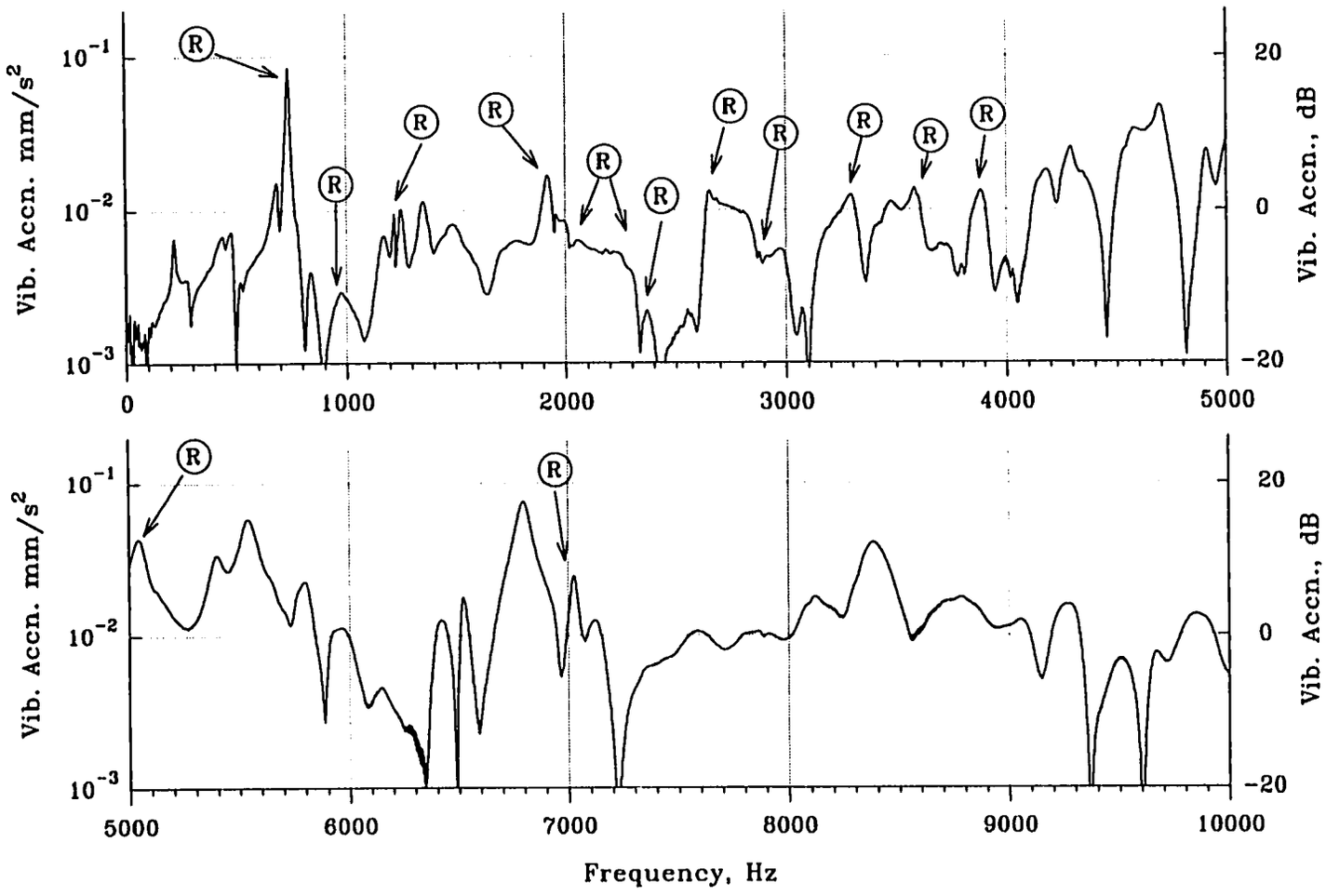

Figure 6.1 : Impulse response, measured using hammer excitation, of the stator of the 10 hp squirrel-cage induction motor.

Table 6.4 : Resonances of the 10 hp squirrel-cage induction motor.

S. No.	Resonant Frequency, Hz	Mode, n
1	730	2
2	970	2
3	1200	*
4	1942	3
5	2046	3
6	2235	*
7	2350	*
8	2650	*
9	2893	*
10	3314	1
11	3628	3
12	3888	4
13	5092	*
14	5134	*
15	6959	*

* : circumferential modes were not well-defined.

components, (F_{S1}-2f), F_{S1}, and (F_{S1}+2f), are 3, 7 and 1, respectively. As expected, the force component at F_{S1} is least effective in exciting the resonances of the stator due to its higher number of pairs of force-poles.

Fig. 6.4 shows the measured magnitudes of vibration components corresponding to the 2^{nd} order slot-harmonic forces. The significant pairs of force-poles associated with the slot-harmonic force components, (F_{S2}-2f), F_{S2}, and (F_{S2}+2f), are 2, 2 and 6, respectively. The measured vibration components corresponding to the slot-harmonic force (F_{S2}+2f) have the least magnitudes in comparison to the vibration components associated with forces (F_{S2}-2f) and F_{S2}.

Table 6.5 : Frequencies at which the various slot-harmonic forces occur when the 10 hp squirrel-cage induction motor, rotor with Z=43, is operated at various supply-frequencies.

Supply-Freq., Hz	24.2	27.2	35.1	39.4	45.1	49.6	55.6	60.0	69.4	79.3	81.8	89.0	95.7
Speed, rpm	726.0	816.0	1052.0	1182.0	1353.0	1487.0	1667.0	1799.0	2080.0	2377.0	2453.0	2669.0	2867.0
Slip, %	0.00	0.00	0.09	0.00	0.00	0.07	0.06	0.06	0.10	0.08	0.04	0.04	0.14
Fs1	471.9	530.4	683.7	768.3	879.5	966.5	1083.5	1169.3	1351.9	1544.9	1594.4	1734.8	1863.3
	520.3	584.8	753.9	847.1	969.7	1065.7	1194.7	1289.3	1490.7	1703.5	1758.0	1912.8	2054.7
	568.7	639.2	824.1	925.9	1059.9	1164.9	1305.9	1409.3	1629.5	1862.1	1921.6	2090.8	2246.1
Fs2	992.2	1115.2	1437.7	1615.4	1849.1	2032.2	2278.2	2458.6	2842.5	3248.4	3352.4	3647.6	3918.0
	1040.6	1169.6	1507.9	1694.2	1939.3	2131.4	2389.4	2578.6	2981.3	3407.0	3516.0	3825.6	4109.4
	1089.0	1224.0	1578.1	1773.0	2029.5	2230.6	2500.6	2698.6	3120.1	3565.6	3679.6	4003.6	4300.8
Fs3	1512.5	1700.0	2191.6	2462.5	2818.8	3097.9	3472.9	3747.9	4333.2	4952.0	5110.4	5560.4	5972.7
	1560.9	1754.4	2261.8	2541.3	2909.0	3197.1	3584.1	3867.9	4472.0	5110.6	5274.0	5738.4	6164.1
	1609.3	1808.8	2332.0	2620.1	2999.2	3296.3	3695.3	3987.9	4610.8	5269.2	5437.6	5916.4	6355.5
Fs4	2032.8	2284.8	2945.5	3309.6	3788.4	4163.5	4667.5	5037.1	5823.9	6655.5	6868.3	7473.1	8027.3
	2081.2	2339.2	3015.7	3388.4	3878.6	4262.7	4778.7	5157.1	5962.7	6814.1	7031.9	7651.1	8218.7
	2129.6	2393.6	3085.9	3467.2	3968.8	4361.9	4889.9	5277.1	6101.5	6972.7	7195.5	7829.1	8410.1
Fs5	2553.1	2869.6	3699.5	4156.7	4758.1	5229.2	5862.2	6326.4	7314.5	8359.0	8626.3	9385.9	10082.0
	2601.5	2924.0	3769.7	4235.5	4848.3	5328.4	5973.4	6446.4	7453.3	8517.6	8789.9	9563.9	10273.4
	2649.9	2978.4	3839.9	4314.3	4938.5	5427.6	6084.6	6566.4	7592.1	8676.2	8953.5	9741.9	10464.8

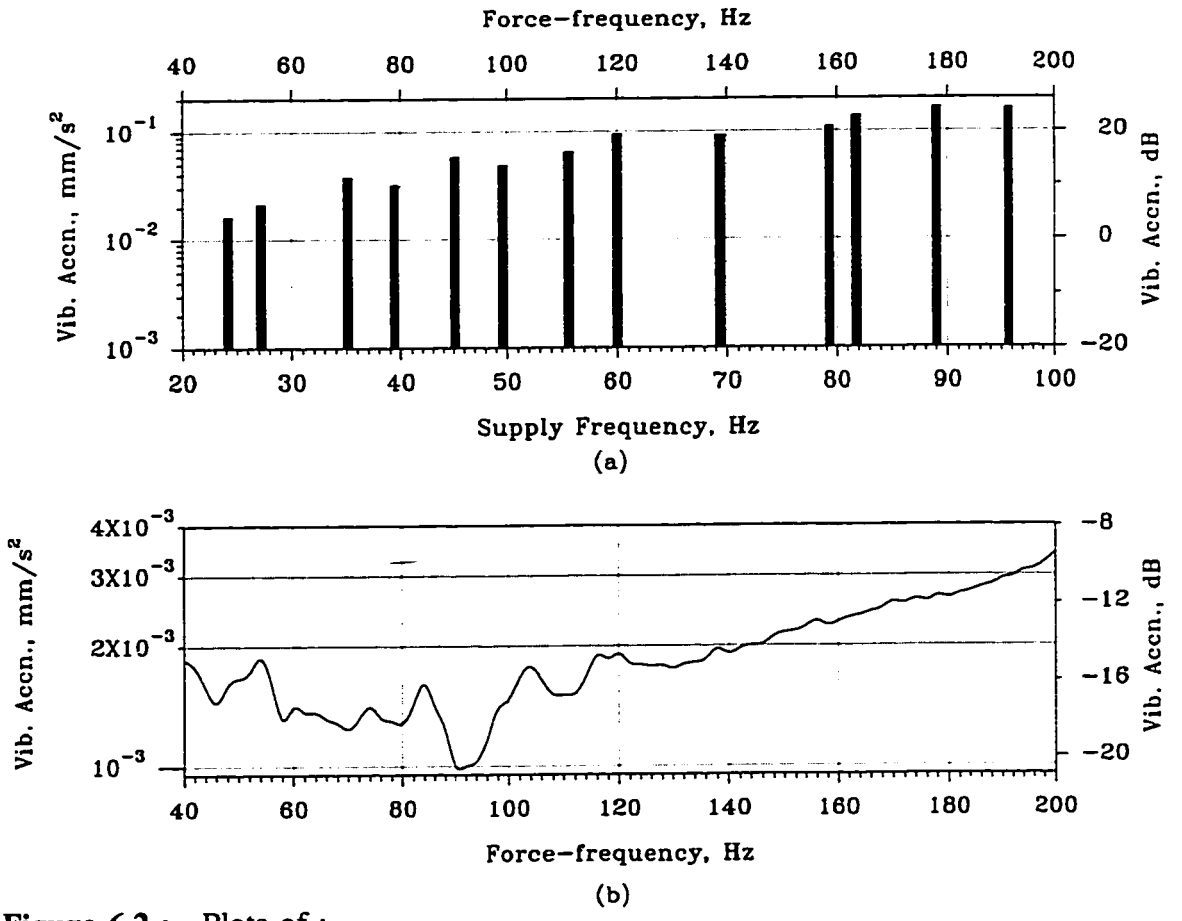

Figure 6.2 : Plots of :

(a) Vibration components of twice the supply-frequency measured when the machine was operated at various supply-frequencies,

(b) Impulse response of the stator of the motor.

Fig. 6.5 shows the measured magnitudes of vibration components corresponding to the 3rd order slot-harmonic forces. The significant pairs of force-poles associated with the slot-harmonic force components, (F_{S3}-2f), F_{S3}, and (F_{S3}+2f), are 9, 3 and 1, respectively. In general, most of the vibration components shown in Fig. 6.5 are quite small.

Fig. 6.6 shows the measured magnitudes of vibration components corresponding to the 4th order slot-harmonic forces. The significant pairs of force-poles associated with the slot-harmonic force components, (F_{S4}-2f), F_{S4}, and (F_{S4}+2f), are 10, 8 and 4, respectively. The vibration components corresponding to force (F_{S4}+2f) are dominant. In general, the vibration components are comparable to those shown in Fig. 6.5.

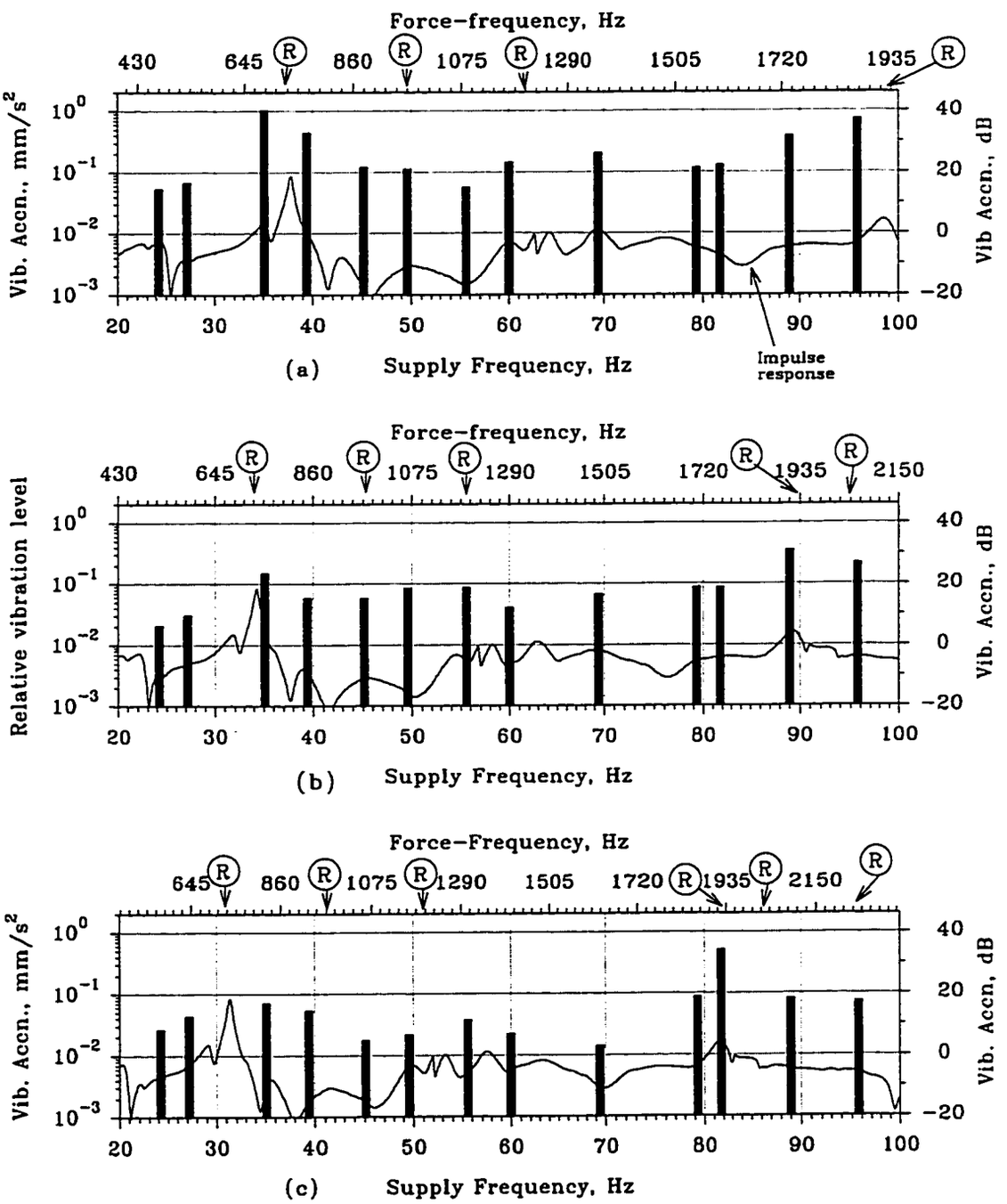

Figure 6.3 : Plots of the measured vibration components due to the 1st order slot-harmonic forces when the machine was operated at the various supply-frequencies. Vibration levels corresponding to;
(a) (F_{S1}-2f), (b) F_{S1}, (c) (F_{S1}+2f).

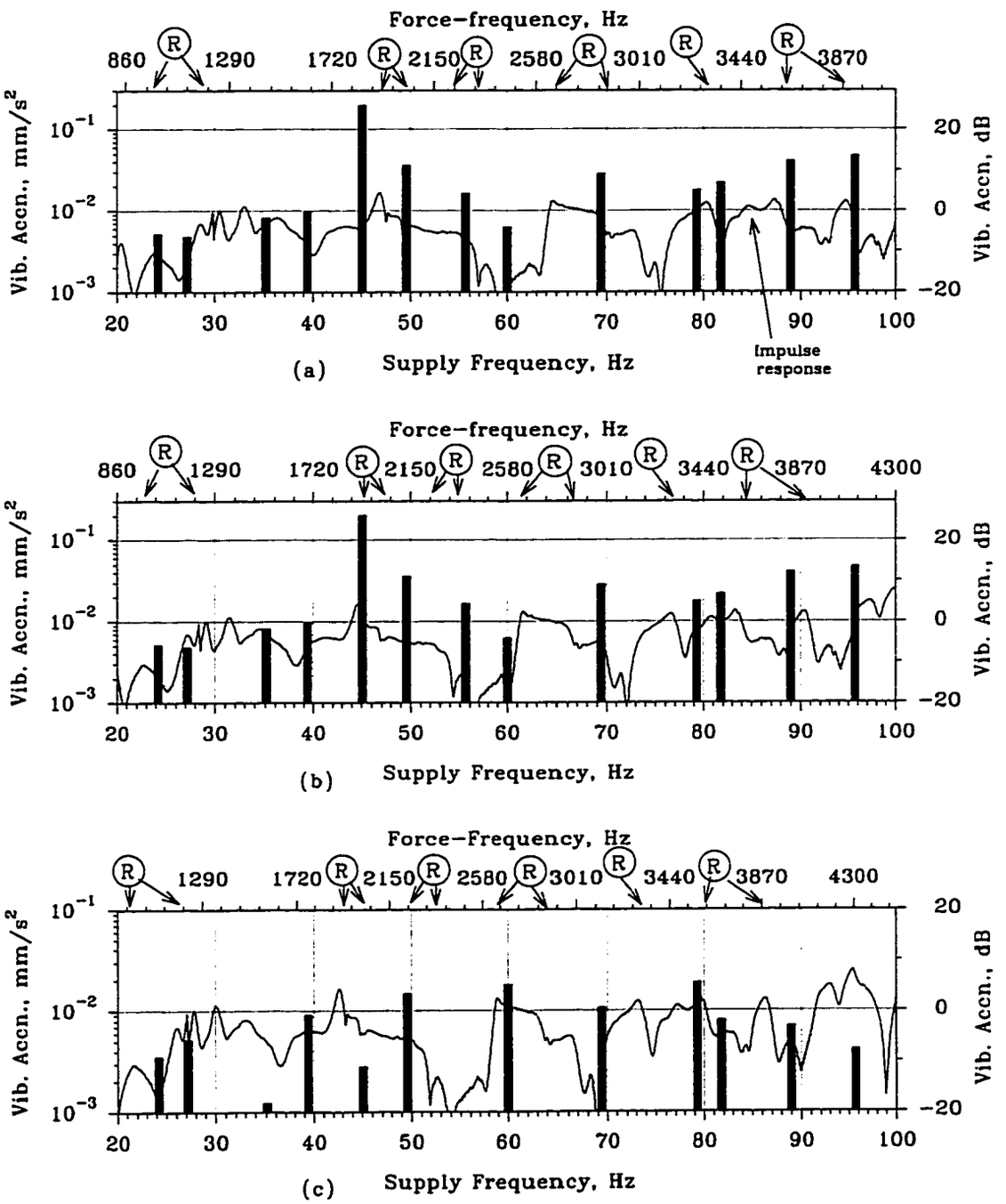

Figure 6.4 : Plots of the measured vibration components due to the 2nd order slot-harmonic forces when the machine was operated at the various supply-frequencies. Vibration levels corresponding to;
(a) (F_{S2}-2f), (b) F_{S2}, (c) (F_{S2}+2f).

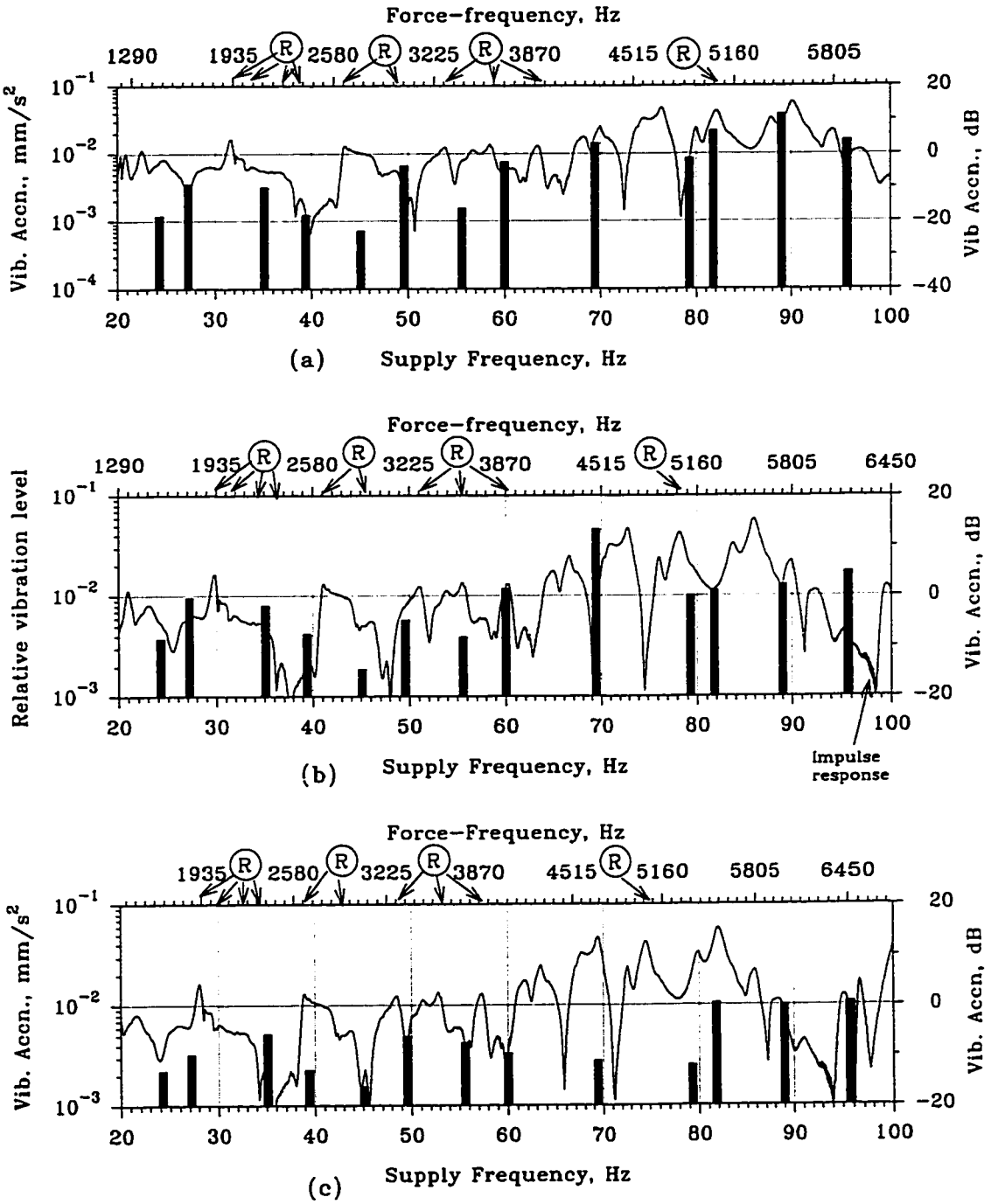

Figure 6.5 : Plots of the measured vibration components due to the 3rd order slot-harmonic forces when the machine was operated at the various supply-frequencies. Vibration levels corresponding to;
(a) (F_{S3}-2f), (b) F_{S3}, (c) (F_{S3}+2f).

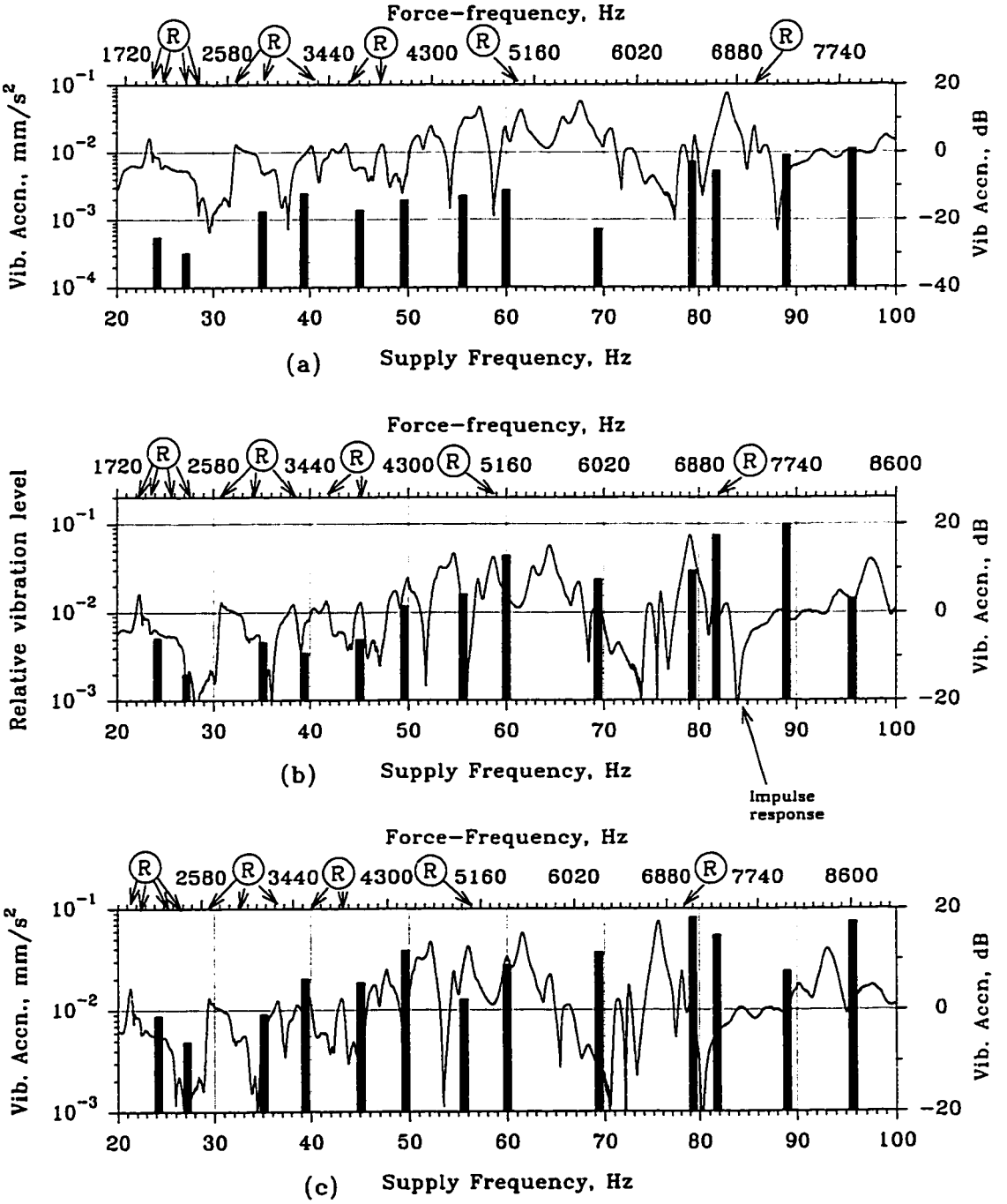

Figure 6.6 : Plots of the measured vibration components due to the 4th order slot-harmonic forces when the machine was operated at the various supply-frequencies. Vibration levels corresponding to;
(a) (F_{S4}-2f), (b) F_{S4}, (c) (F_{S4}+2f).

Fig. 6.7 shows the measured magnitudes of vibration components corresponding to the 5^{th} order slot-harmonic forces. The significant pairs of force-poles associated with the slot-harmonic force components, (F_{S5}-2f), F_{S5}, and (F_{S5}+2f), are 5, 1 and 3, respectively. It is interesting to note that the vibration components corresponding to F_{S5} are quite significant.

6.5 Summarising Comments

In this chapter, the implications arising from the operation of an induction motor on a variable-frequency power supply from the perspective of vibrations and noise are described. Some of the salient considerations involved in the design of a quiet variable-speed drive are:

(i) When a variable speed operation is desired, it is not always possible to avoid excitation of all the resonances of the machine stator. At resonance, the circumferential distribution of the excitation forces determines its ability in inducing vibrations.

(ii) The choice of the number of stator and rotor slots is an important parameter in the design of a quiet induction motor. It was observed from the experimental investigations conducted on the 10 hp squirrel-cage induction motor that the forces associated with fewer pairs of force-poles are the most troublesome from the perspective of vibrations and noise. As discussed, there will be a decrease in the number of significant components in the force spectrum with the increase in the difference between the number of stator and rotor slots.

(iii) The force components with odd number of pairs of force-poles are produced only when an odd number of slots is used for the rotor. The absence of force components with 1 and 3 pairs of force-poles is of advantage, and therefore the choice of odd number of rotor slots must be avoided. With certain slot-combinations involving even number of stator and rotor slots, it is further possible to eliminate the force components with two pairs of force-poles.

(iv) The experimental investigations on the 10 hp squirrel-cage induction motor presented in this chapter describe procedures to determine the important slot-harmonic forces. Unfortunately, the test machine was not very suitable to obtain

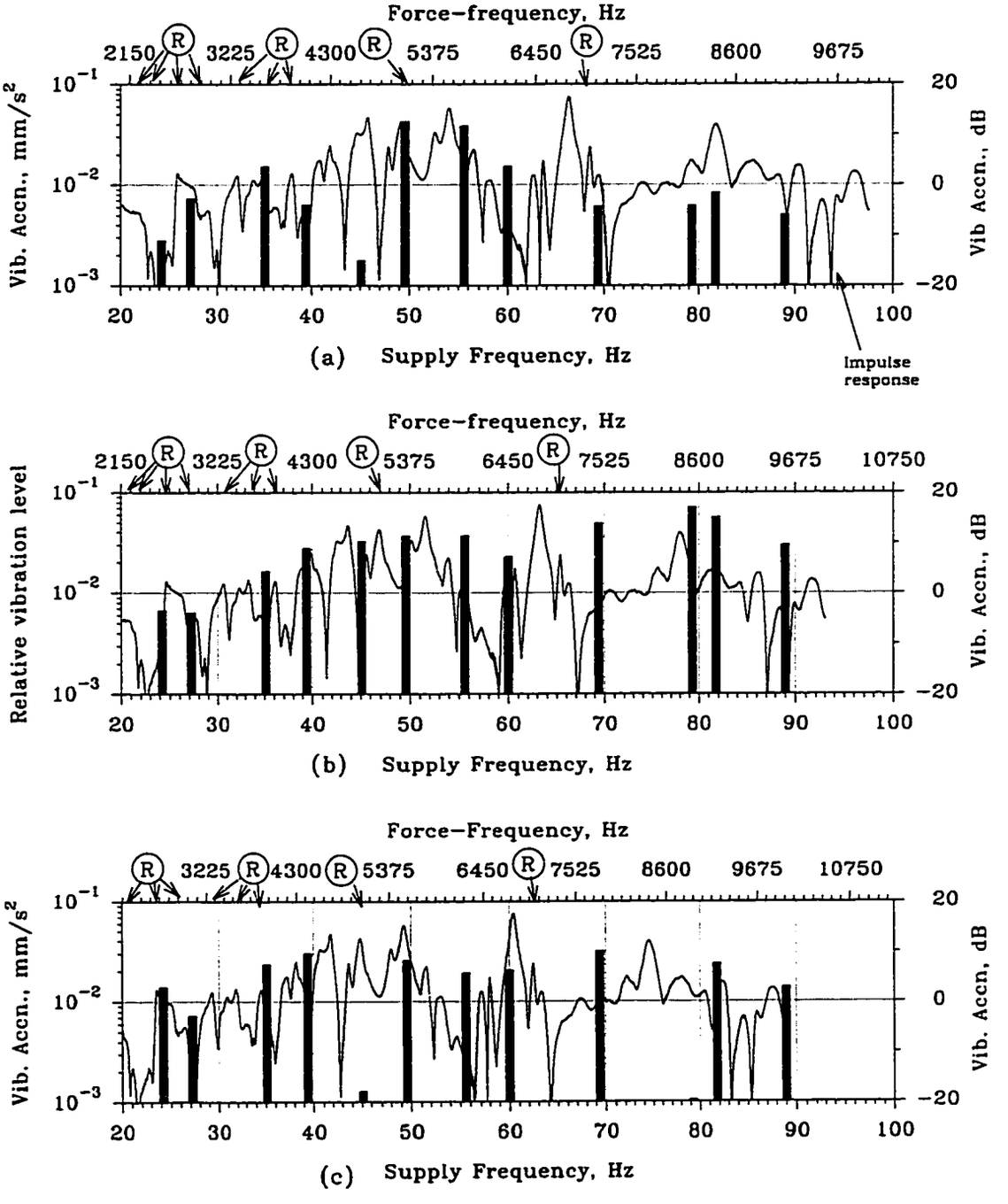

Figure 6.7 : Plots of the measured vibration components due to the 5th order slot-harmonic forces when the machine was operated at the various supply-frequencies. Vibration levels corresponding to;
(a) (F_{S5}-2f), (b) F_{S5}, (c) (F_{S5}+2f).

conclusive results. A specially designed motor will be required to conduct further experimental verifications. Considering the difficulties involved in isolating the interference from the loading-device, the experimental investigations were conducted at no-load. At no-load, since the magnitudes of the slot-harmonic forces are quite small, the higher order effects are not pronounced.

(v) The number of orders of the slot-harmonic fields, and hence the slot-harmonic forces, which need to be considered depends on the machine. All the components within the critical portion of the audio-frequency range, i.e. from 1 to 5 kHz, should be considered. For small and medium size squirrel-cage induction motors, consideration until the 5^{th} order slot-harmonic forces is usually sufficient. Since the force-frequencies are inversely related to the number of pole-pairs of the fundamental air-gap field, more orders of the slot-harmonic forces should be considered for low-speed motors. This is chiefly applicable to large machines, which have many more resonances in the critical portion of the audio-frequency range. Although the magnitudes of the forces are important, the mechanical response at the resonance generally dictates the level of associated vibrations. In wound-rotor induction motors, most of the troublesome slot-harmonic forces are confined to frequencies below 2 kHz, and their magnitudes decrease more rapidly with increasing orders.

(vi) Most of the undesirable vibrations and noise are produced by the slot-harmonic field components. These slot-harmonic fields increase significantly from no-load to the rated load condition. The use of semi-closed slots, magnetic wedges across the slot-openings, skewing of the rotor slots in small and medium size machines are useful measures in limiting the magnitudes of the slot-harmonic fields and hence the slot-harmonic forces.

7. CONCLUSIONS

An analysis of a general nature has been developed for the calculation of the air-gap fields and the electromagnetic radial-forces in induction machines. The analysis is based on the permeance-method for the determination of the air-gap fields. Modifications have been made to the permeance-method in order to incorporate the effects of the rotor MMFs while considering the mutual interactions between the stator and rotor produced fields. The analysis is rigorous, and it can be easily modified to include the effects of different stator and rotor arrangements. The computation techniques used in the thesis are comprehensive and they provide reliable information on the air-gap fields and the electromagnetic radial-forces.

A systematic approach was used to calculate the air-gap fields and the electromagnetic radial-forces produced in a 7.5 kW (10 hp) squirrel-cage induction motor, and a 70 kW (95 hp) wound-rotor induction motor. Various aspects of the calculated results were verified experimentally on the 7.5 kW squirrel-cage induction motor. The following important conclusions are drawn based on the analytical predictions and the experimental results.

7.1 Determination of the Electromagnetic Air-gap Fields

(i) The primary armature reaction involves the consideration of the stator and rotor MMFs produced by their fundamental currents. To obtain sufficiently accurate information about the air-gap fields, it is important to consider the multiple armature reactions. Ignoring the multiple armature reactions between the stator and rotor will result in higher estimates of the magnitudes of the various air-gap fields.

(ii) It was found that the air-gap harmonic fields produce circulating currents of higher frequencies both in the stator and the rotor windings. Some of these

currents may be substantial. These circulating currents damp certain harmonic air-gap fields. In contrast to squirrel-cage induction motors, the current harmonics for wound-rotor induction motors occur at lower frequencies.

(iii) In a squirrel-cage induction motor, when the number of rotor bars is not an integer multiple of the number of phases on the stator, then triplen harmonic air-gap fields are produced. These fields induce zero-sequence voltages in the stator windings. The magnitudes of the corresponding currents would depend on the connections of the stator windings. The zero-sequence currents produce pulsating fields, and they are responsible for the production of zero-sequence torques and other localised leakage-field effects. In distinction to squirrel-cage induction motors, since the stator and rotor of wound-rotor induction machines have polyphase windings, commonly with three phases, the triplen-order fields are generally not produced.

(iv) In both types of motors, the slot-harmonic air-gap fields are the dominant harmonic components in the air-gap field distribution. These fields are produced as a direct consequence of the slotting of the stator and rotor surfaces. The slot-harmonic components increase appreciably with load owing to the increased harmonic content in the rotor MMF. It is important to note that the slot-harmonic fields are responsible for most parasitic effects associated with the operation of induction machines.

(v) While comparing the calculated and experimental values of the slot-harmonic field components in the squirrel-cage induction motor, it was observed that the correlation between the two improved with the load. The increased discrepancy at no-load is not significant. In most cases, the difference between the predicted and the measured amplitudes of the slot-harmonic field components is less than 5% of the amplitude of the fundamental component. The accuracy realised in the calculation of the air-gap field amplitudes is quite satisfactory from the perspective of vibration and noise problems.

7.2 Determination of the Electromagnetic Radial-Forces

(i) The force component at twice the line frequency is produced mainly by the fundamental air-gap field. Generally, the vibration response of the stator is not significant to this force in the case of induction machines. Since its frequency is close to the lower limit of the audible frequency range, this force component is not important with regard to the radiated acoustic noise.

(ii) The other dominant components in the spectrum of the radial-forces are produced by the slot-harmonic fields. In squirrel-cage induction motors, they occur as distinct bands in the spectrum of the radial-forces according to their harmonic orders. For small and medium size machines, considerations up to the 5^{th} order slot-harmonic forces are usually sufficient. Even the higher frequency components need to be considered for a large machine as several resonant frequencies may exist in the audio frequency range.

(iii) By comparing the spectra of the forces produced by the squirrel-cage and the wound-rotor induction motors, it was evident that the squirrel-cage induction motor is very rich in harmonics. In the case of squirrel-cage induction motors, the slot-harmonic forces are usually spread over a major portion of the audio-frequency range. In contrast, the force components for wound-rotor induction motors are confined to the lower portion of the audio-frequency range, and are typically below 2 kHz. The frequencies at which these slot-harmonic forces are produced depend on the number of phases on the rotor windings and the speed of the machine. Further, since it is very common to use 3-phase windings on the stator and the rotor, the slot-harmonic forces do not occur separately as distinct bands in the force spectra of a wound-rotor induction motor.

(iv) Magnetic saturation produces force components at 4f, 6f, 8f, etc., and also the side-bands on either side of the slot-harmonic force. The experimental investigations confirmed the existence of the forces produced by the saturation, and also revealed that they can excite resonances of the machine.

(v) Considering a particular component of the radial-force, its distribution along the air-gap produces a sinusoidal deformation of the stator and rotor. Since the mechanical response of the stator decreases with increasing number of pairs of

force-poles, the forces with fewer poles are of greater significance from the perspective of acoustic noise produced by the induction machine.

(vi) The importance of the stator and rotor slot-combinations in squirrel-cage induction machines were closely examined. The following observations are made with respect to the spectrum of the radial-forces:

(a) The number of dominant components in the spectrum of the radial-forces decreases with the increase in the difference between the number of stator and rotor slots.

(b) The force components with odd number of pairs of force-poles are produced only when an odd number of slots is used in the rotor. The absence of force components with 1 and 3 pairs of force-poles is of advantage, and therefore the choice of odd number of rotor slots should be avoided.

(c) The number of rotor bars such that the difference (Z - S) is an even multiple of p, will produce forces with force pole-pairs of 2p, 4p, 6p, etc. This combination is of benefit in eliminating the force-components with two pairs of force-poles for the machines with p>1.

(vii) In wound-rotor induction motors, it is often desired to have integral-slot windings in the stator and rotor, which constrains the choice of the number of stator and rotor slots. The use of preferred number of slots, such as 36, 48, 72, 96, etc., leads to the various force components having a circumferential distribution with pairs of force-poles of 0, 4, 8, etc. In general, the radial-forces in wound-rotor induction machines are often less tròublesome than their counterparts in squirrel-cage induction machines.

7.3 Experimental Investigations with Distributed Excitation

Extensive experimental investigations were conducted to study the vibration behaviour of electrical machine stators from the perspective of designing quiet electrical machines. The experimental modal-analysis of the stator models were conducted using distributed electromagnetic forces. The following observations about the nature of vibrations associated with the resonances of stators are derived from the investigations:

(i) The frequency of resonance increases progressively with the increasing complexity of the mode of vibration. The modes n=0 and n=1 are exceptions to this rule, and they occur at a higher frequency. The vibration modes n = 2, 3 and 4 are important modes of vibration for small and medium size stators.

(ii) From the viewpoint of experimentally investigating the vibration behaviour of electrical machine stators, the main advantage of the distributed excitation forces is the ability to excite resonances selectively. It was observed that the best vibration response was obtained with the force-distribution that had the same pairs of force-poles as the circumferential mode of vibration associated with the corresponding resonance. Further, the experimental results revealed that there is a significant amount of coupling between the mode n=2 resonances and the force-distribution with 4 pairs of force-poles, and vice versa.

(iii) The distributed electromagnetic forces facilitate the injection of substantially more vibrational energy uniformly into the test models. This was especially important for the laminated stator model with windings.

(iv) The damping-ratios obtained for the solid stator-shell model is within the range of values 1×10^{-4} to 6×10^{-4}, as reported for steel [50]. The results exhibit a decrease with frequency. The decrease of the damping-ratios with frequency signifies the predominance of friction-damping.

(v) It was observed in the case of the laminated stator model with windings that the damping-ratios did not exhibit direct relationship with the resonant frequencies. This suggested the presence of non-linear damping effects which are normally present in composite structures built using different materials. Also, it is indicative of the energy dissipation at the boundaries of the various structural elements. The values of the damping-ratios obtained for this model are approximately 10 to 100 times of that obtained for the solid stator-shell model. Since the actual damping present is proportional to the resonant frequency and the damping-ratio, it follows that the actual damping present in the laminated stator model at higher frequencies is much larger.

(vi) Another significant advantage of using the distributed electromagnetic forces is their ability to induce vibrations in a stator model uniformly. This results in well

defined sinusoidal mode-shape patterns in the measurements as predicted by the theory.

(vii) Contrary to the popular belief, it was observed that stationary "standing-wave" deformation patterns of vibrations were produced at the resonances even with rotating force-distributions.

(viii) From the perspective of designing quieter machines and achieving lower levels of vibrations, it is critical that the force-frequency be kept away from the resonant frequency. It was observed from the experimental investigations that the resonances of the stators were excited by most of the distributed force arrangements. Further, at resonance, the amplitudes of the vibrations depend to a lesser extent on the type of force-distribution. In the course of the investigations, it was ascertained that the force-frequency overrides the importance of the force-distribution.

(ix) Significantly lower levels of vibrations can be achieved at the mode n=1 and n=3 resonances of the machine structure by ensuring that the force-distributions which match these mode-shapes either do not exist or are made as small as possible. For the vibrations at modes n=2 and n=4 resonances, both the force-distributions, with 2 and 4 pairs of force-poles, are equally effective.

7.4 Variable Frequency Operation

Theoretical and experimental investigations were conducted to study the effects of variable frequency operation of an induction motor. The salient observations with regard to important radial-forces an the ensuing vibrations were drawn from the investigations, and they are reported in Chapter 6. Two important conclusions are reported here:

(i) Under the variable frequency operation of induction motors, it is not always possible to avoid excitation of the resonances of the machine stator. The experimental investigations conducted on the 10 hp squirrel-cage induction motor confirmed that the forces associated with fewer pairs of force-poles are the most critical. Further, it was established that the frequency of an exciting force overrides the importance of the mode-shape at a given resonance.

(ii) Most of the undesirable vibrations and noise are produced by the slot-harmonic field components. The use of semi-closed slots, magnetic wedges across the slot-openings and skewing of the rotor slots in small & medium size machines are useful measures in limiting the magnitudes of the slot-harmonic fields, and hence the slot-harmonic forces.

A direct application of the findings of the various studies reported in this thesis is in the design of quieter induction motors suitable for fixed and variable frequency operations. The physical interpretations of the results, obtained in the course of the investigations, would help in acquiring a better understanding of the electromagnetic excitation forces and the vibration response of stators in relation to the problem of electromagnetic acoustic noise in electrical machines. Finally, it is hoped that the theoretical and experimental investigations reported in this thesis would be beneficial to the design engineers in their attempts to build quiet electrical machines and drive systems.

8. REFERENCES

1. Ellison A.J., and Moore C.J., "Acoustic Noise and Vibration of Rotating Electric Machines", Proc. IEE, Vol. 115, No. 11, Nov. 1968, pp. 1633-1640.
2. Cochran P.L., "Polyphase Induction Motors - Analysis, Design and Applications", Marcel and Dekker, New York, 1989.
3. Sacks T., "Europe's drive for efficiency", Electrical Review, West Sussex, England, 26 Nov - 9 Dec 96, Vol. 229, No. 3, pp. 18-21.
4. Yang S.J., and Ellison A.J, "Noise and Vibration", Handbook of Electric Machines, Edited by Nasar S.A., McGraw Hill, 1987, Chapter 14, pp. 14.1-14.55.
5. Talaat M.E., "Calculation of Windage Noise Power Level in Large Induction Motors", AIEE Transactions, 1957, pp. 46 - 55.
6. Behar A., "Legislative Overview : Canada's Workplace Noise Regulations", Occupational Health and Safety Canada - Magazine, March/April 1994, Vol. 10, No. 2, pp. 98-100.
7. Stepkin R., and Mosely R.E., "Noise Control - A Guide for Workers and Employers", An Occupational Health and Safety (OSHA) publication, Published by the American Society of Safety Engineers, 1984.
8. "IEC Recommendations on Rotating Electrical Machines, Noise Limits", IEC Publications No. 34-9, 1990.
9. Girgis R.S., "Theoretical and Experimental investigations on Resonant Frequencies and Natural Response of Stators of Electrical Machines", Ph.D. Thesis, Univ. of Saskatchewan, 1978.
10. Belmans R., Binns K.J., Geysen W., and Vandenput A., "Vibrations and Audible Noise in Alternating Current Machines", NATO ASI series, Series E: Applied Sciences - Vol. 148, Kluwer Academic Publishers, 1986.
11. Fehr R.O., and Muster D.F., "Electric Motor and Generator Noise", Handbook of Noise Control - Harris, 1957, chapter 30, pp 1-24.
12. Timar P.L., Fazekas A., Kiss J., Miklos A., and Yang S.J., "Noise and Vibration of Electrical Machines", Studies in Electrical and Electronic Engineering 34, Elsevier Science Publishing Co., N.Y., USA, 1989.
13. Yang S.J., "Low-Noise Electrical Motors", Clarendon Press, Oxford, U.K., 1981.
14. Heller B., and Jokl A.L., "Tangential Forces in Squirrel-cage Induction Motors", IEEE Transactions on Power Apparatus and Systems, Vol. PAS 88, No. 4, 1969, pp. 484-491.

15. Ellison A.J., and Yang S.J., "Effects of Rotor Eccentricity on Acoustic Noise from Induction Machines", Proc. IEE, Vol. 118, No. 1, Jan. 1971, pp. 174-184.

16. Oberretl K., "The Field Harmonic Theory of the Squirrel-Cage Induction Motor taking Multiple Armature Reaction and Parallel Branches into Account", (in German), Archiv Für Elecktrotechnik, Vol. 49, 1965, pp. 343-364.

17. Oberretl K., "Field Harmonic Theory of Slip-ring Induction Motors Taking Multiple Armature Reaction into Account", Proc. IEE, Vol. 117, No. 8, Aug. 1970, pp. 1667-1674.

18. Binns K.J., and Schmid E., "Some Concepts involves in the Analysis of the Magnetic Field in Cage Induction Machines", Proc. IEE, Vol. 122, No. 2, Feb. 1975, pp. 169-175.

19. Binns K.J., "Calculation of Some Basic Flux Quantities in Induction and Other Doubly Slotted Electrical Machines", Proc. IEE, Vol. 111, No. 11, 1964, pp. 1847-1858.

20. Binns K.J., and Rowlands R.S., "Radial tooth Ripple Forces in Induction Motors due to the Main Flux", Proc. IEE, Vol. 125, No. 11, pp. 1227-1231.

21. Binns K.J., and Kahan P.A., "Effect of load on the Flux Pulsations of Induction Motor teeth", Proc. IEE, Vol. 127, No. 4, Feb. 1980, pp. 223-230.

22. Chari M.V.K. and Sylvester P.P., "Finite Elements in Electrical and Magnetic Field Problems", John Wiley & Sons, 1980.

23. Nehl T.W., and Demerdash N.A.O., "Finite Element - State Space Modeling Environments for Electric Motor Drives", IEEE Tutorial on Adjustable Speed Drives, Course Text, 92 EHO 362-4-PWR, IEEE Publishing Services, 1992.

24. Baldassari P. and Demerdash N.A.O. "A Combined Finite Element-State Space Modeling Environment for Induction Motors in the ABC Frame of Reference: The Blocked Rotor and Sinusoidally Energised Load Conditions", IEEE Transactions on Energy Conversion, Dec. 92, Vol. 7, No. 4, pp. 710-720.

25. Flack T.J., and Williamson S., "Air Gap Fields and Pressure Waves in Closed-Slot Cage Rotor Induction Motor", Sixth International Conference on Electrical Machines and Drives, Oxford, U.K., Sept. 1993, Proceedings : IEE Conference Publication No. 376, pp. 552 - 557.

26. Moreira J.C. , and Lipo T.A., "Modelling of saturated ac machines including air-gap flux harmonic components", IEEE Transactions on Industry Applications, Vol. 28, No. 2, pp. 343-349, March 1992.

27. Lee C.H., "Saturation Harmonics of Polyphase Induction Machines", AIEE Transactions, Vol. 80, Oct. 1961, pp. 597-603.

28. Chalmers B.J., and Dodgson R., "Waveshapes of Flux density in Polyphase Induction Motors under Saturated conditions", IEEE Transactions on Power Apparatus and Systems, Vol. 90, No. 2, Mar./Apr. 1971, pp. 564-569.

29. Yang S.J., and Timar P.L., "The Effect of Harmonic Currents on the Noise of a Three-Phase Induction Motor", IEEE Transactions on Power Apparatus and Systems, Feb. 1980, Vol. 99, pp. 307 - 310.

30. Yacamini R., and Chang S.C., "Noise and Vibrations from Induction Machines Fed from Harmonic Sources", IEEE Transactions on Energy Conversion, Vol. 10, No. 2, June 1995, pp. 286-292.

31. Belmans R., D'Hondt L., Vandenput A., and Geysen W., "Analysis of the audible noise of three phase squirrel cage induction motors supplied by inverters", IEEE Transactions on Industry Applications, Vol. IA-23, September/October 1987, pp. 870-875.

32. Belmans R.J.M., Verdyck D., Geysen W., and Findlay R.D., "Electro-Mechanical Analysis of the Audible Noise of an Inverter-Fed Squirrel-Cage Induction Motor", IEEE Transactions on Industry Applications, Vol. 27, No. 3, June 1991, pp. 539-544.

33. Verma S.P., and Balan A., "Determination of Radial-Forces in Relation to Noise and Vibration Problems of Squirrel-Cage Induction Motors", IEEE Transactions on Energy Conversion, Vol. 9, June 1994, pp. 404-412.

34. Jordan H., "Newest Results in Vibration Testing of Electrical Machines", Electrotechnika, Budapest, Vol. 57, No. 6, 1964, pp. 202-212.

35. Verma S.P., and Girgis R.S., "Considerations in the choice of Main dimensions of Stators of Electrical machines in relation to their Vibration Characteristics", IEEE Transactions on Power Apparatus and Systems, Vol. 94, No. 6, Nov 1975, pp. 2151-2159.

36. Watanabe S., Kenjo S., Ide K., Sato F., and Yamamoto M., "Natural Frequencies and Vibration Behaviour of Motor Stators", IEEE Transactions on Power Apparatus and Systems, Vol. PAS - 102, No. 4, 1983, pp. 949-956.

37. Verma S.P., and Girgis R.S., "Resonance frequencies of Electrical Machine stators having encased construction, Part II : Numerical results and Experimental Verification", IEEE Transactions on Power Apparatus and Systems, Vol. 92, No. 5, Sept./Oct. 1973, pp. 1586-1593.

38. Singal R.K., Verma S.P, and Williams K., "Vibrations of Long and Short Laminated Stators of Electrical Machines Part III: Results for Short Stators and Validity of Simplified Frequency Equation", Journal of Sound and Vibration, 1989, Vol. 129, No. 1, pp. 31 - 44.

39. Williams K., Singal R.K., and Verma S.P., "Vibrations of Long and Short Laminated Stators of Electrical Machines; Part II : Results for Long Stators", Journal of Sound and Vibration, 1989, Vol. 129, No. 1, pp. 15-29.

40. Bert C.W., "Material Damping : An Introductory Review of Mathematical Models, Measures And Experimental Techniques", Journal of Sound and Vibration, Vol. 29, No. 2, 1973, pp. 129-153.

41. Ewins D.J., "Modal Testing: Theory and Practice", Research Studies Press, Hertfordshire, England, 1984.

42 Hadj Amor A., Timar P.L., and Poloujadoff M., "Induction Squirrel Cage Machine Design with Minimization of Electromagnetic Noise", IEEE Transactions on Energy Conversion, Vol. 10, Dec. 1995, pp. 681 - 687.

43. Verma S.P., and Balan A., "Measurement Techniques for Vibration and Acoustic Noise of Electrical Machines", Sixth International Conference on Electrical Machines and Drives, Oxford, U.K., Sept. 1993, Proceedings : IEE Conference Publication No. 376, pp. 546 - 551.

44. Balan A., Determination of Radial Electromagnetic Forces in Squirrel-cage Induction Motors", M. Sc. Thesis, University of Saskatchewan, 1990.

45. Test code for the measurement of airborne noise emitted by rotating electrical machinery, ISO R1680, 1970.

46. IEEE test procedures for airborne sound measurements on rotating electrical machinery, IEEE Std. 85, 1973.

47. Ellison A.J., Moore C.J., and Yang S.J., "Methods of measurement of acoustic noise radiated by an electric machine", Proc. IEE, Vol. 116, No. 8, 1969, pp. 1419-1430.

48. Serridge M., and Licht T.R., "Piezoelectric Accelerometer and Vibration Preamplifier Handbook", Brüel & Kjaer, Denmark, 1987.

49. Anderson R.A., "Fundamentals of Vibrations", The Macmillan Company, New York, 1967.

50. Norton M.P., "Fundamental of Noise and Vibration analysis for Engineers", Cambridge University Press, Cambridge, UK, 1989.

51. Singal R.K. "Vibration Behaviour of Stators of Electrical Machines", Ph.D. Thesis, Univ. of Saskatchewan, 1986.

52. Verma S.P., and Balan A., "Vibration Model for Stators of Electrical Machines Incorporating the Damping Effects", ELECTRIMACS - Conference, Sept. 1996, Saint-Nazaire, France, Proceedings Vol. 2, pp. 755-761.

53. Singal R.K., Williams K., and Verma S.P., "Vibration Behaviour of Stators of Electrical Machines; Part II : Experimental Study", Journal of Sound and Vibration, Vol. 115, No. 1, 1987, pp. 13-23.

54. Adams R.D., "The Damping Characteristics of Certain Steels, Cast Irons and Other Metals", Journal of Sound and Vibration, 1972, Vol. 23, No. 2, pp. 199-216.

55. Chu F.H., and Wang B.P., "Experimental Determination of Damping in Materials and Structures", Proceedings of the Winter Annual Meeting of the American Society of Mechanical Engineers, AMD- Vol. 38, Nov. 1980, pp. 113-122.

56. Kako, F., Tsuruta, T., Nagaishi, K., and Kohmo, H., "Experimental Study on Magnetic Noise of Large Induction Motors", IEEE Transactions on Power Apparatus and Systems, Vol. PAS-102, No. 8, August 1983, pp. 2805-2810.

57. Say M.G., "The Performance and Design of Alternating Current Machines", Sir Isaac Pitman and Sons Ltd., 1987.

58. Petyt M., "Introduction to Finite Element Vibration Analysis", Cambridge University Press, Cambridge, UK, 1990.

APPENDIX A

Effects of the Triplen Harmonic Fields Produced Due to Armature Reaction

With certain slot-number combinations of the stator and rotor, air-gap fields having pole-pairs that are a multiple of 3 are produced. These fields are called triplen harmonic fields. In the case of squirrel-cage induction motors, these triplen harmonic fields are produced when the number of the rotor bars is not an integer multiple of the number of phases on the stator windings. Since the stator and rotor normally house 3-phase windings in wound-rotor induction motors, these triplen harmonics are not produced by the multiple armature reaction effects.

Fig. A1 shows the distribution of the fundamental field and a triplen harmonic field over 2-poles. It is assumed that the various phase-belts are connected in series and the stator phases are connected in a wye configuration. Depending on the connection of the star-point, the two possibilities that arise are a floating neutral and a grounded-neutral arrangement.

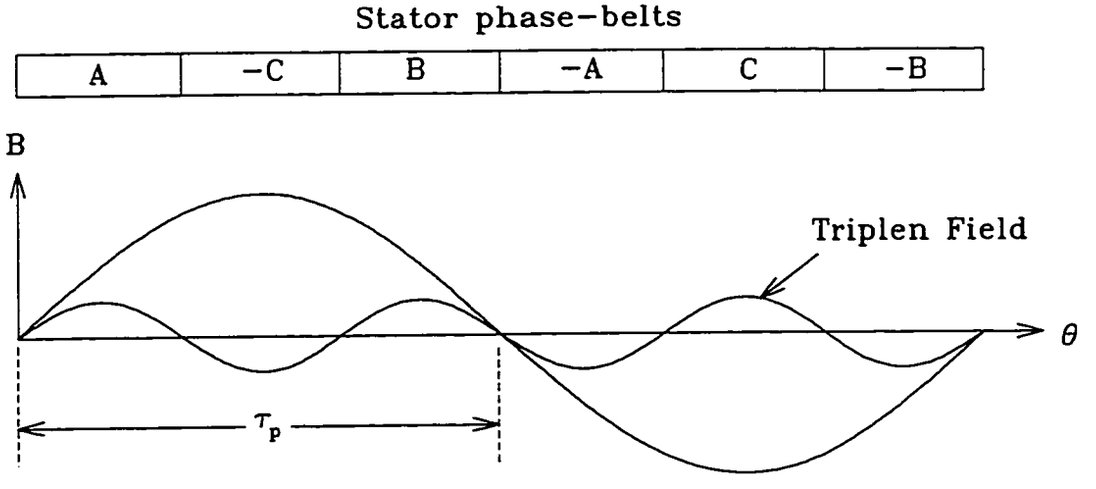

Figure A1 : Distribution of the fundamental and triplen harmonic fields over 2-poles of the 3-phase windings.

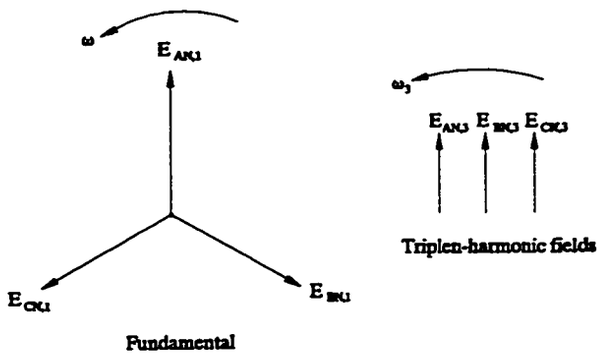

Figure A2 : Phasor diagrams for the voltages induced in the stator windings due to the fundamental and triplen-harmonic rotor fields.

The phasor-diagram of the voltages induced in the stator windings due to the fundamental field and the triplen harmonic field are shown in Fig. A2. For the triplen harmonic fields, the voltages in the stator windings are co-phasors, i.e. their magnitudes are equal and they are in-phase with respect to each other.

Case 1 : Floating neutral

When the star-point of the stator winding is not grounded the voltages induced by the triplen harmonic fields cannot produce the currents. Therefore, the triplen harmonic fields in the air-gap are left undamped by the stator windings. Consequently, these triplen harmonic fields have relatively large amplitudes.

Case 2 : Grounded neutral

When the star-point is connected to ground, a path is created for the triplen harmonic currents to flow in the stator windings. These currents are given by:

$$I_{AN,3} = I_{BN,3} = I_{CN,3} = \frac{E_{AN,3}}{Z_{Stator}}, \qquad \textbf{(A1)}$$

$$\text{giving} \quad I_{neutral} = 3\, I_{AN,3}\,.$$

The field produced by these currents will damp the rotor triplen fields. Being co-phasors, these zero-sequence currents produce pulsating fields, and they are responsible for the production of zero-sequence torques and other localised leakage-field effects.

Appendix B

Computation Procedure for Determination of the Air-gap Fields and Radial-Forces

As explained in the analysis, the distribution of the air-gap MMF and the air-gap permeance along the circumference are expressed as waves. The distribution of the air-gap flux-density and the radial-forces are then obtained and also expressed as waves. The sequence used for these calculations is shown in Fig. B1. Based on these procedures Fortran programs were developed for the calculation of the air-gap fields and the radial-forces.

A wave is expressed as a Fourier series consisting of various cosine functions. For the purpose of computation, the wave is expressed in the form of two complex arrays. Accordingly, the MMF-wave:

$$M(\theta,t) = M_p \cos(p\theta - \omega t + \psi_{11}) + M_{5p} \cos(5p\theta + \omega t + \psi_{12}) + \ldots, \quad (B1)$$

is expressed as:

$$\begin{matrix} (M_p, \psi_{11}) & (p, -f) \\ (M_{5p}, \psi_{12}) & (5p, f) \\ \vdots & \vdots \end{matrix} \quad (B2)$$

Similarly, the permeance-wave:

$$\lambda(\theta,t) = \lambda_0 + \lambda_{S1} \cos(S\theta) + \lambda_{R1} \cos\left[Z\theta - \frac{Z}{p}(1-s)\omega t\right] + \frac{\lambda_{S1}\lambda_{R1}}{2} \cos\left[(Z-S)\theta - \frac{Z}{p}(1-s)\omega t\right] + \ldots, \quad (B3)$$

is expressed as:

$$\begin{matrix} [\lambda_0, 0] & [0, 0] \\ [\lambda_{S1}, 0] & [S, 0] \\ [\lambda_{R1}, 0] & \left[Z, -\left(\frac{Z}{p}(1-s)\omega t\right)\right] \\ \left[\left(\frac{\lambda_{S1}\lambda_{R1}}{2}\right), 0\right] & \left[Z-S, -\left(\frac{Z}{p}(1-s)\omega t\right)\right] \\ \vdots & \vdots \end{matrix} \quad (B4)$$

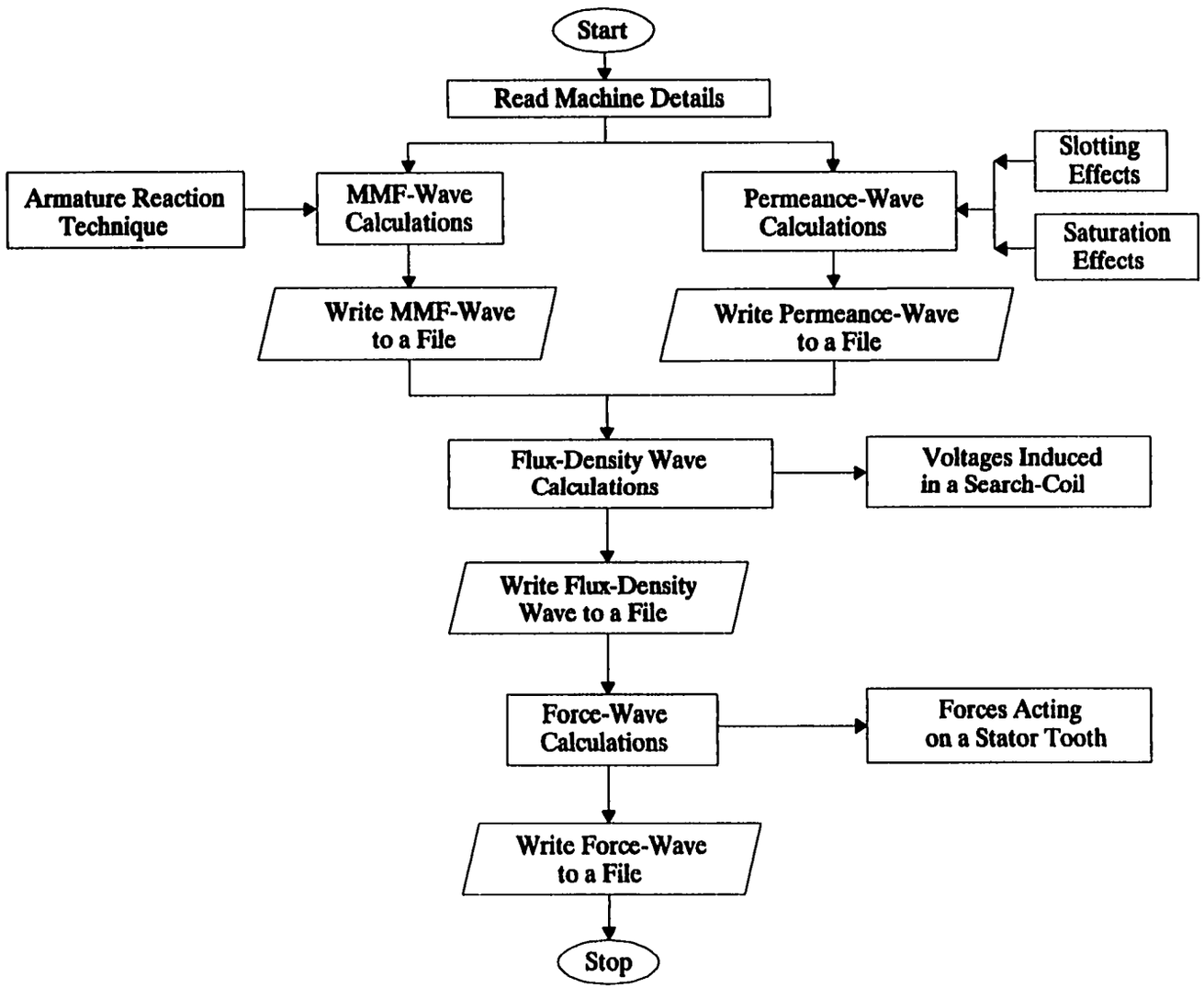

Figure B1 : Flow-chart of the computation procedure.

A procedure for the term-by-term multiplication of two waves was adopted. Thus, the product is again obtained as a wave, and it is also expressed in the form of two complex arrays. This multiplication procedure permits an easier analysis of the harmonic components in the air-gap flux-density and the radial-forces. Further, it presents a convenient means of tracing the harmonics to their origins.

The air-gap flux-density is obtained as a product of the MMF-wave and the permeance-wave. The force-wave is then calculated by squaring the air-gap flux-density wave, and it is multiplied by $\frac{1}{2\mu_0}$ to obtain the various components in N/m^2.

A separate routine was developed for the integration of a wave over specified limits on the stator and the rotor. This is used to determine the flux-linkages of a stator search-coil, and also the absolute force in Newtons that act on a stator tooth. It is explained mathematically as follows. Let the calculated air-gap flux-density wave be:

$$B(\theta,t) = \sum_{k=-\infty}^{\infty} B_k \cos(p_k\theta - \omega_k t + \psi_k). \tag{B5}$$

Fig. B2 shows a schematic view of the machine giving the angular location of the coil-sides of a stator search-coil. The total flux linking with the stator search-coil is found by integrating the air-gap flux-density over the span of the search-coil. It is given by:

$$\phi = \int_{\theta=\theta_{t1}}^{\theta=\theta_{t2}} B(\theta,t) \cdot l_e \cdot r \cdot d\theta, \tag{B6}$$

where r is the radius of the stator-bore and l_e is the effective length of the coil-sides. For any particular instant of time, the integral is evaluated by summing the integrand over a large number of infinitely small sections between $\theta = \theta_{t1}$ and $\theta = \theta_{t2}$. The evaluation of this integral at different successive intervals of time is used to determine the variation of the flux-linkages with time. The voltage induced in the stator search-coil is then determined as the rate of change of flux-linkages with time. It is expressed mathematically as:

$$e = -\frac{d\phi}{dt},$$
$$= -\frac{d}{dt}\left[\int_{\theta=\theta_{t1}}^{\theta=\theta_{t2}} B(\theta,t)\cdot l_e \cdot r \cdot d\theta\right]. \tag{B7}$$

A similar calculation procedure is used for the calculation of the radial-forces which act on a stator tooth. The force-wave is calculated and expressed in N/m^2. The integration of the force-wave over the surface of the tooth will give the absolute value of the radial-force that acts on the stator tooth. It is expressed mathematically as:

$$F_t = \int_{\theta=\theta_{t1}}^{\theta=\theta_{t2}} F(\theta,t)\cdot l_e \cdot r \cdot d\theta, \tag{B8}$$

where $F(\theta,t)$ is the calculated force-wave.

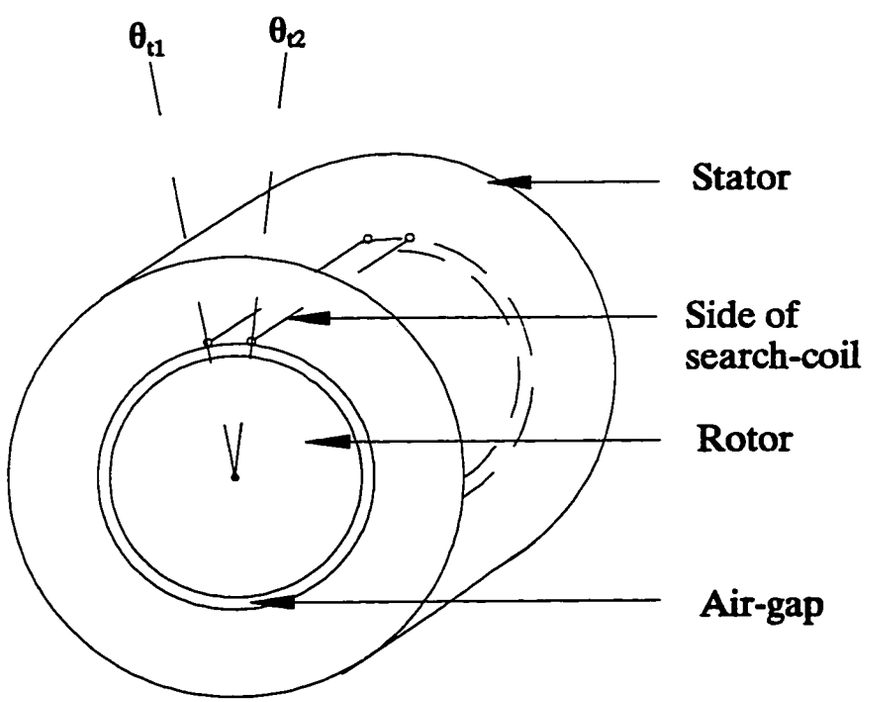

Figure B2 : Schematic view of the machine showing the angular location of a stator search-coil.

Appendix C

Winding Arrangements for the Electromagnetic Surface Excitation System

Although it is desired to have a sinusoidal flux-density distribution along the circumference, it is difficult to achieve in practice since it requires sinusoidal grading of the number of turns in the distribution of the rotor coils. Due to the restriction imposed by the available slot space and the ease of installing formed coils having a fixed number of turns, a winding arrangement with equal number of turns per coil is chosen. Considering the frequency range for the operation of the windings and the voltage limitations of the power-supply, the terminal inductance of the winding is designed to be less than 5 mH. Further, at high frequencies the inter-turn voltages are large, hence a heavy enamel insulation is required on the copper wires. In addition the slot-openings on the rotor impose an additional constraint on the size of the wire to be used. Triple enamel coated copper wire of AWG 20 are therefore used for the windings. To keep the net inductances of the windings small, the 2-pole and 4-pole windings are designed to have many parallel paths. Also, to permit simultaneous operation of both the windings, the mutual inductances between the two windings is designed to be negligible.

Coil Connections for 2-pole Pulsating Magnetic Fields

There are 28 coil-groups that are distributed around the rotor to form the 2-pole winding. The distribution of the coil-groups are shown in Fig. C1. Each coil-group consists of 24 coils of 2 turns each that are connected in parallel. The terminals of the 24 coils in each slot is crimped together and brought out to a terminal-board to permit connection of the various coils in different arrangements. The salient information of the 2-pole winding is provided in Table 4.3, and its operation is described in Section 4.5.

Coil Connections for 4-pole Pulsating Magnetic Fields

The 4-pole winding is designed similar to the 2-pole winding. The various coil-groups of the 4-pole winding have a span of 7 rotor slots, and the distribution of the coil-groups is shown in Fig. C2. Each coil-group of the 4-pole winding consists of 24 coils of 2 turns each that are connected in parallel. Here again, the terminals of the coils

in each slot are crimped together and brought out to the terminal-board. The salient information for the 4-pole winding is provided in Table 4.4, and its operation is described in Section 4.5

The end-view of the combined arrangement of 2-pole and 4-pole windings on the rotor is shown in Fig. C3. Due care was taken during the forming of the coils, and its installation, to ensure that the overhang portions of the 2-pole and 4-pole windings are symmetrically distributed around the periphery of the rotor.

Coil Connections for 2-pole Rotating Magnetic Fields

The coils of the 2-pole windings were connected in a 3-phase configuration in order to produce a rotating force-distribution with 2-force-poles. Since the rotor does not have an integer number of slots per pole per phase, a fractional-slot winding arrangement is used. The coils of the 2-pole winding is connected in accordance to the winding diagram provided in Fig. C4. The individual phases are connected in star, and a current of 4.71 Amperes is maintained constant through each of the phases when the frequency of the supply is varied from 200 Hz to 5 kHz. More information on the operation this winding arrangement is provided in Section 4.5.

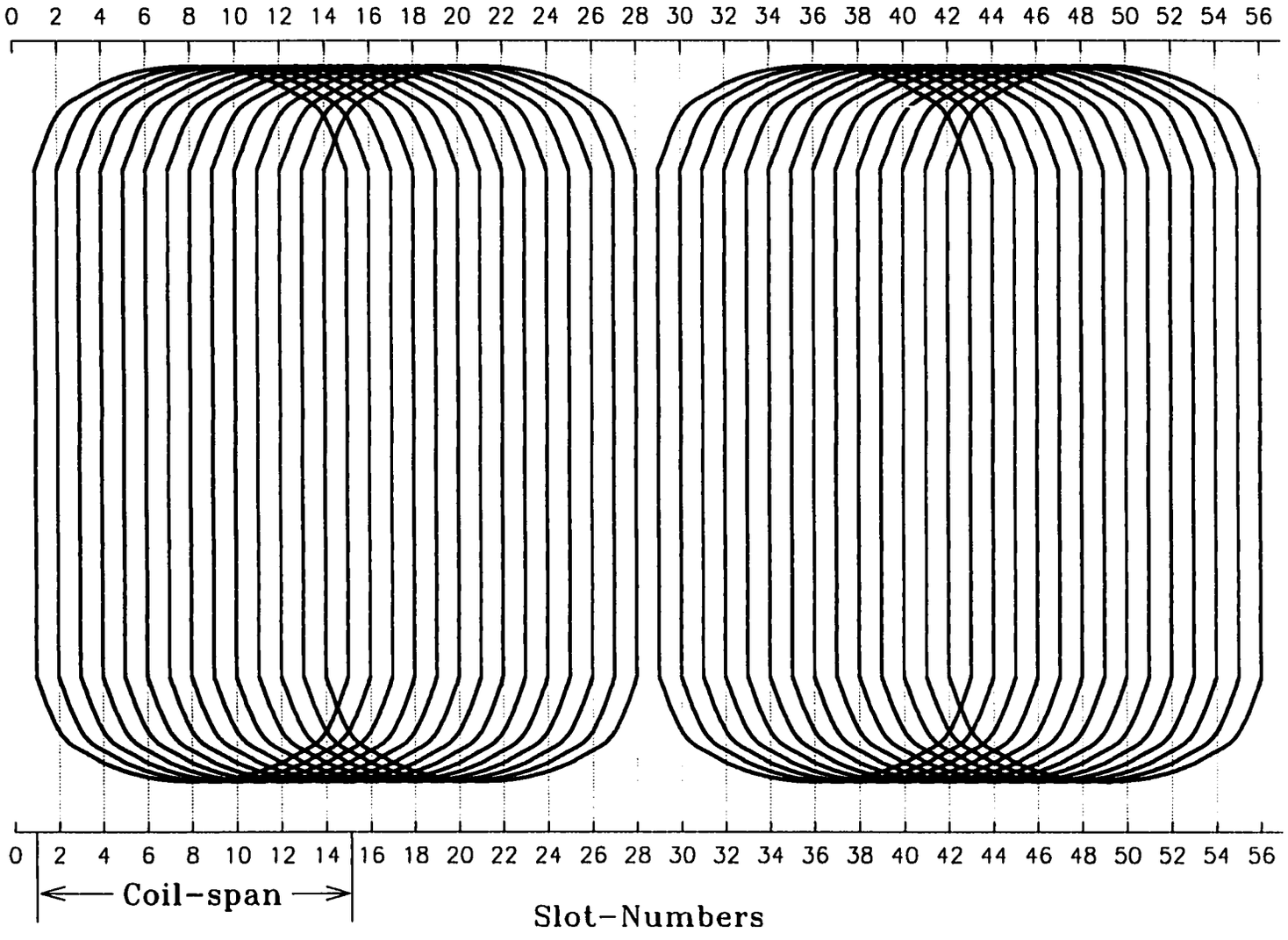

Figure C1 : Distribution of the coil-groups of the 2-pole winding.

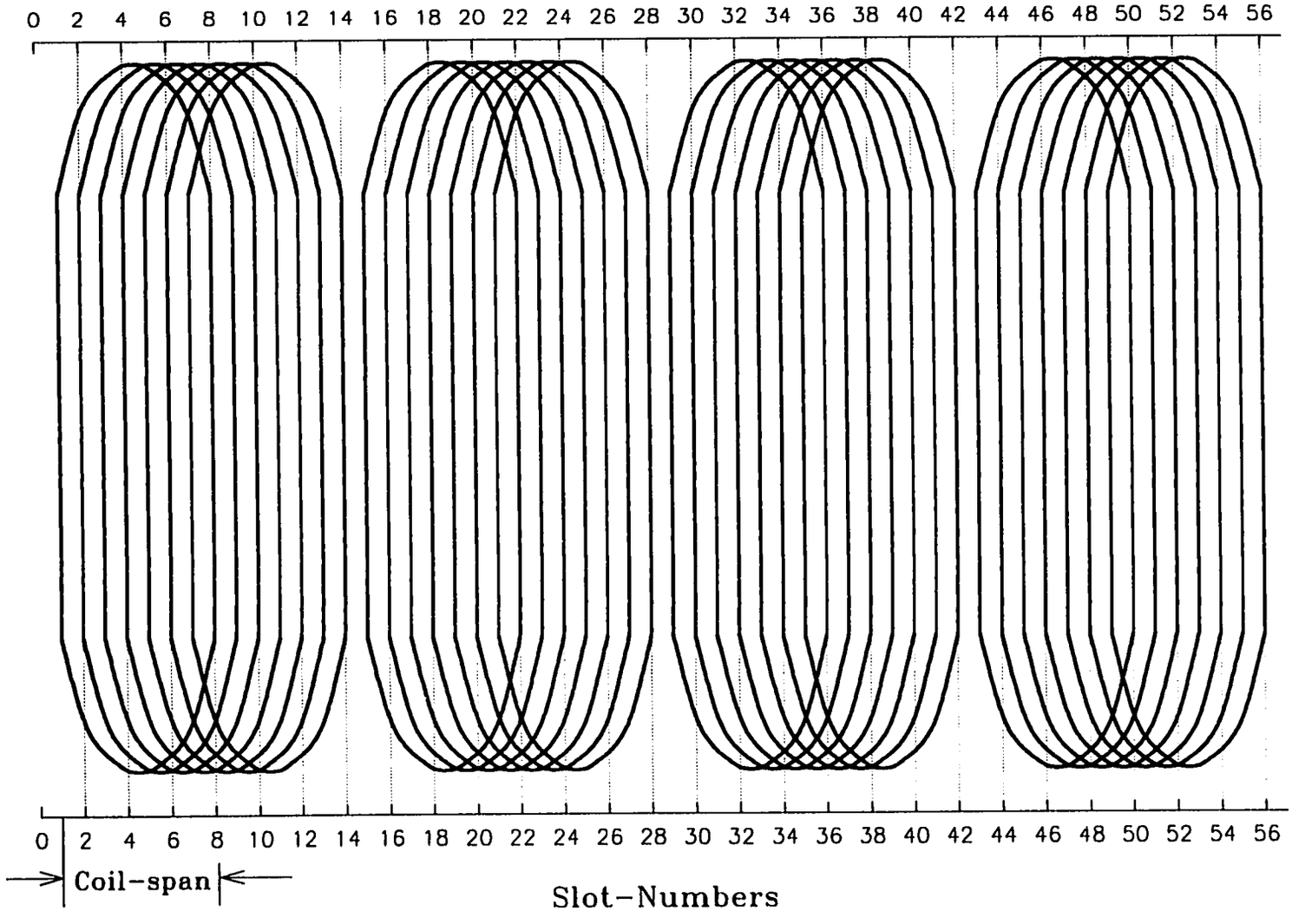

Figure C2 : Distribution of the coil-groups of the 4-pole winding.

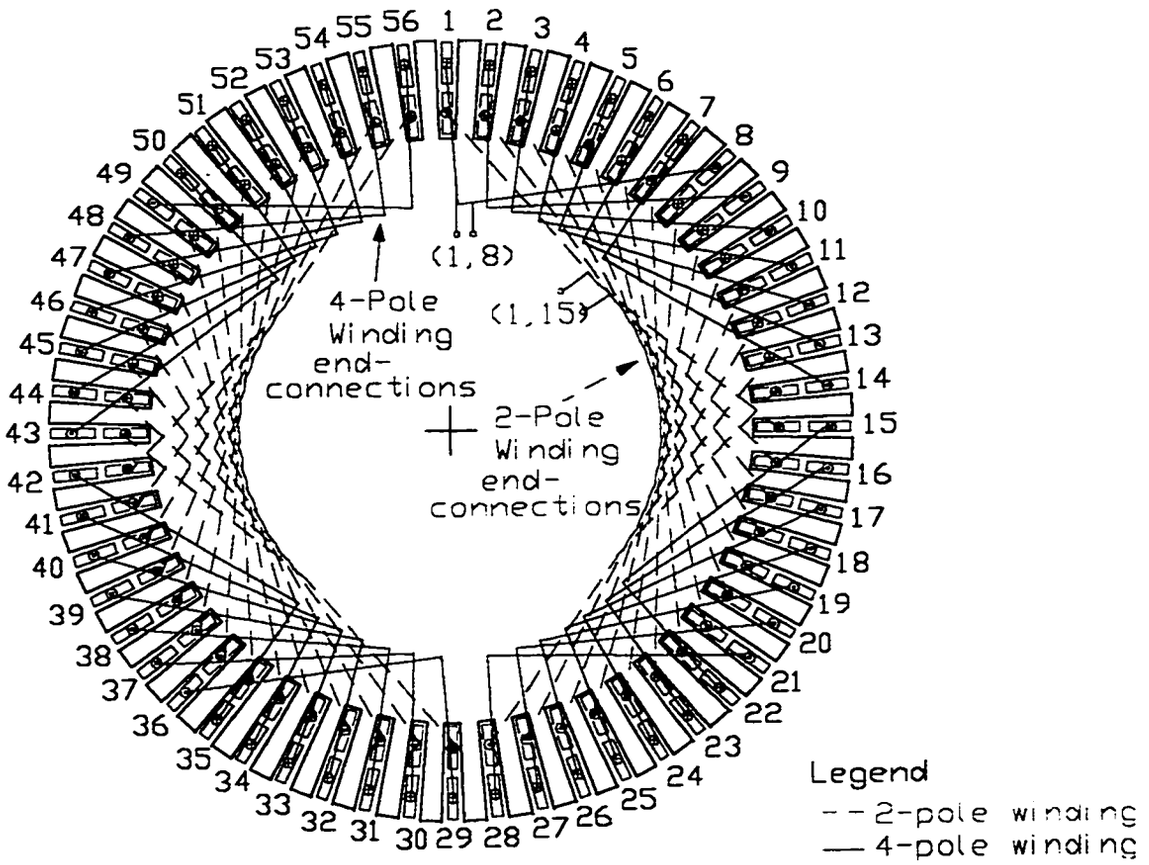

Figure C3 : End-view of the winding arrangements on the rotor.

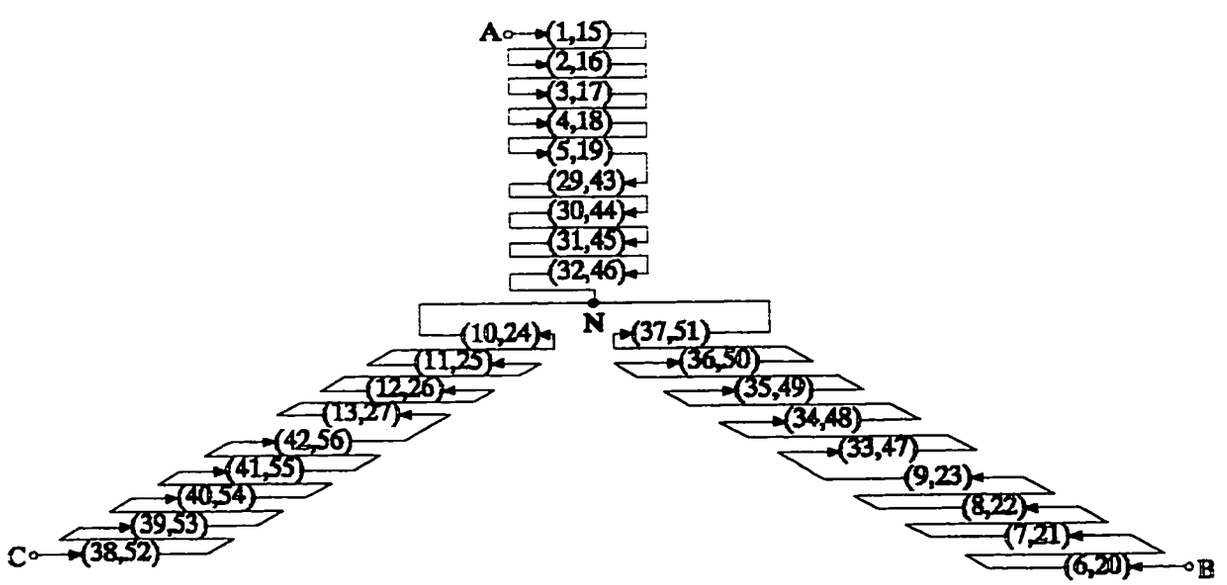

Figure C4 : Coil connections for the operation of the 2-pole winding in a 3-phase configuration.

Appendix D

Relationship Between the Force-distribution and the Circumferential Mode of Vibration

Fig. D1 shows the flux-density in the air-gap of the machine over two poles. The flux-density distribution being sinusoidal, the distribution of the force in the air-gap has a constant component and a sinusoidally varying component having twice as many cycles as the original flux-wave.

For pulsating magnetic fields, the constant and sinusoidal force components pulsate at twice the supply frequency. Considering the circumferential distribution of the forces produced by a 2-pole pulsating field, the stator and the rotor will be subjected to pulsating elliptical deformations. Fig. D2 shows the elliptical deformation of the stator and the rotor due to a two-pole field at a given instant of time. The elliptical deformation pattern corresponds to the n=2 circumferential mode of vibration. Thus, an excitation with 2 pairs of force-poles creates the n=2 mode of vibration.

In the case of rotating fields, the constant component is uniform around the periphery, and hence it produces a constant pull on the stator and the rotor. It does not contribute to the noise produced by induction motors. The sinusoidal force component rotates along with the flux-wave at its synchronous speed. Thus, every point on the stator and rotor will be subjected to a periodic force with 2-cycles per revolution for a 2-pole rotating field. Consequently, every point on the stator is made to vibrate at twice the supply frequency with respect to time. Considering the circumferential distribution of the forces produced by 2-pole rotating field, the stator and the rotor will be subjected to a rotating elliptical deformation.

In general, the number of pairs of force-poles correspond to the associated circumferential mode of vibration.

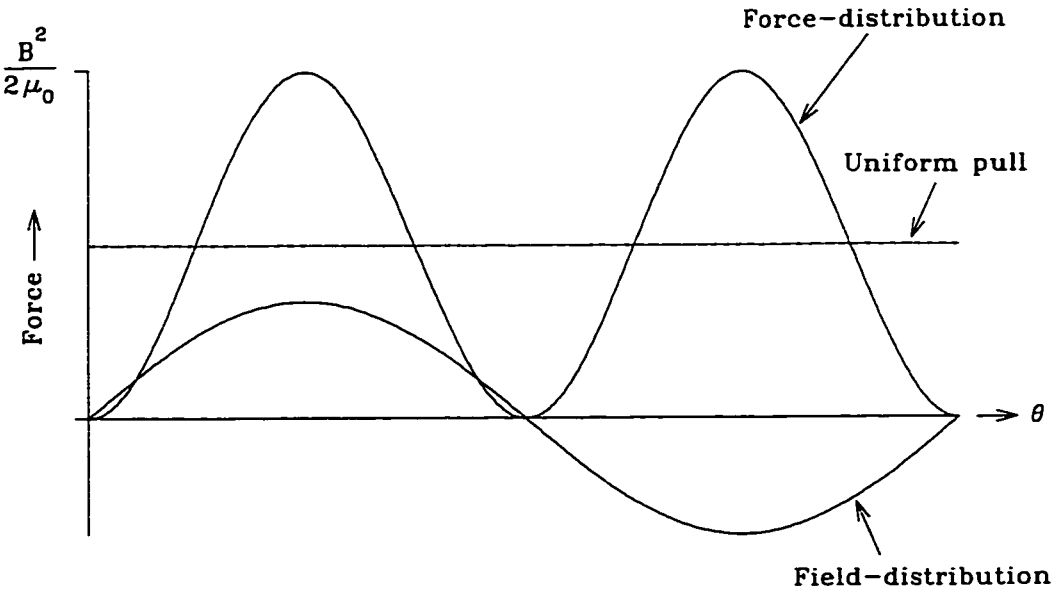

Figure D1 : Force-distribution due to a 2-pole air-gap field.

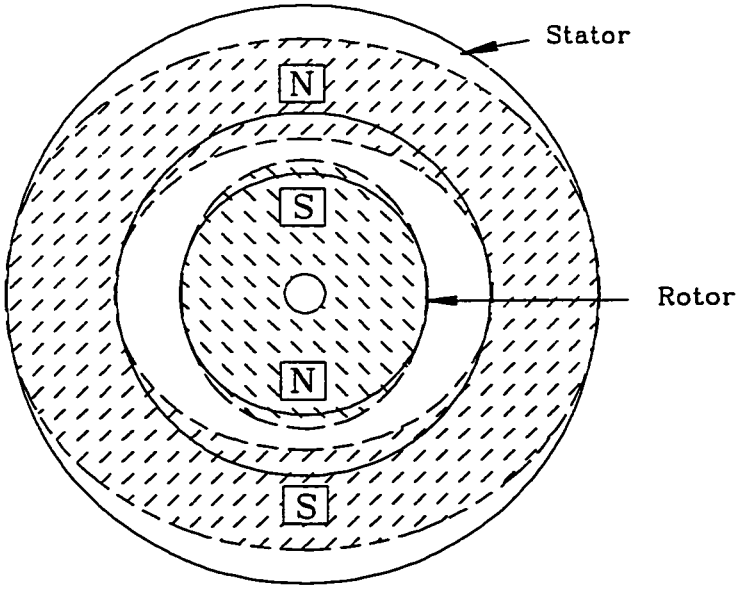

Figure D2 : Elliptic deformation of the stator and rotor produced by a 2-pole field.

Appendix E

Experimental Study of Resonances of the Rotor of 120 hp Motor

The experimental investigations which were conducted to determine the resonances of the rotor of 120 hp induction motor are described in this appendix. The dimensions and details of other constructional features of this rotor are provided in Chapter 4.

The Experimental Arrangements and Procedures

The experimental investigations on the rotor were conducted using a magnetic shaker. The rotor was placed on a specially designed pedestal-stand, and the acceleration levels were measured on the rotor surface using several accelerometers. In order to ensure resilient mounting, one inch thick rubber pads of 40 durometer hardness were placed between the shaft and the pedestals.

In order to determine the circumferential and longitudinal mode-shapes at the various resonant frequencies, the acceleration levels were measured at many locations along the contour of interest. The various measurement locations for the determination of the circumferential and longitudinal mode-shapes are shown in Fig. E1. In the present experimentation, 14 equally spaced measuring locations on the periphery identified by teeth (1,5, ...,53) were used for the determination of the circumferential mode-shapes. Further, nine measuring locations on planes A to H, and Z were used for the determination of the longitudinal mode-shapes.

The resonant frequencies of long models, such as this hp rotor, have axi-symmetric and anti-symmetric longitudinal modes of vibrations associated with them. In order to excite the axi-symmetric longitudinal modes of vibrations, the rotor was excited on the centre-plane at position 40-Z, on tooth #40. An off-centre excitation at 40-C was used to excite the anti-symmetric longitudinal modes of vibrations.

Further, to investigate the effects of the windings on the resonances of the rotor the vibration measurements were initially made on the rotor with no windings in the slots. The experimental investigations were then conducted on the complete rotor with windings installed in the rotor slots.

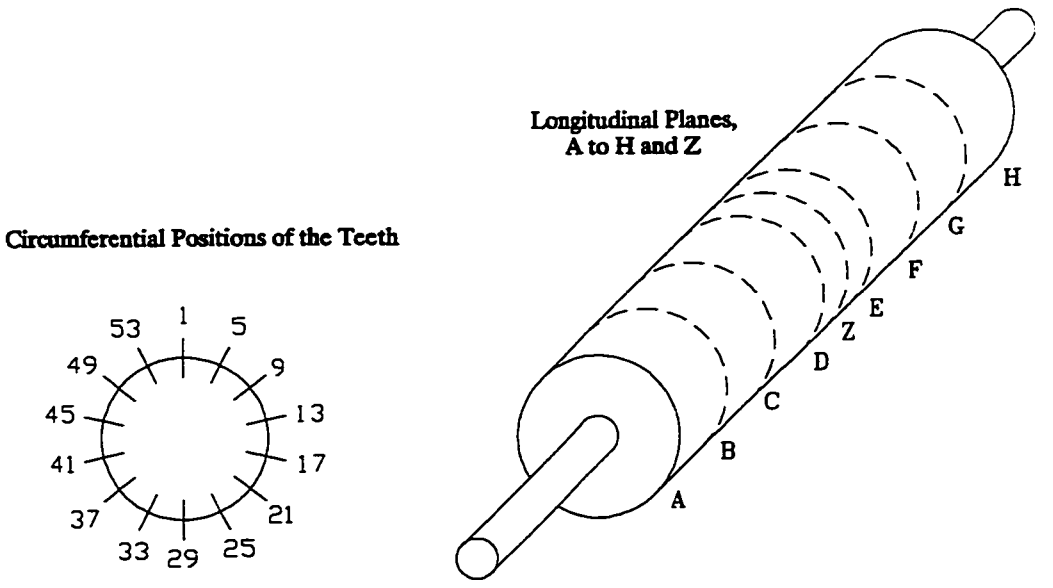

Figure E1 : Arrangement of the measuring points on the rotor.

Axi-symmetric resonant frequencies of the rotor with no windings

The rotor was excited at position 40-Z and the resonant frequencies were measured at position 1-Z. Fig. E2 shows the spectrum of the vibration signal measured on the rotor. The amplitudes of the various components are shown relative to the amplitude of the of the largest peak in the spectrum of Fig. E2. The vibration response was measured at several locations on the central plane (1-Z to 53-Z), and only those peaks that were registered consistently were noted as resonances belonging to the rotor. The circumferential and longitudinal modes of vibrations associated with each of the resonances were individually examined and they are provided in Table E1. The various resonant frequencies according to the serial numbers provided in Table E1 are identified in the spectrum of Fig. E2.

Anti-symmetric resonant frequencies of the rotor with no windings

As mentioned earlier, in order to excite the anti-symmetric resonances of the rotor the rotor was excited at an off-centre location. Fig. E3 shows the spectrum of the vibration signal measured at 1-C, when the rotor was excited at 40-C. All the peaks in

this spectrum are also identified according to Table E1. Here again, the vibration response was measured at several locations on the radial-plane C and also on other locations on the rotor to ensure the elimination of parasitic peaks from being registered as resonances of the rotor.

Circumferential and longitudinal modes of vibrations of the rotor with no windings

In order to determine experimentally the circumferential mode of vibration associated with a particular resonant frequency, the rotor was exited at that frequency of the resonance and the vibration signals were measured at different locations on a radial-plane. Two accelerometers were used for this purpose. The amplitude and phase-difference of the vibration signals measured at various locations were then used to determine the mode-shape.

To determine experimentally the longitudinal mode of vibration, the rotor was excited at the resonant frequency. For axi-symmetric resonances, the rotor was excited at 40-Z. For anti-symmetric resonances, the off-centre position 40-C was used. The vibration signals were measured at different points along the length of the rotor, and the amplitudes with their associated phase-differences were used to obtain the longitudinal mode-shape at the resonant frequency.

Figs. E4 and E5 show the measured circumferential and longitudinal mode-shapes at the various resonances of the rotor. The circumferential distribution at most resonances exhibited a well defined sinusoidal pattern. In contrast, the longitudinal modes at some of the resonant frequencies were not well defined. The amplitudes of vibrations varied significantly along the length of the rotor at these resonant frequencies. Although, the vibration amplitudes show an appreciable change, the phase differences in the vibration signals at various locations along the length were distinct and useful in determining the longitudinal mode of vibration.

Table E1 : Resonances of the rotor with no windings.

Axi-Symmetric Resonances				Anti-Symmetric Resonances			
S.No.	**Freq., Hz**	**n**	**m**	**S.No.**	**Freq., Hz**	**n**	**m**
1	1070	1	2	17	618	1	1
2	1845	1	2	18	1610	1	3
3	2135	1	4	19	2817	1	5
4	2180	1	4	20	3115	1	7
5	2625	2	4	21	9890	3	7
6	2990	1	0				
7	3145	1	4				
8	3770	2	4				
9	4785	2	4				
10	4875	2	4				
11	5294	2	2				
12	5555	2	4				
13	5665	2	2				
14	9140	3	4				
15	9250	3	6				
16	9455	3	4				

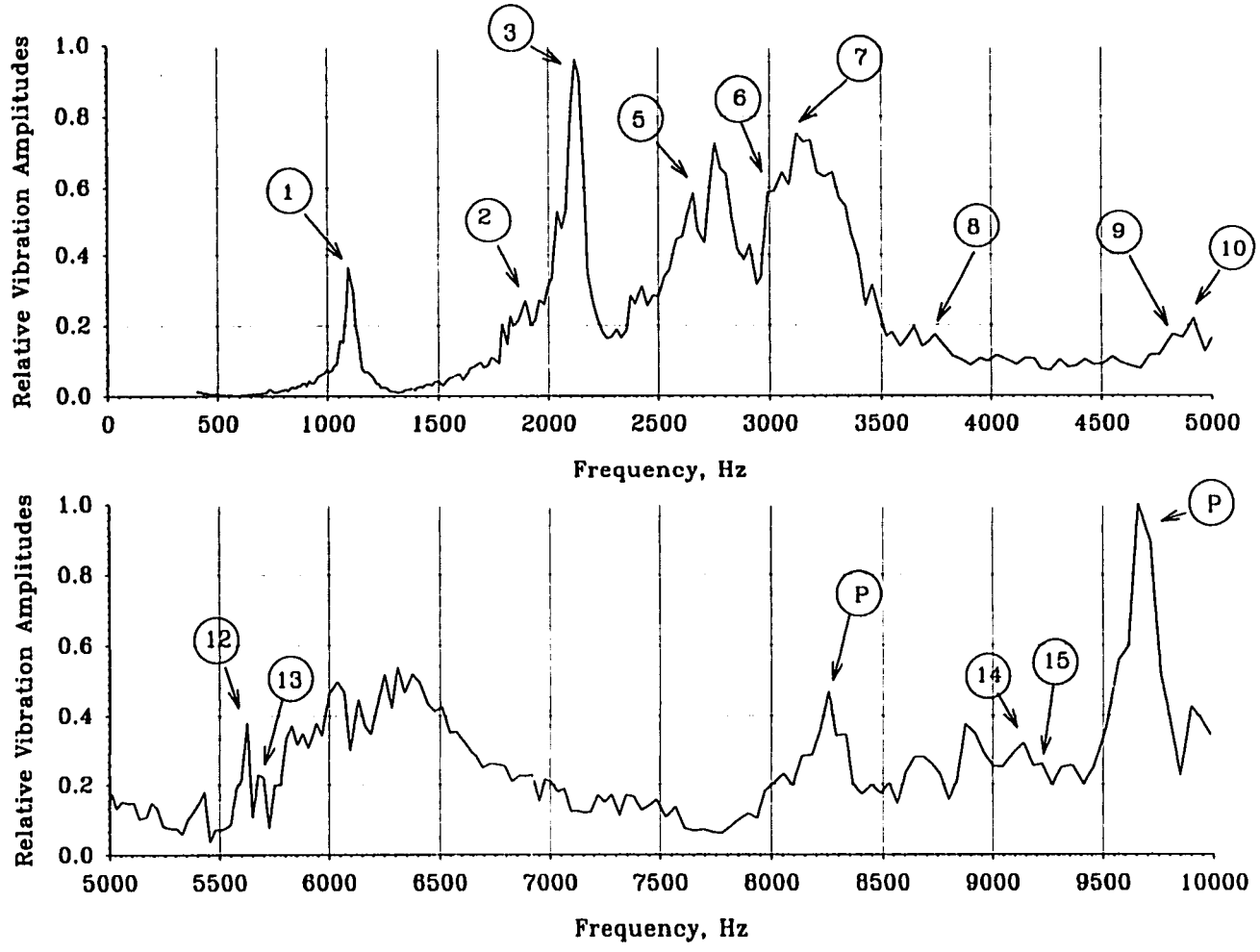

Figure E2 : Spectrum of the axi-symmetric resonant frequencies of the rotor when the rotor was excited at position 40-Z and the response was measured at 1-Z.

((P) = Parasitic peaks).

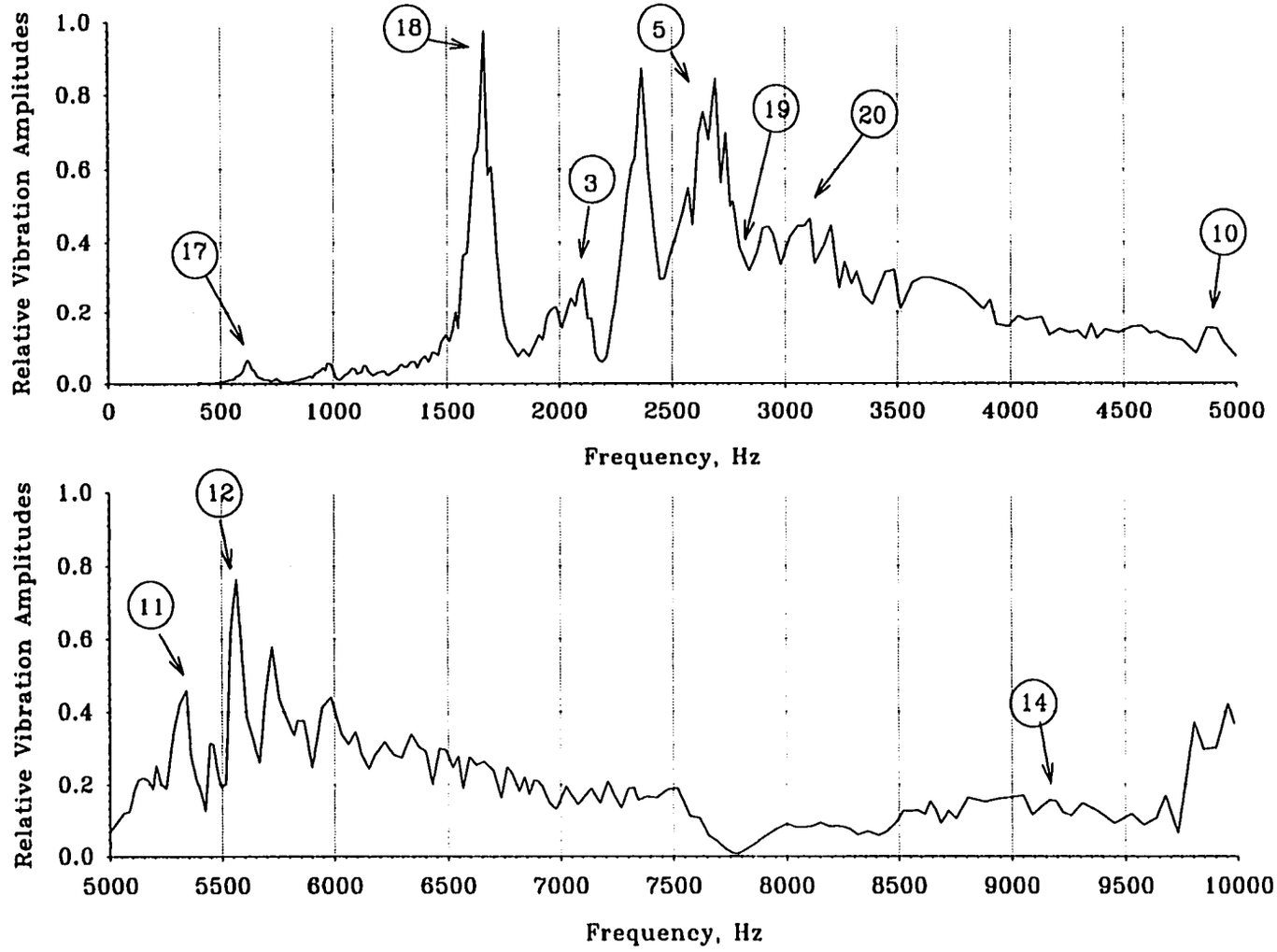

Figure E3 : Spectrum of the anti-symmetric resonant frequencies of the rotor when the rotor was excited at position 40-C and the response was measured at 1-C.

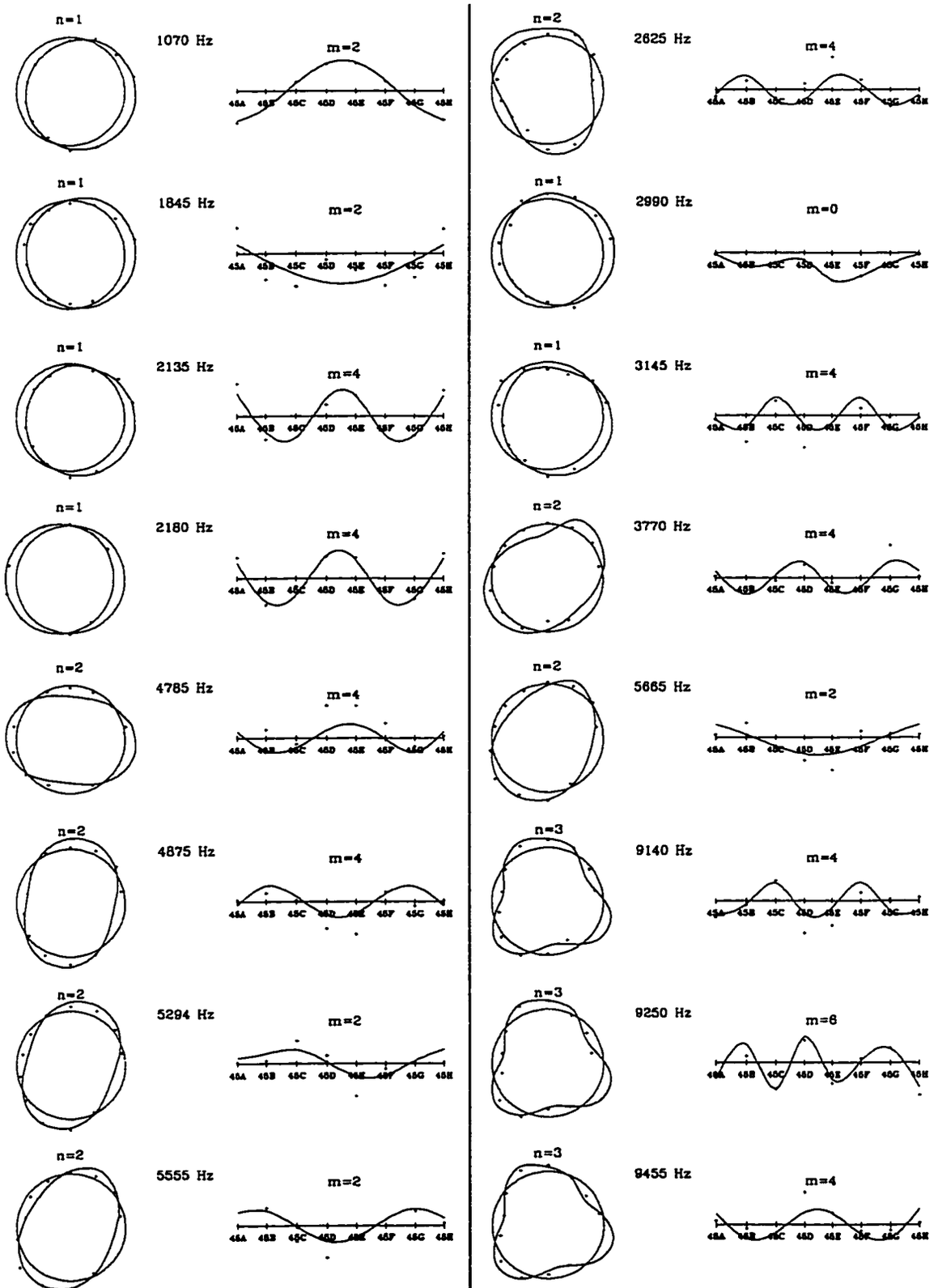

Figure E4 : Mode-shapes associated with the axi-symmetric resonances of the rotor.

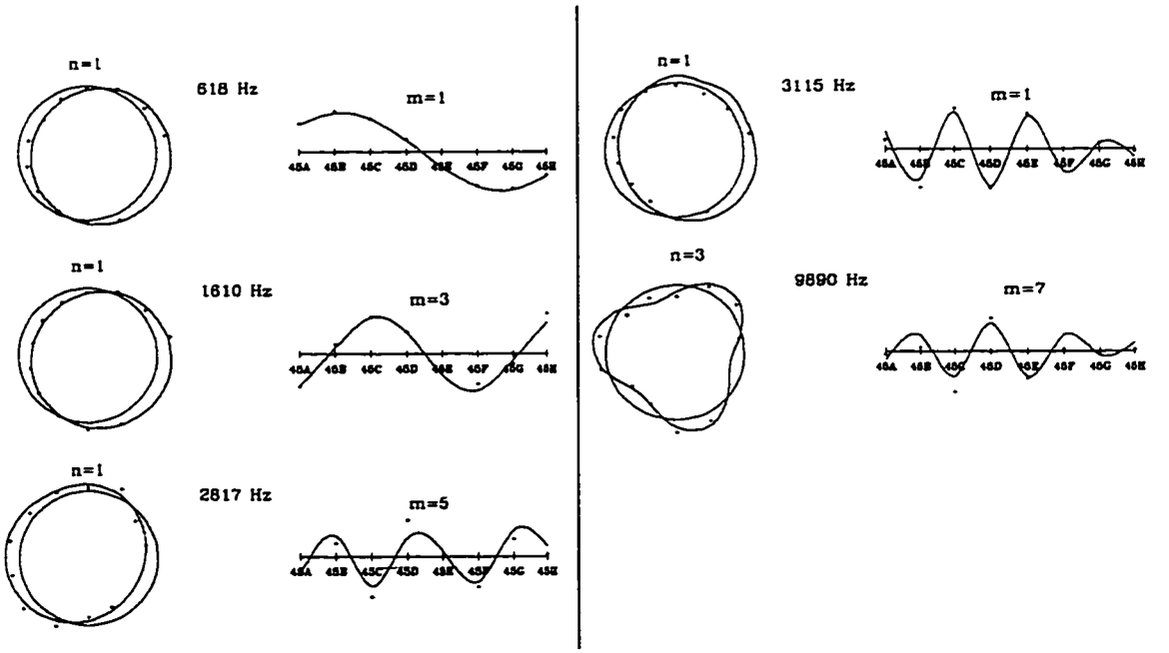

Figure E5 : Mode-shapes associated with the anti-symmetric resonances of the rotor.

Resonances of the rotor with windings

The windings described in Appendix C were installed in the slots of the rotor. Due care was taken in the design and installation of the windings to maintain symmetry, particularly in the overhang sections of the rotor. The findings of the experimental investigations to determine the resonances of this rotor are reported in the following.

Axi-symmetric resonant frequencies of the rotor with windings

Again, in this case the rotor was excited at 40-Z and the resonant frequencies were measured at position 1-Z. Fig. E6 shows the spectrum of the vibration signal measured on the rotor. The vibration response was measured at several locations on the central plane (1-Z to 53-Z), and only the peaks that were registered consistently were noted as resonances belonging to the rotor. The circumferential and longitudinal modes of vibrations associated with each of the resonances were also individually examined and they are provided in Table E2. The various peaks in the spectrum of Fig. E6 are identified according to Table E2.

Anti-symmetric resonant frequencies of the rotor with windings

As mentioned earlier, in order to excite the anti-symmetric resonances of the rotor the rotor was excited at an off-centre location. Fig. E7 shows the spectrum of the vibration signal measured at 1-C when the rotor was excited at 40-C. All the peaks in this spectrum are identified according to Table E2. Here again, the vibration response was measured at several locations on the radial-plane C, and also other locations on the

Table E2 : Resonances of the rotor with windings.

Axi-Symmetric Resonances				**Anti-Symmetric Resonances**			
S.No.	**Freq., Hz**	**n**	**m**	**S.No.**	**Freq., Hz**	**n**	**m**
1	1070	1	2	18	618	1	1
2	2095	1	4	19	1610	1	3
3	2135	1	4	20	2875	1	5
4	3280	1	4	21	3115	1	7
5	4905	2	*	22	9890	3	7
6	4980	2	0				
7	5210	2	4				
8	5325	2	4				
9	5760	2	4				
10	5925	2	4				
11	6460	2	6				
12	9095	3	2				
13	9195	3	6				
14	9380	3	4				
15	9650	3	4				
16	9745	3	4				
17	9840	3	4				

* : was not well-defined.

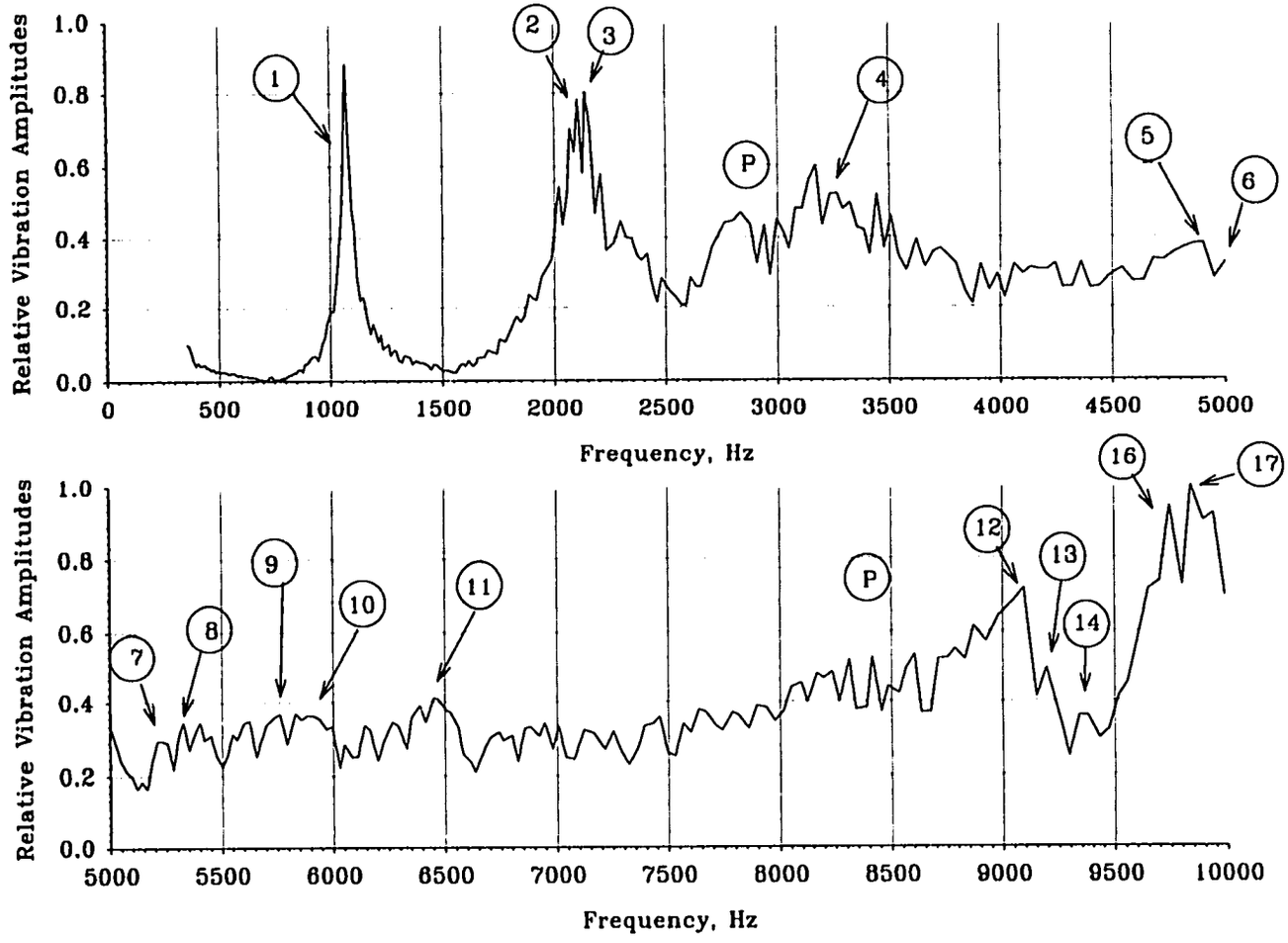

Figure E6 : Spectrum of the axi-symmetric resonant frequencies of the rotor with windings when the rotor was excited at position 40-Z and the response was measured at 1-Z.

((P) = Parasitic peaks).

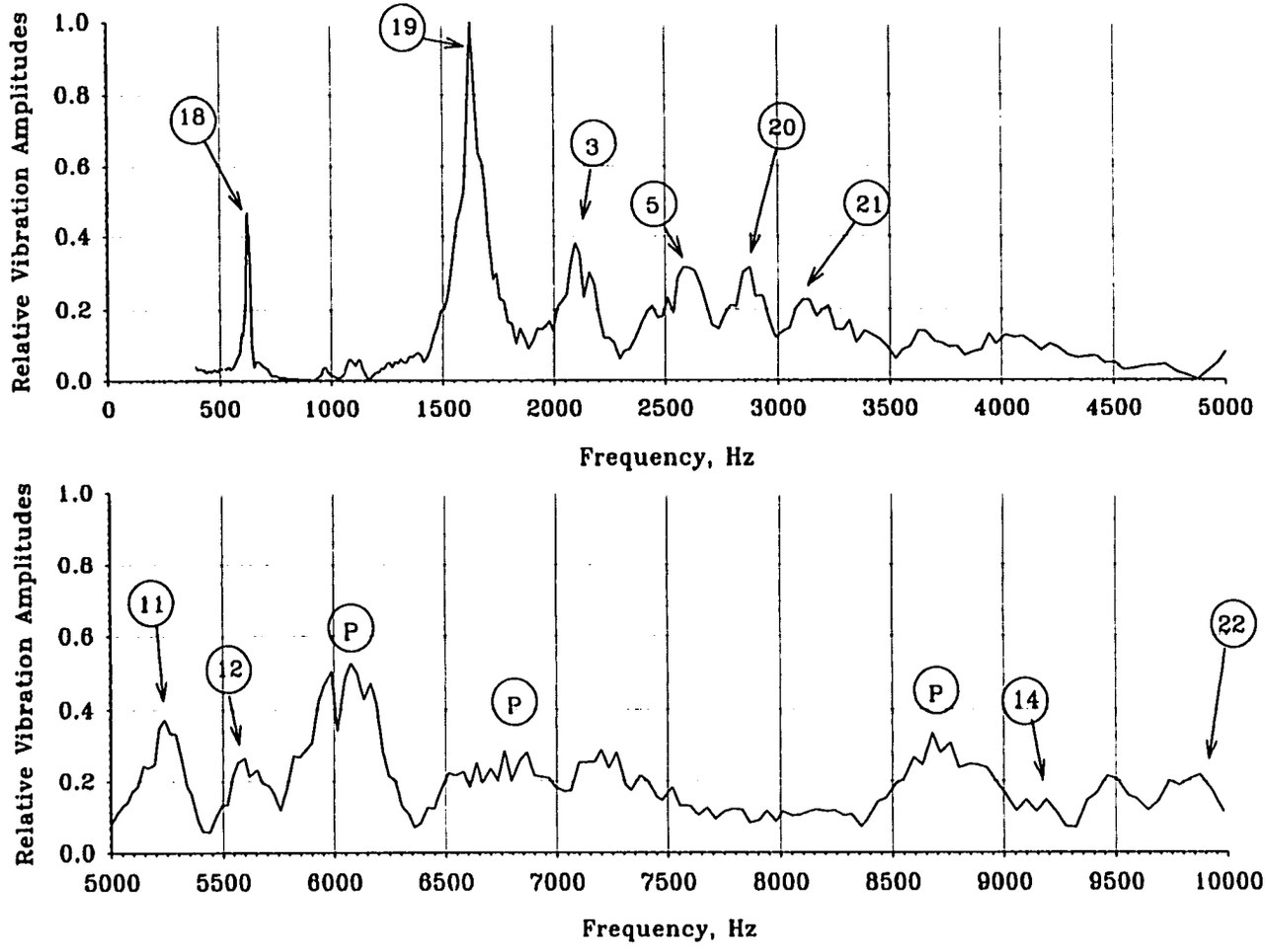

Figure E7 : Spectrum of the anti-symmetric resonant frequencies of the rotor with windings when the rotor was excited at position 40-C and the response was measured at 1-C.

((P) = Parasitic peaks).

rotor, to ensure the elimination of parasitic peaks from being registered as resonances of the rotor.

Contrary to the case of electrical machine stators, the installation of the windings in the rotor did not suppress the anti-symmetric resonances. The anti-symmetric resonances at 633 Hz and 1610 Hz were distinct, and they are associated with modes m=1 and 3, respectively.

In summary, the resonances of the 120 hp induction motor rotor without and with windings were determined experimentally. In distinction to the vibration behaviour of electrical machine stators, the resonances of the rotor are associated with both the axi-symmetric and anti-symmetric longitudinal modes of vibrations. The circumferential modes of vibrations were, in general, well defined and they exhibit sinusoidal deformation patterns.

Appendix F

Damping in Practical Vibrating Structures

The amplitudes of vibrations produced in a practical structure, when it is subjected to an initial disturbance, decays with time. This decay is attributed to the action of damping forces in the system. The damping forces dissipate the energy injected into the system. The damping forces in a real structure manifest in different forms, such as viscous, hysteresis, Coulomb-friction, etc.

As indicated in Chapter 5, it is difficult to formulate explicit expressions for the damping forces in a structure. Often, simplified models representing the hysteresis and viscous types of damping are used. These generalised models are based more on mathematical convenience than the true physical representation of the damping mechanisms. Nevertheless, they are sufficiently reliable in modelling the damping mechanisms present in a real structure.

Under the vibrations of a real system, it is likely that there will be some relative movement of dry or unlubricated surfaces. The resulting friction forces oppose the motion, and they are often idealised as a force of constant magnitude [49]. Such a force is usually referred to as a Coulomb-friction force.

In a solid structure, some of the energy loss must be attributed to the imperfect elasticity or internal friction of the material. Although it is difficult to predict the magnitude of this type of damping, experiments suggest that a resisting force proportional to the amplitude and independent of the frequency serves as a satisfactory approximation. This model for solid-damping is referred to as hysteresis damping or *structural damping*.

Hysteresis Damping Model

Assuming harmonic motion, the damping force is given by:

$$\text{damping force} = -\frac{h}{\omega}\dot{x} = -jhx. \qquad \text{(F1)}$$

where; h is the structural damping factor, x is the vibration displacement, ω is the frequency of vibration and j is the complex operator $\sqrt{-1}$. Thus, it is seen that the

damping force is in anti-phase to the velocity and proportional to displacement. Hysteresis damping can be represented by a frequency dependent damping coefficient:

$$c(\omega) = \frac{h}{\omega}. \tag{F2}$$

The equations of motion incorporating the hysteresis damping effects are given by:

$$[M]\{\ddot{x}\} + [K + jH]\{x\} = [F] \tag{F3}$$

where; [M] and [K] are the mass and stiffness matrices, [H] is the hysteresis damping matrix, {x} is the displacement matrix, and [F] is the force matrix. The term [K+jH] is called the complex stiffness, and it is usually written in the form:

$$[K + jH] = K[1 + j\eta], \tag{F4}$$

where; η is the structural loss factor of the system. The structural loss factor for steel is in the range of 1×10^{-4} to 6×10^{-4}. It should be emphasised here that the hysteresis damping model is applicable only when the excitation is of harmonic nature.

Viscous Damping Model

The model for viscous damping is applicable to all cases irrespective of the form of the excitation forces. The viscous damping forces are considered to be proportional to the velocity of vibration. Viscous damping forces are usually much smaller than the inertia and elastic forces acting on the system. The equations of motion incorporating the viscous damping effects are given by:

$$[M]\{\ddot{x}\} + [C]\{\dot{x}\} + [K]\{x\} = [F] \tag{F5}$$

where: [C] is the matrix of viscous damping coefficients. The most common implementation of the viscous damping is in the form of Rayleigh-damping model. In the Rayleigh- damping model, the damping matrix is assumed to be proportional to a linear combination of the mass and stiffness matrices. Therefore,

$$[C] = \alpha[M] + \beta[K], \tag{F6}$$

where; α and β are some constants. As explained in Chapter 4, the co-ordinate transformation that diagonalises the mass and stiffness matrices will also diagonalise the damping matrix. This helps in decoupling a multiple-degree of freedom system to many single-degree of freedom systems. Rewriting Eqn. 4.21,

$$M_i\ddot{\eta}_i + C_i\dot{\eta}_i + K_i\eta = \{\phi_i\}^T\{F\} = F_i . \tag{F7}$$

Each of the de-coupled equations, Eqn. F7, is of the form:

$$\ddot{\eta}_i + 2\zeta_i\omega_i\dot{\eta}_i + \omega_i^2\eta = F_i , \tag{F8}$$

where; ζ_i is the modal damping-ratio associated with the i^{th} resonance at ω_i. The modal damping-ratio can be represented in terms of its mass-proportional and stiffness proportional components as [58]:

$$2\zeta_i\omega_i = \left(\alpha_i + \omega_i^2\beta\right). \tag{F9}$$

Further, it should be mentioned here that an identical treatment can be applied to a multiple degree of freedom system using the hysteresis damping model. With the assumption of proportional damping, the hysteresis damping matrix [H] of Eqn. F3 takes the form:

$$[H] = \alpha[M] + \beta[K], \tag{F10}$$

where; α and β are some constants [41].

A characteristic variation of ζ_i with ω_i for a practical structure is shown in Fig. F1. Typical variations of the mass- and stiffness-proportional damping-ratios are shown in Fig. F1. In practice, it has been found that mass-proportional damping component can represent friction-damping, while stiffness-proportional damping component can represent internal material damping [58].

The decrease of the damping-ratios with frequency for the solid stator-shell model indicates that the mass-proportional damping component or friction damping is dominant.

In the case of the laminated stator with windings, non-linear damping effects are present due to the composite nature of the vibrating structure. In addition to the damping characteristics provided in Fig. F1, one has to also incorporate the other non-linear effects.

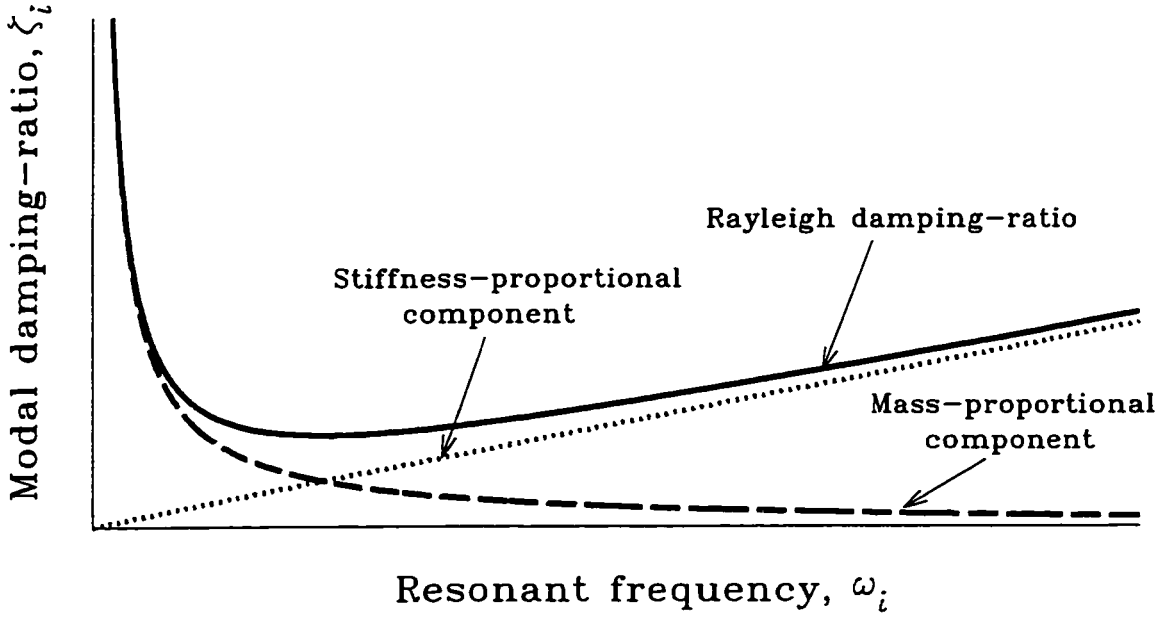

Figure F1 : Typical variation of the modal damping-ratio in the Rayleigh-damping model for practical structures [58].